Electrochemical Actuation of Porous Silicon in Aqueous Electrolytes

Vom Promotionsausschuss der
Technischen Universität Hamburg

zur Erlangung des akademischen Grades

Doktor der Naturwissenschaften (Dr. rer. nat.)

genehmigte Dissertation

von

Manuel Johannes Brinker

aus

Hamburg

2023

Gutachter:
Prof. Dr. rer. nat. Patrick Huber
Prof. Dr.-Ing. Robert Meißner

Tag der mündlichen Prüfung: 7.6.2023

Open Researcher and Contributor Identification (ORCID):
0000-0002-1729-459X

Digital Object Identifier (DOI):
10.15480/882.5201

Abstract

Porous silicon is highly versatile and exhibits outstanding characteristics as a functional material with respect to fundamental properties and applications in a wide variety of research fields, including medical and biological sciences, energy conversion or electronics and optics. Porous silicon can be formed in a self-organised manner in an electrochemical etching procedure, which results in a monolithic, monocrystalline, biocompatible porous material with a substantial inner surface area. An aspect of porous silicon that has up to date not prompted significant research concerns the mechanical properties of porous silicon. It includes in particular a mechanical functionalisation of porous silicon to achieve a reversible, directional change in porous silicon's macroscopic strain state controlled by an applied electric potential in aqueous electrolyte solutions, which is complicated by the non-existence of intrinsic piezoelectricity in the base material silicon.

In this thesis two different electrochemistry-inspired approaches are developed and investigated to integrate an actuator functionality into porous silicon. The first approach aims to utilise electrochemo-mechanical coupling at the interface of a porous silicon electrode immersed in an aqueous electrolyte solution. Due to the controlled, reversible capacitive assembly of ionic charge carriers in the electric double layer at the interface, a change in porous silicon's surface stress is induced and controlled by an applied electrical potential. A detailed electrochemical characterisation of porous silicon's behaviour in acidic and salt solutions is performed, in particular with respect to the role of anodic oxidation. A combined approach of in situ dilatometry and laser cantilever bending demonstrates a stable and highly reproducible actuation of the entire porous silicon structure through an electrosorption-induced surface stress change. The dependency of the actuation strain on the applied potential is inverse. A qualitative comparison to surface-stress-induced actuation at bulk silicon surfaces highlights the importance of the pore morphology, porous silicon's semiconductor features and silicon oxides. The electrocapillary coupling parameter is successfully determined for a bulk silicon surface for the first time within the framework of this thesis.

The second approach comprises the integration of the electroactive, electrically conductive polymer polypyrrole into the porous silicon pore structure to create a hybrid material. In an electrolyte solution an electrochemical change of polypyrrole's oxidation state induced by an applied potential is accompanied by an adjustment of electrolyte anions incorporated into the polymer backbone. As an associated reaction, the polymer exhibits a highly reversible macroscopic expansion or contraction. The hybrid's actuation is investigated by an in situ dilatometry study on the macroscopic level, while an in situ X-ray diffraction study yields insight into its impact on the porous silicon pore wall on the microscopic level. Polypyrrole is electrochemically polymerised in porous silicon with a significantly higher aspect ratio of pore length to pore diameter than reported before in literature. Overall, the hybrid shows a robust and highly reproducible electrochemical actuation that follows the applied potential and the accumulated charge with a highly linear dependency in phase. The hybrid material is well in the range of other polypyrrole-functionalised materials and classical piezo actuators characterised by their work density.

Contents

1. Introduction

Functional materials exhibit outstanding properties due to their inherent characteristics with respect to specific, designated tasks. At the centre of this work is the material porous silicon (pSi). In a wide variety of fields, including medical and biological sciences, energy conversion or electronics, porous silicon is investigated with respect to fundamental aspects of its functionalisation and a functional deployment in applications. In this work, porous silicon will be explored with regard to a mechanical functionalisation to integrate an adjustable, repeatable actuating property into the material.
Porous silicon was discovered by accident by the Uhlirs, husband and wife, working in the 1950s in the Bell laboratories. They aimed at developing an electrochemical method to electropolish silicon disks, called wafers, so that they could further be used to fabricate micro electronic circuits. During one of their procedures though, under the right or, from their point of view, wrong circumstances, the surface of the silicon wafer was not uniformly removed. Rather, etch pits formed on the surface and continued to grow into the wafer along the [100] direction to form pores.[1] Interest in the material rapidly increased in the early 1990s with two key publications. Lehmann and Gösele discovered light absorption effects caused by a quantum confinement in spectra of porous silicon while almost simultaneously Canham published an article on the photoluminescence of porous silicon.[2–4] The discovered quantum mechanical properties and the luminescence of the standard semiconductor silicon have garnered attention and have ever since led to a sustained research effort in a wide variety of research areas.
The base material for the synthesis of porous silicon are monocrystalline silicon wafers. Silicon is the second most common element contained in earth's crust and thus available in abundant quantities.[5] However, in nature silicon is not present in its elemental form but rather in numerous silicate minerals and pure silica.[5] Hence, elemental silicon has to be artificially prepared, often by reducing a silicon oxide compound by heating in the presence of a carbon source. A higher grade of purity is obtained by refining silicon further. Silicon can be produced in unparalleled qualities with impurities as low as one part per 10^{12}.[6] The zone melting process, for instance, allows to purify silicon, as impurity atoms are concentrated in one specific section, which can be separated from the remaining silicon in the end. Additionally, zone melting as well as the related Czochralski method results in a monocrystalline silicon material. These two processes are enabling a production of silicon with a desired purity in industrial quantities, which is of great importance for the semiconductor industry, as impurities in silicon play a decisive role with respect to its electrical and optical properties. Silicon has been and, for the foreseeable future, will be a highly relevant material for the semiconductor industry.[7]
Porous silicon can be formed self-organised in an electrochemical etching procedure with an electrolyte solution of hydrofluoric acid (HF). The synthesis results in a highly porous material with a significant inner surface area. The pore diameter can range over several orders of magnitude from approximately a nanometre to several micrometres. Interestingly, the porous silicon structure retains bulk silicon's highly monocrystalline features.[8]

The synthesised pores are characteristically anisotropic. The pores do not form an isotropic network structure as it is the case for Vycor glass [9] or nanoporous metals such as nanoporous gold (npg) [10]. Rather, porous silicon pores are, in a first order approximation, aligned in parallel. In case of 100 wafers used in this work, the pores are orthogonal to the surface of the wafer. Porous silicon constitutes a material which is synthesised in a monolithic form. This differentiates it from other, silica-based, porous materials, such as MCM-41 [11], SBA-15 [12], or KIT-6 [13] with synthesis routes that result in powders of porous particles. Due to the utilised top-down, electrochemical synthesis approach, porous silicon structures can be integrated into electrical circuit designs in regular micro machined silicon structures, for instance by masking the area meant to be porosified.[14] Thus, porous silicon applications and devices would possibly benefit from the already existing, large manufacturing capacities of standard silicon devices.
On a fundamental research level, porous silicon provides an excellent host material to study confinement effects of matter inside the pores, with regard to structure and dynamics.[15–20] Examples range from diffusion measurements of simple gases such as helium or argon [15, 21] to imbibition measurements with liquids, such as ethanol or water [19].
For energy conversion applications, porous silicon might play a larger role in the future.[22] Common, graphite or carbon-based, anode materials used in lithium ion batteries, begin to reach their theoretical capacitance for the lithium ion intercalation, e.g. $372\,\mathrm{mA\,h\,g^{-1}}$ for graphite.[23] The base material silicon has an exceptionally high, theoretical capacitance for lithium ions – ten fold higher than graphite at $3579\,\mathrm{mA\,h\,g^{-1}}$.[23, 24] However, volumetric expansion that occurs when the lithium ions are alloyed into silicon is about 300 %.[23, 25] Hence, bulk silicon as an anode material is strongly degraded and repeated charging is not possible. Porous silicon can possibly accommodate the significant volumetric expansion through various strategies. In particular porous silicon nanoparticles, nanowires or hollow nanospheres are promising candidates for lithium battery anode materials.[23, 26–31] Even energy harvesting via the use of porous silicon as a thermoelectric material is in the realm of possibilities.[32, 33] In a field more related to fundamental particle physics, porous silicon is also studied with regard to a positronium emitting device.[34]
Besides tuning the properties of porous silicon by changing the pore morphology, functionalisation of the pore space offers an additional mechanism to change, extend or enhance porous silicon's properties and applications drastically. Numerous synthesis schemes exist and are investigated, which use successive procedures to incorporate additional, functional materials into porous silicon pore space.[35] The class of incorporated materials varies greatly, as does their aggregate state and condition in the pore. Examples for such a functionalisation include the thermal conductivity of porous silicon, which can be highly altered by a filling of oil or water.[36, 37] Functionalisation schemes with liquids in general offer miscellaneous opportunities to tune porous silicon's properties and create adaptive hybrid materials, in which the soft phase, i.e. the liquid filling, adds novel functionality while the rigid scaffold structure of porous silicon provides a certain mechanical robustness.[35, 38] A functional filling with liquid crystals changes the optical properties of oxidised porous silicon.[39, 40] Porous silicon also enables direct laser writing of a polymeric photo resist inside the porous silicon pore space, which acts as a host material. The optical properties of lenses and waveguides written in this hybrid material far exceed those formed in the bulk polymer without the porous silicon support.[41] Furthermore, functionalisation is not only aimed at the pore space of porous silicon. Likewise, the

significant inner surface area is the target for adding functionality to porous silicon in interface-dominated applications. An abundance of surface-chemistry modification routes exists. Thereby, molecule groups are altered, added or exchanged directly at the porous silicon surface with customised processes.[42, 43] The modified surface enables a targeted selection of specific molecules and groups, which is especially interesting for applications in the biomedical and life sciences.

Porous silicon has been found to be biocompatible.[44] In the human body it degrades into non-toxic orthosilicic acid ($Si(OH)_4$) in aqueous environments, which easily leaves the body.[35, 45] Furthermore, porous silicon is bioactive. For instance, porous silicon actively promotes calcification on its surface, which would be advantageous for bone tissue implants.[46] Owing to these properties of porous silicon research into biomedical applications has been prompted.[47] For example, it is possible to load drugs into porous silicon. Due to the porous silicon host material, the drug's release kinetics are then tightly controllable.[48] From the early 1990s, a wide variety of different publications addresses applications in biomedical sensors [49–51], optics and electronic applications [52–56]. Particularly, a targeted, intentional modification of porous silicon's surface enables the detection of specific biological agents. For example, enzymes are detected by a change in photoluminescence intensity that occurs when the enzyme adsorbs on the respective surface group, as it opens up a quenching pathway for a non-radiant decay [52, 57]. Another example is a porous-silicon-based heterojunction, used in vivo for the optoelectronic manipulation of tissue, which combines optical, electronic, biomedical properties of porous silicon moulded into a single application.[58]

All these examples show that porous silicon is a highly versatile material. It is involved in a variety of fundamental research topics and covers a wide range of possible applications in energy storage and conversion, bio medical and life sciences as well as photonics or electronics. However, an aspect which has not prompted a significant amount of research yet is the mechanics of porous silicon, which will be outlined within the framework of this thesis – especially that previous studies mechanically characterising porous silicon have not adequately acknowledged the complex mechanics of the material. Moreover, a functionalisation of the mechanics of monolithic porous silicon, in particular, has not been achieved up to date. Owing to the crystal structure of silicon, no piezoelectric effect is present, although an anomalous piezo-resistance is present in strained, single silicon nanowires [59]. The non-existence of intrinsic piezoelectricity in the base material, i.e. silicon, renders a mechanical functionalisation difficult to achieve in porous silicon. Functionalisation refers here, in this classical sense, to receiving a proportional response of the material in the form of a directional strain to an applied electric stimulus. The process of transforming electrical to mechanical energy is then referred to as actuation and the responsible material as an actuator.[60] In measurement and control technology, actuators are widely used. They are often the counterpart to sensors, which convert signals into a mechanical response, and are therefore essential elements for control loops. A typical example of an application of a piezo actuator would be the opening and closing of a valve or a ventilation flap. Porous silicon with an actuator functionality has the benefit that it can also be applied in biological or biomedical environments due to its bio-compatibility. Moreover, an actuator functionality could be combined with porous silicon's vast variety of other properties for unique applications. A porous silicon gas sensor that exhibits an active mechanical reaction upon a detection event, could be for instance conceivable.

Among other materials, porous silicon has been examined with respect to an actuation in-

duced by humidity or gas sorption.[61–63] Also, liquid-adsorption-induced deformation has been investigated with the contributing objective to examine porous silicon's mechanical properties.[16, 64–66] Furthermore, actuation mechanisms achieved by specific electrochemical processes either within the porous silicon pore space or on the inner surface area could also be promising.[67–69] Recently, it has been shown that in a powder of porous silicon particles the cubic symmetry of silicon is slightly reduced to a tetrahedral one. Hence, a piezoelectric response in the powder is measured. A potential emerges when a layer of the powder is under a weight force.[70] However, the study does not explore the piezoelectric effect in monolithic porous silicon. A reversible actuator material involving silicon has been achieved by either depositing piezo-ceramic coatings on silicon or epitaxial heterostructures, particularly within the scope of nano and micromechanical systems, referred to as NEMS and MEMS.[71]

Within the framework of this thesis two approaches are developed and pursued to integrate an actuator functionality into porous silicon. The first approach is to utilise electrochemo-mechanical coupling. A change of surface stress on the inner surface area of a polarisable porous silicon electrode immersed in an electrolyte solution occurs, which is induced and controlled by a reversibly applied electrical potential. It is referred to as electrosorption. In the realm of porous metals, this approach is comprehensively investigated for various types of metals [10, 72–75] and has even been explored for nanoporous carbon monoliths [76]. At the interface of an electrically conductive electrode and an electrolyte solution, also referred to as an ionic conductor, an electric double layer forms.[77] Ions assemble on the electrolyte side of the interface in different layers and are counterbalanced by electrons on the solid, electrode side. The exact setting will be described in more detail in chapter 2. In its essence, the electric double layer, with the two types of charges on opposite sides of the interface, resembles a plate capacitor. Similar to a plate capacitor, the amount of charge stored on the surface of the electrode, can be adjusted by an applied potential. The response of the surface stress to the amount of accumulated charge q is reflected in a change in surface stress f. The electrocapillary coupling parameter ς links f to q and indicates the magnitude of the surface stress response.[78] It constitutes a basic materials parameter that quantifies the material's electrochemo-mechanical coupling to accumulated charge. On a fundamental level, the charge accumulation at the interface of the electrode has an influence upon interface, interatomic bonds, both in the in-plane direction and perpendicular to it. A charge reorganisation ensues, which leads to a force on the interface ions, so-called Hellmann-Feynman forces.[79] Essentially, these forces lead to a change in surface stress. This change itself induces an actuation effect in a non-porous, bulk material. An example is a clean metal surface such as gold or platinum.[75, 80, 81] In ab initio calculations, it is confirmed that, in principle, electrochemo-mechanical coupling can also be observed at silicon-electrolyte interfaces [82], although the semiconductor material silicon has decisively different electrical properties than a metal. Furthermore, the respective porous structure of porous silicon is highly anisotropic compared to the isotropic pore network of porous metals.

For the first time, the present thesis will explore the fundamental relation of accumulated charge and induced surface stress as well as the thereby enabled potential controlled actuation for porous silicon and directly at a non-porous, planar silicon surface. In situ laser cantilever bending along dilatometry experiments combined with cyclic voltammetry and step-coulombmetry will be performed to characterise their electrochemical actuation. The comparison of evolving surface stress at the planar bulk silicon surface and the

electrosorption-induced actuation in porous silicon will reveal mechanistic insights into the electrochemo-mechanical coupling, in particular with respect to the importance of the formation of silicon oxides, the roughness of the pore wall on the single-nanopore scale and the mechanical properties of porous silicon. Importantly, the overall analysis will include a thorough electrochemical characterisation of silicon electrodes in aqueous electrolytes. All in all, porous silicon has the potential to exhibit significant electrosorption-induced actuation. It combines a high inner surface area due to exhibiting an open porosity with directed, parallel pores. Moreover, the electrosorption-induced actuation is achieved in an abundant, biocompatible base material, facilely produced in wafer-scale, self-organised quantities. This would open up novel opportunities with on-chip applications regarding integrated, robust stress or strain generation and actuation.

The second approach comprises the combination of porous silicon as a scaffold structure with the electroactive, electrically conductive polymer polypyrrole (PPy). Polypyrrole's electrical conductivity is finely tunable and can reach a level on a par with carbon.[83] In an electrolyte solution, an electrochemical change of the polypyrrole oxidation state, induced by an applied potential, yields an increase or a decrease of the amount of delocalised charge carriers in the backbone of the polymer.[84, 85] As an associated response, ions from the electrolyte solution are either incorporated into the polymer structure of polypyrrole, or are expelled from it to preserve charge neutrality.[85] This process is highly reversible. Therefore, the whole of the polypyrrole structure experiences a macroscopic expansion or contraction [86], respectively. It renders polypyrrole an active actuation material with possible respective applications [87, 88]. The electrochemical cycling stability of polypyrrole [89, 90] and a generally low operating voltage [87] further accentuates this. Hence, it is referred to as an (artificial) muscle material.[84, 85, 91–94] Apart from the actuator functionality, a change in the oxidation state often is accompanied by a change of polypyrrole's optical features, i.e. absorption of light [95], its ionic permeability [96] and mechanical properties [97, 98].

Polypyrrole has been attracting research interest for quite some time. A main reason is its biocompatibility [99] which enables in vivo, bio-medical, sensor and actuator application elements [94], such as a bladder volume sensor [100]. Other application oriented research topics include microactuators [88], biomimetic robots [101] as well as artificial muscle materials [91, 102].

The actuation process in polypyrrole strongly depends on the transport properties of ions into and within the polymer.[103] Polypyrrole synthesised in thin-film geometries are suitable to facilitate desired transport and ion exchange kinetics and counter a possible actuation retardation.[104] Films of polypyrrole also enable the study of the anion-induced actuation by technique of X-ray reflectivity. By a comparison with electrochemical data, phenomena as a charge compensation by protons or a back flow of solvent molecules can be investigated.[105] Yet, polypyrrole thin-films may experience possible restrictions by the occurrence of creep [106, 107] or non-sustainable stresses during the actuation [108, 109]. In a more general sense, the thin-film geometry is particularly reliant on the supporting substrate, for example, bi-layer cantilevers [110], or fibres of conductive material with a coating of polypyrrole [111]. Thus, the supporting substrate has a significant influence on the overall properties.

A possible solution for these issues and the strategy that will be pursued in this work consists of using porous silicon as a scaffold material, which provides mechanical rigidity and robustness for polypyrrole.[112, 113] Its aim is to mimic various multiscale, biological

composite materials in nature.[114, 115] In effect the hybrid material of polypyrrole and porous silicon consists of merely a few, simple base elemental substances, as hydrogen, carbon, silicon, oxygen, nitrogen and chloride. The porous silicon pores, up to one hundred billions per square centimetre, are filled by polypyrrole and guide its actuation in an electrolyte solution upon potential-induced ion incorporation and extraction. Hence, a direct, controlled electrochemical actuation of porous silicon is achieved and will be thoroughly investigated and characterised here by macroscopic in situ dilatometry measurements and under electrochemical control. The electrochemical actuation of the hybrid system of polypyrrole and porous silicon on the microscopical level is investigated by an accurate in situ X-ray diffraction (XRD) study, specifically, how the polypyrrole-swelling-induced actuation acts on the pore walls in the in-plane and out-of-plane direction of porous silicon films.
The presented thesis is structured as follows. Chapter 2 deals with the theoretical background. It gives a short introduction to semiconductors, in particular silicon, followed by an in-depth description of the semiconductor-electrolyte interface and its electrochemistry. Next, the anodic oxidation of silicon is described and the properties of porous silicon, as the material in focus here, are summarised. For the electrosorption-induced actuation of plain porous silicon, it is important to understand the thermodynamic electrocapillary phenomenon and, thus, it is discussed in section 2.5. For the electrochemical actuation of the polypyrrole-porous-silicon hybrid material, the polymer is vital and the theoretical background chapter ends with a section on polypyrrole.
In chapter 3 the synthesis route of the materials is introduced. This concerns especially the synthesis of porous silicon and the subsequent electropolymerisation of polypyrrole in its pore space and the respective characterisation methods. Furthermore, the measurement schemes developed and utilised for this work are introduced in chapter 3. At its centre are the in situ actuation experiments, which consist of a dilatometer, a laser cantilever bending setup and a synchrotron-based X-ray diffraction setup.
Chapter 4 will present and discuss the results of the electrosorption-induced actuation for porous silicon based on two actuation studies – a dilatometry and a cantilever bending study. Chapter 5 presents and discusses the results of the actuation of the polypyrrole porous silicon hybrid material.
The work concludes with a summary and an outlook, which encompasses the direction of future research on this subject. Furthermore potential enhancements of the introduced material systems are discussed.

2. Theoretical Description

In this chapter the theoretical background will be discussed. First of all, a short introduction to basic principles of semiconductor physics will be given, as the base material for the here investigated material is silicon. Next, the principles of semiconductor electrochemistry, with a focus on the semiconductor-electrolyte-interface, are discussed. The chapter will deal with the phenomenon of anodic oxidation of silicon before proceeding to the thermodynamic concept of solid electrode's electrocapillarity in electrolytes. Lastly, the properties of the electrically conductive, electroactive polymer polypyrrole will be described.

2.1. Properties of Monocrystalline Silicon

Silicon is a semiconducting material. The specific resistivity of intrinsic silicon is in the order of $10\,\mathrm{k\Omega\,cm}$ at room temperature (RT).[7] In comparison, gold has a resistivity of approximately $2.4\,\mathrm{\mu\Omega\,cm}$ [116], which is about ten orders of magnitude smaller than intrinsic silicon. The resistivity of silicon can be intentionally altered in a doping process, which is introduced further below in this section. The above stated resistivity is valid for intrinsic silicon, whereby a material with minimal impurities is referred to. Contamination levels below 10^{11} impurity atoms per cm^3 are achievable [117].
Monocrystalline silicon has a diamond cubic crystal structure. It has a face-centred cubic (fcc) lattice with a two atomic base of identical atoms. One atom is directly on the lattice site, $(0, 0, 0)$ and the second one is shifted for one fourth along the unit cell diagonal, $(1/4, 1/4, 1/4)a$, where $a = 0.543\,\mathrm{nm}$ denotes the silicon lattice constant.[119, 120] The diamond cubic crystal structure is shown in Figure 2.1(a). Each of the silicon atoms has four next neighbours, i.e. has a tetrahedal configuration.[119] The packing density is approximately 34 %. A unit cell possesses eight atoms for the diamond crystal structure, which corresponds to approximately $5 \cdot 10^{22}$ atoms cm^{-3}.[7] In total, bulk silicon has a density of $2.33\,\mathrm{g\,cm}^{-3}$.[52] Since the symmetry of silicon is cubic, the six faces of the unit cell are equivalent and are given by $\{100\}$. Bulk silicon utilised in this work consists of 100 silicon wafers. Wafers in terms of silicon processing represent thin, circular discs, which are sawn out of a monocrystalline silicon rod often grown by the Czochralski method.[121] 100 silicon wafers are accordingly polished on the (100) surface. Besides the [100] direction, other directions of importance for this work are [110] and [111]. The cubic symmetry of silicon is responsible for characteristic differences of the mechanical properties. The values for the Young's modulus in the crystallographic direction are $Y_{100} = 130\,\mathrm{GPa}$, $Y_{110} = 169\,\mathrm{GPa}$ and $Y_{111} = 188\,\mathrm{GPa}$ for [100], [110] and [111] directions, respectively.[122] Poisson's ratio in these directions is $\nu_{100} = 0.28$, $\nu_{110} = 0.064$ and $\nu_{111} = 0.36$.[122] The bulk modulus of silicon amounts to $K = 97.8\,\mathrm{GPa}$.[122]
The electronic structure of a monocrystalline material can be comprehended by considering the periodic crystalline potential of the positive atomic trunks, which act on the

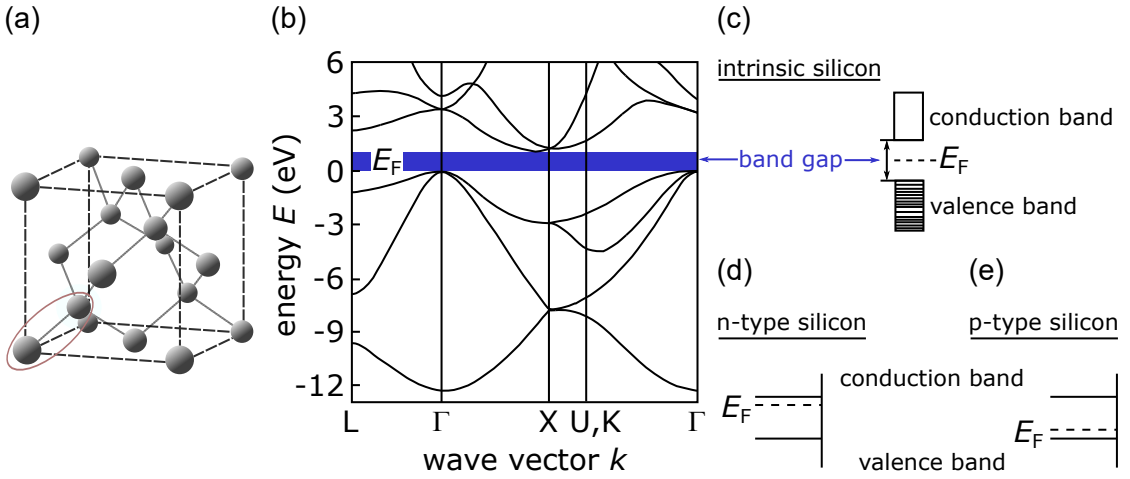

Figure 2.1.: **Basic properties of silicon.** (a) Diamond crystal structure of silicon with an indication of the two atomic base. (b) Detailed view of the band structure of silicon with different k wave vectors in the first Brillouin zone at points L, Γ, X, U and K (abscissa) and the respective energy levels (ordinate). At Fermi energy E_F the bandgap is visible and indicated by the blue rectangle. Modified with permission from reference [118]. Simplified, schematic band structure for (c) intrinsic, (d) n-type and (e) p-type silicon. Indicated are the Fermi energy E_F for intrinsic silicon and the Fermi energies of the donor level in n-type silicon and the acceptor level in p-type silicon, respectively.

electrons. The interaction of all atoms in a crystal influences the energy levels. Essentially, a crystal composed of N atoms has energy levels split into N different states. As a crystal consists of $\approx 10^{22}$ atoms, the variation between the resulting energy states is small and the energy states can be rather considered as continuous energy bands. Another result of the periodic potential on the energy levels of electrons in crystals, is the emergence of forbidden zones or bandgaps. Summarising, qualitatively, at the Brillouin zone border electron waves transform into stationary waves due to Bragg reflections. The energy states at the zone boundary split into different bands that repel each other. Thus, an energy gap is present.[123] The detailed mathematical derivation of the band structure of silicon is beyond the scope of this work. A comprehensive description of these phenomena is found in a standard work on solid state physics, such as references [119, 123]. The consequence of a periodic potential consideration that is important for this work regarding electrical conductivity is the formation of a band structure with intermediate forbidden bandgaps. To obtain the ground state of the crystal at a temperature of 0 K, the energy states are filled according to the Pauli principle from bottom to top. The highest energy that is reached in this manner is the Fermi energy E_F.[123] At temperatures above absolute zero, the strict barrier that E_F represents is softened and their thermal distribution enables electrons to occupy higher states than E_F. This occurs in accordance with Fermi-Dirac statistics. An essential characteristic of a monocrystalline material is defined by the position of E_F with regard to the occupied bands. In principle two different scenarios are possible. The highest band can be either partially filled so that the Fermi energy lies within the respective band. If an electric field is applied, an electron can readily occupy

a higher state and can gain an additional momentum. Hence, a current flows in an unimpeded manner. This holds true for metallic conductors. On the other hand, the Fermi energy can be located in the bandgap between the highest, fully occupied band and the lowest, empty band.[123] Depending on the magnitude of the bandgap, the material can be a semiconductor or an insulator. If a potential is applied to the crystal, the electrons cannot easily gain an additional impulse since all bands are occupied. However, an electrical conductivity is accomplished if charge carriers are excited to the next band. In the case of an electrical insulator, moderate electrical fields cannot provide the energy in the eV-range to overcome the bandgap. Semiconductors at temperatures higher than absolute zero, e.g. room temperature, possess a bandgap which is small enough so that a considerable amount of charge carriers enter otherwise unoccupied bands above E_F in consensus with Fermi-Dirac statistics. This results in a finite electrical conductivity in semiconductors.[123] For electrical insulators the bandgap is too large to be overcome due to thermal fluctuations.[123] A detailed graph of the band structure of silicon is displayed in Figure 2.1(b). The figure shows the existing bands (ordinate) for different directions in the first Brillouin zone (abscissa, L, Γ, X, U and K points). The bandgap between the highest occupied and the lowest empty band is highlighted. For silicon it amounts to 1.17 eV at $T = 0\,\mathrm{K}$.[124] A band structure schematic of silicon, often used to discuss fundamental aspects related to its conductivity, is displayed in Figure 2.1(c). Here, the band structure is simplified with regard to the wave-vector dependency. The highest occupied band is at the Γ point, i.e. $k = (0, 0, 0)$ and is referred to as the valence band. By contrast, the minimum of the conduction band, i.e. the lowest unoccupied band, is located close to the X point at approximately $0.85\pi/a$ along the $(1, 0, 0)$ direction.[119] Thus, silicon is also referred to as an indirect semiconductor since both points are not at an identical k value.[119]

Figure 2.1(c) shows the band schematic of intrinsic silicon, which has an impurity concentration of $1.5 \cdot 10^{10}\,\mathrm{cm}^{-3}$.[123] A crucial property of semiconductors is the ability to introduce other atomic species in a controlled manner as deliberate impurities to tailor the conductivity – a process called doping. Thereby, the electrical conductivity is adjusted and increased by orders of magnitude. If an atom with five valence electrons, e.g. phosphorus (P), arsenic (As) or antimony (Sb), replaces a silicon atom in the lattice the fifth, additional, outer shell electron is not required for the tetrahedral covalent bond. Hence, only a small amount of energy is required to split the electron off of its atomic trunk. The doping atom is also referred to as a donor. The energy required is approximately 30 meV and is in the range of thermal energy at RT, which amounts to roughly 25 meV. Thus, the extra electron of the doping atom is readily provided for charge transport at RT. In the band diagram the doping atom is expressed as an additional energy band that is located directly below the conduction band.[123] The respective band diagram for this n-type silicon is depicted in Figure 2.1(d).

p-type silicon is doped with a trivalent atom, such as boron (B). The doping atom is missing one electron for the tetrahedral binding. That means, it readily accepts an electron. Accordingly, the doping atom is called an acceptor. Formally, the missing electron is described as a positively charged (electron) hole. So, the charge conduction in p-type silicon is carried by these positive charges. A hole is generated when an electron is excited from the valence band into the acceptor band. The acceptor band is located approximately as close to the valence band in the bandgap as the donator band is with respect to the conduction band [123], cf. band diagram Figure 2.1(e). Doping has a negligible effect on

the mechanical properties of silicon.[122]
The interface of a semiconductor, e.g. silicon to a metal constitutes an interesting case for different applications. The Fermi energies of a semiconductor and a metal are in general at different levels with respect to the vacuum level.[119] The position of the Fermi energy in a metal is denoted by the work function

$$W_{\mathrm{m}} = (E_{\mathrm{vac}} - E_{\mathrm{F}}) > 0, \tag{2.1}$$

where E_{vac} is the vacuum energy. The work function essentially describes the difference in energy of an electron in the metal and the theoretical case of an electron at rest at an infinite distance.[119] In a metal a possible shift of E_{F} through flow of charge carriers to or from the contacted silicon is negligible since the electron density in the metal's conduction band is high. E_{F} in silicon heavily depends on the type and density of doping, as described above. Thus, in terms of a silicon-metal-interface it is more expedient to consider the electron affinity $\chi_{\mathrm{s}} > 0$ from vacuum level to conduction band edge. The difference between the Fermi level and the conduction band edge is $eV_{\mathrm{c}} = E_{\mathrm{c}} - E_{\mathrm{F}}$. Together they yield the work function for silicon [123]

$$W_{\mathrm{s}} = (E_{\mathrm{vac}} - (e\chi_{\mathrm{s}} + eV_{\mathrm{c}})) > 0. \tag{2.2}$$

Essentially, two characteristic cases are differentiated when metal and silicon are not in contact which are $W_{\mathrm{m}} > W_{\mathrm{s}}$ and $W_{\mathrm{m}} < W_{\mathrm{s}}$, respectively. If the two materials are brought in contact with each other, E_{F} on both sides of the interface will equilibrate to a common level. This leads to an up or downward bending of the silicon conduction and valence band at the interface.[123]
In principle, the metal-silicon-contact is comparable to a silicon electrode in contact with an electrolyte solution, where the metal work function is akin to a redox potential of an electrolyte species. The outcome is comparable, i.e. a band bending ensues. The case of a semiconductor-electrolyte-contact will be extensively discussed in the next section 2.2. There, the analysis of band diagram will also feature depictions of band bending. In the remaining part of this section, the metal-silicon-contact will be approached in a condensed fashion. The focus will be on the nature of its electronic contact due to its importance for the experimental work, as will be further discussed in chapter 3.
For n-type silicon, $W_{\mathrm{m}} > W_{\mathrm{s}}$ causes an upward bending of conduction and valence band in proximity to the interface. Thus, the majority charge carriers, i.e. electrons, migrate away from the interface and a space charge region (SCR) emerges, as only the positively charged atomic trunks remain.[123] On the metal side of the interface, electrons assemble in a very thin layer ($< 1\,\mathrm{nm}$).[123] Electrons are impaired to enter the SCR. Qualitatively, the flow of charge carriers across the SCR does not linearly depend on the voltage. Rather, the contact has an exponential dependence of current on voltage and can thus be characterised as more diode like.[123]
The same holds true for p-type semiconductors if $W_{\mathrm{m}} < W_{\mathrm{s}}$ but shall not be elaborated further here for the sake of concision. A metal silicon contact exhibiting such a diode-like, rectifying behaviour is referred to as a Schottky contact.[123]
On the other hand, $W_{\mathrm{m}} < W_{\mathrm{s}}$ leads to a downward band bending for n-type silicon at the metal interface and thus electrons can easily accumulate at the interface. As a consequence, electrons can flow in an unimpeded manner across the silicon metal contact in response to a change in voltage. The dependence of current on voltage is linear and the

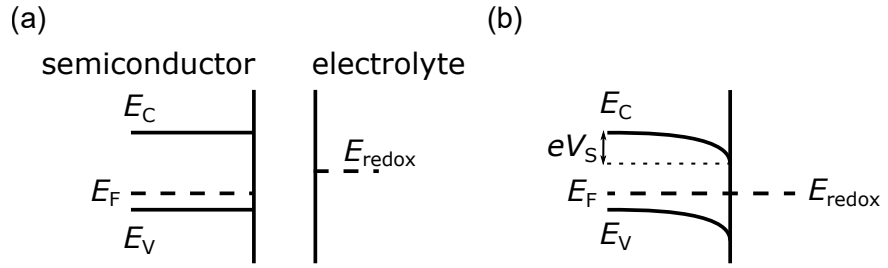

Figure 2.2.: **p-type semiconductor-electrolyte interface.** (a) Band structure of a p-type semiconductor, on the left side, and the redox potential E_{redox} of an electrolyte, on the right side, when both are not at contact. (b) Band structure of a p-type semiconductor in contact with an electrolyte at their interface. Visible is a band bending of conduction and valence band with band drop potential V_{S} due to the equilibration of E_{F} and E_{redox}.

contact is then referred to as ohmic.[123] For p-type silicon this is the case for $W_{\mathrm{m}} > W_{\mathrm{s}}$. Such an ohmic behaviour is important for various processes in the semiconductor industry. For this work the establishment of an ohmic contact to both p- and n-type silicon is necessary, as current flows, generated by conducted electrochemical experiments, would be altered by a non-ohmic contact to the silicon electrodes. In practice, an ohmic contact to n-type silicon is established by depositing a gold-antimony (Au-Sb) layer, which contains 0.1 % antimony.[52] For p-type silicon an ohmic contact can be accomplished by a layer of aluminium (Al).[52] For both types of silicon, the following method also works. Liquid gallium-indium (Ga-In) eutectic is worked into the silicon surface by scratching with a carbide or diamond scribe and subsequently sealed off by conductive silver paint.[52]

2.2. Principles of Semiconductor Electrochemistry

This section provides the basic concepts of the electrochemistry of semiconductors in general and silicon in particular. The section follows the theoretical description of reference [120].

2.2.1. The Electric Double Layer

As already discussed in section 2.1, the energy spectrum of electrons in an idealised crystal as silicon is described in terms of energy bands. The highest filled band and the lowest unfilled band, i.e. the valence and conduction band, respectively, are of importance for the here discussed phenomena.
The electrons in an electrolyte associated with the electrolyte's ions can be characterised in an equivalent manner to their semiconductor counterparts. Thereby, the redox potential E_{redox} describes the disposition of the involved species to provide or accept electrons. Thus, E_{redox} can be considered as the electrolyte solution's effective Fermi level. When the electrolyte solution is brought into contact with a semiconductor surface, the two respective energy levels in both phases equilibrate, i.e. $E_{\mathrm{F}} = E_{\mathrm{redox}}$. Figure 2.2(a) exemplarily depicts the case of a p-type semiconductor electrolyte interface with a Fermi energy lower than the redox potential. To counter this deviation, electrons flow from the electrolyte

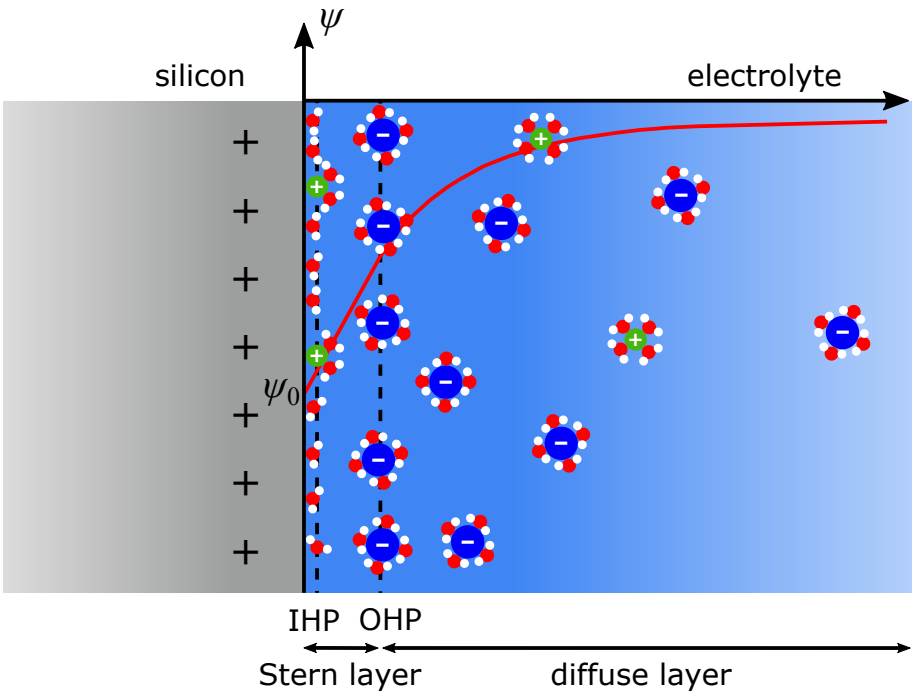

Figure 2.3.: **Electric double layer.** Detailed schematic of the electric double layer developing at the interface of a semiconductor with an electrolyte. Inner (IHP) and outer Helmholtz planes (OHP) are the planes of specifically adsorbed ions (in the depicted case cations (green)) and non-specifically adsorbed anions (blue), respectively. Both ion species have solvation shells of water molecules (red and white), which also accumulate at the surface of the semiconductor. The assemblies of immobile ions at the IHP and OHP form the Stern layer. By contrast, the anions in the diffuse, or Gouy-Chapman, layer are mobile. Their concentration is decreasing with increasing distance from the interface. The course of potential ψ is also indicated.

to the semiconductor, which in turn leads to a surplus charge in the semiconductor. In a metal these charge carriers reside in an Å-thick layer at the surface. By contrast, in a semiconductor the excess charge carriers are distributed over the space charge region below the surface. The resulting electric field of the accumulated charge is responsible for the bending of the bands. In case of a p-type semiconductor it is a downward bending, as depicted in Figure 2.2(b). The semiconductor is then negatively charged with respect to the electrolyte. The potential of the band drop is denoted as V_S.
Conversely, at the electrolyte side of the interface ions are assembling in a charged layer themselves. This ionic layer is referred to as the electric double layer and is depicted in Figure 2.3. It can be further divided. The outer Helmholtz plane (OHP) denotes the point of closest approach for mobile, solvated ions from the bulk electrolyte solution. Ions that are attracted to the charged interface to counterbalance the charge accumulated in the SCR on the semiconductor side of the interface are located at this OHP. These ions are of opposite sign with respect to the SCR charge. In the case of Figure 2.3, a positively charged semiconductor is considered and the SCR holds a surplus of holes. Therefore, an-

ions are assembling at the OHP. As the relevant electrolytes used in this work are aqueous, polarised water molecules need to be taken into account. Accordingly, in Figure 2.3 these are depicted as well and form a solvation shell around the ions to screen the respective electric field of the ion.[125] Moreover, the water molecules also bond to the polarised semiconductor surface according to their dipole moment. Ions directly in contact with the interface, in the case of Figure 2.3 cations, lose a part of their solvation shell and bond directly to the surface due to chemically interacting with the surface in a chemisorption process.[126] The location of these ions is named the inner Helmholtz plane (IHP). The entirety of these ions at the interface constitutes an adsorbed, immobile layer of ions up to the OHP and is referred to as the Helmholtz or Stern layer.
Conversely, beyond the OHP mobile, solvated ions, which satisfy Poisson-Boltzmann statistics, are present in a diffuse or Gouy-Chapman layer up to the point where the concentration reaches that of the bulk electrolyte solution. The thickness of the diffuse layer is essentially determined by the Poisson-Boltzmann theory on the potential distribution in an electrolyte in contact with a charged surface. For the idealised case of a planar, indefinitely expanded surface the potential distribution $\psi(x)$ in the direction normal to the surface x is calculated by [125, 127]

$$\psi(x) = \psi_0 \cdot \exp(-\kappa x), \tag{2.3}$$

with ψ_0 being the potential at the surface ($x = 0$) and

$$\kappa = {\lambda_\mathrm{D}}^{-1} = \sqrt{\frac{2c_0 e^2}{\varepsilon_\mathrm{r}\varepsilon_0 k_\mathrm{B} T}}, \tag{2.4}$$

where λ_D denotes the Debye length, e the elementary charge and ε_r and ε_0 are the relative and vacuum permittivity, respectively. k_B symbolises the Boltzmann constant and T requires the absolute temperature in K. c_0 here denotes the concentration of a monovalent ion of a singular type, as mainly these specific electrolytes are considered in this work. In the case of several ionic charge carriers with various valencies and concentrations c_0 has to be replaced by a sum of $\sum_i {z_\mathrm{i}}^2 \cdot {c_0}^2$ over different species i with their charge valence z.[125] It should be noted that the concentration has to be provided in particles per m^3 in this general form of the equation. For a monovalent salt diluted in water at 25 °C the Debye length of equation 2.4 simplifies to

$$\lambda_\mathrm{D} = \frac{3.04\,\text{Å}}{\sqrt{c_0 \frac{\mathrm{L}}{\mathrm{mol}}}}, \tag{2.5}$$

now with the concentration c_0 in $\mathrm{mol\,L^{-1}}$. A concentration of $0.1\,\mathrm{mol\,L^{-1}}$, for instance, yields a Debye length of $\lambda_\mathrm{D} = 9.6\,\text{Å}$. For higher concentrations, the shielding becomes even more effective and the Gouy-Chapman layer effectively merges with the Helmholtz layer at the OHP.
The differential capacitance C_GC of the Gouy-Chapman layer is described by the charge per surface area on the electrode Q and ψ_0 by [125]

$$C_\mathrm{GC} = \frac{\mathrm{d}Q}{\mathrm{d}\psi_0} = \sqrt{\frac{2e^2 c_0 \varepsilon_\mathrm{r}\varepsilon_0}{k_\mathrm{B} T}} \cdot \cosh\left(\frac{e\psi_0}{2k_\mathrm{B} T}\right) = \frac{\varepsilon_\mathrm{r}\varepsilon_0}{\lambda_\mathrm{D}} \cdot \cosh\left(\frac{e\psi_0}{2k_\mathrm{B} T}\right). \tag{2.6}$$

For small potentials the last term is approximated by unity and equation 2.6 yields $C_{\mathrm{GC}} = \frac{\varepsilon_{\mathrm{r}}\varepsilon_0}{\lambda_{\mathrm{D}}}$. Hence, C_{GC} remarkably resembles the capacitance of a plate capacitor per plate area, where the Debye length λ_{D} denotes the distance of the plates.

2.2.2. Energy Levels at the Semiconductor-Electrolyte Interface

In the next part of this section the energy levels at the semiconductor electrolyte interface will be discussed. The Nernst equation addresses the electrons' chemical potential of a redox couple by [120]

$$\psi_{\mathrm{redox}} = \psi^0_{\mathrm{redox}} + k_{\mathrm{B}}T \ln\left(\frac{a_{\mathrm{ox}}}{a_{\mathrm{red}}}\right), \tag{2.7}$$

where ψ^0_{redox} is the standard redox potential and a_{ox} and a_{red} are the activities of the oxidised and the reduced species. Generally, ψ_{redox} is denoted versus the standard hydrogen electrode potential (SHE). This is a convenient method of referring to electrochemical potentials since the SHE has an exactly defined energy, $E_{\mathrm{SHE}} = -4.5\,\mathrm{eV}$, with respect to the free electron energy in vacuum. Accordingly, the electrode potential of the redox couple is represented by $E_{\mathrm{redox}} = E_{\mathrm{SHE}} - e \cdot \psi_{\mathrm{redox}}$. The redox potential E_{redox} represents the averaged reduced and oxidised states' energies of the species involved. E_{redox} can be further divided into the energy levels of the reduced and oxidised species, E_{red} and E_{ox}, respectively, with $E_{\mathrm{redox}} = 1/2 \cdot (E_{\mathrm{red}} + E_{\mathrm{ox}})$. In this regard, E_{red} and E_{ox} solely represent the most probable energy levels. These levels are subject to a distribution because solvent molecules with dipoles surround the ions in the solution. As a result of the constant rotation and fluctuation of the solvation shell's molecules, a fluctuation in the polarisation is induced, which causes a broadening of the electron's energy level. For a comprehensive description, the density of occupied reduced and oxidised states is described by a Gaussian distribution. However, for the further treatment of the semiconductor electrolyte interface the unified energy level of E_{redox} is here sufficient.
As already mentioned, when the semiconductor comes into contact with the electrolyte, the equilibrium condition at the interface demands an equalising of the energy levels in both media, i.e. $E_{\mathrm{F}} = E_{\mathrm{redox}}$. Therefore, electrons are migrating across the interface and change the charge distribution at the interface until equilibrium is accomplished. Figure 2.4(a) shows a schematic depiction of the band structure in the interface area. While V_{S} quantifies the band bending at the semiconductor side, as already described above, V_{H} indicates the potential drop across the Helmholtz layer and is accordingly termed the Helmholtz potential. By adjusting the pH value of the electrolyte solution, V_{H} can be decreased and even tuned down to zero. This specific pH values is accordingly termed point of zero charge. For a silicon electrode the point of zero charge approximately amounts to pH 2.2. Silicon is readily covered by a native oxide layer, as discussed below in section 2.3. Thus, the point of zero charge is similar to that of silicon dioxide.[128, 129]
The position of the band edges directly at the interface are labelled E_{CS} and E_{VS} for conduction and valence band, respectively. An external polarisation of the semiconductor electrode is achieved by an applied potential V_{m}. In case no potential is applied, V_{m} is the open-circuit potential or abbreviated OCP. The applied potential V_{m} influences E_{F} and V_{S}. It is possible to achieve a semiconductor state without a charge excess at the interface. This state is accompanied by the absence of an SCR and thus a disappearing

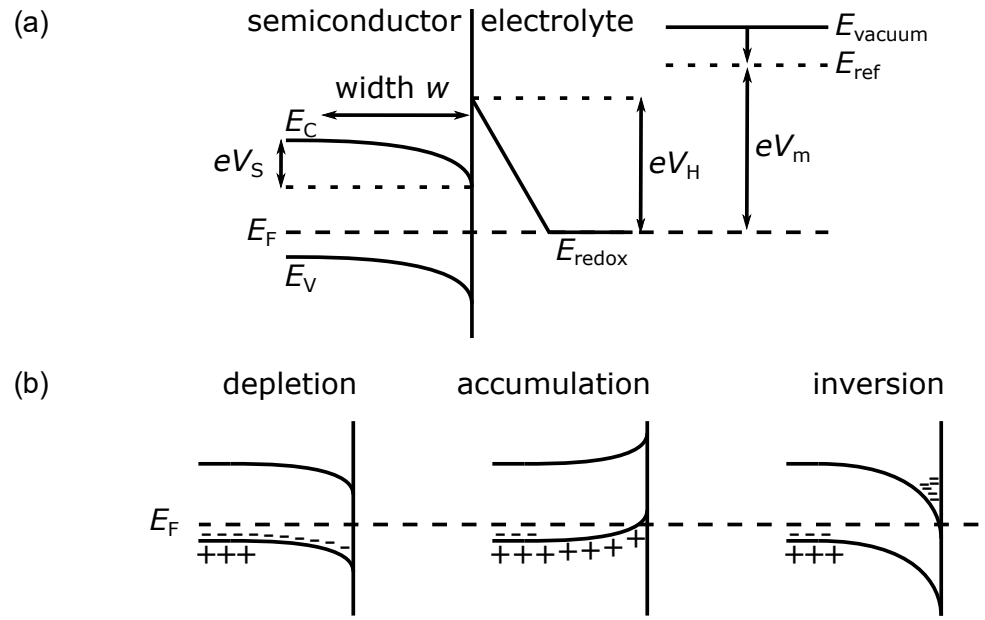

Figure 2.4.: **Energy levels at the semiconductor electrolyte interface.** (a) Energy levels at the interface of a p-type semiconductor side, including the band bending potential V_S (multiplied with the elemental charge e for an energy centred consideration) and the width w of the SCR. On the electrolyte side of the interface, the potential dropped in the Helmholtz layer V_H is depicted as well as the applied potential V_m with respect to a reference. Adapted with permission from reference [120]. (b) Depletion, accumulation and inversion states with p-type semiconductor bands at the electrolyte interface caused by different applied potentials.

of band bending. Therefore, the potential under which this state occurs is termed the flatband potential V_{fb}. In general, the flatband potential is expressed as

$$V_{fb} = V_m - V_S. \tag{2.8}$$

The flatband potential is an important quantity since it connects semiconductor charge carrier energy levels and electrolyte redox couple. Furthermore, it constitutes a parameter that can be determined experimentally and has a link to those parameters derived in semiconductor physics and electrochemistry.

2.2.3. Potential and Charge Distribution in Space Charge Layer

To gain a deeper understanding of the benefit of V_{fb}, the charge distribution of the SCR has to be investigated. It is described by the Poisson equation

$$\frac{d^2V}{dx^2} = \frac{e}{\varepsilon_r \varepsilon_0} \cdot [N_d - N_a - n(x) - p(x)], \tag{2.9}$$

with x denoting the distance from the interface. While N_d and N_a are the donor and acceptor atom density, respectively, $n(x)$ and $p(x)$ are the electron and hole densities. The latter follow the Boltzmann distribution in the absence of a current.[120] They read

$$n(x) = n_0 \exp\left(-\frac{eV}{k_\mathrm{B}T}\right) \tag{2.10}$$

and

$$p(x) = p_0 \exp\left(\frac{eV}{k_\mathrm{B}T}\right), \tag{2.11}$$

where $V = \psi_\mathrm{Bulk} - \psi(x)$ denotes the polarisation. The carrier density in the bulk of the silicon, far from the surface, is denoted by n_0 and p_0 for electrons and holes, respectively. They are connected via the intrinsic carrier density n_i, an important metric for semiconductors, defined by $n_0 p_0 = n_\mathrm{i}^2$.[130] Outside of the SCR, in the bulk of the semiconductor charge neutrality must prevail and therefore $N_\mathrm{d} - N_\mathrm{a} = n_0 - p_0$.[130]
Within the SCR the charge carrier density is determined by the doping atoms and thus the electron and hole densities are $n_0 = N_\mathrm{d}$ and $p_0 = N_\mathrm{a}$, respectively. At the interface, i.e. $x = 0$, V equals V_S and equations 2.10 and 2.11 convert to

$$n(x)_{x=0} = n_\mathrm{int} = n_0 \exp\left(-\frac{eV_\mathrm{S}}{k_\mathrm{B}T}\right) \tag{2.12}$$

and

$$p(x)_{x=0} = p_\mathrm{int} = p_0 \exp\left(\frac{eV_\mathrm{S}}{k_\mathrm{B}T}\right). \tag{2.13}$$

Depending on the applied potential and the equilibrium conditions at the semiconductor, three possible states might prevail at the interface. These are depletion, accumulation and inversion and are illustrated for a p-type material in Figure 2.4(b).
The first case considered here is depletion. The depletion layer plays an important role in the electrochemistry of semiconductors and is discussed here in detail. A depletion layer is formed when the interface area is depleted of majority charge carriers due to the respective band bending. That is, in an n-type semiconductor a positive band bending deprives the interface region of electrons and a negative band bending in a p-type semiconductor depletes the interface region of holes. The charge left in the depletion layer stems from the remaining ionised dopants. Hence, the Poisson equation 2.9 for a p-type material simplifies to

$$\frac{\mathrm{d}^2V}{\mathrm{d}x^2} = -\frac{eN_\mathrm{a}}{\varepsilon_\mathrm{r}\varepsilon_0} \cdot \left[\exp\left(\frac{eV}{k_\mathrm{B}T}\right) + 1\right], \tag{2.14}$$

where the first term addresses the contribution of the holes in the valence band, which are depleted from the SCR, and the second term represents the immobile, negatively charged dopant ions in the silicon.
One integration over $\mathrm{d}V/\mathrm{d}x$ with the constraint $V(x = 0) = 0$ yields

$$\left(\frac{\mathrm{d}V}{\mathrm{d}x}\right)^2 = -\frac{2eN_\mathrm{a}}{\varepsilon_\mathrm{r}\varepsilon_0} \cdot \left[V - \frac{k_\mathrm{B}T}{e}\left(\exp\left(\frac{eV}{k_\mathrm{B}T}\right) + 1\right)\right]. \tag{2.15}$$

Assuming that the band bending potential V_S directly at the interface, i.e. $V = V_\mathrm{S}$, is small, the factor $\exp\left(eV_\mathrm{S}/(k_\mathrm{B}T)\right) \approx 0$ is neglected. Hence, equation 2.15 is reduced to

$$\frac{\mathrm{d}V}{\mathrm{d}x}(V = V_\mathrm{S}) = \left(-\frac{2eN_\mathrm{a}}{\varepsilon_\mathrm{r}\varepsilon_0} \cdot \left[V_\mathrm{S} - \frac{k_\mathrm{B}T}{e}\right]\right)^{1/2}. \tag{2.16}$$

In this present case of a p-type semiconductor in depletion state the band at the interface is bend downwards and V_S is negative. Hence, the square root results in a real value. Gauss' law relates equation 2.16 to the total charge in the SCR per electrode surface area Q_{scr} by

$$\mathrm{d}V/\mathrm{d}x(V = V_S) = Q_{scr}/(\varepsilon_r\varepsilon_0) \tag{2.17}$$

Subsequently, an expression for the capacitance of the SCR C_{scr} is obtained by

$$\begin{aligned} C_{scr} &= \frac{\mathrm{d}Q_{scr}}{\mathrm{d}V_S} = \frac{\mathrm{d}}{\mathrm{d}V_S}\left(\varepsilon_r\varepsilon_0 \cdot \mathrm{d}V/\mathrm{d}x(V = V_S)\right) \\ &= \frac{\mathrm{d}}{\mathrm{d}V_S}\left(\left(-2eN_a\varepsilon_r\varepsilon_0 \cdot \left[V_S - \frac{k_BT}{e}\right]\right)^{1/2}\right) \\ &= \left(\frac{-eN_a\varepsilon_r\varepsilon_0}{2\left(V_S - \frac{k_BT}{e}\right)}\right)^{1/2} \end{aligned} \tag{2.18}$$

$$\begin{aligned} \Rightarrow C_{scr}^{-2} &= -\frac{2}{eN_a\varepsilon_r\varepsilon_0}\left(V_S - \frac{k_BT}{e}\right) \\ &= -\frac{2}{eN_a\varepsilon_r\varepsilon_0}\left(V_m - V_{fb} - \frac{k_BT}{e}\right). \end{aligned} \tag{2.19}$$

Equation 2.19 is the Mott-Schottky equation. It is a broadly applied and useful equation, which connects the flatband potential V_{fb} to the applied voltage V_m and the capacitance of the space charge region C_{scr}. In a simple experimental setup, C_{scr} can be determined by electrochemical impedance spectroscopy (EIS) at varying applied potentials V_m. In a plot of the linear relation of C_{scr}^{-2} versus V_m the slope $\mathrm{d}C_{scr}^{-2}/\mathrm{d}V_m = -2/eN_a\varepsilon_r\varepsilon_0$ yields the doping concentration N_a if the respective material and thus its permittivity is known.[131] The analysis of an n-type semiconductor, i.e. with a positive band bending, by the same means, yields a dependence with a positive sign of C_{scr}^{-2} on V_m.[120] Hence, the two fundamentally different conduction mechanisms can be differentiated. Furthermore, flatband potential V_{fb} can be derived from the C_{scr}^{-2} versus V_m plot as the crossing point with zero, i.e. at $C_{scr}^{-2} = 0$, where $V_m = V_{fb} + k_BT/e$.[1] From equation 2.18 it is evident that the capacitance of the SCR is largest around the flatband potential, i.e. $V_S = V_m - V_{fb} \approx 0$. Finally, the width of the SCR is obtained with the determined quantities. The total surface specific charge in the SCR is expressed as $Q_{scr} = eN_aw$, where w marks the width of the SCR.[120] Then, with equations 2.16 and 2.17, one readily finds [119]

$$w = \sqrt{-\frac{2\varepsilon_r\varepsilon_0}{eN_a}\left(V_S - \frac{k_BT}{e}\right)} = \sqrt{-\frac{2\varepsilon_r\varepsilon_0}{eN_a}\left(V_m - V_{fb} - \frac{k_BT}{e}\right)}. \tag{2.21}$$

Apart from the case of a depletion layer, the other two possible configurations at the semiconductor side of the interface are the accumulation and the inversion layer. These two other types of layers are depicted in Figure 2.4(b). In the case of an accumulation layer,

[1] The flatband potential enables the determination of the potential of the valence band edge at the surface V_{VS} by

$$V_{VS} = V_{fb} - \frac{k_BT}{e\ln\left(N_v/N_a\right)}, \tag{2.20}$$

where N_v denotes the effective density of states in the valence band. The Schottky barrier height ψ_{SB} is calculated by $\psi_{SB} = e(V_{redox} - V_{VS})$.[120]

the interface region in the semiconductor is populated by an excess of majority charge carriers caused by a reversal of the band bending. That means, in a p-type semiconductor the bands are not bend downward at the interface, as it is the case for the depletion layer, but upward. Hence, majority charge carriers, i.e. holes, readily accumulate in the valence band at energy levels near E_F at the interface. The opposite holds true for an n-type semiconductor. The bands at the interface are curved downward and electrons are in surplus at the conduction band.
An inversion layer is achieved by applying a large enough positive potential to the semiconductor with respect to the electrolyte side of the interface. By this means, the potential increase is responsible for the valence band to approach E_F or even exceeds it. Thus, holes are able to occupy an abundance of states. This marks the onset of a drastic change in the conduction behaviour of the semiconductor to rather metallic characteristics. This transformation is termed degeneration.
An inversion layer, on the other hand, develops due to minority charge carriers. Ensuing from the depletion layer, the band edge of the respective minority carrier eventually reaches E_F when the bands are further bend in the respective direction of the depletion layer, e.g. downwards for a p-type semiconductor. Hence, minority charge carriers are accumulating at the semiconductor interface and might even surpass the bulk majority charge carrier concentration. The formation of an inversion layer at a semiconductor electrolyte interface is usually perturbed by concurrent electrochemical reactions, which consume these minority charge carriers.[120]
For p-type semiconductors the capacitance of the SCR in case of an accumulation and an inversion layer, respectively, can then be expressed by [132]

$$C_\mathrm{scr} = \sqrt{N_\mathrm{a} \frac{e^2 \varepsilon_\mathrm{r} \varepsilon_0}{2 k_\mathrm{B} T}} \exp\left(+\frac{e V_\mathrm{S}}{2 k_\mathrm{B} T}\right) \tag{2.22}$$

and

$$C_\mathrm{scr} = \sqrt{n_0 \frac{e^2 \varepsilon_\mathrm{r} \varepsilon_0}{2 k_\mathrm{B} T}} \exp\left(-\frac{e V_\mathrm{S}}{2 k_\mathrm{B} T}\right) \tag{2.23}$$

2.2.4. Helmholtz Layer Potential

The drop of the potential across the Helmholtz layer is defined as [120]

$$V_\mathrm{H} = \psi_1 - \psi_2 = \frac{Q_\mathrm{H}}{\varepsilon_\mathrm{r} \varepsilon_0}, \tag{2.24}$$

with the potentials at the semiconductor surface ψ_1 and at the OHP ψ_2. Q_H marks the charge stored in the Helmholtz layer that originates from the ions at the OHP. On the semiconductor side, charge arises in three different forms, namely an accumulation of free charge carriers, charge embedded in surface states and ions might be adsorbed. For a non-degenerated semiconductor free charges at the surface play a minor role.
Surface states are energy levels at the semiconductor's surface which are able to exchange electrons not only with the solid but also with the electrolyte side of the interface. Chapter B in the appendix discusses surface states in more detail. The discontinuance of the bulk structure at an otherwise clean surface results in dangling bonds, which are called intrinsic surface states. Since these dangling bonds in silicon are generally terminated by

hydrogen or other species, intrinsic surface states are of minor importance for silicon. In addition to intrinsic surface states, two other types of surface states might be present on a semiconductor surface. Lewis sites constitute one type and generally result from the acid or basic properties of the surface. Another type of surface states results from adsorbed electroactive species, other than hydroxide or hydrogen ions, which are capable of accepting or donating electrons. Thus, intermediates from chemical reactions at the surface may be considered surface states. Partially oxidised silicon atoms during the anodic oxidation of a silicon surface, which will be discussed below in section 2.3, can serve as transitional surface states.[120]
Generally the transfer of charge from the surface of a non-heavily doped semiconductor to the electrolyte is negligible. By contrast, the charge transferred in adsorption and desorption processes at the surface is generally a few orders of magnitude larger. Thus, an applied potential can be considered to drop exclusively in the SCR and the Mott-Schottky equation 2.19 remains valid.[120] The capacitance associated with the Helmholtz layer C_{H} is assumed to be independent of the Helmholtz potential. That means, a change in potential leads to a change of charge carriers on both sides of the interface. Thus, the interface resembles a plate capacitor, as already discussed in equation 2.6. While the Helmholtz capacitance for a clean metal surface is in the range of $15 - 30\,\mu\mathrm{F\,cm^{-2}}$ [133], C_{H} values of $1.5 - 3\,\mu\mathrm{F\,cm^{-2}}$ have been reported for a silicon electrode [134, 135].

2.2.5. Capacitance of the Semiconductor Electrolyte Interface

In this section the total capacitance of the ensemble of semiconductor and electrolyte at the interface will be discussed. Therefore, the total potential shift ΔV is investigated. ΔV is shared across the SCR and the Helmholtz layer and is given by [120]

$$\Delta V = \Delta V_{\mathrm{scr}} + \Delta V_{\mathrm{H}}. \tag{2.25}$$

The voltage drop across the SCR is described in terms of $\Delta V_{\mathrm{scr}} = \Delta V_{\mathrm{S}}$.[120]
Charge neutrality demands that the charge on the semiconductor side, composed of the SCR and surface states, equals the charge in the electrolyte

$$Q_{\mathrm{elec}} = Q_{\mathrm{scr}} + Q_{\mathrm{SS}}. \tag{2.26}$$

The overall capacitance C can then be expressed by [120]

$$\frac{1}{C} = \frac{\Delta V}{\Delta Q} = \frac{\Delta V_{\mathrm{S}}}{\Delta Q_{\mathrm{scr}} + Q_{\mathrm{SS}}} + \frac{\Delta V_{\mathrm{H}}}{Q_{\mathrm{elec}}} = \frac{1}{C_{\mathrm{scr}} + C_{\mathrm{SS}}} + \frac{1}{C_{\mathrm{H}}}. \tag{2.27}$$

Hence, the total capacitance equals an equivalent circuit, where C_{scr} and C_{SS} are in parallel and are connected in series to C_{H}. A representation of the equivalent circuit is depicted in Figure 2.5. Thereby, the capacitance of the space charge layer C_{scr} is shorted by the surface states and the resistance associated with the SCR R_{scr}. Furthermore, R_{S} denominates the resistance of the electrolyte solution and is linked in series. An existing oxide film on top of the silicon surface requires that the equivalent circuit is extended by another parallel RC component in series with the rest. This is particularly important in non-hydrofluoric acid containing aqueous electrolytes.
In the treatment of the semiconductor electrolyte interface in particular with regard to

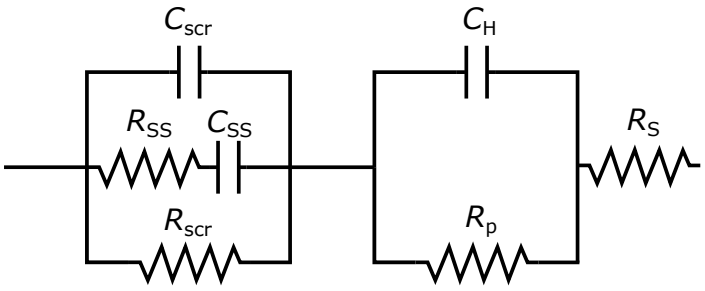

Figure 2.5.: **Equivalent circuit of the semiconductor-electrolyte interface.** C_{scr} and R_{scr} denote capacitance and resistance of the SCR, respectively. C_{SS} and R_{SS} are capacitance and resistance of surface states. C_H is the capacitance of the Helmholtz layer, while R_p and R_S are the resistances associated with the charge transfer into the electric double layer and the resistance of the electrolyte solution. Adapted with permission from reference [120].

the determination of the flatband potential, some considerations have to be taken into account. In the theoretical case of the absence of an oxide layer and further conditions such as a negligible density of surface states, i.e. $C_{SS} \ll C_{scr}$ and when $C_H \gg C_{scr}$, the total capacitance of the semiconductor electrolyte interface, stated in equation 2.27, becomes $C \approx C_{scr}$. The interface capacitance can accordingly be expressed by the Mott-Schottky equation (cf. equation 2.19). Thus, as described above, it is valid to infer the doping concentration N_a and flatband potential V_{fb} from the analysis of a Mott-Schottky plot.
In a realistic experimental setup, the flatband potential is possibly influenced by different factors. For highly doped semiconductors, the assumption of $C_H \gg C_{scr}$ might not hold true. Thus, a non-negligible part of the externally applied potential is dropped in the Helmholtz layer.[136] In particular, this pertains to potentials close to V_{fb}. In general, doping levels smaller than $N_a = 10^{20}\,\mathrm{cm}^{-3}$ (i.e. dopant-atoms per cm^3) do not demand for this correction and the regular determination of V_{fb} according to equation 2.19 is sufficient.[130]
As a final point, the sheer presence of an oxide layer on the silicon surface might also lead to a shift of V_{fb}. The resulting potential drop ΔV_{ox} across the oxide layer is estimated by

$$\Delta V_{ox} = U_s d \varepsilon_{Si} / \varepsilon_{ox}, \tag{2.28}$$

where U_s denotes the electric field at the surface, d is the thickness of the oxide layer and ε_{Si} and ε_{ox} are the dielectric constants of the silicon and the oxide layer, respectively. For a thin oxide film of 20 Å the potential drop equals $\Delta V_{ox} = 40\,\mathrm{mV}$.[120] Thus, such a relatively thin oxide layer itself has not a large influence.
All in all, in this section the contributions to the total capacitance of a semiconductor electrode in contact with an electrolyte solution is comprehensively described. The different components of the interface that contribute to the capacitance are established. In this work, different types of silicon electrodes will be investigated. A main focus will be on the capacitive behaviour of the electric double layer at the silicon-electrolyte interface and if it performs also in experimental terms as a capacitor. In this regard, charging or capacitive currents, also termed non-Faradaic currents, flow when a potential is applied to the semiconductor electrode and charge compensation exclusively occurs in the form of

non-specific adsorption of ions in the electric double layer.[2] By contrast, Faradaic currents indicate a charge transfer across the electrode-electrolyte interface in electrochemical reactions, e.g. characteristic reduction or oxidation processes. These can occur in response to a charge surplus or deficit on the electrode surface by an applied potential. In a reduction or oxidation a transfer of electrons across the interface occurs, which can originate from species from the electrolyte or adsorbed on the electrode surface. These currents are described by Faraday's laws of electrolysis

$$Q = nz\mathrm{F}, \tag{2.29}$$

where Q denotes the exchanged charge, n the converted amount of substance, z the charge of the involved species and $\mathrm{F} = 96\,485.332\,12\,\mathrm{C\,mol^{-1}}$ is the Faraday constant. Thus, only electrodes that are close to an ideal polarisability, i.e. which exhibit negligible Faradaic currents, show an ideal capacitive behaviour.[127] This point will be further discussed in section 2.5. In this case, the reversible adsorption and desorption of ions from the electrolyte at the outer Helmholtz plane is exclusively controlled by the applied potential and is called electrosorption.[137]

2.3. Anodic Oxidation of Silicon

Silicon oxide can exist in a variety of crystalline forms, e.g. quartz, as well as non-crystalline forms, such as vitreous silica.[120] Furthermore, it is possible to synthesise silicon oxide by different techniques. The most commonly used synthesis route in silicon processing is thermal oxidation. Due to its importance for the silicon industry, this oxidation method has been extensively studied in comprehensive detail. For the fabrication of silicon components, silicon oxide layers are widely utilised as gate insulation in metal oxide semiconductor (MOS) chips. Furthermore, silicon oxides are used for other insulation purposes, e.g. to insulate conducting layers from each other. They are also used as planarisation, dielectric interlayers, passivation layers, especially to reduce electrically active surface defects, or as a masking material.[138, 139] Thin oxide layers can also be included in circuits to act as capacitances. Similar to the electric double layer, the charge stored is inversely proportional to the thickness of the silicon oxide layer.[120]
A thermal oxidation of silicon can be carried out in a furnace at temperature ranging from 900 °C to 1200 °C in a dry or wet oxygen atmosphere. The latter contains water in the form of vapour or steam produced by passing dry oxygen and nitrogen over water close to its boiling temperature. Water can also be present in the furnace merely due to the prevalent ambient conditions. In general the oxidation process that utilises a wet oxygen atmosphere leads to higher growth rates of silicon oxide. Overall the following reactions occur [120],

$$\mathrm{Si} + \mathrm{O_2\,(gas)} \rightarrow \mathrm{SiO_2} \tag{2.30}$$

$$\mathrm{Si} + \mathrm{2H_2O\,(gas)} \rightarrow \mathrm{SiO_2} + \mathrm{2H_2\,(gas)}. \tag{2.31}$$

In the case of a dry atmosphere oxidation the first reaction prevails, whereas in the case of a wet atmosphere the latter equation describes the predominant oxidation process. In

[2] Pseudo-capacitive currents comprise both specific and non-specific adsorption processes for charge compensation in response to a potential variation.

general the temperature, the oxide thickness and the silicon substrate orientation influence the oxidation rate of the thermal process. The oxidation kinetics in dependence of oxidation time t are given by [140]

$$\chi \cong \sqrt{B}\sqrt{t}, \tag{2.32}$$

where χ denotes the thickness of the oxide and B is a proportionality constant. The square root dependency displayed in equation 2.32 is only valid for relatively large times. At short times, the oxidation process follows another regime, in which the kinetics have shown to be of linear dependence.[140]
Moreover, the structure of thermally fabricated silicon dioxide is amorphous.[120] It generally is assembled in a precise stoichiometric configuration, i.e. SiO_2.[120] Typically, a silicon oxide layer fabricated by this thermal method has a larger thickness by a factor of approximately 2.3 than an unoxidised substrate of an identical initial thickness.[120] The silicon-silicon interatomic distance in a silicon dioxide layer increases by about 30 %.[141] The thermal oxidation process will be made use of in this thesis to create an insulation layer.[3] Further details are given in section 3.5.2.
Silicon that is in contact with ambient air, water or aqueous solutions develops a thin oxide layer at the surface by itself. This oxide layer is referred to as the native oxide layer. Essentially, a native oxide layer of a certain composition and thickness covers all silicon surfaces due to the inevitable presence of air and water in most environments.[143] The thickness of this native oxide layer may strongly vary depending on the preparation conditions of the surface. In general, the oxide formation on a clean silicon surface, fabricated through the cleaving method, proceeds quickly when in contact with air. The native oxide layer reaches a thickness of $5 - 7$ Å within a few minutes.[144] Then, the growth slows down. For instance, after 24 hours in an air environment the thickness of the native oxide layer approaches $11 - 13$ Å.[144] Conversely, a silicon surface without an oxide layer is obtained by a minute-long etching treatment with hydrofluoric acid to remove any oxides. The specifics of this process will be further discussed in section 2.4. The treatment leaves the silicon surface bonds as Si-H. Thus, this state is accordingly termed hydrogen terminated. The evolution of the native oxide layer after an HF treatment is slower than for a freshly cleaved surface, which is attributed to the passivating effect of the hydrogen termination. Thus, the Si-H bonds have to be broken so that the first monolayer of silicon oxide forms. After this initial stage the growth of the native oxide layer follows the time logarithmically.[145] Along with the initial condition of the silicon surface, the silicon properties govern the growth of the native oxide layer. For doping concentrations exceeding $10^{19}\,\mathrm{cm}^{-3}$ both p- and n-type silicon exhibit a distinctively faster native oxide layer growth than low or moderately doped substrates, which show similar growth rates.[144, 145] Moreover, at the same doping level, the oxide layer growth proceeds faster for n- than p-type silicon above the doping threshold of $10^{19}\,\mathrm{cm}^{-3}$.[145] Concerning the crystal orientation, (111)-oriented surfaces exhibit larger growth rates compared to surfaces with an (100)-orientation. The composition of the air, in particular its humidity, i.e. water

[3] Silicon dioxide films can also be fabricated by means of a chemical vapour deposition (CVD) process. A silane or alkoxysilane film is pyrolytically oxidised, which follows the process of [142]

$$SiH_4 + O_2 \rightarrow SiO_2 + 2H_2. \tag{2.33}$$

This fabrication scheme has typically larger growth rates than the thermal method.

content, has a strong effect on the native oxide layer growth.[145] Thereby, the adsorption of oxygen and water molecules on the surface determines the growth kinetics.[146–148]
Apart from air, water – and to a certain extend other solvents – is another important environment to consider in the discussion of the native oxide growth. In the presence of water, a silicon surface will always develop a coverage with a thin oxide layer. A cleaved and thus clean silicon surface immersed in water shows a $3-4\,\text{Å}$ thick oxide layer after $5-10\,\text{min}$.[144] The oxide layer increases to a stable thickness of about $5-10\,\text{Å}$. For an HF treatment, the growth kinetics are very similar to those observed for an HF-treated silicon surface in air. Thus, the process initially starts with a slow growth phase, in which the already mentioned hydrogen termination has to be replaced by a hydroxyl one. Then, after a few hours, the speed increases.[145] These OH groups have a weakening effect on the bond of the Si surface atom to its next bulk Si neighbour due to their strong electronegativity. Thus, the back bond is attacked by a water molecule so that the back Si atom forms a hydrogen bond [149]

$$\text{Si}-\text{SiOH} \;+\; \text{H}_2\text{O} \rightarrow \text{SiH} \;+\; \text{OH}-\text{Si}-\text{OH}. \tag{2.34}$$

The hydrogen bond is eventually replaced by water so that

$$\text{Si}-\text{H} \;+\; \text{H}_2\text{O} \rightarrow \text{Si}-\text{OH} \;+\; \text{H}_2. \tag{2.35}$$

Ultimately, a bridging reaction forms the oxide through

$$\text{Si}-\text{OH} \;+\; \text{Si}-\text{OH} \rightarrow \text{Si}-\text{O}-\text{Si} \;+\; \text{H}_2\text{O}. \tag{2.36}$$

In water, after the initial removal of the silicon oxide layer by HF, the native silicon oxide layer grows back to a thickness of only $1\,\text{Å}$ to $6\,\text{Å}$ after 100 minutes and 50 hours, respectively.[149] In addition, solved oxygen may strongly influence the native oxide layer in water. With an increasing concentration of solved oxygen, the native oxide layer reaches a larger thickness.[120] Conversely, an HF presence in the water may hinder the evolution of an oxide layer. Thereby, an HF concentration of higher than 10 ppm is even prohibiting the formation of an oxide layer altogether.[150] In addition, the growth of an oxide layer can be promoted by an oxidising agent, such as hydrogen peroxide (H_2O_2). When its concentration is relatively high, it can even negate a hindering effect on oxide layer growth if HF is present. Interestingly, when both the concentration of the oxidising agent and HF are relatively high, the native oxide layer is both rapidly created and removed so that the silicon surface in total is etched.[120] In non-aqueous solvents, e.g. acetonitrile or dimethyl sulfoxide, a native oxide layer only develops because residual water is present in the solvent.[151, 152] All in all, the large variation of the native oxide layer's thickness exemplifies that the conditions under which the oxide layer forms have a great influence on the oxide growth. Minute changes in the environmental conditions or small differences of the silicon properties, may lead to distinctively different native oxide layers.
It is possible to fabricate oxides with a thickness exceeding that of the native oxide layer by applying a potential to the silicon and passing an anodic current from electrolyte to bulk silicon across the interface. This process is labelled anodic oxidation. It is important for the here presented work, as electrochemical experiments will be carried out on silicon electrolyte interfaces in aqueous electrolytes. Anodic oxidation will also be deliberately utilised to obtain electrochemically stable surfaces, as will be explored in the results in

section 4.1.
In general, anodic oxidation can be performed in a broad variety of inorganic and organic electrolyte solutions of different composition. The anodic oxidation process is carried out in two distinct approaches, either by applying a constant potential or under a constant current density. Hereby, the current is normalised to the contact area of the silicon electrode with the electrolyte.
The details about the single steps of the oxidation reaction are not entirely understood, yet.[120] A possible start of the anodic oxidisation reaction is the initial formation of silicon-hydroxide bonds at the silicon surface. For this reaction a positive charge carrier, i.e. a hole h, has to be supplied by the silicon side of the interface. Subsequently, two of these hydroxide bonds split off a water molecule and establish two $\mathrm{Si-O}$ bonds similarly to the proposed growth model of native oxide in equation 2.36. An insertion reaction of oxygen atoms by place exchange then may break up the polarisation of the Si-Si back bond that is created in the previous step.[153] Thus silicon dioxide eventually forms on the surface. The respective steps are given in the following [153],

$$\mathrm{Si} \; + \; 2\mathrm{H_2O} + 4h \rightarrow \mathrm{SiOH} \; + \; 4\mathrm{H^+} \tag{2.37}$$

$$2\mathrm{SiOH} \rightarrow \mathrm{Si_2O} \; + \; \mathrm{H_2O} \tag{2.38}$$

$$2\mathrm{Si_2O} \rightarrow \mathrm{SiO_2} \; + \; 3\mathrm{Si}. \tag{2.39}$$

The presented reaction requires monovalent, positively polarised silicon atoms, i.e. $\mathrm{Si^+}$ as intermediates. An additional contribution of silicon atoms with higher oxidation states, e.g. $\mathrm{Si^{2+}}$ or $\mathrm{Si^{3+}}$, which may be present at the interface, cannot be excluded.[154] These partially oxidised silicon species can be considered as surface states, as already mentioned in section 2.2. Due to an electron tunneling process into the conduction band, a further oxidation of these surface states can proceed at lower potentials. Therefore, in n-type silicon this process contributes to the further growth of the oxide, after an initial formation of a thin layer.[120]
The overall reaction in the anodic oxidation process is given by [120]

$$\mathrm{Si} \; + \; 2\mathrm{H_2O} \; + \; nh \rightarrow \mathrm{SiO_2} + 4\mathrm{H^+} \; + \; (4-n)\mathrm{e} \qquad (n \leq 4), \tag{2.40}$$

where h denotes a hole charge carrier and n is the number of converted holes per reaction, equalling four for a full conversion during the oxidation process. The water molecules participating in this reaction are the major source of oxygen. Hence, in aqueous electrolyte solutions the available oxygen used in the oxidation process is not originating from other components, e.g. the electrolyte species.[4] Alternatively, oxygen may also originate from the dissolution of salts containing oxygen. However, in general the dissolution of salts merely plays a minor role.[5] Oxygen might also develop through an applied overpotential, which decomposes water if it is the solvent.[120]

[4] Conversely, in a dry organic electrolyte solution the oxygen to sustain the silicon oxidation may be supplied by a reaction that decomposes the solvent into water at least partially at the electrode surface. Hence, in general the efficiency of this oxidation process will be lower as less oxygen is available. For glycol, for example, the anodic decomposition yields about $1\,\mathrm{molF^{-1}}$ of water, where F denotes the Faraday constant.

[5] Under specific circumstances this effect can provide oxygen. For example, oxygen-containing anions, such as $\mathrm{NO_3^-}$ or $\mathrm{HPO_4^-}$, in an electrolyte with dry methanol as the solvent may be the main source of oxygen.[155]

The anodic oxidation process, as presented in equation 2.40, involves the transfer of holes. Whereas these are the majority charge carriers in p-type silicon, in n-type silicon holes constitute the minority one. Thus, the anodic oxidation in n-type silicon requires the generation of holes either by illumination or an excess voltage, i.e. an avalanche breakdown. The latter is the relevant process in this work since no illumination is used. In an n-type silicon electrode with an inversion layer, i.e. at reverse bias, few positive charge carriers are present in the SCR. A sufficiently high electric field is responsible for the charge carriers to gain enough kinetic energy to break covalent bonds in the silicon lattice through collision. The impact creates electron hole-pairs and thus new charge carriers, which can then partake in further collisions. Hence, an avalanche effect is created.[120] The potential at which an avalanche breakdown appears is foremost dependent on the doping density.[7] The respective affect is also further discussed in the next section 2.4 in the context of porous silicon formation.
The anodic oxidation process requires a migration of ions over the oxide layer towards the interface with bulk silicon. For the oxide growth to proceed, the migration has to occur even when the oxide layer is growing thicker. In general, the issue of the ion movement across has not been fully understood as different studies produce seemingly opposing results.[120] The respective ions partaking in the migration process might either be cations from the bulk, i.e. most importantly Si^+, or oxygen containing anions from the silicon oxide interface with the electrolyte. Water enters into the first layers of the created oxide and can then dissociate into ions. These anions are most importantly hydroxide (OH^-) groups. They are found to migrate to the bulk-oxide interface if an electric field is applied.[155] The concentration of hydroxide decreases with the distance from the interface within the oxide film. Thus, the rate limiting process appears to be the oxidation process and not the hydroxide drift.[155] In general, the nature of the ionic drift seems to heavily depend on the experimental conditions, which can produce vastly different outcomes by merely slight changes. Organic, water-free electrolyte solutions at high electric fields seem to favour the cationic, outward directed migration, whereas in an aqueous electrolyte under relatively low electric fields an inward movement of anions seems to dominate.[120] The latter is the more relevant for the experimental results presented in this work, as only aqueous electrolytes at voltages below 5 V are experimentally investigated. Under the additional assumption that the migration of the anions through the oxide layer during anodic oxidation is drift limited, a description of the growth kinetics of the oxide layer is obtained. Drift limited here implies that the reaction of anions and Si atoms at their respective interface is faster than the anion migration process to the interface. The current of anions J_i is then given by [156]

$$J_\mathrm{i} = n_\mathrm{i} q_\mathrm{i} \mu_\mathrm{i} U = n_\mathrm{i} q_\mathrm{i} \mu_\mathrm{i} \frac{V}{\chi(t)} = q_\mathrm{i} f, \tag{2.41}$$

where n_i, q_i and μ_i denote the anionic concentration, mobility and charge in the oxide layer. U and V are electric field and potential across the oxide layer of thickness $\chi(t)$ and f denotes the flux of anions. The flux is expressed in terms of the thickness $\chi(t)$ as [156]

$$f = N_\mathrm{i} \frac{\mathrm{d}\chi(t)}{\mathrm{d}t} \Rightarrow J_\mathrm{i} = q_\mathrm{i} N_\mathrm{i} \frac{\mathrm{d}\chi(t)}{\mathrm{d}t}, \tag{2.42}$$

where N_i is the number of anions per unit volume of silicon oxide.
The anionic current through the silicon oxide may be accompanied by an electric current

J_e that possibly results from electron injection from electrolyte states into the conduction band of the oxide by tunneling.[120] The overall current J would then equal $J = J_i + J_e$. However, J_e is negligible for the low potentials used in this work. The voltage V is derived by [156]

$$V = V_0 - JAR, \tag{2.43}$$

where V_0 denotes the voltage applied across the electrodes, A is the surface area in contact with the electrolyte and R is the sum of the bulk silicon resistance and the electrolyte resistance. Injecting V from equation 2.43 into 2.41 results in [156]

$$J_i = \frac{n_i q_i \mu_i V_0 \eta_{avg}}{\chi \eta_{avg} - n_i q_i \mu_i RA}, \tag{2.44}$$

where η_{avg} is the current efficiency $\eta = J_i/J$, which is assumed to only change slowly over time and can thus be averaged over the whole oxidation process. Setting equal J_i from equations 2.41 and 2.44 yields

$$\frac{d\chi(t)}{dt} = \frac{n_i q_i \mu_i V_0 \eta_{avg}}{N_i q_i \eta_{avg} \chi(t) - n_i q_i^2 \mu_i N_i RA}. \tag{2.45}$$

Integrating the equation yields

$$\chi(t) = \chi_{init} + \frac{n_i q_i \mu_i RA}{\eta_{avg}} + \sqrt{\left(\frac{n_i q_i \mu_i RA}{\eta_{avg}}\right)^2 + \left(\frac{2 n_i q_i \mu_i V_0}{N_i q_i}\right) t}, \tag{2.46}$$

where χ_{init} is the initial thickness of the oxide layer at $t = 0$. For the reasonable assumptions [156]

$$t \gg 0 \quad \text{and} \quad \left(\frac{2 n_i q_i \mu_i V_0}{N_i q_i}\right) t \gg \left(\frac{n_i q_i \mu_i RA}{\eta_{avg}}\right)^2, \tag{2.47}$$

finally an expression for $\chi(t)$ can be found

$$\chi(t) = \chi_{init} + \left(\frac{2 n_i q_i \mu_i V_0}{N_i q_i}\right)^{1/2} t^{1/2}. \tag{2.48}$$

Thus, inserting $\chi(t)$ in a final step into equation 2.44 yields the desired relation of the anionic current J_i in dependence of time t

$$J_i(t) = \frac{1}{2} N_i q_i \left(\frac{2 n_i q_i \mu_i V_0}{N_i q_i}\right)^{1/2} t^{-1/2} = \left(\frac{n_i q_i^2 \mu_i N_i V_0}{2}\right)^{1/2} t^{-1/2}. \tag{2.49}$$

Interestingly, the evolution of the anodic oxide thickness χ, cf. equation 2.48, has the identical square root dependence on time t as the growth of the thermal oxide, as seen in comparison to equation 2.32. It is reasonable in the sense that the assumptions of both models are akin. More precisely, both models operate under the assumption of constant driving forces. In the case of anodic oxides it is a constant potential, whereas it is a constant oxidant concentration gradient within the thermal oxide layer. Furthermore, the oxidant transport in both models is assumed to linearly depend on the driving force.[120]

2.4. Porous Silicon

Porous silicon is fabricated by etching monocrystalline bulk silicon in an electrochemical procedure, in which a current is applied between an electrode and a silicon wafer in an electrolyte solution that contains HF. The details of the setup will be discussed in more detail in section 3.2.
As described in section 2.3, silicon is thermodynamically unstable in an atmosphere that contains oxygen or water and a native oxide layer readily develops. The native oxide layer needs to be removed since it is electrically insulating and prohibits the synthesis of porous silicon. For this purpose, an aqueous HF solution is used. The presence of HF leads to a spontaneous dissolution of SiO_2.[52] The specific steps involved in the dissolution process are complicated and still under discussion.[120] For instance, the intermediates in the reaction are debated as is the role of HF_2^- and H^+ ions during the etch process.[120] However, the overall reaction may be described by

$$SiO_2 + 6HF \rightarrow SiF_6^{2-} + 2H^+ + 2H_2O, \tag{2.50}$$

where the resulting silicon hexafluoride anion (SiF_6^{2-}) is stable and highly soluble in water. The dangling bonds on a silicon surface, treated with such a procedure that chemically removes SiO_2, will be hydrogen terminated, i.e. covered by Si−H bonds, as already mentioned in section 2.3. The hydrogen termination is executed on a timescale of one minute.[120]
As the fabrication of porous silicon includes the reactions of different types of silicon bonds, it is worthwhile to investigate these bonds further. The most important silicon surface bonds are Si−Si, Si−H, Si−O and Si−F. Thermodynamic measurements suggest that the bond with the highest enthalpy, i.e. the strongest bond, is the one from silicon to fluoride, followed by the bonds to oxygen, hydrogen and silicon.[52] For the stability of the respective species on a silicon surface, rather the electronegativity of the constituent is the decisive factor. Thus, Si−F surface bonds are highly reactive, while Si−H or Si−C bonds tend to have a passivating impact, as already mentioned in section 2.3. Highly electronegative elements, such as fluoride or oxygen, form polar bonds to a silicon atom and weaken the respective Si−SiF back bond by rendering it prone to a nucleophilic attack.[157] Thus, Si−F surface bonds, which might themselves have replaced the Si−O of the oxide layer, are attacked and replaced by Si−H bonds according to the following reaction [157]

$$Si{-}SiF_3 + HF \rightarrow Si{-}H + SiF_4, \tag{2.51}$$

where SiF_4 quickly reacts to SiF_6^{2-} and dissolves. The respective process is also illustrated in Figure 2.6 for an (100) silicon surface. The surface atom in this case is terminated by two hydrogen atoms. For an (110) or (111) surface the termination tends to be by SiH_3 or SiH, respectively, because the surfaces have different numbers of dangling bonds.[120]
Due to the low electronegativity of the hydrogen atom, no strong polarisation of the bond to the silicon atom occurs. The difference in polarisation with respect to a Si−Si bond is small. By comparison the fluoride atom has a larger polarising effect. Thus, a hydrogen surface bond does not enforce a strong polarisation onto the silicon back bonds and in return a hydrogen terminated surface is less susceptible for a nucleophilic attack and remains stable.[120, 158] However, di and tri-hydride surface bonds have one or two more Si−H bonds than monohydride. Hence, the back bonds are slightly more

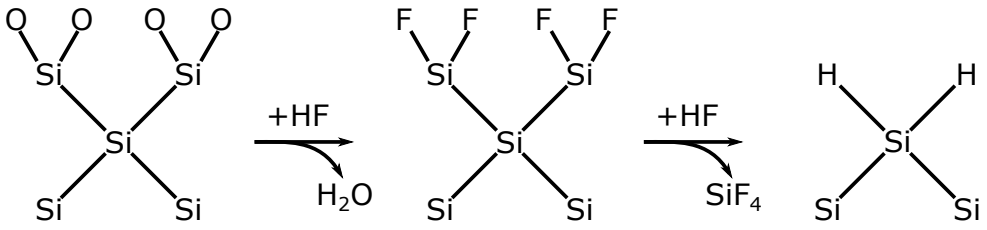

Figure 2.6.: **Chemical reaction of the hydrogen termination on an** (100) **silicon surface.** Si−F surface bonds are replaced by Si−H bonds. Thus, the (100) surface is terminated by $Si-H_2$. Adapted with permission from reference [157].

polarised and di and trihydrides tend to be removed. As a result monohydride formation is promoted.[159] Additionally, the activation energy needed to break the respective surface bond is significantly lower for the Si−OH and especially the Si−SiF3 bond than for Si−SiH and $Si-SiH_3$ bonds.[160] Hence, a fluoride termination is readily replaced and the formation of a stable hydrogen termination is further promoted.
Hydrogen terminated silicon is relatively stable in HF solutions at OCP. It chemically dissolves with an etch rate in the order of $10^{-3}\,\text{Å}\,\text{s}^{-1}$.[161] The dissolution progresses by the involvement of OH^- anions according to the reaction [162]

$$\text{Si} + 2\text{OH}^- + 2\text{H}_2\text{O} \rightarrow [\text{Si(OH)}_2\text{O}_2]^{2-} + 2\text{H}_2, \tag{2.52}$$

where silicon is removed in the form of an $[Si(OH)_2O_2]^{2-}$-anion, which is in solution. A dilution of HF ($< 25\,\%$) results in an increased concentration of OH^- ions and as a result the etch rate increases by approximately one order of magnitude.[163] Interestingly, reaction 2.52 is also the reason why it is possible to, chemically and even electrochemically, etch silicon in basic solutions such as KOH, in which an abundance of OH^- anions is available.
Furthermore, another manner to chemically etch hydrogen terminated silicon exists. If positive electronic carriers, i.e. holes, are present at the silicon surface of the interface, HF can directly attack the silicon bonds. Since only few carriers, owing to their thermodynamic distribution, are present at the surface at OCP, the etch rate is relatively low. A value of approximately $0.2\,\text{Å}\,\text{min}^{-1}$ has been reported.[164] The mechanism that causes the chemical dissolution process at OCP is the same that is responsible for the electrochemical etching, i.e. not at OCP, of silicon. Summarising, a potential leads to an aggregation of holes at the surface of silicon immersed in an HF-containing solution and the HF molecules are enabled to remove silicon atoms from the surface. The etching rate of this electrochemical process is drastically increased compared to a pure wet chemical etching. This process in total will be discussed in detail for the rest of this section, as the mechanism itself and its characteristics are vital for the preparation of porous silicon.
The electrochemical dissolution process of silicon can be separated into two different regimes – porous silicon fabrication and electropolishing. The difference between these two regimes lies in the exact electrochemical procedure that unfolds when a current is running between a counter electrode (CE), or cathode, and the silicon electrode immersed in electrolyte solution. The silicon electrode is acting as the working electrode (WE), a term which is properly introduced in section 3.1. In terms of the etching the WE is also

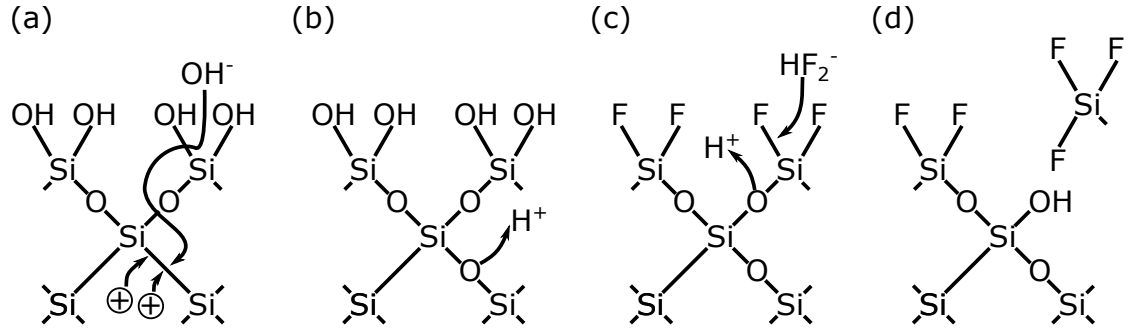

Figure 2.7.: **Electrochemical, tetravalent dissolution of silicon.** (a) Anodic oxide formation and diffusion of OH^- ions through the oxide. (b) Formation of an $Si-O-Si$ bridge on Si backbone under consumption of two holes. (c) Nucleophilic attack of HF_2^-, or another fluoride containing agent, on Si surface atom. (d) Removal of Si surface atom and termination of Si surface with hydroxyl (OH) group. Adapted with permission from reference [7].

referred to as the anode. Thus, the dissolution process is also termed anodisation. At lower current densities, porous silicon is fabricated, whereas above a critical current $J_{\text{crit.}}$ the silicon surface is etched isotropically, which is referred to as electropolishing.
First the electropolishing regime will be discussed. Due to the applied current, a potential is present at the silicon electrode. It is larger than the OCP and the potential present during the porous silicon formation. The process responsible for the electropolishing etching regime is initiated by the formation of an anodic oxide. Hydroxide ions are assumed to be responsible for the evolving etch process.[165] Due to the induced potential, OH^- ions are attracted to the silicon surface and diffuse through the oxide layer.[7] Upon the consumption of two holes, the hydroxide anion forms a bridging unit on one of the Si-Si back bonds, as sketched in Figure 2.7(a) and (b). The actual dissolution of silicon atoms proceeds by fluoride in the form of HF, $(HF)_2$ or the fluoride containing anion HF_2^-. These molecules perform a nucleophilic attack on the Si surface atom.[7] Simultaneously, an electrophilic attack of H^+ ions on the oxygen in the silicon back bond occurs. The result is the dissolution of the bond while an Si surface atom is removed.[166] The dangling bond on the Si atom, which is the new surface atom, is terminated by OH. The specific steps are shown in Figure 2.7 (c) and (d). These two steps determine the etching rate that limits the electropolishing process. The formation of the oxide and its subsequent dissolution proceeds in a simultaneous or oscillatory manner.[7] In the entire process four charge carriers are consumed and the electropolishing process is also termed accordingly tetravalent dissolution. The electropolishing process has no dependence on the crystal orientation of the silicon substrate. During electropolishing no hydrogen evolution is observed.
In the reaction responsible for the formation of porous silicon, only two charges are consumed. It is accordingly referred to as the divalent dissolution of silicon. This process is initiated by a hole that is attracted to the surface of the silicon electrode by means of a potential. Subsequently, a nucleophilic attack on the Si surface atom follows as shown in Figure 2.8(a). The hole weakens the Si back bond and thus enables the nucleophilic attack by a bi-fluoride anion (HF_2^-), which dissociates into HF and an F^- anion, or by a similar HF containing species, i.e. HF or $(HF)_2$.[167] The rate of dissolution is determined

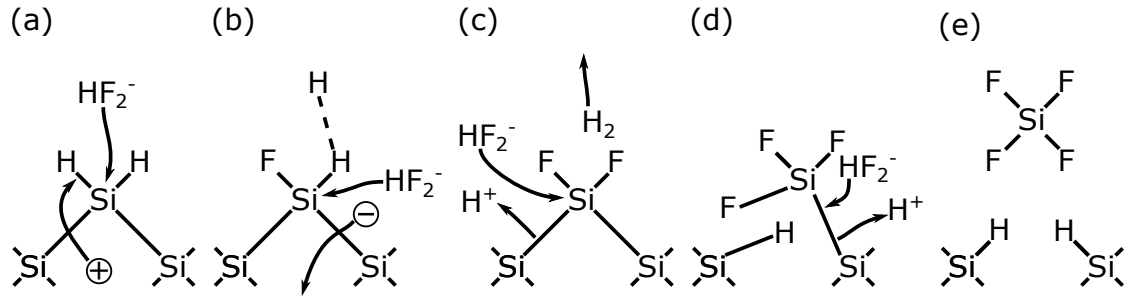

Figure 2.8.: **Electrochemical, divalent dissolution of silicon.** (a) Approach of the Si surface by a hole charge carrier and the subsequent nucleophilic attack of the Si bond by an HF_2^- anion. (b) Second nucleophilic attack of HF_2^- on the remaining, polarised surface bond under injection of an electron. (c) and (d) Remaining back bonds, polarised by the established surface F−Si bonds, are detached by HF_2^- in nucleophilic attacks under release of hydrogen gas. (e) New, hydrogen terminated silicon surface atoms and the removed SiF_4 molecule. Adapted with permission from reference [7].

by this first nucleophilic attack and is the origin of the formation of pores. As a result, the surface bond is fluoride terminated. Another nucleophilic attack, see Figure 2.8(b), replaces the second hydrogen terminated Si surface bond by fluoride. In addition, an electron is injected into the silicon. The second nucleophilic attack is not initiated by a charge carrier from the bulk silicon and the electron injection is the consequence of the respective chemical reaction. During these reactions the former surface hydrogen atoms are ejected as hydrogen gas, i.e. H_2, as seen in Figure 2.8(c). Thus, the evolution of hydrogen gas distinctly differentiates divalent from tetravalent dissolution. The two fluoride-terminated Si surface bonds induce a sufficient polarisation onto the two remaining back bonds so that they are readily broken by HF. The Si surface atom is completely removed. The nascent SiF_4 molecule quickly reacts with two more HF units and two protons to $SiF_6{}^{2-}$. It is, in contrast to SiF_4, not gaseous but soluble in water (in the range of several mol L^{-1}).
The shift from the initial removal of single Si surface atoms to the formation of pores is the decisive feature that differentiates this regime from the electropolishing regime. While during electropolishing the surface of silicon is removed isotropically, porous silicon is formed by a distinct difference in dissolution rate between the pore tip and the evolving pore wall.[7] Hence, uniformly nucleated pores, having no particular order on the surface unless a pre-patterning exists, experience a preferential removal of Si atoms and a current flow at the pore tip. By contrast, the pore walls are in a passive state and are not the primary target of dissolution. Once the pores have formed, they are not undergoing any redistribution or reconstruction that would significantly merge pores or shift pore walls.[52] The active-passive contrast of pore tip to wall is characteristic for porous silicon formation. The passivation thereby constitutes an energy barrier to a possible charge transfer from silicon to electrolyte, which is overcome at the pore tip. In aluminium electrodes the growth of a passivating oxide layer on the pore wall is responsible for the formation of porous alumina.[168] However, passivating oxide layers at the silicon surface are readily wet-chemically dissolved by HF, see reaction 2.50, and in the case of currents larger than $J_{\text{crit.}}$, the oxide layer merely represents an intermediate step

during electropolishing. Therefore, anodic oxides are not responsible for stabilising pore walls in porous silicon. The relevant mechanisms will be discussed next and, as will be seen, they vary for different pore sizes of porous silicon.
Resulting pore diameters in the preparation of porous silicon, in general, span over more than four orders of magnitude, from approximately 1 nm as the lower boundary to a few µm as the upper.[7] A convention by the *International Union of Pure and Applied Chemistry* (IUPAC) divides porous materials into three categories: microporous (pore diameter $D < 2\,\mathrm{nm}$), mesoporous ($2\,\mathrm{nm} < D < 50\,\mathrm{nm}$) and macroporous ($D > 50\,\mathrm{nm}$).[169] The term nanoporous bears no meaning in this definition and is in general loosely used to refer to structured materials with a structure size of less than 100 nm.[52]
In microporous silicon, in particular, the geometrical dimension of the porous structure itself, is the origin of a passivation of pore walls and the growth of pores. In the restricted volume of the pore wall the energy of holes or electrons increases. It may be approximated as a quantum wire. Thus, the charge carriers inside the pore wall are under a quantum confinement effect. Their energy levels are discrete with an increased ground energy state.[2] Thus, charge carriers need more energy to enter the pore wall. This constitutes an energy barrier that is in addition to the silicon bandgap. At the pore tip a spatial confinement effect is less distinct and holes preferentially accumulate here. The silicon continues to be dissolved at the pore tip. The energy barrier due to quantum confinement does not involve any electric field, it is rather a pure result of pore geometry. Formation of microporous silicon by quantum confinement is independent of doping type and density.[7] Often it is in superposition with pore formation mechanisms due to SCR effects, discussed in the next paragraph. The quantum confinement effect is observed in optical transmission measurements. In the case of microporous silicon the absorption edge of light is observed at significantly lower wavelengths compared to a transmission spectrum of bulk silicon.[2] It is subject to a blueshift. The discovery of this quantum confinement effect and the simultaneous observation of photoluminescence from microporous silicon [3] lead to the drastic increase in research activity with regard to porous silicon.
Semiconductors establish a space charge region when in contact to an electrolyte, as discussed in detail in section 2.2. The SCR might act as a passivating layer. The fact that both p-type as well as n-type silicon are in a depletion state during the anodisation process supports the concept of the SCR as a passivating layer.[170] The limiting factor for the transfer of charge carriers is neither the reaction kinetics nor diffusion of ions in the electrolyte but the supply of charge carriers in the silicon electrode. For pore formation to occur, charge carriers need to cross the SCR at the pore tip, i.e. the passivating layer needs to be overcome. Different mechanisms might take effect for charge carriers to cross the SCR, which lead to a variety of different pore morphologies. In general the mechanisms by which the SCR is crossed are avalanche breakdown, thermionic emission, minority carrier collection and tunneling. For n-type silicon, with doping densities of less than $10^{18}\,\mathrm{cm}^{-3}$, avalanche breakdown by an applied potential in excess of approximately 10 V dominates.[2] Another method to produce a significant current across the SCR in this type of silicon utilises the injection of minority charge carriers, i.e. holes, by illumination. This is also of relevance for anodic oxidation, cf. section 2.3. Both of the methods lead to the fabrication of macroporous silicon.[7] For p-type and n-type silicon with doping densities larger than approximately $10^{18}\,\mathrm{cm}^{-3}$ the dominant current-generating effect is quantum mechanical tunneling. Porous silicon fabricated in this regime results in pore diameters in the mesoporous range. It is the material of interest investigated in this work

and is properly introduced in chapter 3.
Additionally, the high curvature radius at the tip of the pore enhances the electric field present at this spot. Therefore, holes are preferentially accumulated at the tip.[52] This mechanism affects all discussed pore formation regimes.
A key feature during the formation of porous silicon is the inclination of pores to parallelly align along the [100] direction. These pores are also referred to as crystallographic pores. Essentially, the formation occurs due to differences in the Si-H surface bonds that prevail at the silicon surface in contact with an HF solution.[52] When the (111) plane is terminated by hydrogen, the H atom is located directly above the Si atom and thus their bond is orthogonally oriented to the (111) plane. Conversely, the Si-H bonds on the (100) face are strained. Hence, these bonds are more prone to be attacked by HF so that the anodisation preferentially proceeds in the [100] direction. If the [100] direction is perpendicular to the wafer surface, i.e. the silicon wafer possesses an (100) orientation, the pores will grow orthogonally to the wafer surface.[52] Thus, the resulting porous structure is highly anisotropic.[6] These crystallographic pores are aligned to a crystal orientation, whereas pores oriented to current lines might form during the preparation process and do not obey to any crystal orientation. These so called current pores nucleate at the main pore and branch off. Equipotential planes that are parallelly oriented to the silicon wafer surface, can guide the flow of holes.[52, 171, 172] In the case of an 100 silicon wafer current pores branch off in perpendicular direction to the main pore and form smaller side-pores.
When a porous silicon layer is fabricated, it might exhibit a gradient in its density along the growth or etching direction. That means, the pores themselves will show a conicity with respect to their diameter. In other words, the porosity Φ, defined as the volume fraction of accessible pore space normalised to the total outer volume V of the whole porous silicon layer, has a gradient. In particular, this effect can occur when thick layers, and thereby long pores, are fabricated. In this case, the wet chemical dissolution of silicon, as discussed above, cannot be considered as negligible any more. An increased period of contact between the pore walls and the HF solution leads to more dissolved silicon. Thus, for long etching times the pore openings tend to feature increased diameters compared to the pore tips.[173–175] Conversely, it is also possible that the opposite takes effect, i.e. the porosity is largest at the tip and smallest at the opening of the pore. It is governed by the diffusion limitation of HF molecules along the pore axis, which leads to an increased porosity at the pore tip.[175, 176] This effect is mainly observed in the preparation of macroporous silicon. By contrast, a porosity decrease along the pore, indeed affects the mesoporous materials studied in this work.[177]
In general, doping type and density presets the pore formation regime. Pore diameter and porosity are mainly controlled by the applied current density and the HF concentration. For the p-type porous silicon investigated in this work, porosities of approximately $30-75\,\%$ and pore diameters of $4-15\,\mathrm{nm}$ are attainable through the choice of the suitable current density in the range of $10-240\,\mathrm{mA\,cm^{-2}}$ and HF concentration of $10-35\,\mathrm{vol\,\%}$, respectively. Increasing the current density at constant HF concentration, leads to an increase in pore diameter and porosity. In turn, increasing the HF concentration at constant applied current density leads to lower porosities and a decrease in average pore diameter.[174]

[6] As opposed to other common porous materials such as nanoporous gold [10] or nanoporous Vycor glass synthesised by spinodal decomposition [9], which possess an isotropic network of pores.

In general, it is possible to prepare porous silicon in two significantly different types. Once the desired porous silicon layer thickness is achieved, the etch can be stopped. This leaves the porous silicon layer attached to the bulk silicon underneath. The pores are only open at the top of the layer, i.e. dead-end pores. This sample geometry is in this work referred to as an epi-layer. The removal of the porous silicon layer from the bulk silicon requires an applied current increased beyond $J_{\mathrm{crit.}}$. Hence, the tetravalent etching mode is active and silicon is etched isotropically, proceeding from the pore tip. The whole porous silicon layer is under-etched. Eventually, it is detached and a free-standing porous silicon membrane with open pores forms. Porous silicon possesses a hydrogen terminated surface directly after preparation, which includes the inner surface area of the pore walls. Porous silicon is hydrophobic due to the hydrogen termination.[52]
The silicon fraction within porous silicon, i.e. the silicon pore walls, remains highly monocrystalline.[8] Thus, porous silicon retains bulk silicon's diamond crystal lattice structure, introduced in section 2.1. However, the lattice constant of porous silicon might differ from bulk silicon because of surface stresses evolving at the pore-wall interfaces.[178] The crystalline properties of bulk and porous silicon will be of importance for the X-ray diffraction study discussed in this work, see materials and experimental methods in section 3.5.3 and results in section 5.5.

2.5. Electrocapillarity of Solid Electrodes in Electrolytes

Solid electrodes and, in the context of this work, semiconductor-electrodes in particular develop characteristic layers of charge distribution on both sides of the interface when in contact with a liquid electrolyte, as described in detail in section 2.2. On the fluid side of the interface an electric double layer forms, whereas on the solid side a space charge region forms. This section will explore the ensuing consequences of the interface formation due to capillary effects. The electrode-liquid interface in terms of surface tension, also called surface free energy or simply surface energy, and surface stress as well as the markedly distinction between these two thermodynamic concepts will be discussed. Moreover, it will be explained how an actuator functionality will be integrated into porous silicon by utilising surface stress at the silicon surface.
The change in surface tension γ of an electrode is captured by Gibbs adsorption equation. For solids, Gibbs adsorption equation reads [78]

$$\mathrm{d}\gamma = -\sigma \mathrm{d}T - \Gamma_i \mathrm{d}\mu_i - q\mathrm{d}E + \mathbf{s}\mathrm{d}\mathbf{e}, \tag{2.53}$$

where the variables are denoting the following quantities – σ is superficial excess entropy, T is temperature, Γ_i is superficial excess of i-th component of the electrolyte solution, μ_i is chemical potential of ith component, q is charge per unit area of surface and E is electrode potential, which will be interchangeably referred to as applied potential throughout this work. Thus, it is the same quantity as V_{m}, introduced in section 2.2. The second rank surface stress tensor is denoted by $\mathbf{s}$ and $\mathbf{e}$ is the strain tensor at the surface, i.e. tangential stress and strain in the surface plane. A relaxation of the surface in direction normal to it is allowed.[78]
The surface tension γ is defined by the response in Helmholtz free energy ∂F to a reversible change of surface area ∂A under the conditions of constant T and μ_i.[179] These

simplified assumptions are justifiable since the experiments carried out throughout this work are conducted under constant temperature. The measures taken to ensure this will be described in chapter 3. Furthermore, a constant composition of the surface is assumed so that the influence of changing chemical potentials can be omitted. At a further assumption of constant elastic strain of the surface atoms, γ obeys

$$\gamma = \left.\frac{\partial F}{\partial A}\right|_{\mathbf{e},T,\mu_i}. \tag{2.54}$$

In thermodynamics the energy needed to add new or change surface unit area is a characteristic concept that governs the properties of condensed matter. For a liquid to form or change its surface, atoms from the bulk of the liquid are readily added to the surface by diffusive processes. The high mobility of atoms in liquid phase ensures that the surface composition, i.e. the average density in the surface and the configuration of the atoms among themselves, stays unchanged in comparison to the undeformed state. Thus, surface is formed in a manner referred to as *plastic*.
The Young-Laplace equation essentially describes this phenomenon for a fluid droplet. It links the change in pressure $\Delta P = P - P_{\text{external}}$ of the ambient and internal pressure to surface tension γ and the curvature of the surface κ by [125]

$$\Delta P = 2\gamma\kappa. \tag{2.55}$$

By increasing its bulk density a liquid droplet can decrease its surface area and thereby its surface excess energy while an energetically favourable atomic structure of the surface remains unchanged. The structure of surface and bulk are decoupled as shear stress in liquids is non-existent.
The last term, i.e. $\mathbf{s}\mathrm{d}\mathbf{e}$, in equation 2.53 is only valid for solids. For fluids, it is not present in the Gibbs adsorption equation. In contrast to fluids, in solids the formation of surface unit area comprises an *elastic* process. Solids, by comparison, are capable of facilitating shear stress. The surface atoms are coupled to the underlying bulk. They are restricted to stay in registry with the underlying bulk crystal lattice. The free flow of atoms to the surface, as present in fluids, is not feasible in solids.[78] Surface area can then be elastically formed or altered by increasing the interatomic distance of surface atoms, while their number stays constant. In effect, a strain in the surface atoms emerges. The formation of surface by elastic means is represented in equation 2.53 by the introduction of tangential strain $\mathbf{e}$. So, the reversible work normalised to unit area required to strain an existing surface is related to surface stress $\mathbf{s}$ by [179]

$$\mathbf{s} = \frac{\partial(\gamma A)}{\partial \mathbf{e}} = \gamma\mathbf{I} + \frac{\partial\gamma}{\partial\mathbf{e}}, \tag{2.56}$$

with $\mathbf{I}$ being the second rank identity tensor.
Equation 2.56 gives the derivative of surface excess free energy γA with regard to the strain $\mathbf{e}$. In result the equation states that there is a distinctive difference between surface tension and surface stress in, to highlight this, solids. In liquids the last term of equation 2.56 is zero and surface tension equals surface stress. Thereby, the different concepts of surface area formation are reflected by this equation. In solid electrodes the surface stress will have a significant non-zero value, as the dangling bonds on the surface will create bonds in the surface plane. Thus, the result is a stress on the underlying bulk crystal. This

stress emerging at the surface bonds constitutes a capillary force, for which the surface stress gives the magnitude. At clean metal surfaces the surface stress usually leads to a strengthening of the surface bonds. Thus, it has a positive sign and is inclined to compress the underlying bulk. However, for other materials this does not have to necessarily be the case and the opposite is possible – a negative surface stress value which expands the bulk.[78]
Equation 2.56 is referred to as the Shuttleworth equation. In its scalar form, so for a general surface, with off-diagonal components being zero, the equation can be written as

$$f = \gamma + \frac{\partial \gamma}{\partial e}, \tag{2.57}$$

where f and e are scalar surface stress and strain. Here, it should be mentioned that the Shuttleworth equation, as represented in equation 2.57, is stated in laboratory coordinates. The state variables used to describe a deformed surface, are the actual, physical surface area in the deformed state $\tilde{A}$ and the strain between the atoms e. In contrast, Lagrangian coordinates may be introduced, with the state variables being the surface area of surface atoms in an undeformed state A_0 and strain e as well. The two conceptually different methods to cause a change of ϵ to the surface area, i.e. plastic and elastic, are captured by these state variables. A plastic deformation increases the surface area by $A = (1 + \epsilon)A_0$, but it leaves the strain invariant, i.e. $e = 0$. By contrast, an elastic deformation leaves the surface area $A = A_0$ unchanged but alters the strain $e = \epsilon$. In the Shuttleworth notation a purely elastic strain has an influence on both, surface area $\tilde{A}$ and strain e.[78][7]
Coming back to Gibbs adsorption equation 2.53 and only taking into account a stiff electrode, i.e. constant strain $\mathbf{e}$, at constant temperature and composition of the electrolyte, i.e. constant T and μ_i, respectively, the adsorption equation is reduced to [78]

$$\left.\frac{\mathrm{d}\gamma}{\mathrm{d}E}\right|_{\mathbf{e},T,\mu_i} = -q. \tag{2.58}$$

Equation 2.58 is referred to as the Lippmann equation. It states the fundamental conclusion that the excess charge on the electrode surface q determines the slope of a potential dependent surface tension curve, also referred to as an electrocapillary curve. Under the assumption of a potential-independent capacitance, here noted as the double layer capacitance c_{DL}, compare equation 2.6, $c_{\mathrm{DL}} = \mathrm{d}q/\mathrm{d}E$ and thus also $\mathrm{d}E = \mathrm{d}q/c_{\mathrm{DL}}$. Thus, the Lippmann equation yields

$$\begin{aligned} &\frac{\mathrm{d}^2\gamma}{\mathrm{d}E^2} = -\frac{\mathrm{d}q}{\mathrm{d}E} = -c_{\mathrm{DL}} \\ &\Rightarrow \gamma - \gamma_0 = -\frac{1}{2}c_{\mathrm{DL}}(E - E_{\mathrm{zc}})^2 \end{aligned} \tag{2.59}$$

[7] Another aspect to consider is the following. In contrast to fluids, where internal pressure is related to the surface stress by the Young-Laplace equation, cf. equation 2.55, in solids a change to the density in the tangential direction to the surface will affect the atomic surface structure and thus causes a surface stress.[78] The relation of P and f in its scalar form obeys [180]

$$3V\langle P - P_{\mathrm{external}}\rangle_{\mathrm{B}} = 2A\langle f\rangle_{\mathrm{S}},$$

where the angular brackets with the index of B and S denote averages over bulk volume V and surface area A, respectively

and

$$\frac{\mathrm{d}\gamma}{\mathrm{d}E} = -q \Rightarrow \mathrm{d}\gamma = -q\mathrm{d}E = \frac{-q}{c_{\mathrm{DL}}}\mathrm{d}q$$
$$\Rightarrow \gamma - \gamma_0 = -\frac{1}{2}\frac{q^2}{c_{\mathrm{DL}}}, \tag{2.60}$$

with the potential of zero charge E_{zc}. Comparing equations 2.59 and 2.60 yields

$$\gamma - \gamma_0 = -\frac{1}{2}c_{\mathrm{DL}}(E - E_{\mathrm{zc}})^2 = -\frac{1}{2}\frac{q^2}{c_{\mathrm{DL}}}. \tag{2.61}$$

Hence, the surface tension γ quadratically depends on the applied potential E and the accumulated charge q. At the maximum of the $E - E_{\mathrm{zc}}$ parabola, where the slope of the curve equals zero, the maximum surface tension γ_0 is reached. At this point no charge is present, i.e. $q = 0$, and thus, the respective potential is called potential of zero charge E_{zc}.[78]
The surface tension γ relates to the state variables by its first derivative, as readily seen in the fundamental Gibbs adsorption equation, cf. equation 2.53. By contrast, in phenomenological thermodynamics the second derivative of the free energy function formally yields material parameters. The capacitance of the double layer adheres to this notion

$$c_{\mathrm{DL}} = \frac{\partial^2\gamma}{\partial E^2} = \left.\frac{\mathrm{d}q}{\mathrm{d}E}\right|_{\mathbf{e},T,\mu_i}, \tag{2.62}$$

as already stated above. In a similar manner, another important material parameter, i.e. the electrocapillary coupling coefficient ς, is found in the definition of the surface stress variation with the charge density [78]

$$\varsigma = \frac{\partial^2\psi}{\partial e\partial q} = \left.\frac{\mathrm{d}f}{\mathrm{d}q}\right|_{\mathbf{e},T,\mu_i}. \tag{2.63}$$

Here, ψ denotes the free energy density per surface area of the electrode. It stems from the thermodynamic discussion of the free energy of elastic surfaces and is properly introduced in reference [78].[8] At equilibrium a Maxwell relation connects the electrocapillary coupling coefficient ς to [78]

$$\varsigma = \left.\frac{\mathrm{d}E}{\mathrm{d}e}\right|_{q,T,\mu_i}. \tag{2.64}$$

Hence, comparing equations 2.63 and 2.64, the surface stress response of an electrode to a change in surface charge density at constant strain is equal to the potential response upon an elastic strain change at constant charge density.
The electrocapillary coupling coefficient is vital to the scope of this work, as it relates the change in surface stress to the accumulated charge on the surface area. Essentially, a changing electrosorption of charge carriers on the surface has an influence on the bonds at the surface of the electrode in the in-plane and in the normal direction. Thus, a charge

[8] For relatively small elastic electrode deformations and a sufficiently symmetric surface, which possesses at least a three fold rotational symmetry [181], its fundamental equation is $\psi = E\mathrm{d}q + f\mathrm{e}$ [78]. ψ is connected to γ via a Legendre transformation of $\gamma(E, e) = \psi(q, e) + fde$ so that $\mathrm{d}\gamma = -q\mathrm{d}E + f\mathrm{e}$. These equations are noted in Lagrangian coordinates.

reorganisation occurs, which in turn leads to electrostatic Hellman-Feynman forces acting on the surface ions.[79] For a clean gold surface the electrocapillary coupling parameter has been determined at weak ion adsorption near E_{zc}. It is $\varsigma_{\mathrm{Au}} = -2.0\,\mathrm{V}$.[80] Thus, the electrocapillary coupling parameter for gold is negative. So, an increase in charge δq leads to a decrease in surface stress f.
The measurement method, i.e. in situ cantilever bending, used in this work allows to measure the surface stress in a direct manner through the curvature of a cantilever-shaped sample. Note that the cantilever is fully immersed in the electrolyte solution so that no contact angle is observed. The change in surface tension may be connected to the charging of the surface, as described in the Lippmann equation 2.61. Thus, the simultaneous determination of surface stress and surface tension are possible through the analysis of the mechanical and the electrochemical signals of the measurement. The details will be discussed in sections 3.5.2 and 4.3.
Despite a significant accumulation of charge carriers in the electric double layer at the interface, e.g. up to $0.3\,\mathrm{C\,m^{-2}}$ in metals [133], the resulting surface stress in bulk electrodes does not lead to a significant actuation effect because of the low surface-to-volume ratio of the bulk material. For nanoporous electrodes with considerable inner surface area though, an electrochemically-induced change in surface stress can drastically alter the compensating bulk stresses.[180] Thus, it is possible to significantly strain the entirety of a nanoporous electrode.[10] The microscopic description of the phenomenon may be transferred to macroscopic electrodes. The nanoporous material is regarded as an effective medium.[182] If a uniaxial, external load per area of the electrode cross-section L is present, an elastic strain ε is defined in load direction of the sample, as

$$\varepsilon = \frac{l - l_0}{l_0}, \tag{2.65}$$

where l and l_0 are strained length and initial length, respectively. An effective strain-charge coefficient, A^* is introduced as [182]

$$A^* = \left.\frac{\mathrm{d}\varepsilon}{\mathrm{d}q_{\mathrm{V}}}\right|_L, \tag{2.66}$$

where q_{V} denotes the total charge normalised to the volume V of the electrode. The actuation performance can be assessed by means of A^* and is thus very helpful to this work, as different porous sample types will be investigated.
The surface stress response upon an electrosorption of ions, is also termed electrochemo-mechanical coupling. For planar metal surfaces as well as nanoporous metals, e.g. gold or palladium, electrochemo-mechanical coupling has been extensively studied.[75, 183–187] Here, the aim is to establish, thoroughly investigate and evaluate the electrochemo-mechanical coupling in a nanoporous material based on the semiconductor silicon, i.e. porous silicon. Ab initio calculations corroborate that an electrochemo-mechanical coupling is not only present on clean metal surfaces, but it can also be observed on a clean silicon surface.[82] Thus, a central point of the presented work will be to investigate if the connection of charge carrier electrosorption in the electric double layer of the silicon surface leads to a quantifiable actuation effect. Therefore, porous silicon has to be in accordance with the precondition that it exhibits a polarisability. That means, an electrochemical measurement shows a finite potential region in which ionic charge carriers from the electrolyte exclusively assemble in a capacitive manner on the porous silicon

surface. Thus, charge density q is only affected by other state variables. By contrast, it also means that in the respective potential range no irreversible processes occur that involve an electrochemical reaction of the involved species, i.e. Faradaic currents must not arise.[78] Hence, a key point will be to evaluate if bulk and porous silicon, respectively, exhibit polarisability.

2.6. Polypyrrole - An Electrically Conductive Polymer

The second approach to integrate an actuator functionality aims to embed the electroactive, electrically conductive polymer polypyrrole into the pore space of porous silicon in an electrochemical polymerisation process. To understand this process, this section will have a short overview of fundamental electrical conduction mechanisms of electrically conductive polymers in general and polypyrrole in particular. Moreover, the synthesis and basic properties of polypyrrole will be discussed.

2.6.1. Fundamentals of Electrical Conductivity

A carbon atom possesses four electrons in its outermost shell, which are distributed among its one 2s and three 2p orbitals. In the ground state two electrons occupy the 2s orbital as well as two further 2p orbitals. For the atoms to bond to another carbon atom, the four electrons transition into hybrid states. Thereby, one of the 2s electrons is excited into the 2p orbitals. If it is in the prior unoccupied 2p orbital, an sp^3 hybridisation is established with four equal orbitals arranged in a tetrahedron. By contrast, if the electron is excited to one of the occupied 2p orbitals, an sp^2 hybrid orbital is created. The three ensuing sp^2 orbitals triangularly arrange in the plane, while the remaining 2p orbital is orthogonally oriented. In a bond between two sp^3 hybrid carbon atoms the electrons are engaged in covalent singular bonds, which result from the overlap of two sp^3 hybrid orbitals. This type of bond is referred to as a σ-bond.[188, 189] If the carbon atoms have an sp^2 hybridisation, two free sp^2 orbitals overlap and establish a σ-bond. However, the remaining 2p orbitals of each atom cannot directly overlap. Thus, a π bond is created. The π bond is weaker than the σ bond and is more readily broken.[188]
Electrically conductive polymers are sp^2 hybridised along their main chains. Thus, in principle, a delocalised π electron system should form.[190, 191] However, the Peierls-instability along one dimensional polymer chains leads to an energetically favourable dimerisation. Hence, alternating single and double bonds are found along the polymer chain.[190] These types of polymers are referred to as conjugated. The simplest case of an electrically conductive polymer constitutes polyacetylen, shown in Figure 2.9(a). It will serve here as a model to explore the basics of electrical conductivity in polymers. Polyacetylen has two energetically degenerate ground states.[95, 190] They can be distinguished by a shift of the alteration of single and double bonds, as shown in Figure 2.9(a) by the regions in the polymer marked I and II. The different ground states may occur on the same single chain. The transition between them is then not abrupt but proceeds over approximately seven monomer units.[192] This defect possesses a free radical charge, which is delocalised over the monomer units. This transition defect is referred to as a soliton.[190] It constitutes a basic charge conductivity mechanism as the ground energy of the polymer chain is not dependent on the position of the soliton and, thus, it can freely move along the chain.[192–194] The electrons in conjugated polymer chains solely need to

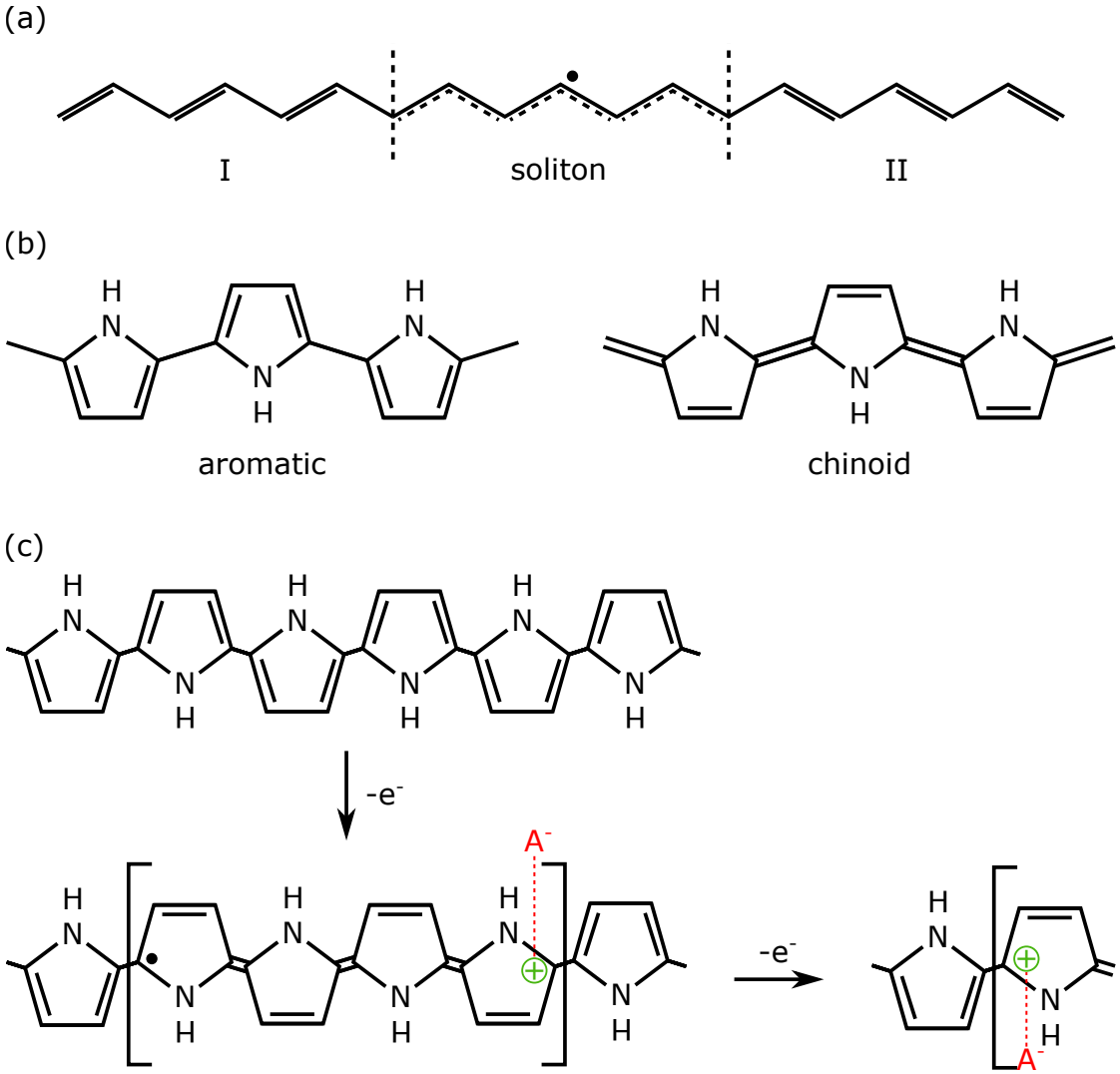

Figure 2.9.: **Properties of conductive polymers.** (a) A conjugated polyacetylen polymer chain with two degenerate, energetically equal ground states (I and II) and their transition region (soliton), which carries a delocalised free radical charge (dot). Adapted with permission from reference [190]. (b) The lower energy, aromatic and higher energy, chinoid polypyrrole ground states. (c) Different charge states of the polypyrrole chain. An oxidation leads to the emergence of a soliton (dot, left side) and an anti-soliton (right side). Together they form a polaron, which stabilises the chinoid section of the chain. Anions (A^-) are incorporated into the chain to counterbalance positive charges. A further oxidation leads to the creation of a second anti-soliton at the left side of the chinoid section, which now is referred to as a bi-polaron.

change their bond partner for an electrical conductivity to occur. So, all in all, the mechanism is rather a movement of the soliton defect, instead of a movement of electrons. In an as-prepared state, polyacetylen is a polymeric semiconductor with a bandgap of 1.5 eV with an intrinsic resistivity of about $10^6\,\Omega\,\mathrm{cm}$.[195] By deliberately performing an electrochemical oxidation, electrons are removed from the polymer chains, additional solitons are created and it is possible to reduce the resistivity to approximately $10^{-4}\,\Omega\,\mathrm{cm}$.[196] In terms of polymers this process is known as doping. In comparison with semiconductors this terminology seems reasonable, as doping leads to an increase in charge carriers and thus electrical conductivity.
Solitons are electrically neutral, negatively or positively charged. If the electrical charge and the molecular charge of the polymer chain have the same magnitude but opposite sign, the soliton is neutral. In an oxidation or reduction reaction of the polymer, the unpaired electron of the soliton is altered before the remaining electrons since it is on a higher energy level.[194] An oxidation removes the electron and leads to a positively charged soliton. Vice versa, a reduction adds an electron to the soliton, which is then negatively charged. An anti-soliton describes a soliton that counterbalances the perturbation of the polymer chain by a second soliton.
In contrast to polyacetylen, the electrically conductive polymer polypyrrole does not have degenerate ground states. The monomer unit of polypyrrole is a ring with two double bonds and composed of five constituents: four carbon atoms and one nitrogen atom. Polypyrrole is in one of two ground states – the lower energy aromatic and the higher energy quinoid ground state, which are depicted in Figure 2.9(b).[194] If the single and double bonded molecules are exchanged, the rings are either connected by a single or by a double bond in the polypyrrole chain. This differentiates the two ground states. If a soliton emerges in the polypyrrole chain, it separates an aromatic from a quinoid section. Hence, a soliton would migrate to the end of the polymer chain to minimise the number of quinoid chain parts and thus the energy. A soliton can only be stabilised by an adjacent anti-soliton, as illustrated in Figure 2.9(c). A neutral soliton and a positively charged anti-soliton are attracted to confine the quinoid region to a number of approximately four monomer units.[95] As the two cannot combine, they form a stable structure called polaron.[194] A further reduction charges the neutral soliton and a bi-polaron is created. The doping of polypyrrole leads to an increase in the number of polarons. This is represented in the band structure of the polymer as increasingly widened inter-bands between valence and conduction band exist. The inter-bands do not overlap with neither, not even at maximal oxidation.[95] Thus, polypyrrole does not possess a metallic conductivity, but its conductivity is rather sustained by (bi-)polaron transport along the polymer chains.[197] Therefore, the conductivity is particularly defined by the transport characteristics along polypyrrole chains, between connected polypyrrole chains and between different polypyrrole particles.[198, 199] Long polypyrrole chains in an ordered polypyrrole network have a higher conductivity than surrounding unordered polypyrrole.[198, 199]

2.6.2. Synthesis

The synthesis of polypyrrole can be achieved via a chemical or an electrochemical polymerisation procedure of pyrrole monomers. The latter involves the application of a potential in a solution of pyrrole monomers to initiate and facilitate polymerisation. For the presented work, it represents the method of choice. In general, the process is separated

into two different stages: the onset or initiation of the polymerisation and the growth of polypyrrole chains. The process is illustrated in Figure 2.10. In the electrochemical process a potential is applied between a working electrode and a counter electrode. As a result, pyrrole monomers are oxidised, i.e. an electron is stripped off and passes to the working electrode. The pyrrole monomers are then in the form of a cation radical.[200] The radical has several resonance forms. The remaining unpaired electron can be on either of the ring positions or on the nitrogen position.[200] In a next step, two radicals in the resonance form, depicted in Figure 2.10(a), under loss of two protons are forming a dimer to stabilise, see Figure 2.10(b).[200] The dimer is oxidised again and then forms a dimer radical cation as shown in Figure 2.10(c). The dimer has a lower oxidation potential than the monomer since the unpaired electron is delocalised over two monomer units and, thus, the dimer is more readily oxidised by the applied potential.[200] Subsequently, the dimer radical cation forms a trimer in another reaction with a monomer radical cation and by de-protonation, as shown in Figure 2.10(d). The sequence of oxidation, coupling and de-protonation repeats itself so that increasingly longer chains of polypyrrole form, see Figure 2.10(e). Since an oxidised radical oligomer ion is in one of several resonance forms, the coupling between two of these might also occur at any monomer unit within the oligomer and, precisely, not at the end of the oligomer chain. The latter dominates at shorter chain lengths. The probability of this type of intra-chain coupling progressively increases with longer polypyrrole chains.[200] Thus, polypyrrole has a relatively short average chain length with only approximately 64 monomer units at maximum [201] and the chains are cross-linked.[99, 199, 202, 203]
The electrochemical polymerisation results in a state of the polypyrrole that is charged by (bi-)polarons since the potential required to polymerise monomers/oligomers is higher than the potential to oxidise the freshly fabricated polypyrrole polymer.[99] During the polymerisation, two electrons per monomer unit are necessary for the polymerisation. Furthermore, an additional 0.2 to 0.4 electrons per monomer unit are employed for the oxidation, i.e. doping, of polypyrrole.[99, 200, 204–206] The charge in the polymer is compensated by an anion that is added to the polymerisation solution. Thus, polypyrrole is doped when the fabrication process is finished. The choice of electrolyte contributes to the ordering of the polypyrrole. In case of a planar electrode, a large plate-like anion as para-toluene sulphonate leads to a more parallel orientation to the electrode surface.[207] In contrast, small, spherically shaped anions lead to an amorphous structure [208, 209] but are readily inserted and extracted from the polypyrrole network [94]. Examples for this class of anions are SO_4^{2-}, BF_4^- or the here used ClO_4^-.

2.6.3. Electrochemical Actuation

Oxidation of polypyrrole generates (bi-)polarons, as described above. In an electrolyte solution these charged conjugation errors are compensated by an incorporation mechanism of electrolyte ions of opposite charge into the polymer network. The polymer network reacts to the counterbalance of electrolyte ions with a change in volume, i.e. an actuation. An electrochemical reduction of polypyrrole leads to a decrease in doping. In principle, this involves a decrease in bond length of the polypyrrole rings.[95, 194] An oxidation entails a higher doping and longer bond lengths. However, the critical mechanism for the actuation is not a change in bond length but an ion exchange of polypyrrole with the electrolyte.[94] In general, polypyrrole expands if electrolyte ions and soluble molecules

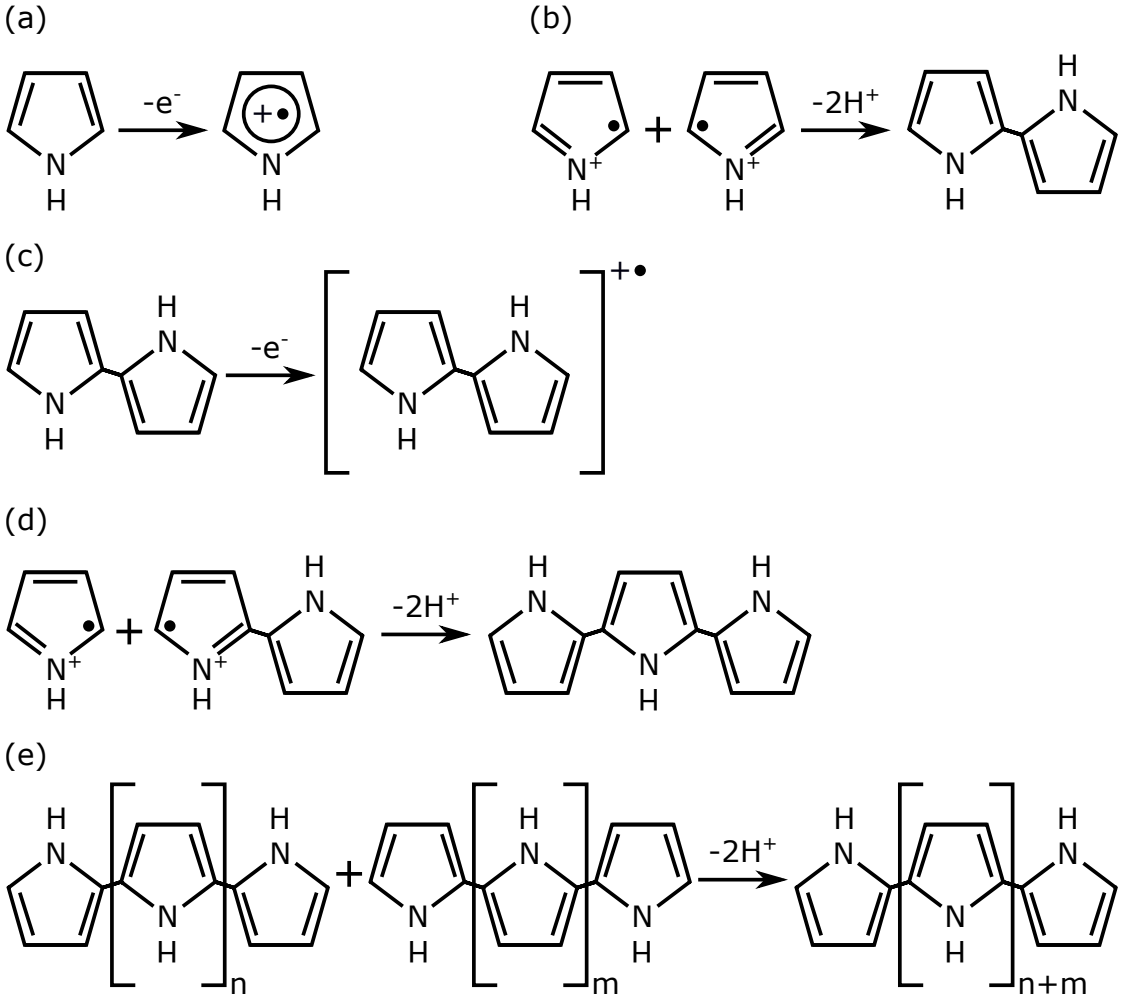

Figure 2.10.: **Polymerisation process of polypyrrole.** (a) A monomer gets oxidised by an applied potential and is in one of several resonance forms. (b) Two radical monomer units form a dimer under the loss of two protons. (c) The dimer is oxidised and is in one of a few radical resonance forms again. (d) A radical monomer and dimer for a trimer under de-protonation. (e) Eventually longer chains form. Partially adapted with permission from reference [200].

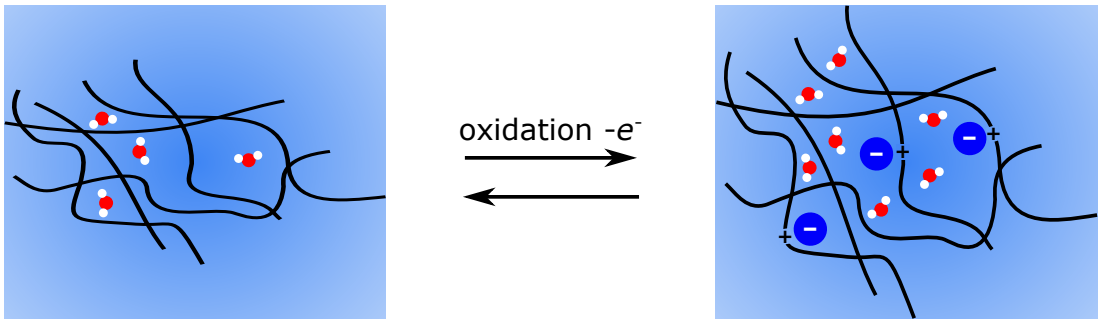

Figure 2.11.: **Electrochemical actuation mechanism of polypyrrole.** Polypyrrole, illustrated here by the network of polymer chains, incorporates anions upon an oxidation of the polymer chains and, thus, expands. Vice versa, a reduction leads to an expulsion of anions and a contraction of the polymer network. Adapted with permission from reference [94].

enter into the polymer network and, vice versa, polypyrrole contracts by the expulsion of the two.[94] If polypyrrole is oxidised, the emerging positive charges in the polypyrrole network is compensated by one of two mechanisms. First, large anions cannot easily be incorporated into or ejected from the polypyrrole network. Thus, cations from the electrolyte solution are employed in the charge compensation.[210] By contrast, small anions are readily exchanged between polypyrrole network and electrolyte solution and thus sustain the actuation without a significant assistance of cations. The ions used for electrochemical actuation measurements presented in this work, i.e. chloride anions (Cl^-) and perchlorate anions (ClO_4^-), are considered small in the context of ion size.[103, 211] Thus, the polypyrrole volume increases, i.e. it expands, if electrolyte anions and the molecules of the soluble enter into the polypyrrole network. Polypyrrole contracts by expulsion of anions. The mechanism is illustrated in Figure 2.11. Thereby, the number of transferred anions is directly proportional to the change in the amount of conjugation errors along the polypyrrole chains, which in turn can be quantified by the charge that is transferred to and from polypyrrole.[212] In conclusion, polypyrrole performs a reversible actuation by the incorporation and expulsion of electrolyte anions under electrochemical control. Its volume change is proportional to the transferred charge.[94] A uniaxial strain-charge coupling coefficient is defined as [213]

$$\psi = \frac{\delta\epsilon}{\delta q_\mathrm{V}}, \tag{2.67}$$

where $\delta\epsilon$ denotes the volume change and δq_V the change in transferred charge normalised to the volume of polypyrrole material. ψ varies between 0.03 and 0.5 $\mathrm{mm^3\,C^{-1}}$ foremost depending on the type of anion.[213] However, as anions form a solvation shell, as already discussed in section 2.2, the volume change also depends on the type of solvent. Furthermore, the conditions of the synthesis might also influence ψ. For perchloric acid ($HClO_4$), i.e. perchlorate anions with water as the solvent, and a polypyrrole film prepared under constant potential, a value of $\psi = 0.17\,\mathrm{mm^3\,C^{-1}}$ has been reported.[213]

3. Materials and Experimental Methods

In this section, basic principles of electrochemical methods and measurements will be introduced, as these are the basis for both the fabrication of porous silicon and polypyrrole-porous-silicon hybrids as well as the electrochemical actuation experiments on these. Furthermore, the methods to analyse the fabricated materials are explained. Lastly, the focus will be on the experimental methods to characterise the electrochemical actuation of both materials.

3.1. Principles of Electrochemistry

The electrochemical fabrication of porous silicon and the subsequent polymerisation of polypyrrole in its pores as well as the electrochemical actuation experiments are conducted under electrochemical control. Therefore, the basic principles of the electrochemical side of the setups and the respective measurement methods will be explained in this section. Some aspects are already partially addressed in chapter 2 but will be summarised here again.
An electrochemical setup basically consists of two electrical conductors that are immersed in an electrolyte solution and are referred to as electrodes. A potential can be applied between the two electrodes. Charge transport is accomplished by electrons in the electrodes or ions in the electrolyte solution, respectively. Whereas the electrons are not changing the electrode's state, the ions can alter the electrode surface or the electrolyte composition at the interface. In total, the electrochemical reactions occurring are the combination of the reactions at each of the two electrodes in response to an applied potential.[127] The electrode that is not investigated in the actual experiment is the counter electrode, or abbreviated CE. It has to fulfil the precondition of being a good conductor with a high surface area to establish the current flow to the other relevant electrode. A platinum mesh or carbon cloth is used as a counter electrodes in this work. The electrode of interest is referred to as the working electrode, short WE. An electrochemical characterisation of the WE encompasses that reactions occurring are related to a well-known, defined potential. The CE is current-carrying and the potential of it is dependent on the current amplitude.[214] Thus, using the CE as the potential reference introduces measurement inaccuracies. Therefore, a third, reference electrode (RE) is necessary. The RE typically carries a negligible current and has well-known potential relative to the SHE potential, as already discussed in section 2.2. Reference electrodes used in this work are a thin silver-silver chloride (abbreviated Ag/AgCl) reference electrode (SE11, Sensortechnik Meinsberg) with a diameter of 5 mm, a thicker Ag/AgCl RE (Double-Junction 6.0726.107, Metrohm) or a reversible hydrogen electrode (Hydroflex, Gaskatel). The RE is positioned between WE and CE. This arrangement is a three electrode setup in contrast to the two electrode setup, in which the CE acts also as RE. In a three electrode setup the amplitude of current is determined between CE and WE and the potential is measured between RE and WE by a potentiostat with high input impedances (Metrohm-Autolab PGSTAT30,

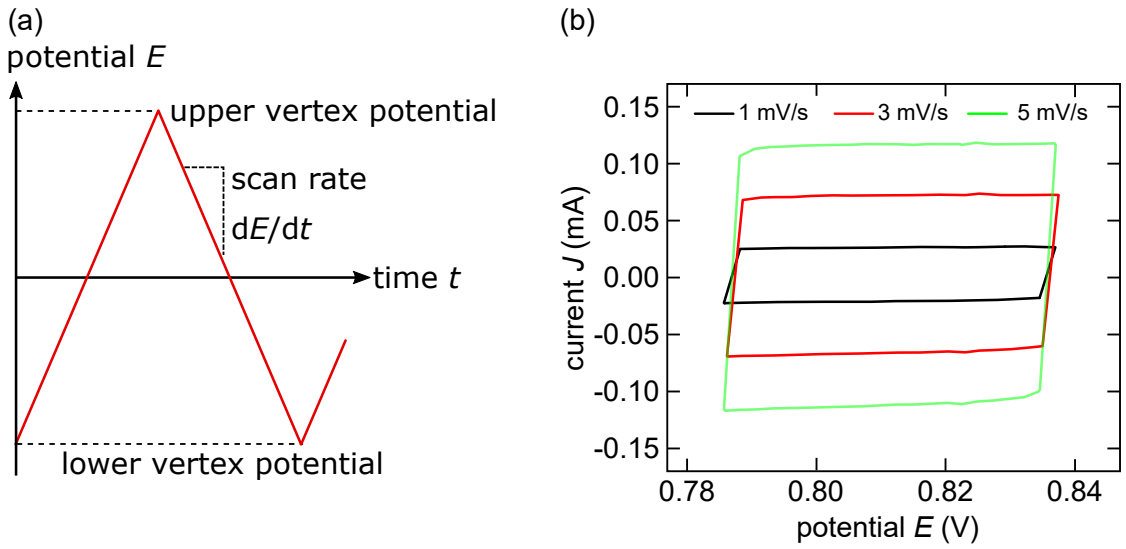

Figure 3.1.: **Cyclic Voltammetry.** (a) CV measurement illustrated by a plot of the linear change in potential E versus time t from the lower to the upper vertex potential with the scan rate $\mathrm{d}E/\mathrm{d}t$. (b) Characteristic CV measurements recorded on a nanoporous gold electrode in $1\,\mathrm{mol\,L^{-1}}$ perchloric acid electrolyte in the potential range of $0.787\,\mathrm{V}$ to $0.837\,\mathrm{V}$ with scan rates of $1\,\mathrm{mV\,s^{-1}}$ to $5\,\mathrm{mV\,s^{-1}}$. Adapted with permission from reference [215].

PGSTAT302N or PGSTAT204). The potentiostat controls the applied potential E. In this work all potentials are denoted versus the standard hydrogen electrode. The potentiostat measures simultaneously the current J which runs between WE and CE and also yields the accordingly consumed charge Q.
A powerful tool to investigate electrochemical reactions are cyclic voltammetry (CV) measurements. In CV measurements the applied potential is linearly changed with a constant slope between a lower and higher potential, also called lower and upper vertex potential. At these points the sign of the potential slope is changed, i.e. the direction of the potential scan is reversed. The rate $\dot{E} = \mathrm{d}E/\mathrm{d}t$ with which the potential is varied is the sweep or scan rate. The choice of the vertex potentials depends on the processes the WE exhibits and are probed. Furthermore, the solvent sets the maximum potential range. Exceeding this range leads to electrochemical reactions of the solvent itself, although, under experimental conditions, solvents have different over-potentials. Aqueous solutions, which are used throughout this work, have a theoretical potential range between $0\,\mathrm{V}$ and $1.223\,\mathrm{V}$. Below $0\,\mathrm{V}$ a reduction of the soluble water sets in so that hydrogen gas forms. At potential values higher than $1.223\,\mathrm{V}$ water begins to oxidise leading to oxygen gas evolution. These potential values are valid for pH 0. They reduce with an increasing pH value. The oxygen and hydrogen evolution limit the accessible potential range for experiments since the Faradaic currents generated by these processes superimpose and interfere with any currents generated by the investigated electrode. Figure 3.1(a) shows an explanatory illustration of a CV measurement, with potential E versus time t. In the analysis of CV measurements, a plot of current J versus potential E reveals the electrochemical characteristics of the WE. Figure 3.1(b) shows an exemplary CV for nanoporous gold, conducted in $1\,\mathrm{mol\,L^{-1}}$ $HClO_4$

electrolyte. Current J is plotted versus potential E varied with scan rates of $1\,\mathrm{mV\,s^{-1}}$ to $5\,\mathrm{mV\,s^{-1}}$.[215] The nanoporous gold electrode exhibits a virtually ideal polarisability in this potential range. The course of the signal almost instantly increases from the lower vertex point and reaches a near constant value. Vice versa, the current quickly decreases to the negative constant counterpart when the sweep direction is reversed at the upper vertex point. Thus, the course of up- and down-sweep encompasses an area of current. The same amount of charge, accumulated by non-specific adsorption in the electric double layer, on the up-sweep, is released on the down-sweep and thus all of the charge is recoverable. In total, charge is capacitively stored in the electric double layer. In particular, no peaks due to a reduction or oxidation reaction are visible.[216] Starting from the lower vertex point, the current increases according to

$$J = \frac{\mathrm{d}E}{\mathrm{d}t} C \left(1 - \exp\left(\frac{-t}{R_\mathrm{S} C}\right)\right), \tag{3.1}$$

where C is the capacitance of the double layer, cf. equation 2.27, and R_S the resistance of the solution.[127] After a certain time interval, i.e. $t \gg R_\mathrm{S}C$, current J settles to a constant value of

$$J = \frac{\mathrm{d}E}{\mathrm{d}t} C. \tag{3.2}$$

Thus, the double layer capacitance C can be determined by the ratio of the scan rate and the according constant current value. Furthermore, it is possible to extract the (electrochemically active) surface area A of the sample investigated if the surface area specific capacitance c^* is known. For example, gold has a minimum reference value of $40\,\mathrm{\mu F\,cm^{-2}}$.[217] For silicon a value for c^*_Si will be determined in this thesis.
Another noteworthy type of electrochemical measurement is step-coulombmetry. The potential is changed in an instant from a lower potential to a higher value and then retained at a constant value for a defined time period. Afterwards, in a step-like fashion, the potential is switched back to the lower value. Due to these periodic instant potential steps, it is possible to investigate the charge kinetics of the electric double layer and accompanying electrochemical processes. This type of measurement yields characteristic time constants. Lastly, the potential can also be held constant at a single value while the potentiostat records current and charge.
The described electrochemical methods are implemented using a modern potentiostat, which applies a potential sweep in discrete steps. The current is also not measured continuously but at the end of each potential step.[218] Thus, the time difference of applying potential and measuring current might be a source of error. The potentiostat needs to be equipped with an extension, a linear scan generator, to apply a potential in a truly linear manner. On the downside, the linear scan generator has limitations, such as a minimal scan rate of $10\,\mathrm{mV\,s^{-1}}$. In section 5.2 measurements will be presented to evaluate if a difference between the two measurement types is noticeable.
Another electrochemical technique is electrochemical impedance spectroscopy. EIS is also performed in a three electrode setup. In contrast to the linearly varying potential of a CV measurement, EIS employs an alternating, sinusoidal potential E_s. It consists of a static potential E_stat that stays constant for the duration of the measurement and a sinusoidal potential. The amplitude E_0 of the sinusoidal potential is comparatively small. Here

10 mV are used. The resulting harmonic current response J_s is measured between WE and CE. Potential and current are given by [219]

$$E_s(t) = E_{stat} + E_0 \cdot \exp(i2\pi ft) \quad \text{and} \quad J_s(t) = J_{stat} + J_0 \cdot \exp(i2\pi ft - \phi(f)), \tag{3.3}$$

where J_{stat} and J_0 denote the current response to static and alternating potential, respectively, while $\phi(f)$ is the frequency-dependent phase angle of J_s with respect to the potential. The overall electrochemical response of an electrode to EIS is characterised by the electrochemical impedance Z, which follows [219]

$$Z = \frac{E_s(t) - E_{stat}}{J_s(t) - J_{stat}} = \frac{E_0}{J_0} \cdot \exp(i\phi) = Z_{re} + iZ_{im}, \tag{3.4}$$

with Z_{re} and Z_{im} being the complex impedance's real and imaginary parts, respectively. The potentiostat needs to be equipped with an impedance analyser module (Metrohm Autolab FRA32) to perform EIS.
For an EIS analysis of the electrochemical processes occurring at the material the frequency is swept over several decades while the impedance is recorded and averaged over a defined number of periods at each frequency step. The result is displayed in a Nyquist plot that shows $-Z_{im}$ versus Z_{re}. A schematic Nyquist plot is shown in Figure 3.2(a). The plot shows the characteristic response of an electric double layer charging process along explanations for the different phenomena occurring. The points with the highest frequencies are located closest to the abscissa at the beginning of the half-circle, whereas the low frequency points are at higher Z_{re} values where $-Z_{im}$ increases. Different parameters can be inferred from this type of plot. The different quantities are also marked in Figure 3.2(a).
Firstly, the intersection of the high frequency points with the Z_{re} axis at the onset of the half-circle marks the resistance of the electrode. The next regime starts at the end of the half-circle. The width of the half-circle is related to the bulk resistivity of the electrolyte. The sum of electrode and electrolyte resistance is also referred to as the internal resistance R. The next regime with intermediate frequencies marks an interplay of the diffuse layer and the electrolyte resistance in series with the capacitance c_{EIS} of the electric double layer retrieved from the EIS measurements. The differential capacitance obtained for example from CV measurements may vary from c_{EIS}.[220] Depending on the ratio of the two resistances, the slope of this intermediate regime is either larger, i.e. the charging process is controlled by electric double layer formation, or smaller, which means the process is limited by the diffusivity of ions in the electrolyte.[219] At last, at lower frequencies the signal converges to a vertical line at frequency f_c. Here, exclusively at the lowest frequencies, the electrical double layer is fully charged and the electrode is approximated by the internal resistance in series with the equilibrium capacitance c_{EIS}.[219] An approximation of the entire EIS signal with an equivalent circuit, as discussed in section 2.2.5, is complex. It is often equivocal and prone to errors introduced by intuition [219]. However, in this last, low-frequency regime such an equivalent circuit approximation is simpler and can be performed via an RC equivalent circuit. While Z_{re} is identical with the resistance in the RC-circuit, the capacitor is linked to the capacitance c_{EIS} of the electrode. In this case, the imaginary part simplifies to [219]

$$Z_{im} = -\frac{1}{2\pi c_{EIS} f}, \quad \text{for} \quad f < f_c. \tag{3.5}$$

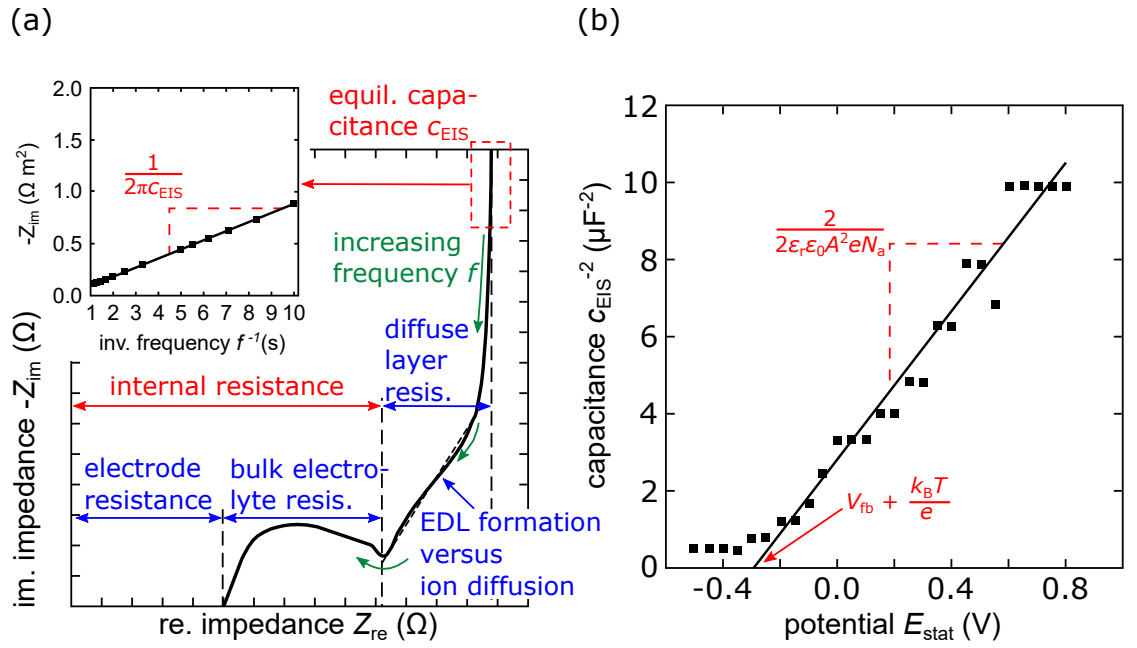

Figure 3.2.: **Electrochemical impedance spectroscopy of electric double layer charging.** (a) Nyquist plot, i.e. minus imaginary part versus real part of impedance Z, of a typical electric double layer charging with increasing frequencies f for the single measurement points. The plot shows a typical characteristic half-circle, the intermediate regime and the conversion to a vertical line. Several parameters can be inferred from such a Nyquist plot. Z_{re} of the half-circle's onset marks the electrode resistance and the Z_{re} width of the half circle is related to the bulk electrolyte resistance, which together are referred to as the internal resistance. The intermediate regime is due to competitive electric double layer (in the Figure referred to as EDL) charging and ion diffusivity and the slope in this regime marks which effect dominates. Lastly, the vertical regime is related to the equilibrium capacitance c_{EIS} of the electric double layer determined by EIS. A plot of these data points versus their inverse frequency f^{-1} yields a linear dependence, as shown in the inset, and allows a determination of c_{EIS}. Adapted with permission from reference [219]. (b) Mott-Schottky plot of an exemplary, n-type ZnO semiconductor. c_{EIS}^{-2} determined by EIS is plotted versus an increasing static potential E_{stat}, which is applied during the single EIS measurements. The data shows a plateau and a following linear increase. The slope of a linear fit to the data enables the determination of the doping concentration N_a, while the intersection of the fit with the abscissa yields the flatband potential V_{fb}. Adapted with permission from reference [131].

Thus, the linear slope of a plot of $-Z_{\mathrm{im}}$ points that lie on the vertical line, i.e. $f < f_{\mathrm{c}}$, versus inverse frequency $1/f$ yields c_{EIS}. An example of such a plot is shown in the inset in Figure 3.2(a).[219] A comprehensive study on the interpretation and evaluation of Nyquist plots of EIS data is found in references [219, 221].
Lastly, the static potential E_{stat} is changed over a set of EIS measurements. The obtained capacitance in the form of c_{EIS}^{-2} plotted versus the respective static potential yields a Mott-Schottky plot for a semiconductor. An example of an n-type ZnO semiconductor is shown in Figure 3.2(b).[131] As discussed in section 2.2, a fit to the linear regime of the data yields the flatband potential V_{fb} as the intersection of the fit with the abscissa. The doping concentration N_{a} can be inferred via the fit's slope s which equals [131]

$$s = -\frac{2}{eN_{\mathrm{a}}\varepsilon_{\mathrm{r}}\varepsilon_0 A^2}, \tag{3.6}$$

cf. equation 2.19. The vacuum permittivity is denoted by ε_0 and a pure silicon interface has a relative permittivity of $\varepsilon_{\mathrm{r}} = 11.68$.[222] Note that the slope s given in equation 3.6 is negative, which applies for a p-type semiconductor. Furthermore, the slope is normalised to the surface area A of the respective sample to obtain the doping concentration.

3.2. Porous Silicon Preparation

At the centre of this work is the material porous silicon. So, firstly, the preparation with all its details will be described. As experiments will be presented in chapters 4 and 5 on both porous silicon prepared from p- and n-type silicon wafers, both synthesis routes are introduced here. Firstly, the preparation of p-type porous silicon will be explained.
The base material for the sample preparation is a highly boron-doped p-type silicon wafer, which has a specific resistivity amounting to $0.01 - 0.02\,\Omega\,\mathrm{cm}$, which corresponds to a doping level of approximately $3 \cdot 10^{18} - 8 \cdot 10^{18}\,\mathrm{cm}^{-3}$ [7]. The wafers have an (100) orientation. For the fabrication of various types of porous silicon samples, wafers of different thickness are employed. Thus, it is possible to fabricate porous silicon which matches the needs of the specific experiment. The thickness of the wafer is specified by the supplier (Si-Mat Silicon Materials GmbH) and are $525 \pm 25\,\mu\mathrm{m}$, $381 \pm 25\,\mu\mathrm{m}$ and $100 \pm 10\,\mu\mathrm{m}$. The respective thickness will be listed in the discussion of the experiment in chapters 4 and 5. The top side of the wafer is polished by the manufacturer. In case of the $100\,\mu\mathrm{m}$ thick wafers, the back side is polished as well. The wafer includes two flats, i.e. cut-off sites of the otherwise round wafer, to indicate the doping type and, more importantly, the $\langle 110 \rangle$ directions.[52] The latter is especially important since the wafer can be sectioned into a defined rectangular geometry along these $\langle 110 \rangle$ cleavage lines. A line or a notch is prepared on the wafer with a diamond scribe and the wafer will break easily along this line.[52] The same process can be applied to porous silicon since it retains its mono-crystallinity, as already mentioned in section 2.4. The cleaving technique is used to prepare the actual samples in the right dimensions from the prepared porous silicon material.
Porous silicon is prepared in an electrochemical etching procedure with an HF-containing solution. The wafer is installed into an electrochemical etching cell, schematically depicted in Figure 3.3. The cell body and lid are fabricated out of polytetrafluoroethylene (PTFE) to safely handle HF. Furthermore, an O-ring sits at the bottom of the cell. By tightening screws, the body of the electrochemical cell is pressed onto the wafer, the O-ring is pressed

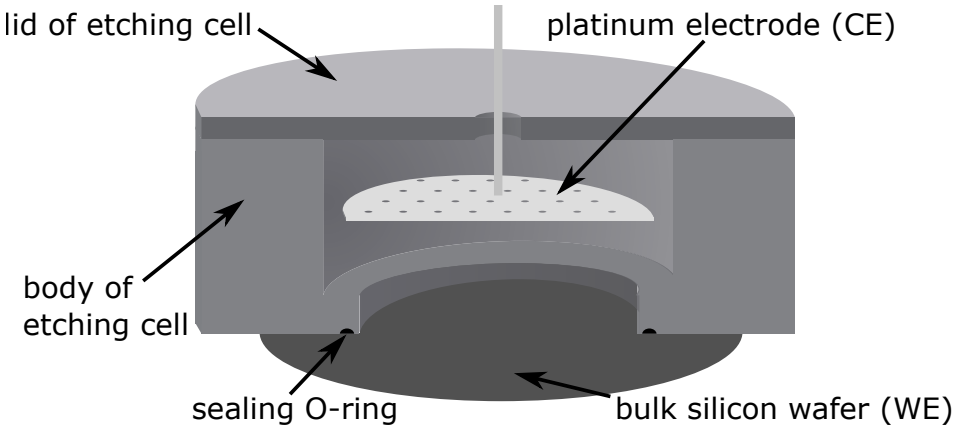

Figure 3.3.: **Preparation of porous silicon.** Electrochemical etching cell for the preparation of porous silicon with the relevant components of PTFE lid and body of the cell, an FKM O-ring to prevent the leakage of HF solution, a bulk silicon wafer acting as the WE and a platinum CE to apply the etching current.

flat and seals. The O-ring is made out of a fluorocarbon-based fluoroelastomer (FKM). For the fabrication of porous silicon two different electrochemical etching cells are used, which only differ in their size. The smaller cell has an O-ring with an inner diameter of 3.16 cm. Hence, the area in the cell that is in contact with HF amounts to 7.84 cm^2. For the larger cell the respective parameters are a diameter of 6.60 cm and an area of 34.21 cm^2. The wafer is electrically contacted on its back side via aluminium foil to form an ohmic contact, as described in section 2.1.[52]
In a first step, the native oxide layer is removed from the silicon wafer by filling a 10 vol % HF solution into the cell for a period of five minutes. The solution is prepared from HF (48 vol %, Merck Emsure) and ultra-pure water (resistivity of 18.2 MΩ cm). Afterwards, the actual electrolyte to perform the porous silicon etching is filled into the cell. It is a 2 : 3 volumetric mixture of HF (48 vol %, Merck Emsure) and ethanol (absolute, Merck Emsure). The ethanol reduces the surface tension of the electrolyte solution and enables an undisturbed imbibition into the forming pores and an escape of emerging hydrogen bubbles.[52] The HF solution equilibrates for five minutes. Then, a disk like platinum counter electrode is inserted into the cell so that it is fully immersed in the electrolyte solution. Etching pores into silicon requires that a current is applied between the CE and the silicon wafer acting as the working electrode, as already described in section 2.4. This configuration of electrodes is a two electrode setup.[52] A current source (Keithley Sourcemeter 2461) applies a suitable potential so that the set current is maintained between WE and CE. The current density is set to 12.5 mA cm^{-2}. Thus, the actual currents applied in the small and large cell translate to 98 mA and 428 mA, respectively. Generally, the time the current is applied determines the length of the etching process and thus the thickness of the porous layer or, in other words, the length of the pores reaching into the bulk silicon. The porous silicon etching with the stated parameters proceeds with an average rate of $0.7 - 0.75\,\mu m\,min^{-1}$.[223] In this state, the porous silicon layer is still attached to the remaining bulk silicon, i.e. an epi-layer.
For a free-standing membrane the current is increased in a final step to detach the porous

silicon layer from the remaining bulk silicon by the use of an electropolishing process, as discussed in section 2.4. The current is slowly increased to a value of $260\,\mathrm{mA\,cm^{-2}}$ and applied for 30 s. Subsequently, the CE and etching solution are removed from the cell. Lastly, the prepared material, either epi-layer or membrane, is rinsed three times with deionised water and allowed to dry for three hours under ambient atmosphere.
The process to fabricate n-type porous silicon is, in its main features, similar to p-type porous silicon fabrication. In this paragraph, solely the key differences are highlighted and explained. The base material for the fabrication process are antimony-doped wafers that are polished on both the front and back side by the supplier (SIL'TRONIX Silicon Technologies). They possess a resistivity of $0.01 - 0.025\,\Omega\,\mathrm{cm}$, which corresponds to a doping level of approximately $9 \cdot 10^{17} - 4 \cdot 10^{18}\,\mathrm{cm^{-3}}$, an (100) orientation and a thickness of $100 \pm 10\,\mu\mathrm{m}$. An etching of n-type silicon, as discussed in section 2.4, can be realised in an electrochemical etching cell which enables a simultaneous illumination of the wafer. Since such a cell is quite elaborate, another approach is adopted here. A strong oxidising agent is added to the electrolyte solution to enable pore growth and promote a widening of the pores during formation[224, 225]. As an oxidising agent, $KMnO_4$ (purity >99 %, Sigma Aldrich) with a concentration of $8\,\mathrm{mmol\,L^{-1}}$ is added to a 6 vol % aqueous HF solution. A current density of $11.48\,\mathrm{mA\,cm^{-2}}$ is applied, which translates to an absolute current value of 90 mA for the smaller etching cell. Finally, the resulting porous silicon material is also rinsed three times with deionised water and dries for three hours.
It is possible to fabricate both p- and n-type porous silicon in the form of a double epi-layer. In this regard, a porous silicon layer is synthesised on both front and back side successively. The wafers have to be polished on both of these sides. The respective fabrication process is executed on one of the sides first, as described above for p-type and n-type silicon. After the cell disassembly, the wafer is turned upside down and the same process is repeated on the second side. The thickness of each layer has to be the same. Otherwise the whole sample might bend due to differing strain states between the layers. Furthermore, the two layers are not extending over the whole thickness of the wafer. Thus, a thin bulk silicon layer intersects the two epi-layers in the middle, as a support and means of establishing an electrical contact to the pSi epi-layer, as will be described below in section 4.1.

3.3. Characterisation Methods for Porous Silicon

The physical properties of fabricated porous silicon are characterised by different methods that will be introduced here. A scanning electron microscope (SEM; either Zeiss Leo 1530 or Zeiss Supra VP 55) is used to record micrographs on a freshly cleaved porous silicon profile. The SEM is able to utilise energy-dispersive X-ray spectroscopy (EDX) to determine the composition of the material based on the element specific energy signal. The EDX detector records and averages the energy specific signal while the electron beam illuminates a certain area, here in side view across the total profile of a porous silicon layer. The EDX spectrum is recorded until 500 000 counts are surpassed to achieve significant statistics.
Additionally, the thickness of the porous silicon layer is determined by a profile recorded with the SEM. The total outer volume V of the porous silicon layer can be extracted with the knowledge of the specific sample's thickness and its lateral dimensions. For the latter,

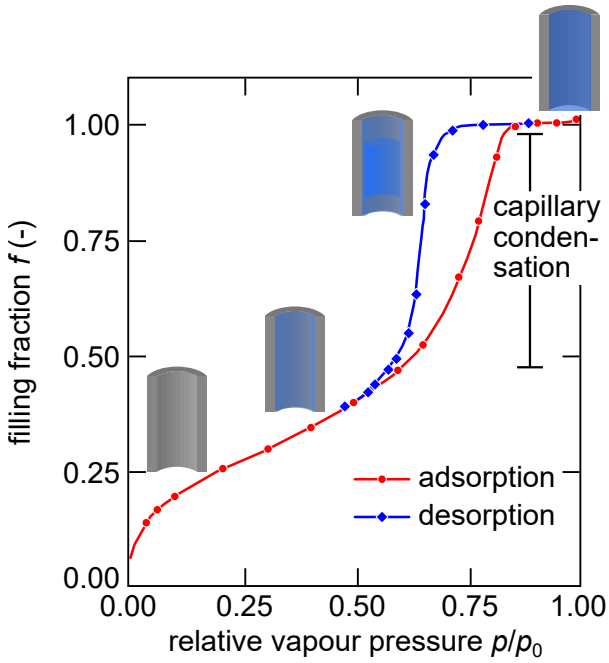

Figure 3.4.: **Nitrogen sorption of porous silicon.** Characteristic nitrogen sorption isotherm measurement with filling fraction f on the ordinate and relative pressure p/p_0 on the abscissa and an adsorption and desorption branch. Clearly visible is the distinct hysteresis between the two branches. At the respective point of the sorption isotherm, schemes illustrate an empty pore, single layer adsorbed onto the pores surface, the formation of menisci and a fully filled pore. Adapted with permission from reference [174].

a picture of the material on millimetre paper is recorded. Then the dimensions are readily accessible, which are length l and width w in case of a rectangular sample or surface area A for more general sample shapes.
The main characterisation method for porous silicon is nitrogen sorption isotherms conducted in a nitrogen sorption setup (Quantachrome autosorb iQ). The porous silicon is baked out at 300 °C in a vacuum prior to the sorption isotherm. In the actual measurement, nitrogen gas is passed into the measurement cell, which is cooled down to the temperature of liquid nitrogen. Hence, nitrogen adsorbs on the surface of the sample. The adsorbed quantity of nitrogen is measured in dependency of the nitrogen partial pressure p/p_0. A typical sorption measurement is depicted in Figure 3.4. It illustrates the characteristics of such an adsorption measurement on porous silicon. The measurement starts with the adsorption of first a single mono-layer of nitrogen molecules on the inner surface area of porous silicon. Then, a multi-layer growth ensues. After an initial regime up to $p/p_0 \approxeq 0.2$, the filling fraction f increases approximately linearly up to a value around $p/p_0 \approxeq 0.6$. On this section of the sorption measurement, the BET model (Brunauer-Emmett-Teller) is applied to determine the inner surface area of the porous silicon material.[226] Increasing the partial pressure further leads to the onset of capillary condensation, which means that menisci and liquid nitrogen bridges form inside the pores. Upon a further increase of relative vapour pressure, these menisci are driven out

to the end of the pores. Lastly, the porous silicon material is saturated and filling fraction and partial pressure reach $f = p/p_0 = 1$. At this point the total porous volume can be extracted and the filling fraction is set relative to this value. Then, the desorption branch of the isotherm measurement commences. Thus, pressure is reduced, p/p_0 decreases and nitrogen desorbs from the menisci until the menisci vanish. However, the adsorption and desorption branches of the measurement exhibit a distinct hysteresis, characteristic for porous materials in the mesoporous range.[174] Thereby, nitrogen menisci vanish at lower relative partial pressures compared to the partial pressures they form. Another model is applied on the desorption branch of the measurement – the BJH (Barrett-Joyner-Halenda) model. It yields the distribution of pore radius r (or diameter D) and the volume of the pores V_{por} and thus also porosity $\Phi = V_{\mathrm{por}}/V$.
Transmission electron microscopy (TEM) is used to record high resolution pictures of single sites of porous silicon. The images shown in this work are recorded by scanning transmission electron microscopy (STEM) with a high angle annular dark-field detector. Whereas nitrogen sorption isotherms yield quantitative data averaged over the whole porous silicon material, the purpose of TEM images is to obtain a highly resolved qualitative impression of the porous structure. These TEM images can then also be converted into micromechanical (finite element) models to perform simulations on pSi, as will be discussed in section 5.4.3. The transmission electron microscope (FEI Talos F200X) also possesses EDX detectors and hence, the elemental composition of a material can be determined in a highly-resolved manner. The EDX intensity of the relative elements can be added to the micrograph to obtain information about the site-specific elemental distribution.

3.4. Electrochemical Polymerisation of Polypyrrole in Porous Silicon

After the initial porous silicon preparation step, the aim is an electrochemical polymerisation of polypyrrole inside the pSi pores. The sample is installed into a second electrochemical cell. Similar to the etching cell, the polymerisation cell is also fabricated out of PTFE. The cell is clamped on the epi-layer, which acts as the WE, in a similar fashion with an O-ring sealing the cell around the circular porous silicon surface. The O-rings are made of ethylene-propylene-diene-monomer (EPDM) rubber to withstand the chemicals used for the polymerisation. The area exposed to the electrolyte solution is also $7.84\,\mathrm{cm}^2$, corresponding to the HF etching cell. A platinum mesh CE is placed at the top. It has a hole in the middle so that it is possible to insert an Ag/AgCl (Sensortechnik Meinsberg) RE. The RE's tip is positioned between WE and CE. Thus, the electrochemical polymerisation is realised in a three electrode setup. Figure 3.5(a) schematically shows the setup. Subsequently, the solution for the polymerisation is filled into the cell and it is permitted to imbibe into the pores for 15 minutes. The polymerisation requires pyrrole monomer units, i.e. C_4H_4NH molecules. The concentration of the monomer is $0.1\,\mathrm{mol\,L}^{-1}$. Before the polymerisation process, a distillation of the pyrrole monomer is conducted at $130\,^{\circ}\mathrm{C}$ to maximise the monomer amount. As already mentioned in section 2.6, the polymerisation results in a charged state of the polymer. Therefore, a lithium perchlorate ($LiClO_4$, Thermo Scientific) electrolyte is added to the polymerisation solution to compensate the emerging charge. Hence, the perchlorate anions are incorporated into the polymer during the synthesis, i.e. polypyrrole is doped. $LiClO_4$ is added with an equal concentration of

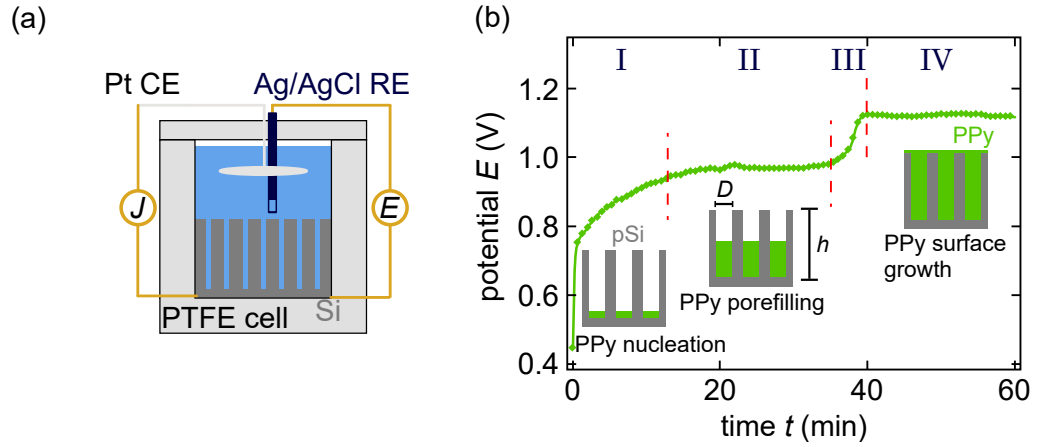

Figure 3.5.: **Polymerisation of polypyrrole in porous silicon.** (a) Illustration of the electrochemical polymerisation cell used for filling porous silicon with polypyrrole by electrochemical polymerisation. Indicated are the PTFE body of the cell with a lid filled by the polymerisation solution (blue), porous silicon contacted as WE, a mesh-shaped platinum CE and the Ag/AgCl RE to determine the potential. (b) Evolution of potential E over the electrochemical polymerisation process of polypyrrole in porous silicon pores. Adapted with permission from reference [206] – in particular, the ordinate is displayed versus the SHE, whereas in the reference the potential is measured against a platinum pseudo-RE. Depicted are the characteristic stages of (I) the nucleation of polypyrrole molecules at the pore bottom, (II) the continued filling of the pores by polypyrrole and finally (III) the complete filling of the pores and a successive transition stage to (IV) a polymerisation of polypyrrole on the outer surface of porous silicon.

$0.1\,\mathrm{mol\,L^{-1}}$. The solvent used is acetonitrile (gradient grade, Merck Emsure).
The electrochemical polymerisation is performed under galvanostatic conditions. That means, a constant current is applied by the potentiostat while the potential is monitored via the RE. The applied current is set to 2 mA, which translates to a current density of $0.255\,\mathrm{mA\,cm^{-2}}$ with respect to the area of the contact area of electrolyte solution. The current of 2 mA is chosen for the standard process. In section 5.1 the influence of the current will be explored further. The potential, raised by the applied current, oxidises pyrrole monomer units, which are then unstable and form dimer units under de-protonation. Dimers are again oxidised so that eventually longer polymer chains form, as described in detail in section 2.6. While this holds true for a general electrochemical polymerisation of polypyrrole, the process involves specific phases when it proceeds in porous silicon. These phases can be precisely monitored by the potential evolution over the time of the electrochemical polymerisation.[227] The evolution is recorded with a temporal resolution of 1 s. An example for a typical potential evolution from literature is shown in Figure 3.5(b).[206] First, the potential quickly increases from its open circuit potential of approximately 0.25 V to approximately 0.4 V. Afterwards, the potential increases more slowly to a plateau of about 0.6 V within 12 min. This initial increase in the potential is associated with an oxidation of the pSi pore walls by the applied potential and an

ensuing nucleation of polypyrrole at the pore tips.[227] The subsequent potential plateau of 0.6 V, which lasts from approximately 12 min to 35 min, signals the continued growth of the polymer inside the pore space. The pores are filled from bottom to top.[227] The following transition to an increased potential of approximately 0.8 V at 40 min marks the gradual filling of the pores. The transition is not at once since the polymerisation proceeds with slightly different speeds in each pore.[206] The following potential plateau is caused by an ongoing growth of polymer on the top surface of the porous silicon. Here, polypyrrole is polymerised without the distinct geometrical confinement of the pSi pores. The pores are responsible for a certain degree of ordering of the polymer. Outside the pores, polypyrrole is not as restricted and polymerises in a network-like manner. Thus, at the pore filling stage the polypyrrole's electrical resistivity and thus the occurring potential is lower compared to the stage of surface polypyrrole growth.[227] For this reason, the applied current is switched off when the transition stage becomes apparent since a coverage by bulk polymer is not desired. Such a bulk coverage could lead to a distortion of the actuation characteristics of the polypyrrole-filled porous silicon (PPy-pSi). The stages of the pore filling process are also indicated in Figure 3.5(b). After a successful electrochemical polymerisation, the fabricated hybrid material is rinsed once with ethanol and then three times with deionised water to remove possible remaining pyrrole molecules and other contaminants. Afterwards, it is dried for three hours under ambient atmosphere.
To determine the degree of filling by polypyrrole, the increase in mass $\Delta m = m_{\mathrm{PPy}} - m_{\mathrm{pSi}}$ is determined gravimetrically between the mass of empty porous silicon m_{pSi} and the filled hybrid m_{PPy}.
Similar to unfilled pSi, SEM and TEM micrographs are recorded. With the help of EDX measurements it is possible to visualise the polypyrrole distribution, which is identified by the signal that the single nitrogen atom per monomer unit produces. Various conceivable contaminations might be present, which could also produce a nitrogen EDX signal. Furthermore, the overall EDX signal of nitrogen is low. Hence, this techniques yields a qualitative impression of the polypyrrole filling and a more quantitative assessment of the polypyrrole filling via these microscopy techniques is here not feasible.
Lastly, up to this point the electrochemical polymerisation in porous silicon is described in an epi-layer as the starting material. If the polymerisation is performed in a membrane, the bulk silicon layer at the bottom is not present. Furthermore, it is difficult to establish an ohmic contact on the pore walls themselves.[35, 228] Thus, a conductive layer of gold is deposited on the bottom of the membrane, where polypyrrole can nucleate and the electrochemical polymerisation of polypyrrole can commence. The gold layer with a thickness of 20 ± 0.5 nm is deposited by sputtering (SCD 050, BAL-TEC) on the back side of the membrane. The polymerisation setup changes slightly. The cell with its O-ring is pressed onto a PTFE base plate so that the polymerisation cell is closed tight. The membrane is then placed inside the cell. A gold wire contacts the gold layer at the bottom of the membrane, which acts as WE. Apart from these changes, the electrochemical polymerisation proceeds in the same manner as described above.

3.5. In Situ Electrochemical Actuation Setups

In this section different in situ experimental methods are introduced that will be used to characterise the electrochemical actuation of porous silicon and polypyrrole-filled porous silicon.
In this work, one of two electrolyte solutions will be used in the different in situ setups. The first electrolyte is perchloric acid with a concentration of $1\,\mathrm{mol\,L^{-1}}$, prepared from ultra-pure water and perchloric acid (70 vol %, Merck Suprapur), which is often used in electrosorption-induced actuation measurements.[80] The other electrolyte solution is an aqueous sodium chloride solution with a concentration of $154\,\mathrm{mmol\,L^{-1}}$ (isotonic saline solution), as it is omnipresent in biological and medical environments. The solution is prepared from ultra-pure water and NaCl (purity 99.99 %, Merck Suprapur).

3.5.1. Dilatometry

To directly measure the expansion of the porous silicon, dilatometry measurements in an in situ electrochemical setup are performed. The sample is placed into a vertical dilatometer (Linseis L75) to measure in situ the change in strain $\varepsilon = (l - l_0)/(l_0) = (\Delta l)/(l_0)$, see equation 2.65. l denotes the measured sample length and l_0 the length of the as-prepared sample, which will be stated for each respective sample below in the results chapters 4 and 5. The sample has to be placed into the dilatometer in an upright standing position so that the dilatometer quartz probe may be placed on top of the porous silicon sample. Thus, the pSi pores are horizontally oriented so that the [100] direction is parallel to the ground. A sketch of the sample orientation is shown in Figure 3.6(a). Initially, the pushrod is carefully lowered onto the porous silicon sample. The dilatometer uses a static force of 0.4 N to fix the sample in place. The dilatometer has a resolution of 0.1 nm, declared by the manufacturer. In practice, it is able to effectively detect changes in membrane length l with a resolution of approximately 10 nm, probably due to vibrations.[112] The time resolution of the dilatometer is set to 0.1 s.
The sample, with the probe on top, is located in a glass beaker. Then the sample is fully immersed in the chosen electrolyte solution. Together with the sample a carbon cloth CE and a reversible hydrogen RE are placed in the glass beaker. The three electrode setup is completed when the sample is electrically contacted as the working electrode. It is contacted at the bottom end by a contact fabricated out of aluminium. A gold wire is attached to the contacted area, which is connected to the potentiostat via an alligator clip. As the measurements are performed among other in an acidic solution, the aluminium contact needs to be protected from corrosion. The bottom end of the sample, including the contact, is encased in epoxy for a length of approximately 1 cm. Thus, it can also be ensured that the sample is in the desired upright position, as described above and also shown in Figure 3.6(b). In Figure A.1 in the appendix a picture of a PPy-pSi membrane installed in the in situ dilatometry setup is shown.
The in situ dilatometry setup will be used to characterise the electrosorption-induced actuation in porous silicon and the electrochemical actuation in polypyrrole-filled porous silicon. The actuation mechanism of the latter is illustrated in Figure 3.6(c)[1]. When a lower voltage, in the case of the illustration 0.4 V, is applied, the electrolyte molecules

[1] The electrosorption-induced actuation mechanism of bare porous silicon is depicted in the appendix in Figure A.2

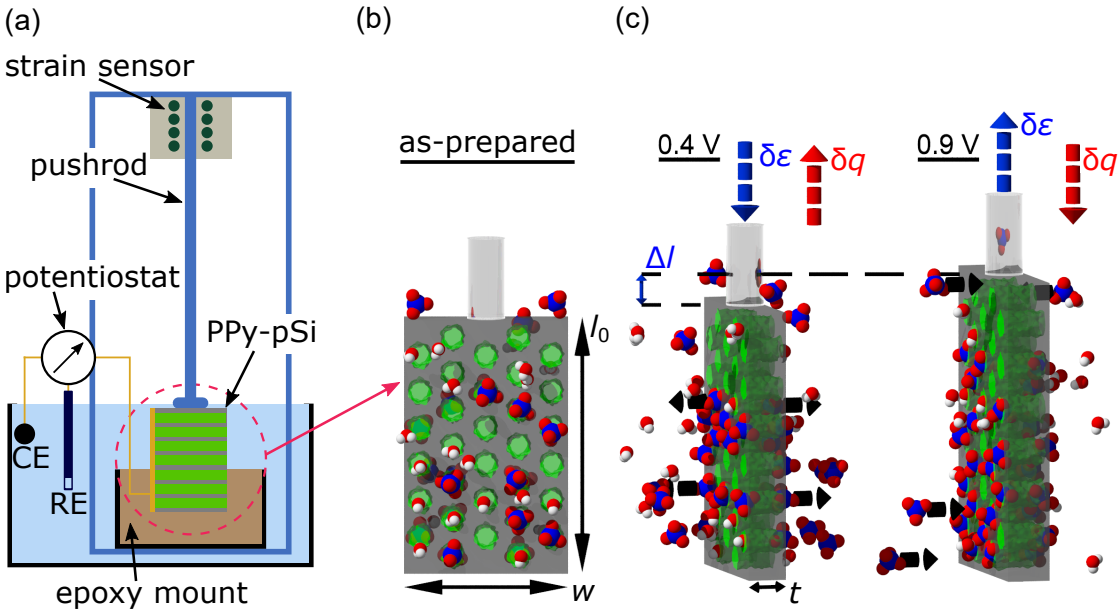

Figure 3.6.: **Dilatometry setup for in situ actuation measurements.** (a) Schematic of the in situ dilatometry setup that records a change in sample length l during an actuation measurement. A glass pushrod is lowered onto the investigated polypyrrole (green)-porous silicon (grey) (PPy-pSi) membrane and clamps it at the top. The whole membrane is inside a glass beaker that is filled by the respective electrolyte solution (light blue). The change of sample length l is measured at the top of the pushrod by a position sensor. The PPy-pSi material is encased at the bottom by epoxy so that it is standing in an upright position. Furthermore, the electrical contact to the PPy-pSi is isolated from the electrolyte solution by the epoxy. The sample is connected to the potentiostat, which also contacts a carbon cloth CE and a reversible hydrogen RE. (b) Illustration of an as-fabricated PPy-pSi membrane installed in the dilatometer with the glass pushrod on top. Its dimensions are length l_0 and width w. (c) Illustration of the electrochemical actuation principle of a PPy-pSi membrane immersed in an aqueous electrolyte solution. The electrolyte in this case is perchloric acid ($HClO_4$) indicated by blue and red molecules and red and white water molecules. The thickness of the membrane is indicated by t. The left section shows the contracted condition of the membrane. A lower voltage (0.4 V) is applied and as a result, the electrolyte anions (ClO_4^-) are ejected from the polypyrrole leading to the contraction of the whole membrane. Vice versa, the right section shows the case of a higher applied voltage (0.9 V). The polypyrrole pore filling incorporates the anions and a subsequent expansion ensues. Δl indicates the change in length.

are expelled from the polypyrrole, which resides in the porous silicon pores. As a result, the entire PPy-pSi hybrid membrane contracts and ε decreases. Vice versa, through a higher voltage (0.9 V) anions are incorporated into the polymer and as a consequence the membrane expands. The pushrod is lifted upwards, which is detected by the position sensor of the dilatometer and strain ε increases.

3.5.2. Laser Cantilever Bending

Another precise method to measure an electrochemical actuation is an in situ laser cantilever bending measurement. Summarising the actuation mechanism in porous silicon, cf. section 2.5, electrolyte ions are accumulated on the silicon surface when the applied potential is changed. This holds true on a bulk silicon surface as well as on porous silicon's inner surface area. The accumulated charge induces a change in surface stress on the respective silicon surface. If the back side of a rectangular silicon wafer is electrically insulated, charge carriers are solely accumulated on and dispersed off the silicon wafer's front side. Thus, a change in surface stress Δf leads to a bending of the wafer. Equally, an induced surface stress on the inner porous silicon surface area, leads to an expansion or contraction of the whole porous silicon layer. If porous silicon is attached to an underlying bulk silicon, i.e. an epi-layer, it bends as well. An illustration of the measurement method and setup is depicted in Figure 3.7.
The purpose of the setup is to measure the bending caused by the processes on the front side of the wafer. Therefore, the back side needs to be electrically insulated. At the beginning of the preparation, the whole wafer is thermally oxidised, as described in section 2.3. The respective wafer is placed in an oven and heated to 850 °C with a heating ramp of 200 °C h^{-1}. At the target temperature, the wafer is oxidised for 16 hours at ambient atmosphere and subsequently cooled down to room temperature with the same ramp of 200 °C h^{-1}. The created oxide layer is non-conductive. Ellipsometry is used to determine the thickness of the layer to be 96.3 nm. Afterwards, a 10 vol % HF solution removes the oxide layer on the front side. The HF exposure is performed for five minutes. The remaining fabrication process will subsequently proceed on the surface where the oxide is removed.
The curvature of the bending is detected and measured with a laser setup. The setup is installed on a vibration insulated table to minimise the impact of vibrations and it is surrounded by housing to reduce vibrations by air flow. The setup is located in a room equipped with an air conditioner, which is set to 21 °C to reduce any thermal drift. The whole setup (Multi-Optical Stress Sensor, k-Space associates [229, 230]) is described in great detail in reference [80]. A laser beam is split up into multiple beams, which are arranged in a rectangular pattern. The laser array spots are reflected off the insulated back side of the cantilever-like sample into a CCD detector. The spot spacing Δd changes with curvature and thus evolving surface stress. The curvature change parallel to the long axis of the cantilever sample $\Delta\kappa$ is the relevant parameter and is determined by [80]

$$\Delta\kappa = \frac{\Delta d}{d_0}\frac{\cos(\alpha)}{2Ln}, \tag{3.7}$$

where d_0 denotes the unimpeded array spot spacing, averaged over one minute, $\alpha = 4\,°$ the incident angle of the beam array, $L = 110$ cm the distance from the laser to the CCD camera and $n = 1.33$ the refractive index of water as an approximation for the diluted

aqueous electrolyte solutions used in this work. Figure 3.7 shows an illustration of the setup, with the respective parameters. As described above, a bulk silicon sample bends due to induced surface stress Δf. Stoney's equation calculates Δf by [80, 231, 232]

$$\Delta f = \frac{1}{6} M h^2 \Delta\kappa, \tag{3.8}$$

where $M = 180\,\mathrm{GPa}$ [122] and h are biaxial modulus and thickness of the bulk silicon sample, respectively. The latter will be stated for each individual sample.
By contrast, for samples with a porous silicon layer on top of bulk silicon, a surface stress on the porous silicon surface leads to the evolution of a film stress σ in the porous silicon layer. Assuming an isotropy of σ in the layer plane, Stoney's equation relates it to $\Delta\kappa$ by [213, 233]

$$\Delta\sigma = \frac{1}{6} M \frac{h^2}{h_\mathrm{l}} \Delta\kappa. \tag{3.9}$$

Here, h and h_l denote bulk silicon substrate thickness and porous silicon layer thickness, respectively. It is noteworthy that this method explicitly does not require knowledge of the mechanical properties of the layer. Merely the biaxial modulus of the substrate has to be considered instead. Furthermore, the layer thickness h_l must not exceed substrate thickness h by a factor of $2 \cdot 10^{-3}$.[234] Therefore, it can be assumed that a contribution of the porous silicon layer to the overall bending stiffness is negligible. Here, the ratio of h_l/h is well within that range. The specific cantilever bending setup used in this work resolves a curvature of the cantilever up to a bending radius of 250 km, which is sufficient for the measurements performed here.[213] The time resolution of the setup is set to 1 s.

3.5.3. X-Ray Diffraction

Lastly, as a third method, an in situ X-ray diffraction study is performed to characterise an electrochemical actuation on the scale of the crystal lattice. The measurements with this method are performed on a polypyrrole-filled porous silicon epi-layer. Such an XRD study on a porous silicon epi-layer constitutes a widely used method.[8, 141, 178, 235–238] It is well investigated with regard to a variety of different in situ measurements, reaching from the determination of strains induced by anodic oxidation [141, 235], wetting [235] and gas adsorption [178, 237]. It is a simple, yet elegant method to investigate the electrochemical actuation on the scale of the lattice.
The electrochemical etching of the pores into the silicon, introduces an interface between the pSi pore wall and the ambient atmosphere. A surface stress evolves at these interfaces, which acts on the lattice constant inside the pore wall.[178] Therefore, the lattice constant in the porous silicon is slightly different compared to the underlying bulk silicon. This results in two different Bragg peaks in an XRD measurement. This difference is used to characterise various processes that act on the pSi lattice. For example, an adsorption of species from the gas phase onto the pSi pore walls can further change the lattice constant.[178] Either, it induces changes in the interfacial stress (Bangham's law of adsorption-induced deformation [239, 240]) or capillary forces emerge due to condensed liquid inside the pore (Laplace pressure effect [125, 241]).[16, 64–66, 242] Thus, a measurement of the lattice difference yields information about the adsorption process. In this work, the expansion and contraction of the incorporated polypyrrole, transfers a strain

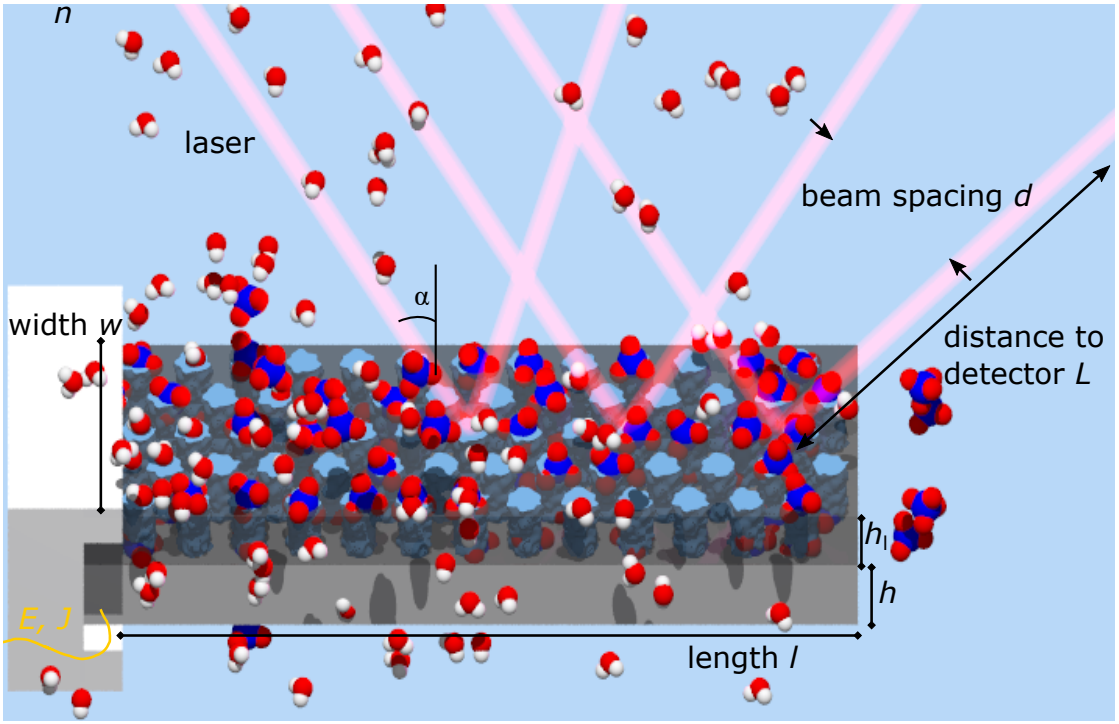

Figure 3.7.: **In situ laser cantilever bending setup.** A porous silicon epi-layer consisting of the porous layer (dark grey) attached to an underlying bulk silicon layer on the bottom (light grey) is installed in the in situ cantilever bending setup. An aqueous electrolyte solution fills the pores, which is indicated by the blue colour inside the pores and the ClO_4^- (blue, red) and H_2O (red, white) molecules. The size of the epi-layer is determined by its length l, its width w as well as the thicknesses of the porous and adjacent bulk layer h_l and h, respectively. The epi-layer is fixed on the left side by a PTFE clamp. Here, the epi-layer is also electrically contacted by aluminium with an attached gold wire and acts as the WE. An electrosorption-induced actuation leads to a bending of the entire epi-layer, as the porous silicon layer is clamped by the adjacent bulk silicon. At the opposite side of the clamp-contact an array of laser beams, with incidence angle α, is reflected off the epi-layer into a CCD-detector positioned with distance L. By the spacing of the laser beams d the curvature κ of the epi-layer is determined. For illustration purposes the laser is reflected off the porous side of the epi-layer. In the proper experiment, the laser array is aimed at the back side. The setup is housed in an electrochemical PTFE-cell, which is covered by a transparent glass plate. Furthermore, the refractive index n at the water-air interface also has to be considered.

onto the lattice of the pSi pore wall. Measuring the pSi lattice constant, enables the characterisation of the mechanical response.
The PPy-pSi epi-layer is prepared in the same manner, as described above in sections 3.2 and 3.4. The porous silicon layer has a thickness of approximately 25 µm, while the bulk silicon has a thickness of approximately 500 µm. The actual thickness will be stated in section 5.5. The polypyrrole-filled porous silicon samples are prepared by cleaving. The samples have a width of approximately 3 mm and a length of 2 cm.
The measurements are conducted in a cell which enables electrochemical control simultaneous to XRD measurements. The cell is fabricated out of PTFE to safely handle the electrolyte solution, as it is perchloric acid. The sample is installed on a PTFE sample holder, which is then mounted into the measurement cell. The sample is sited in a vertical hanging, upside down position. It is longer than the holder so that the lower part of the sample protrudes downward beyond the sample holder into the cell. Neither front nor back side of the sample is here obstructed by the holder. The upper part of the sample is electrically contacted on the back side by aluminium and an attached gold wire. The electrical contact needs to be insulated with a thermoplastic film (Bemis Parafilm) to protect it from corrosion. Together with the sample an Ag/AgCl-RE (Sensortechnik Meinsberg) and a carbon cloth CE are installed in the cell. Perchloric acid with a defined volume of 7.1 mL is then filled into the cell so that sample, CE and RE are immersed. A potentiostat completes the three electrode setup. A lid with an insulation is screwed on the cell to seal it. Figure 3.8(a) shows a detailed illustration of the cell and the installation of the electrodes and the sample.
The in situ X-ray diffraction measurements are conducted at the 3$^{\text{rd}}$ generation synchrotron PETRA III at Deutsche Elektronen-Synchrotron (DESY), beamline P08. In the centre of the beamline is a motorised six-circle closed Eulerian cradle (Kohzu NZD-3). It facilitates a comprehensive coverage of possible diffraction geometries. The energy of the photon beam is set to $E_{\text{beam}} = 18\,\text{keV}$. The spot size of the beam amounts to $200 \times 200\,\mu\text{m}^2$. The cell has a window with significantly reduced wall strength of 2 mm, where the X-ray beam enters and the scattered beam leaves the cell. Thus, the intensity loss through the passage of PTFE is minimised. Perchloric acid fills the cell, exactly up to the upper edge of the window, as shown in Figure 3.8(a). The scattered intensity is measured by a 2D detector (Pilatus 100K, pixel number 487×195 (horizontal $\times$ vertical), pixel size $p = 172 \times 172\,\mu\text{m}^2$). The distance $\mathcal{L}$ from the sample to the detector is measured and amounts to $\mathcal{L} = 955.6 \pm 1.4\,\text{mm}$.[243] The scattered intensity used here, is gained by summing the scattered beam's intensity over the central detector region.
The XRD measurements are conducted in the form of $\theta - 2\theta$ scans, where θ denotes the incidence angle. Crystal planes with the interplanar distance d and with diffraction order n are probed. According to Bragg's law,

$$n\lambda = 2d\sin(\theta), \tag{3.10}$$

where

$$\lambda = \frac{\text{c} \cdot \text{h}}{E_{\text{beam}}}, \tag{3.11}$$

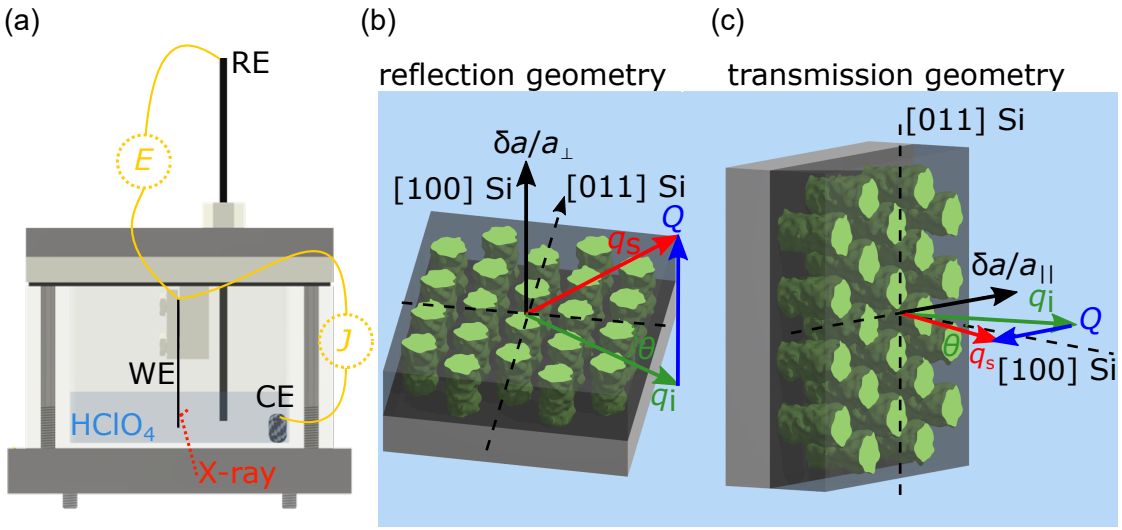

Figure 3.8.: **In situ X-ray diffraction study on the electrochemical actuation of PPy-pSi.** (a) In situ electrochemical measurement cell for X-ray diffraction measurements depicting the PPy-pSi sample in its holder in the middle. The lower part of the sample is immersed in the electrolyte solution (perchloric acid). The sample is connected as the WE. As a CE a carbon cloth is used and an Ag/AgCl RE measures the applied potential. The in situ cell is fabricated out of PTFE. The wall strength is significantly thinned down to 2 mm in the area of the electrolyte filling. Here, the probing X-ray beam penetrates the cell and is scattered off the sample. The thinner wall helps to retain the intensity of the scattered beam when it is leaving the cell. The middle and right sections show schematics of in situ X-ray diffraction experiments in (a) reflection and (b) transmission geometry. The diffraction geometries are depicted on porous silicon layer (dark grey) with its polypyrrole pore filling (green) attached to an underlying bulk silicon layer (light grey). Incident and scattered beam are indicated by q_i and q_s, respectively. The transfer from incident to scattered wave vector is marked by Q. In the schematics of the diffraction geometries, the crystallographic directions are marked accordingly. Moreover, the schematic shows in which direction lattice mismatches (a) $\delta a/a_\perp$ and (b) $\delta a/a_{||}$ are probed. Whereas the incident beam hits the PPy-pSi epi-layer under an angle θ on its porous front side in reflection geometry, in transmission geometry, it hits the back side first before being transmitted through the PPy-pSi epi-layer. The incident beam then leaves with an angle of θ with respect to the epi-layer.

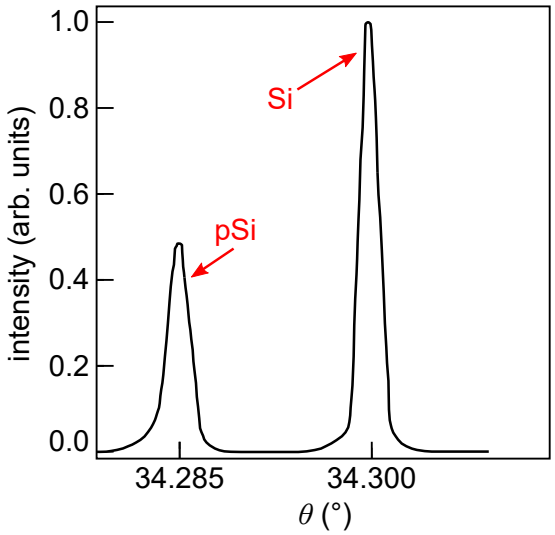

Figure 3.9.: **X-ray diffraction measurement on a porous silicon epi-layer.** Exemplary X-ray diffraction measurement in reflection geometry on the 400 Bragg peak of a porous silicon epi-layer. Clearly visible are two distinct peaks. The peak at a smaller angle is due to the porous silicon layer, whereas the Bragg peak at 34.3 ° is caused by the underlying bulk silicon. Adapted with permission from reference [8].

where c and h denote speed of light and Planck's constant, respectively. For a cubic system, d and the respective Miller indices hkl of the probed planes are related to the lattice constant a, by

$$d = \frac{a}{\sqrt{(h^2 + k^2 + l^2)}}. \tag{3.12}$$

The epi-layer consists of porous silicon and an adjacent bulk silicon layer, which both exhibit distinct Bragg peaks, as described in section 2.4. An exemplary $\theta - 2\theta$ XRD measurement from literature is depicted in Figure 3.9, in which these two peaks are clearly visible.[8] The peaks are at angles θ_{Si} and θ_{pSi}, respectively. The lattice constant of porous silicon a_{pSi} is directly related to the difference of θ_{Si} and θ_{pSi} by [178]

$$\frac{\delta a}{a_{\mathrm{Si}}} = \frac{a_{\mathrm{pSi}} - a_{\mathrm{Si}}}{a_{\mathrm{Si}}} = \frac{\delta\theta}{\tan(\theta_{\mathrm{Si}})} = -\frac{\theta_{\mathrm{pSi}} - \theta_{\mathrm{Si}}}{\tan(\theta_{\mathrm{Si}})}, \tag{3.13}$$

where $a_{\mathrm{Si}} = 0.543\,\mathrm{nm}$ is the lattice constant of bulk silicon [7]. It should be noted that values for θ are warranted in radians.
A larger value for a_{pSi} with respect to bulk silicon corresponds with a positive value for $\delta a/a_{\mathrm{Si}}$, which can be inferred in the XRD measurement by $\theta_{\mathrm{pSi}} < \theta_{\mathrm{Si}}$. The porous silicon lattice is expanded compared to the bulk silicon lattice. Vice versa, a negative $\delta a/a_{\mathrm{Si}}$ is signalised by $\theta_{\mathrm{pSi}} > \theta_{\mathrm{Si}}$ and means a smaller pSi lattice constant and hence, a contracted lattice. All in all, the determination of $\delta a/a_{\mathrm{Si}}$ is only explicitly dependent on $\theta_{\mathrm{Si}} - \theta_{\mathrm{pSi}}$. Thus, the absolute value for θ is not decisive. Only the relative difference $\delta\theta$ determines the strain of lattice constant. The method reduces error introduced by measurement parameters as, for instance, a perfect alignment, which would affect both Bragg peaks. It is thus beneficial and renders the conducted study simple. Moreover, the underlying bulk

silicon layer is much thicker than the porous silicon layer. Hence, it reduces a bending of the epi-layer through the expansion and contraction of the porous silicon layer. It stabilises and minimises a possible distortion of the respective $\theta - 2\theta$ scans. The lattice constant change $\delta a/a_{\mathrm{Si}}$ is hereafter referred to as lattice mismatch and denominated in an abbreviated form as $\delta a/a$. The X-ray diffraction study is only sensitive to changes of the porous silicon lattice and explicitly not to the polypyrrole filling of the pore space.
Two types of XRD measurements are conducted with two equal, rectangularly shaped polypyrrole-filled porous silicon samples $\mathrm{S_{refl}}$ and $\mathrm{S_{trans}}$. Each sample is probed under a different incidence angle. For each of the samples a different sample holder is used to achieve the desired measurement geometry. The two measurement geometries are presented in detail in Figure 3.8(b)-(c). The incident beam hits the front side of $\mathrm{S_{refl}}$, i.e. the porous silicon layer, and is varied around an angle in the range of $\theta \approx 29.4\,^{\circ}$. The detector is positioned accordingly with an equal angle of θ_{refl} with respect to the surface to detect the scattered beam. Hence, planes with an hkl-index of (400) are probed since the angle for this plane is $2\theta_{\mathrm{refl}} = 29.3934\,^{\circ}$ according to equation 3.10. These planes are parallel to the sample surface. Equation 3.13 then yields the lattice mismatch $\delta a/a_{\perp}$ in the out-of-plane, [100] direction orthogonal to the surface. This measurement setup is here referred to as reflection geometry.
To probe the lattice mismatch $\delta a/a_{||}$ in-plane, parallel to the surface in the transmission geometry, the incident beam hits the back side of $\mathrm{S_{trans}}$. Thereby, it passes trough bulk silicon first and porous silicon second. The measurement is also conducted as a $\theta - 2\theta$ scan, although it could be more accurately termed $(\theta - 90\,^{\circ}) - 2\theta$. The probed (044) lattice planes are located orthogonally to the surface. The measurement requires an angle of $\theta_{\mathrm{trans}} = 42.0517\,^{\circ}$ in accordance with equation 3.10.
The uncertainty of the XRD measurements will be discussed in the following. For the XRD measurement, the angular uncertainty $\Delta\theta$ of the recorded intensity at the detector is estimated by [244]

$$(\Delta\theta)^2 = \frac{\cos^4(2\theta)}{16\mathcal{L}^2}\left[\tan^2(2\theta)(t^2 + 2\mathcal{H}^2) + p^2 + \frac{t^2}{\cos^2(2\theta)} + \frac{\mathcal{L}^2\varphi^2}{\cos^4(2\theta)}\right], \tag{3.14}$$

where $\mathcal{L}$ is the detector distance and t denotes the sample thickness. For the in-plane, transmission geometry, the thickness of the porous silicon layer equals t. However, in case of the reflection, out-of-plane measurement, the beam size is the relevant parameter and is considered as t. The thickness of the detector's detection layer is denoted as $\mathcal{H} = 320\,\mu\mathrm{m}$. p is the pixel size and the vertical beam divergence at beamline P08 amounts to $\varphi = 12\,\mu\mathrm{rad}$. Furthermore, the number of measurement points N of the $\theta - 2\theta$ diffraction measurement, needs to be considered. For the fit of the Bragg peaks, which will be shown in section 5.5, the uncertainty of both peaks $\Delta\theta_{\mathrm{pSi}}$ and $\Delta\theta_{\mathrm{Si}}$ is reduced by $\sqrt{N}$. The uncertainty of the lattice mismatch is then obtained by considering the propagation of uncertainty for equation 3.13, as

$$\Delta(\delta a/a) = \sqrt{\left(\frac{\Delta\theta_{\mathrm{pSi}}}{\tan(\theta_{\mathrm{Si}})}\right)^2 + (\Delta\theta_{\mathrm{Si}})^2\left(\frac{1}{\tan(\theta_{\mathrm{Si}})} + (\theta_{\mathrm{pSi}} - \theta_{\mathrm{Si}})\frac{1}{\sin^2(\theta_{\mathrm{Si}})}\right)}. \tag{3.15}$$

The values for the respective uncertainty, which will be stated in the results section 5.5 for the lattice mismatches, originate from these considerations. An exception will be the

electrochemically controlled measurements. Here, different voltages will be repeatedly applied and the uncertainty is obtained by averaging over several of these potential cycles. If such an average is applied, it will be noted.

4. Electrosorption-Induced Actuation of Porous Silicon

This chapter will discuss the morphologic and electrochemical properties of porous silicon. Furthermore, in situ dilatometry and laser cantilever bending experiments on the electrosorption-induced actuation of porous silicon in aqueous electrolytes will be discussed. Firstly, the actuation properties of p-type porous silicon will be characterised in an in situ dilatometry study. An in situ cantilever bending study will be presented that gives further, more detailed insight into the electrosorption-induced actuation and compares it to the actuation at bulk silicon surfaces with respect to fundamental aspects of the surface stress induction and the role of the porous morphology in porous silicon. Furthermore, it will be explored if fundamental differences of the actuation mechanisms between p-type and n-type porous silicon are present.

4.1. Morphological and Electrochemical Characterisation of Porous Silicon

For the dilatometry measurements a double epi-layer is fabricated. Each layer is etched with a respective time of 47 min. Porous silicon, as mentioned, has a highly anisotropic porous structure, which consists of parallel pores, orthogonally oriented to the silicon surface. Thus, an induced surface stress on the porous surface might cause a macroscopic bending rather than a preferred lateral expansion of a porous silicon layer. Therefore, the double epi-layer sample with equal thicknesses on front and back is used to minimise such a bending. The sample is symmetric in the direction orthogonal to the surface. An expansion of the whole sample in its plane is achieved, while a possible induced bending of one of the porous layers is compensated by the opposing porous layer. Furthermore, establishing an electrical contact, which exhibits an ohmic characteristic, to fully porous silicon, i.e. a membrane, is difficult, as mentioned in section 3.4. Hence, the electrical contact is provided by the bulk silicon layer, which is located between the two epi-layers. Thus, no special contacting method is required and an electrical contact can be accomplished by a simple aluminium layer on the bulk silicon layer. A cross section TEM micrograph of the resulting p-type porous silicon is depicted in Figure 4.1(a). The TEM cross section shows that a resemblance of the pore network to a randomised honeycomb structure is present, as discussed in more detail in [112]. A SEM micrograph of the material is shown in Figure 4.1(b). The dendritic side-pores, discussed in section 2.4, are clearly visible. Another SEM micrograph of the entire sample profile gives the thicknesses of the bottom and the top porous silicon layer as 35 µm and 38.6 µm, respectively. The thickness of the remaining bulk silicon layer in between amounts to 26.6 µm.
Figure 4.1(c) depicts a nitrogen sorption isotherm of the double epi-layer porous silicon

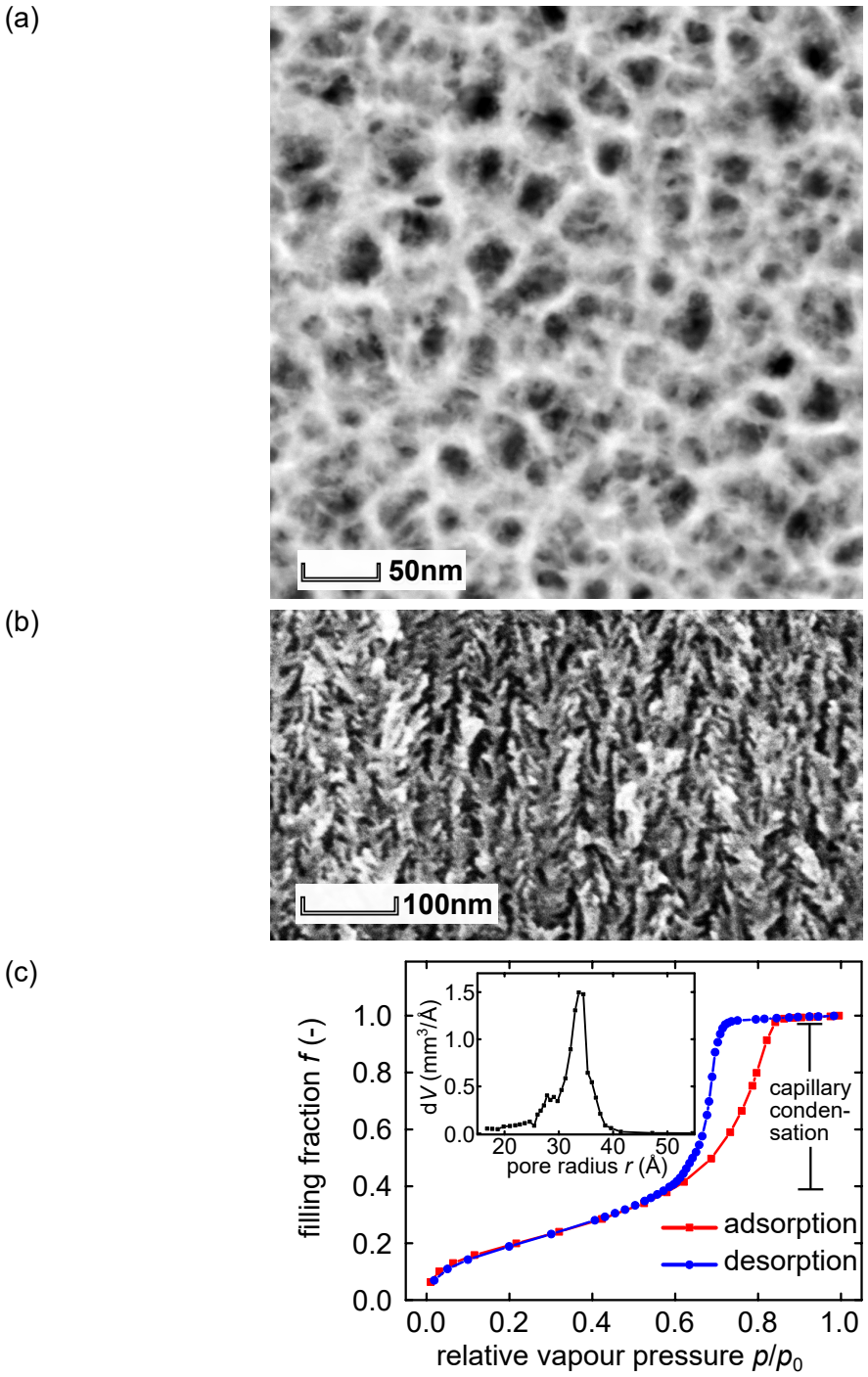

Figure 4.1.: **Synthesised porous silicon.** (a) TEM micrograph of p-type porous silicon. (b) SEM micrograph of the porous silicon profile. Visible are the pores, with the etch direction from the top to the bottom and the dendritic side-pores. (c) Nitrogen sorption isotherm of as-prepared porous silicon at $T = 77\,\mathrm{K}$. The volume filling fraction f is plotted against the relative vapour pressure p/p_0. Visible are the characteristic stages, single layer adsorption, capillary condensation and desorption. The inset depicts the BJH analysis of the distribution of pore radii.

material. The material has an outer porous silicon volume of $0.0165\,\mathrm{cm}^3$. The isotherm exhibits the typical characteristics of such a measurement on porous silicon. Increasing relative vapour pressure p/p_0 initially leads to the adsorption of multi-layers of nitrogen on the porous silicon inner surface area. Up to a value of $p/p_0 = 0.7$ the filling fraction increases approximately linearly. In this region, the BET model is used and allows to determine the actual inner surface area. The result equals $A_{\mathrm{por}} = 4.003\,\mathrm{m}^2$. Beyond $p/p_0 = 0.7$ capillary condensation sets in and menisci form. Eventually, the pores are entirely filled at a volume, which corresponds to a filling fraction of $f = 1$. The adsorption and desorption branch exhibit a characteristic hysteresis. The BJH model is applied to the desorption branch and yields a distribution of pore radii, shown in the inset of 4.1(c).[245] The peak of the distribution is at radius $r = 3.3\,\mathrm{nm}$ or pore diameter $D = 6.6\,\mathrm{nm}$. The distribution has a shoulder on the left of the main peak towards a smaller radius, which might be caused by the small dendritic side-pores, observed in the SEM. The BJH model also yields a porous volume of $V_{\mathrm{por}} = 0.009\,\mathrm{cm}^3$. Thus, the porosity of the double epi-layer amounts to $\Phi = 54\,\%$.

A pore diameter evaluation of the TEM micrograph in Figure 4.1(a) results in a span of approximately $6 - 25\,\mathrm{nm}$, which is in contrast with the diameter obtained from the nitrogen sorption isotherm. This seemingly contradicting result can be explained by the following consideration. The pore diameter of a porous silicon pore conceivably has a varying diameter along its length. The SEM micrograph in Figure 4.1(b) shows that the side-pores branching off lead to narrowing of the main pore at their bifurcation. The pore radius evaluation of the sorption isotherm is performed at desorption, as the menisci form and are driven out of the pore. They are pinned by the thinnest part of the pore, until the pressure p/p_0 is reached that leads to their vanishing. As a result, the evaluation assumes the smallest pore diameter for the whole pore. Thus, the sorption isotherm evaluation can here only give a lower boundary for the pore diameter.

First, the as-prepared porous silicon will be electrochemically characterised. Initially a CV measurement is conducted. It will be examined if a porous silicon electrode exhibits ideal polarisability. The respective measurement is shown in Figure 4.2(a). It comprises five consecutive cycles conducted with a scan rate of $10\,\mathrm{mV\,s^{-1}}$ in the potential range of 0 to 1.2 V. It is visible that the current increases with an increasing potential. When the upper vertex at 1.2 V is reached and the scan direction is reversed, the current decreases from its peak value of 0.316 mA. It decreases with a larger slope. The current is not following the course of the up-sweep. Thus, an area of current is encompassed by up- and down-sweep. It also becomes visible in the inset, which only depicts the lower potential range. Hence, the measurement indicates a capacitive charging, although a current that is of oxidative nature eminently superimposes the capacitive current. This inherent oxidative current increases in an exponential manner with potential E. However, the peak current at the upper vertex potential successively decreases from cycle to cycle. This also illustrates the irreversible character of this oxidative process.

The characteristics of this CV are attributed to an oxidation of the porous silicon walls under applied potential in an aqueous electrolyte solution, as discussed in section 2.3.[120, 246, 247] The porous silicon surface directly after fabrication is hydrogen terminated. However, the sample is not handled in an inert ambient atmosphere and thus, a native oxide layer readily forms. For the purpose of foregrounding the capacitive current and suppress oxidative currents, the oxidation of the porous silicon surface has to be drawn to a close. This is achieved by anodic oxidation. Therefore, a constant potential of 1.2 V

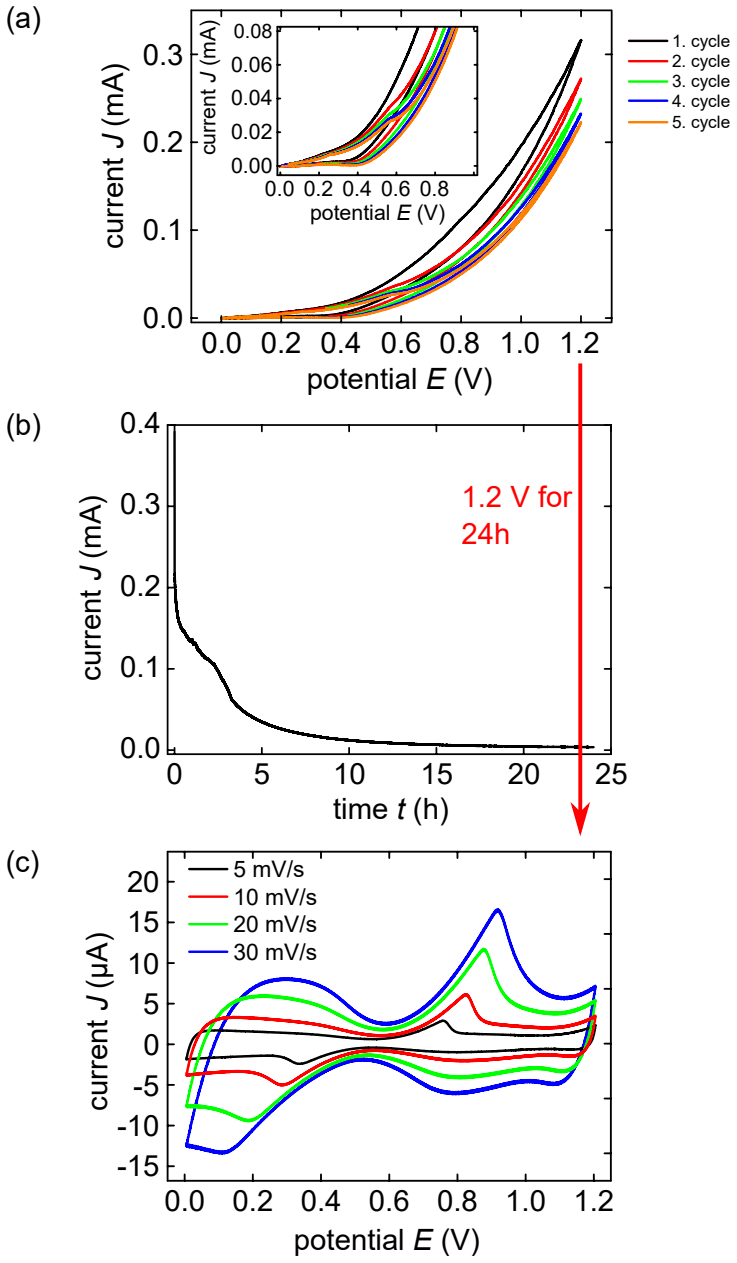

Figure 4.2.: **Initial electrochemical characterisation of as-prepared porous silicon.** (a) CV measurement of as-prepared double epi-layer porous silicon. Current J is plotted against the applied potential E. The potential scan rate is set to $10\,\mathrm{mV\,s^{-1}}$. The measurements are conducted in $1\,\mathrm{mol\,L^{-1}}$ $HClO_4$ electrolyte. (b) Constant potential of 1.2 V applied to double epi-layer porous silicon. (c) CV measurements, conducted after an applied constant potential of 1.2 V, with different scan rates of 5 to $30\,\mathrm{mV\,s^{-1}}$.

is applied for 24 hours. The respective measurement is depicted in Figure 4.2(b), which shows the resulting current J over time. It is clearly visible that J drastically decreases until it approaches zero asymptotically. Finally, a current of $J \approxeq 3.6\,\mu A$ is reached. As the potential is applied, porous silicon surface area is oxidised. Thus, the surface that is not yet oxidised successively decreases and so does the current. A shoulder is visible in the current evolution around 2.5 h. Since hydrogen terminated porous silicon after its preparation is hydrophobic, $HClO_4$ electrolyte solution might not be fully imbibed from the beginning. The increasing oxidation of the surface therefore might enable a successive imbibition. The electrolyte comes in contact with unoxidised porous silicon surface, which in turn leads to a slower decrease of the current.
A set of CV measurements, also called CVs, which is recorded following the applied constant potential is depicted in figure 4.2(c). Shown are CVs with scan rates from 5 to $30\,mV\,s^{-1}$. The large currents, which occur in the unoxidised state, are vastly reduced at the upper vertex potential. Here, for example, the current peak value for the measurement with a scan rate of $10\,mV\,s^{-1}$, declines from 0.316 mA to 0.051 mA. In general, the features of the CV are more pronounced.
In the inset of figure 4.2(a) a peak in the slope of the up-sweep is slightly visible at approximately 0.5 V. In the oxidised state, all CVs feature a clear peak in the up-sweep, which shifts from 0.758 V to higher potential values for larger scan rates, i.e. 0.920 V for $30\,mV\,s^{-1}$. Additionally, a peak becomes visible in the down-sweep at 0.336 V for $5\,mV\,s^{-1}$. By contrast, this peak shifts to smaller potential values for increasing scan rates so that the splitting of the two peaks increases. For $30\,mV\,s^{-1}$ the peak is located at 0.117 V, but it is barely visible any more. In this potential range, the oxygen reduction reaction successively comes into effect.[213] Thereby, a progressive reduction of oxygen in the potential range from 0.4 V to the lower vertex potential 0 V generates negative currents. A negative current slope is particularly visible for the largest scan rate, for which the oxygen reduction current superimposes currents generated by ordinary electrochemical reactions of porous silicon. In total, the two peaks resemble a redox couple of an oxidation and reduction process. The synthesis path of silicon dioxide by anodic oxidation involves an intermediate step in which silicon hydroxide is created, as discussed in equation 2.37. This reaction may be responsible for the reversible peak resembling a redox peak. The OH-groups may be ad and desorbed in a chemisorption process, which has been reported and measured before in a similar manner.[248] It should be noted that the focus in this work is on the investigation of electrochemically stable capacitive features of porous silicon as well as bulk silicon electrodes. Therefore, the aim is to not further characterise and analyse possible redox reactions. Furthermore, a possible redox reaction is not associated with an electrochemical actuation effect of any kind. Here, an actuation reaction is caused by electrosorption-induced, capacitive ion assembly. The peak couple is only mentioned for the sake of completeness.
The CV measurements in Figure 4.2(c) show that a potential region with electrochemically stable capacitive features exists. More explicitly, currents due to a capacitive charging of the internal porous silicon surface area are present, while Faradaic currents are negligible. Such a potential range is found from approximately 0.8 V to 1.1 V in the CV with a scan rate of $5\,mV\,s^{-1}$. This range will be explored in more detail.
Figure 4.3(a) shows cyclic voltammetry measurements in the reduced potential range of 0.8 V to 1.1 V on oxidised porous silicon. Depicted are CVs with various scan rates from $10\,mV\,s^{-1}$ to $100\,mV\,s^{-1}$. Starting from the lower vertex, the current J almost instantly

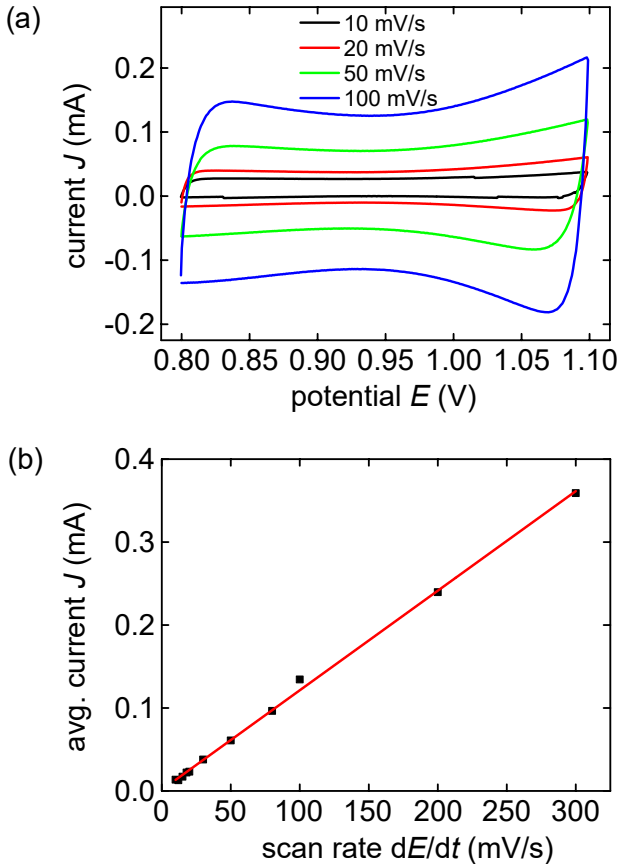

Figure 4.3.: **CV Measurements on oxidised porous silicon in a capacitive regime.** (a) CV measurements of double epi-layer oxidised porous silicon. Measurements are conducted in $1\,\mathrm{mol\,L^{-1}}$ $HClO_4$ electrolyte with increasing scan rates from $10\,\mathrm{mV\,s^{-1}}$ to $100\,\mathrm{mV\,s^{-1}}$. (b) Values for the current of J, averaged in the potential range of $0.9 - 0.95\,\mathrm{V}$, plotted against increasing potential scan rates $\mathrm{d}E/\mathrm{d}t$ from $10\,\mathrm{mV\,s^{-1}}$ to $300\,\mathrm{mV\,s^{-1}}$. The red line indicates a linear regression. The slope yields a capacitance of $c_{2\mathrm{xpSi}} = 1.20 \pm 0.02\,\mathrm{mF}$.

increases to a near constant value and has the same absolute current value on the downsweep. Thus, it exhibits the features of a capacitive charging. This behaviour holds true for the courses of all depicted scan rates $\mathrm{d}E/\mathrm{d}t$, albeit from $50\,\mathrm{mV\,s^{-1}}$ on, a slight increase towards the upper vertex is visible. In particular, an increasingly extended time for the approach of constant current is not visible – neither is a linearly increasing current instead of a plateau. Thus, the measurement does not exhibit signs of a diffusion limitation up to scan rates of $100\,\mathrm{mV\,s^{-1}}$.[214, 249] Absolute current values for each CV and for both sweep directions are averaged in the range of $0.9 - 0.95\,\mathrm{V}$. These values are plotted versus their respective scan rate. The plot is depicted in Figure 4.3(b). The averaged current points are approximated according to equation 3.2 and the slope of the fit yields the capacitance c. The fit has no large deviations up to scan rates of $300\,\mathrm{mV\,s^{-1}}$. The capacitance obtained is $c_{2\mathrm{xpSi}} = 1.20 \pm 0.02\,\mathrm{mF}$. The capacitance per outer volume of porous silicon is determined to compare different porous silicon samples. The length and width of the

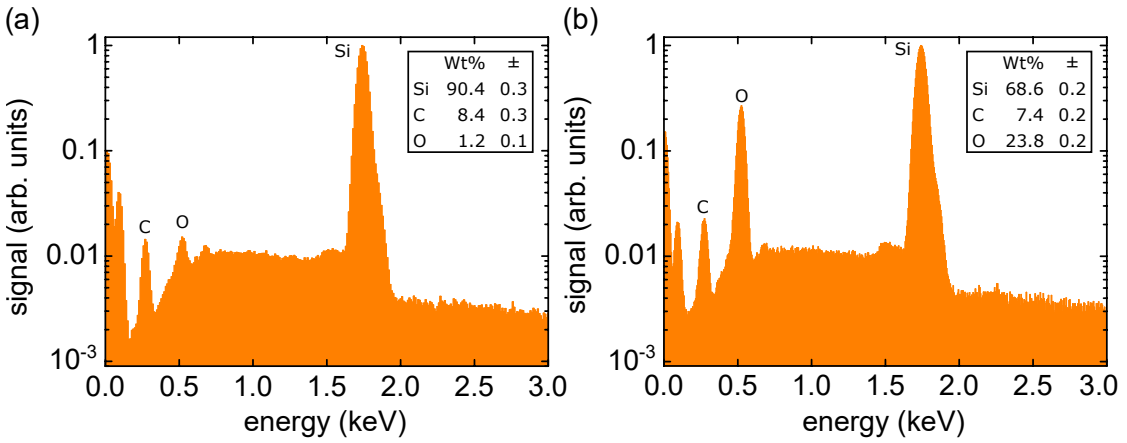

Figure 4.4.: **Energy dispersive X-ray measurement of oxidised porous silicon.** Energy dispersive X-ray measurement recorded in an SEM for (a) as-prepared and (b) oxidised porous silicon. The peaks of silicon (Si), carbon (C) and oxygen (O) are marked. The legend states the weight percentage (Wt%) of the respective elements.

sample here equal $l_0 = 0.48 \pm 0.01\,\mathrm{cm}$ and $w = 0.285 \pm 0.001\,\mathrm{cm}$, also stated below in the next part on the dilatometry results. Together with the respective thicknesses of the porous silicon epi-layer on back and front a porous silicon volume of $1.007\,\mathrm{mm}^3$ is obtained. Thus, the capacitance per outer volume of porous silicon equals $1192\,\mathrm{mF\,cm}^{-3}$.
The anodic oxidation procedure and its morphological impact on the porous silicon structure is further investigated. An essentially identical porous silicon sample is fabricated. However, it does not consist of a double epi-layer but only has a single epi-layer on the front side. The silicon is etched for 26 min and 40 s, which results in a porous silicon layer thickness of 25.4 µm. An essentially equal anodic oxidation procedure is conducted, whereby a constant potential of 1.2 V is applied for 42 h in $HClO_4$. The current decreases in a similar fashion to the anodic oxidation depicted in Figure 4.2(b) to a value of 22 µA. The charge consumed in this anodic oxidation amounts to 65.175 C. The anodic oxidation proceeds according to equation 2.40. Thus, assuming a hole conversion of $n = 4$, the anodic oxidation results in a silicon dioxide amount of $0.169 \cdot 10^{-3}$ mol. This equals 10.15 mg. The weight of the sample is determined before and after the anodic oxidation procedure. It yields a 2.6 % increase in weight of $\Delta m_{SiO_2} = 6.9\,\mathrm{mg}$, which is in good agreement with 10.15 mg if side reactions, which consume additional charge, are considered.
Figure 4.4 depicts EDX measurements recorded in an SEM on (a) as-prepared porous silicon and (b) anodically oxidised porous silicon. Both samples consist of a 25.4 µm thick epi-layer profile. The respective EDX spectra show only signals of silicon, oxygen and carbon. Carbon, with a weight percentage around eight, is likely present due to organic contaminations from the environment. By comparison, it is easily visible that the oxygen signal increases. Thus, the success of the anodic oxidation is evident. It has to be noted that the here recorded EDX only serve a qualitative purpose. For a quantitative assessment more care during the preparation would be necessary with respect to organic contaminations. A preparation in a clean room would prevent those.
A nitrogen sorption isotherm measurement is performed to evaluate if the anodic oxidation

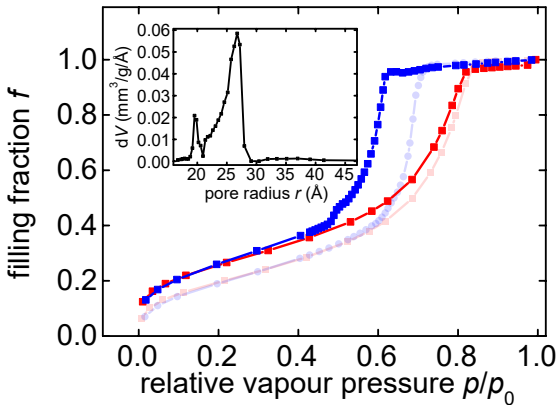

Figure 4.5.: **Nitrogen sorption isotherm of oxidised porous silicon.** Nitrogen sorption isotherm measurement recorded of oxidised porous silicon. The inset shows the pore radius distribution obtained by analysis with the BJH model. As reference, the adsorption and desorption branches of a measurement on unoxidised porous silicon, cf. Figure 4.1(c), are displayed faded in red and blue, respectively.

changes the morphology of porous silicon. The measurement is depicted in Figure 4.5. The sorption isotherm exhibits the characteristics, already discussed for as-prepared porous silicon, cf. Figure 4.1(c). The typical hysteresis between adsorption and desorption branch is clearly visible. However, it is noticeably more pronounced than for the as-prepared porous silicon. The desorption of nitrogen starts at a lower relative vapour pressure. The analysis of the pore radius distribution by the BJH model yields a large peak at 2.7 nm. This means a reduction of pore radius by $\Delta r = 0.6\,\mathrm{nm}$ in comparison to unoxidised porous silicon. Furthermore, a smaller peak at 2 nm is visible, as depicted in the inset of Figure 4.5. The smaller peak is more pronounced compared to the unoxidised material, which only shows a slight shoulder. The BJH determined porosity of the oxidised porous silicon is $\Phi = 35.7\,\%$ and has thus noticeably decreased. An analysis with the BET model yields a value for the inner surface area, referred to, here, as the physical inner surface area. It amounts to $2.36\,\mathrm{m}^2$. A nitrogen sorption isotherm for an equal sample without the anodic oxidation has a larger surface area of $4.76\,\mathrm{m}^2$. For the actual double epi-layer sample a value $A_{\mathrm{2xpSi}} = 2106\,\mathrm{cm}^2$ of oxidised surface is obtained. All in all, the analysis by nitrogen sorption shows a significant decrease in pore diameter as well as the inner surface area through the anodic oxidation procedure. A homogeneous growth of silicon dioxide in the pore space serves as the explanation.
In a next step the physical inner surface area, determined by the nitrogen sorption measurements, is compared to the inner surface area that is electrochemically addressed in CV measurements. The aim is to determine the specific capacitance per surface area c^*_{Si} of silicon. Then, by knowledge of the capacitance of the porous silicon electrode in question, a value for the electrochemically active surface area will be extracted. Here, electrochemically active designates the inner surface area of the porous silicon that accumulates charge when a potential is applied, i.e. electrosorption occurs. A bulk silicon sample with a surface of $A_{\mathrm{Si}} = 24.346\,\mathrm{cm}^2$ is prepared. An equal anodic oxidation in $HClO_4$ is performed on the bulk silicon. A potential of 1.2 V is applied for 15 h until the current decreases to

a value of approximately 100 nA. The thickness of the resulting oxide layer is determined by an ellipsometry measurement and is 1.4 nm. After the successful anodic oxidation of the bulk silicon, an atomic force microscope is used to determine the roughness of the oxidised surface. An increase of the surface area by a factor of 1.00075 is obtained.
The course of current J is depicted in Figure 4.6(a). It can be seen that it drastically decreases from over 2 µA within the first three hours and asymptotically approaches $J = 0\,\mathrm{A}$. For the purpose of checking whether the observed anodic oxidation progresses in accordance with the theory described in section 2.3, the course of current J is approximated by function 2.49. The functional dependence is $t^{-1/2}$, i.e. time to the power of $-1/2$. It is visible that this dependence fits the data well. Thus, the drift-limited migration of hydroxide ions into the bulk silicon seems to be present and the reaction with the silicon proceeds faster than the ion migration. In contrast, a successful fit of function 2.49 to current J recorded during the anodic oxidation of not bulk but double epi-layer porous silicon, shown in Figure 4.2(a), cannot be performed. Thus, the anodic oxidation of this porous silicon sample does not have the same time dependence, which is possibly caused by a limited reaction of hydroxide with silicon atoms. The surface of the pore walls is not smooth. Due to the side-pores, the surface can rather be described as rough. This pore morphology may render the ion migration more difficult. Furthermore, the pore walls are passivated, as discussed in section 2.4. Thus, the movement of hole charge carriers, which are required for anodic oxidation, is possibly hindered. Overall, the controlled anodic oxidation procedure is applied here with the purpose of establishing a robust electrochemical state of the porous silicon surface. It is not associated with the reversible electrosorption-induced actuation. Furthermore, it is possible to produce thicker oxide layers beyond 10 nm by applying higher potentials.[120, 250] However, these would result in a full oxidation of the pore walls and are thus not expedient for a capacitive charging.
Subsequently, CV measurements in the range of $0.2 - 1.2\,\mathrm{V}$ with scan rates from $10 - 50\,\mathrm{mV\,s^{-1}}$ are conducted. Figure 4.6(b) depicts these measurements. The bulk silicon is also showing a capacitive behaviour. A linear regression of the currents, averaged in the range of $0.6 - 0.8\,\mathrm{V}$ yields a capacitance of $c_{\mathrm{Si}} = 38.51 \pm 0.08\,\mu\mathrm{F}$, as shown in Figure 4.6(c). Hence, bulk silicon has a surface-area-specific capacitance of $c^*_{\mathrm{Si}} = c_{\mathrm{Si}}/(A_{\mathrm{Si}} \cdot 1.00075) = 1.579 \pm 0.003\,\mu\mathrm{F\,cm^{-2}}$, which coincides well with the range given in section 2.2. c^*_{Si} is approximately a factor of 25 times smaller than the surface specific capacitance of gold. The surface area specific capacitance c^*_{Si} is an important quantity and its determination is useful in this work and in other contexts.[233]
With the determination of c^*_{Si} it is possible to compare the physical inner surface area of the oxidised double epi-layer sample A_{2xpSi} to the electrochemically active surface area. A value of $c_{\mathrm{2xpSi}}/c^*_{\mathrm{Si}} = 1.20\,\mathrm{mF}/1.579\,\mu\mathrm{F\,cm^{-2}} = 760\,\mathrm{cm^2}$ is obtained. This value translates to a ratio of $760\,\mathrm{cm^2}/A_{\mathrm{2xpSi}} = 760\,\mathrm{cm^2}/2106\,\mathrm{cm^2} = 36.1\,\%$ of the physical inner surface area. Hence, the electrochemically active inner surface area is only about one third of the physical one. The disparity between these two values for surface area might have various reasons. Due to the anodic oxidation procedure, parts of the porous silicon wall, especially thin parts, may be fully oxidised. Thus, they would be electrically insulating and the pore wall above these sites are not longer electrically contacted. Hence, they would not participate in the electrochemical capacitive charging, which would explain the reduction of electrochemically active inner surface area compared to the physical surface area. Such a reduction of electrochemically active surface down to 30 % by anodic oxidation has been reported.[246] This reduction might also be caused by the small dendritic side-pores,

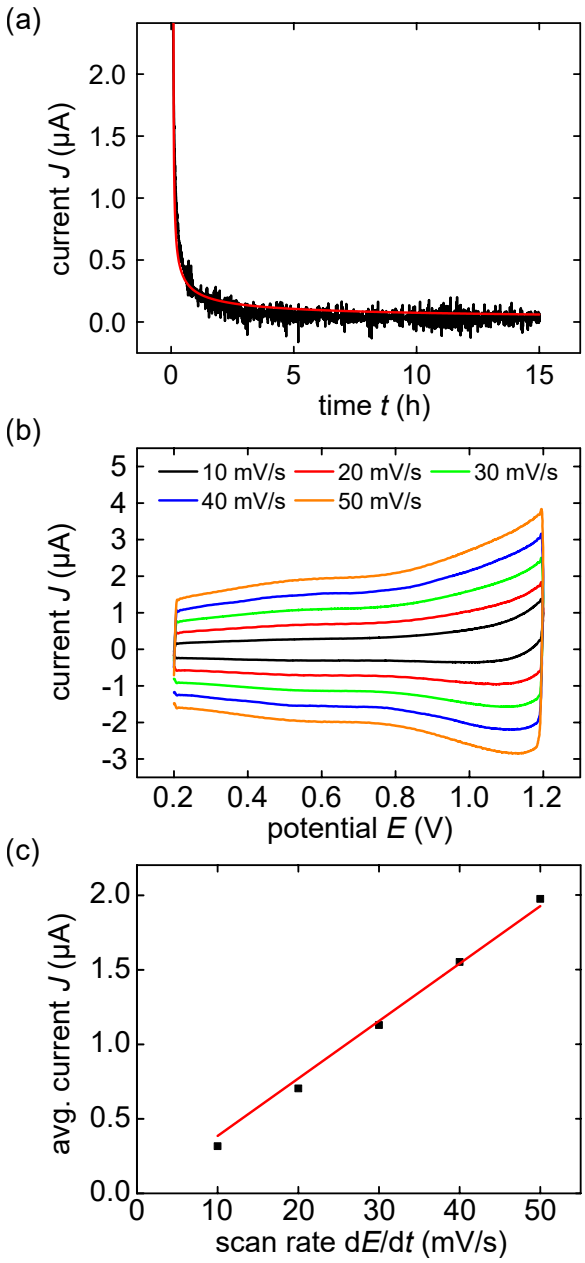

Figure 4.6.: **Electrochemistry of oxidised bulk silicon.** (a) Applied constant potential of 1.2 V on bulk silicon silicon with the course of current J. The red line indicates a fit of J according to equation 2.49. (b) CV measurements of oxidised bulk silicon in $HClO_4$ with scan rates from $10 - 50\,\mathrm{mV\,s^{-1}}$. (c) Values for the current J, averaged between $0.6 - 0.8$ V are plotted versus scan rate. The red line indicates a linear regression, which yields a capacitance of $c_{\mathrm{Si}} = 38.51 \pm 0.08\,\mu\mathrm{F}$.

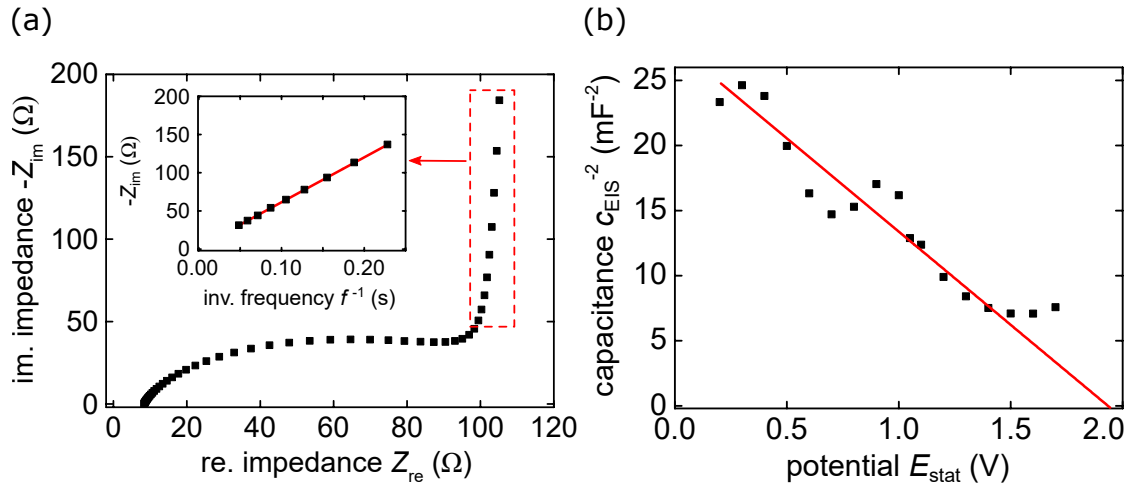

Figure 4.7.: **Electrochemical impedance spectroscopy of electric double layer charging of an anodically oxidised porous silicon electrode.** (a) Characteristic Nyquist plot of an anodically oxidised porous silicon electrode in $1\,\mathrm{mol\,L^{-1}}$ perchloric acid at a static applied potential of 0.2 V with frequencies in the range of 100 kHz to 4.3849 Hz. The course closely resembles an electric double layer charging process recognisable by a half-circle and the subsequent vertical increase. The data points of this regime are plotted versus their inverse frequency f^{-1}, which is depicted in the inset. A linear fit to the data points yields a capacitance of $c_{\mathrm{EIS}} = 0.21\,\mathrm{mF}$. (b) Mott-Schottky plot of an anodically oxidised porous silicon electrode. The capacitances determined by EIS are plotted in the form of c_{EIS}^{-2} versus the respective static potential E_{stat}. A linear fit to the data yields a flatband potential of $V_{\mathrm{fb}} = 1.9 \pm 0.2\,\mathrm{V}$ and a doping concentration of $N_{\mathrm{a}} = (3.1 \pm 0.1) \cdot 10^{19}\,\mathrm{cm^{-3}}$.

discussed above and depicted in Figure 4.1(b). These can contribute to the physical surface area but may not be electrically conductive. Since they have a small diameter, these side-pores may be under the influence of the quantum-wire effect, discussed in section 2.4. This would render them electrically insulating. Hence, they would not contribute to the potential adjusted capacitive charging of the surface.

Lastly, an EIS characterisation is performed on oxidised porous silicon. Figure 4.7(a) shows a characteristic Nyquist plot of an anodically oxidised porous silicon electrode with a porous silicon layer thickness of 630 nm in $1\,\mathrm{mol\,L^{-1}}$ perchloric acid. In the depicted case, the static applied potential is set to 0.2 V. The depicted measurement points have frequencies ranging from 100 kHz to 4.3849 Hz. It is apparent that the Nyquist plot has the characteristic features of an electric double layer charging. The onset of the half circle is at $Z_{\mathrm{re}} = 8.38\,\Omega$, which marks the resistance of the oxidised porous silicon WE. The half circle is not as pronounced as in the exemplary plot in Figure 3.2(a) in section 3.1. The diameter of the half-circle determines the bulk electrolytes resistance and here amounts to $82.1\,\Omega$, which is in good comparison to the resistivity determined in literature.[251] Following the half-circle, $-Z_{\mathrm{im}}$ converges to its cut-off frequency f_{c} of approximately 4 Hz. The intermediate regime between half-circle and cut-off is not pronounced. This indicates that the electric double layer charging is not inhibited by the bulk-electrolyte resistance.

In a next step, the low-frequency measurement points that are in the range with the vertical line are analysed. A plot of $-Z_{\mathrm{im}}$ versus f^{-1} reveals the linear dependency. The capacitance c_{EIS} of the electrode is determined by a linear fit. Its slope equals $(2\pi c_{\mathrm{EIS}})^{-1}$, see equation 3.5. Thus, for an applied potential $E_{\mathrm{stat}} = 0.2\,\mathrm{V}$ a value of $c_{\mathrm{EIS}} = 0.21\,\mathrm{mF}$ is obtained, which is in the range of the differential capacitance of $c_{\mathrm{diff}} = 0.26\,\mathrm{mF}$ determined by cyclic voltammetry.
The described procedure is repeated for different E_{stat} values in the range of $0.2 - 1.7\,\mathrm{V}$. The resulting capacitances are displayed as a Mott-Schottky plot in the form of c_{EIS}^{-2} versus E_{stat} in Figure 4.7(b). It is apparent that the c_{EIS}^{-2}-values are decreasing with an increasing potential until an ensuing plateau is reached around 1.5 V. Overall, a linear dependency of c_{EIS}^{-2} on E_{stat} with a negative slope is visible. Thus, the p-type doping of the silicon material is confirmed. However, at around 1.0 V a slight deviation from the linear behaviour that could be described as a peak is present. The presence of surface states would result in such a deviation to higher values in the Mott-Schottky plot.[120] These surface states are likely occurring on the oxidised surface of the pSi pore walls, as described in sections 2.2 and 2.3. Apart from this deviation, a linear course is ascertained and a fit to the data is performed. The fit yields two important parameters. Firstly, the intersection of the fit with the abscissa marks the flatband potential $V_{\mathrm{fb}} = 1.9 \pm 0.2\,\mathrm{V}$. Thus, oxidised porous silicon is in the depletion regime when electrochemical, e.g. CV, measurements are conducted up until V_{fb}. An equal measurement is performed on anodically oxidised bulk silicon with the same degree of doping. The respective Mott-Schottky plot is displayed in the appendix in Figure A.3. It yields a flatband potential of $1.4 \pm 0.1\,\mathrm{V}$ and is, thus, at a slightly lower potential compared to porous silicon. So, porous silicon seems to have an increased flatband potential, which has been reported before in literature.[170, 252] The value determined here for the flatband potential is larger than a flat band potential of $V_{\mathrm{fb}} = 0.38\,\mathrm{V}$ found in literature.[253] However, the cited study is performed on bulk silicon with four orders of magnitude lower doping density and in an HF solution. Porous silicon with a higher conductivity investigated in a non-HF aqueous electrolyte might have a higher flatband potential, as seen here.[254]
Moreover, the fit's slope s yields the doping concentration N_{a} by equation 3.6. The equation requires the electrochemically active surface area A, which can be inferred by $c_{\mathrm{diff}}/c_{\mathrm{Si}}^{*} = 0.26\,\mathrm{mF}/1.579\,\mu\mathrm{F\,cm^{-2}} = 164.7\,\mathrm{cm^2}$. Hence, a doping density of $N_{\mathrm{a}} = (3.1 \pm 0.1) \cdot 10^{19}\,\mathrm{cm^{-3}}$ is obtained. The value is slightly larger than the doping density provided by the distributor. However, the analysis performed on oxidised bulk silicon yields $N_{\mathrm{a}} = (2.6 \pm 0.3) \cdot 10^{19}\,\mathrm{cm^{-3}}$, which is in good agreement with the doping density found in porous silicon.
With the knowledge of the flatband potential V_{fb} and the doping density N_{a} the width of the SCR in oxidised porous silicon is determined by equation 2.21. The boundaries of the range of applied potential are 0 V and 1.2 V and yield widths of $8.9 \pm 0.2\,\mathrm{nm}$ and $5.4 \pm 0.1\,\mathrm{nm}$, respectively. The widths of the space charge region seem to be reasonable since the pore wall thickness is situated in the same range.
All in all, the analysis of the electrochemical characteristics shows that an anodic oxidation procedure on porous silicon yields stable capacitive features. Thus, anodically surface-oxidised porous silicon can be considered as ideally polarisable.

4.2. Dilatometry

Next, porous silicon is investigated with the scope on a possible actuation of a macroscopic sample, in response to the electrosorption of anionic charge carriers in the capacitive potential region. The porous silicon sample is installed in the dilatometer and immersed in $HClO_4$ electrolyte solution. The section of the sample that is in contact with the electrolyte solution has a length of $l_0 = 0.48 \pm 0.01\,\mathrm{cm}$ and a width of $w = 0.285 \pm 0.001\,\mathrm{cm}$. Thus, the sample has an outer volume of $V_{\mathrm{pSi,dila}} = 1.368\,\mathrm{mm}^3$.
Recording the sample length l change during a CV measurement allows a direct and comprehensive characterisation of the electrosorption-induced actuation. The respective measurements are depicted in Figure 4.8(a)-(d).[1] The dilatometer measurement is conducted in the reduced potential range of 0.8 V to 1.1 V that has already been used to explore the capacitive features of porous silicon, see Figure 4.3. In the actuation measurement the scan rate is set to $30\,\mathrm{mV\,s^{-1}}$. While the applied potential is reversibly changed from lower to upper vertex potential (see Figure 4.8(a)), the current is measured and thus it is possible to quantify the accumulated charge. Normalised to the sample volume $V_{\mathrm{pSi,dila}}$ it is referred to as the volume specific charge q_{V}, depicted in Figure 4.8(b). The course of q_{V} visibly coincides with applied potential E in a linear fashion. Thus, an increase in potential causes charge carriers to accumulate in the electric double layer. Vice versa, a decreasing potential leads to a reduction of charge carriers. Similarly, the strain ε linearly follows E and q_{V}, albeit with an inverse proportionality, i.e. a proportionality with a negative sign, see Figure 4.8(c). Thus, an increase in potential prompts an accumulation of charge carriers, which is in turn responsible for a contraction of porous silicon. The subsequent decrease in potential deprives charge carriers from the double layer. The result is an expansion. The change of the strain is clearly visible, although the amplitude is small and noise almost exceeds the signal. However, the strain amplitude exhibits no sign of a decrease. From cycle to cycle, it repeatedly reaches a level of $-0.0006\,\%$. Changing the scan rate is not affecting the amplitude of the electrosorption-induced actuation. At scan rates larger than approximately $100\,\mathrm{mV\,s^{-1}}$ the time resolution of the dilatometer is not sufficient to resolve the actuation. Overall, the strain measurement demonstrates a robust, reversible actuation induced by charge carrier electrosorption on the porous silicon surface.
Additionally, an average of ε and q_{V}, conducted over five cycles of the CV measurement, yields further details about the actuation. The strain amplitude average is $\varepsilon = ((4.16 \pm 0.03) \cdot 10^{-4})\,\%$. This amplitude translates to a change in length of $\Delta l = 19.97 \pm 0.14\,\mathrm{nm}$. Figure 4.8(d) depicts a plot in the associated potential range of averaged strain ε versus accumulated specific charge q_{V}. The plot exhibits the linearity between the two measured parameters. A linear data fit yields the corresponding strain-charge coupling parameter $A^*_{\mathrm{2xpSi}} = -0.0129 \pm 3 \cdot 10^{-4}\,\mathrm{mm^3\,C^{-1}}$.
Overall, the actuation measurements conducted in an electrochemical in situ dilatometry

[1] As a side note, the figures displaying actuation measurements will have a small, schematic illustration in the upper right corner. As the actuation measurements are resembling each other, the illustration is supposed to clarify which specific experimental situation is explored in the respective figure. The illustrations either show a dilatometry or a laser cantilever bending setup. Furthermore, by the colour of the pores it is specified if either bulk silicon (no pores), electrolyte-filled porous silicon (blue pores) or polypyrrole-filled porous silicon (green pores) is examined. The electrolyte is symbolised by the molecules surrounding the sample. Either perchlorate (red and blue molecules) or sodium chloride (green and blue molecules) are displayed.

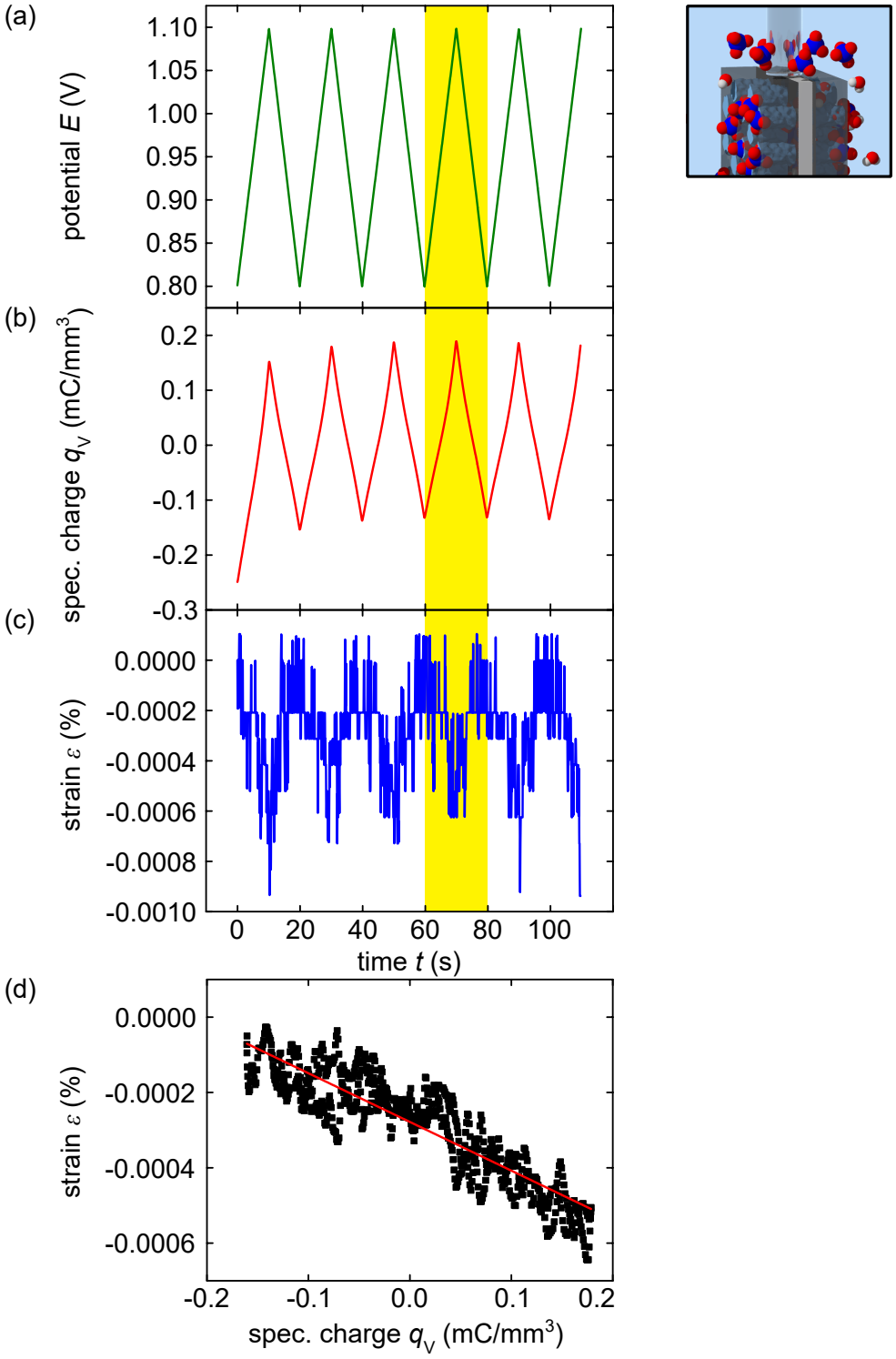

Figure 4.8.: **Electrochemical actuation measurement of porous silicon.** Curves of the electrosorption-induced actuation measurement with a scan rate of $30\,\mathrm{mV\,s^{-1}}$, as (a) five representative potential cycles E, (b) resulting volumetric charge q_V and (c) resulting effective change in strain ε of porous silicon conducted in perchloric acid. (d) Averaged strain ε versus accumulated volumetric charge q_V and a linear fit to determine the strain-charge coupling parameter A^*.

study exhibit a measurable actuation of porous silicon caused by electrosorption of ions on the porous silicon surface. Qualitatively, an inverse proportionality of strain in dependence on the accumulated charge can be inferred. However, the actuation amplitude is small with respect to noise and in absolute terms. The bulk silicon, which is located between two adjacent porous silicon layers, definitely hinders a free expansion and contraction of the porous silicon layers. Thus, the determined amplitude of the strain-charge coupling parameter studied on a double epi-layer geometry can only be considered to be correct within an order of magnitude, at most. Summarising, the experiments conducted are qualitatively valuable, but for a quantitatively reliable study another method is needed. An in situ laser cantilever bending setup is chosen here.

4.3. Laser Cantilever Bending

The method utilised in this section is in situ laser cantilever bending, described in detail in methods section 3.5. The laser cantilever bending method uses a thin porous silicon layer, whose actuation is supposed to be probed, to be attached to an underlying bulk silicon layer. Here, the bulk silicon clamps the adjacent porous silicon layer. Therefore an actuation of the porous silicon layer results in a bending, which can ultimately be translated into a changing film stress of the porous silicon layer, according to equation 3.9. Hence, the clamping of the porous silicon is not detrimental in this method, whereas in the in situ dilatometry study it represents a major disadvantage. Furthermore, the in situ laser cantilever bending study is simple to bring in accordance with the requirements of porous silicon. Concerning establishing an electrical contact the adjacent bulk silicon is an intrinsic component of the sample design. Overall, laser cantilever bending is a sensitive experimental method to investigate the electrosorption-induced actuation of porous silicon.

The sample for the cantilever bending study is prepared in the above established manner and the characteristics of the fabricated porous silicon are checked by nitrogen sorption isotherm. The etching time is set to 1 min so that a porous silicon layer with a thickness of $h_\mathrm{l} = 630\,\mathrm{nm}$ is formed. The underlying bulk silicon has a thickness of $h = 109.37\,\mu\mathrm{m}$. The sample is prepared from this material by cleaving. It has a rectangular shape with a length of $l = 2.990 \pm 0.002\,\mathrm{cm}$, a width of $w = 1.796 \pm 0.002\,\mathrm{cm}$ and thus a volume of the porous silicon layer of $V_\mathrm{pSi,CB} = 0.338\,\mathrm{mm}^3$, where the abbreviation CB denotes cantilever bending.

Afterwards, the sample is installed in the in situ electrochemical cell of the cantilever bending setup. Firstly, the sample is oxidised with a potential of 1.2 V for 20 h. The resulting course of the current is shown in Figure 4.9(a). The already known drastic decrease in current is visible here as well. A successful fit with equation 2.49 approximates the course of J well. This is in clear contrast to porous silicon with larger thicknesses. Hence, a 630 nm thin porous silicon layer apparently exhibits the same anodic oxidation kinetics as bulk silicon, whereas it is noticeably hindered in porous silicon beyond a thickness of 25.4 µm. This would corroborate the theory, discussed in response to Figure 4.2(a) that the porous silicon morphology and the charge transport within is responsible for the retardation, as the effect is smaller for thinner layers and thus a smaller influence of the porous silicon morphology. A significant film stress of $\Delta\sigma = 42.06\,\mathrm{MPa}$ accompanies the anodic oxidation procedure. It increases asymptotically, as the current declines. It can be

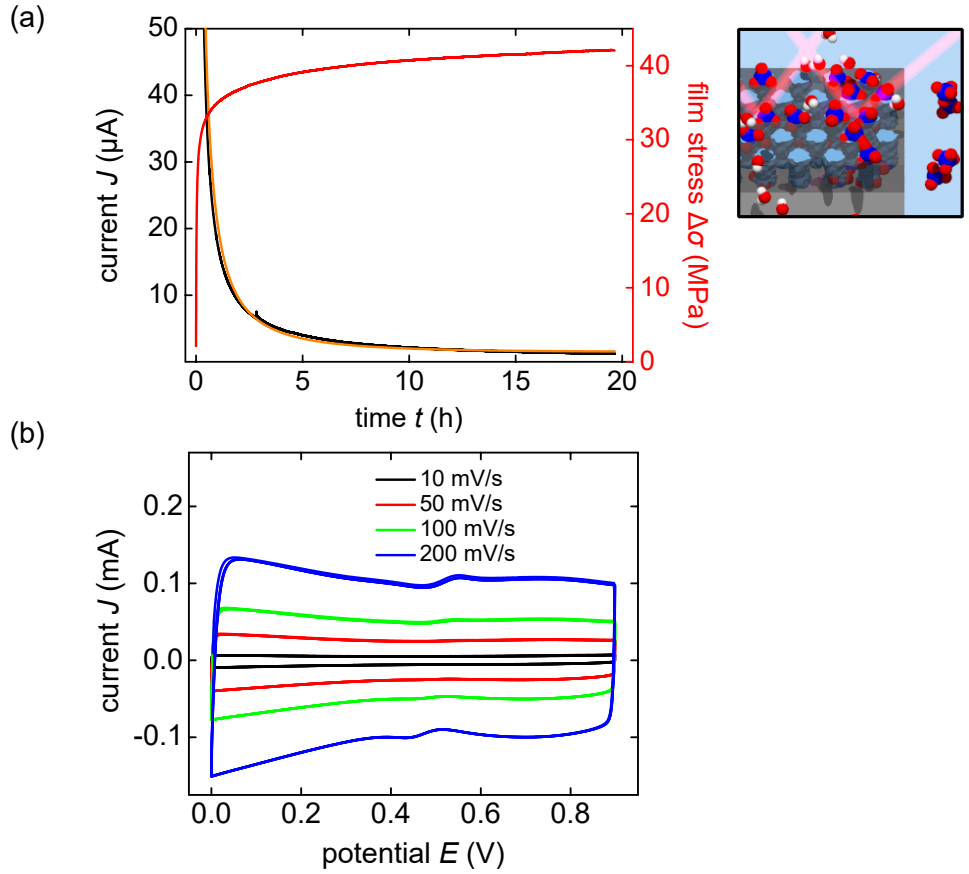

Figure 4.9.: **Electrochemical characterisation of porous silicon used for in situ laser cantilever bending.** (a) Applied constant potential of 1.2 V on a porous silicon epi-layer cantilever with a porous silicon thickness of 630 nm. Depicted is the course of current J (black) and the simultaneous change in film stress $\Delta\sigma$ (red) in the in situ cantilever bending setup. The orange line indicates a fit of J according to equation 2.49. (b) Cyclic voltammetry measurements of porous silicon in 1 mol L^{-1} $HClO_4$ electrolyte solution. The current J is plotted against the applied potential E in the range of $0.0-0.9$ V. The potential scan rate is increased from 10 mV s^{-1} to 200 mV s^{-1}.

explained by the different lattice constants of the remaining silicon in the pore walls and the adjacent silicon oxide layer on top.[141]
Figure 4.9(b) depicts cyclic voltammetry measurements in a potential range of $0.0 - 0.9\,\mathrm{V}$ with scan rates from $10 - 200\,\mathrm{mV\,s^{-1}}$ for porous silicon after anodic oxidation. These measurements exhibit the established capacitive characteristics. The CV with a scan rate of $200\,\mathrm{mV\,s^{-1}}$ features a peak in the up-sweep at $0.553\,\mathrm{V}$ and another peak in the down-sweep at $0.431\,\mathrm{V}$. In total, the two peaks resemble the redox couple, already discussed with respect to Figure 4.2 for the oxidised double epi-layer pSi. By contrast, the peak here is not as pronounced, which might be due to the reduced thickness of the layer. The analysis, see Figure A.4 in the appendix, yields a capacitance of $c_{\mathrm{pSi,CB}} = 0.466 \pm 0.004\,\mathrm{mF}$. This value translates to $1377\,\mathrm{mF\,cm^{-3}}$, which is slightly more than the value determined in the dilatometry study but still in the same order of magnitude.
The measurement of the change in film stress $\Delta\sigma$ in situ in the laser cantilever bending setup, in response to a CV measurement, enables a comprehensive characterisation of the electrosorption-induced actuation. The respective measurements are shown in Figure 4.10(a)-(d). The potential is reversibly changed from $0.0\,\mathrm{V}$ to $0.9\,\mathrm{V}$ (4.10(a)). The change in curvature $\Delta\kappa$ is not displayed in the figure. It is already converted to a change in film stress $\Delta\sigma$, according to equation 3.9. The volumetric charge q_{V} follows the change in potential in a clear linear manner (4.10(b)). So, an increasing potential leads to an accumulation of charge and vice versa, a decrease in potential is responsible for a decrease in charge. Thus, the potential response of q_{V} coincides with the already established characteristics from the dilatometer measurements, see Figure 4.8 and the accompanying discussion. In a similar manner, the film stress $\Delta\sigma$ reversibly shifts from a level of $-210\,\mathrm{kPa}$ to $170\,\mathrm{kPa}$ (4.10(c)). The film stress has to be slightly corrected. Thereby, it is not starting at and is not centred around zero, which is acceptable since only the relative change in surface stress is measured. From cycle to cycle, $\Delta\sigma$ exhibits no sign of a decrease. However, as opposed to q_{V}, the dependence of $\Delta\sigma$ on potential E has an inverse proportionality. Thus, a decrease in E deprives the electric double layer of charge and leads to an increase in film stress $\Delta\sigma$. Hence, the porous silicon layer expands. Vice versa, a contraction of the silicon wafer and, thus, a decrease of $\Delta\sigma$ is caused by an increasing potential and the accompanying accumulation of charge. This dependency of the sample length change on potential and charge has already been established by the dilatometry measurements, see Figure 4.8, and thus confirms these results. Overall, the experiment demonstrates the robust and reversible actuation by electrosorption of porous silicon.
Furthermore, averaging $\Delta\sigma$ and q_{V} over five cycles, yields further characteristics of the actuation. The mean peak-to-peak amplitude of film stress and charge are $\Delta\sigma_{\mathrm{avg}} = 406.3 \pm 0.3\,\mathrm{kPa}$ and $q_{\mathrm{V_{avg}}} = 1.54 \pm 0.04\,\mathrm{mC\,mm^{-3}}$, respectively. Figure 4.10(d) shows the two quantities in a plot of $\Delta\sigma$ versus q_{V} in the associated potential range of $0.0 - 0.9\,\mathrm{V}$. The inverse proportionality is confirmed. However, the relation of the two is not entirely linear. It is evident that the slope of $\Delta\sigma$ on q_{V} is smaller in the lower end of the range at approximately -0.8 to $-0.4\,\mathrm{mC\,mm^{-3}}$ than in the higher end. Moreover, the plot exhibits a hysteresis between up- and down-sweep from $-0.4\,\mathrm{mC\,mm^{-3}}$ onwards. This hysteresis is observed for all scan rates. Therefore, the surface stress state of the electrode might not be solely dependent on the capacitive volumetric charge q_{V}. The hysteresis might be present due to specific adsorption of ions on the electrode surface.[80] Perchlorate anions are known to specifically adsorb on certain electrode surfaces.[255] Nonetheless, a linear fit is performed to determine the corresponding coupling coefficient ξ, which connects film

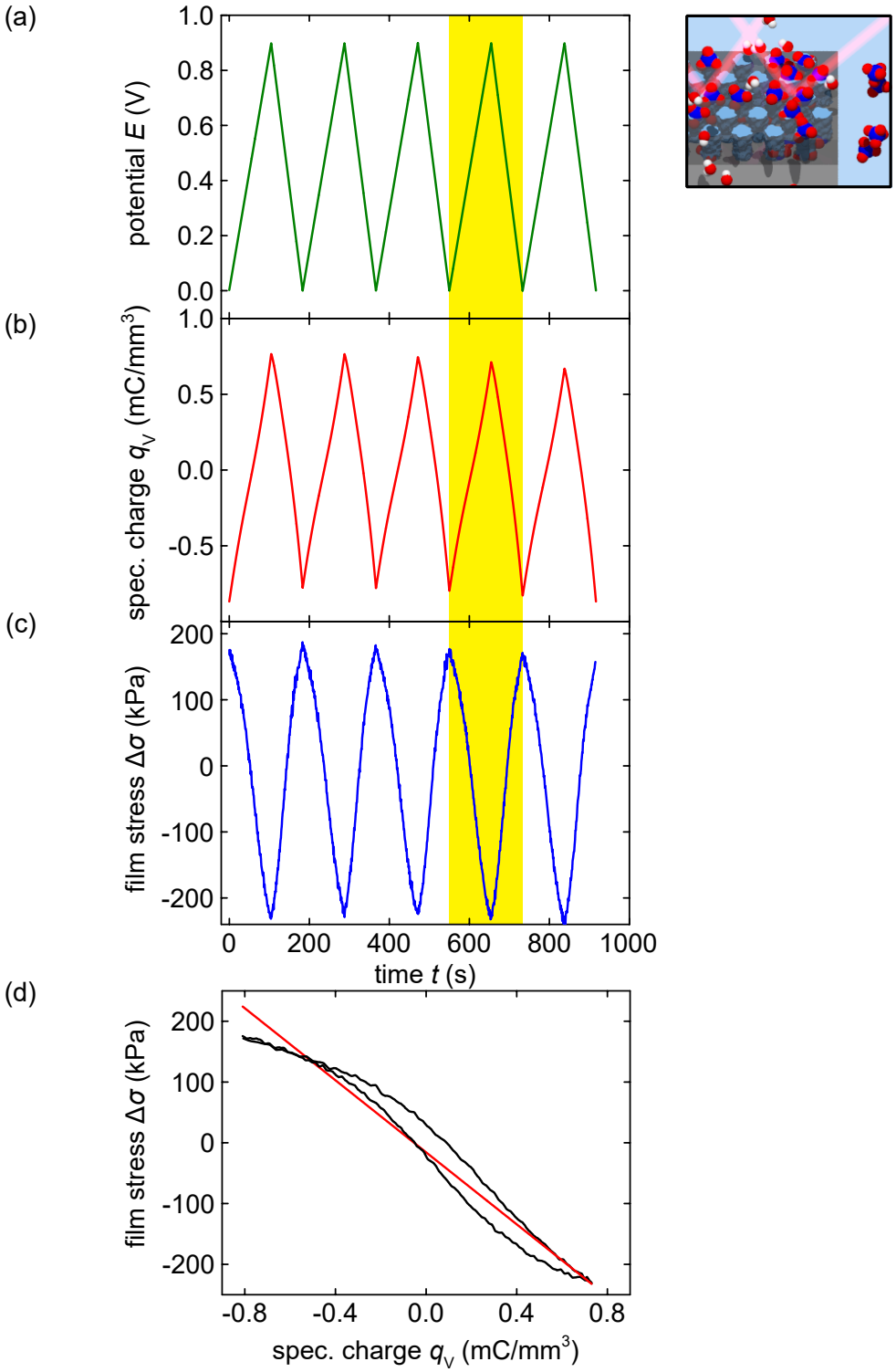

Figure 4.10.: **In situ laser cantilever bending experiments on electrosorption-induced actuation of porous silicon.** Electrosorption-induced actuation measurement conducted in perchloric acid with a scan rate of 10 mV s^{-1} with (a) five representative potential cycles E between 0 V and 0.9 V, (b) resulting volume specific charge q_V and (c) induced change in film stress $\Delta\sigma$ in porous silicon. (d) Film stress change $\Delta\sigma$ versus accumulated volume specific charge q_V averaged over five respective cycles. The linear fit yields the stress charge coupling parameter $\xi = -296 \pm 1$ mV.

stress to charge. The result is $\xi = -296 \pm 1\,\mathrm{mV}$. Thus, by the determination of ξ a measure for porous silicon is obtained that allows an assessment of the electrochemo-mechanical coupling that drives the actuation.

4.3.1. Isotonic Saline Solution

To explore if the electrosorption-induced actuation exhibits different characteristics with another electrolyte, analogous measurements are conducted. An isotonic saline solution, i.e. aqueous sodium chloride with a concentration of $154\,\mathrm{mmol\,L^{-1}}$, is used. Since it is omnipresent in biological and medical environments, the saline solution simulates a possible in vivo application of porous silicon and its associated actuation. The respective measurements are depicted in Figure 4.11. Section (a) shows CV measurements conducted in the same potential range of 0.0 to 0.9 V with scan rates of $10\,\mathrm{mV\,s^{-1}}$ to $100\,\mathrm{mV\,s^{-1}}$. An equal capacitive regime in the chosen potential range is visible, as before with perchlorate anions. Thus, a fit of the averaged current yields the capacitance, as depicted in the appendix in Figure A.5(a). The result is $c_{\mathrm{pSi,CB,iso}} = 0.473 \pm 0.003\,\mathrm{mF}$, which is in excellent agreement with the capacitance $c_{\mathrm{pSi,CB}} = 0.466 \pm 0.004\,\mathrm{mF}$ obtained before with perchlorate anions. The aforementioned suspected redox peak, here at approximately 0.5 V might be less pronounced.
In Figure 4.11(b) the electrosorption-induced actuation measurement with the NaCl electrolyte is displayed. A scan rate of $10\,\mathrm{mV\,s^{-1}}$ is used. The film stress $\Delta\sigma$ exhibits the established characteristics. Namely, in response to a change of E and thus q_{V}, the film stress follows with an inverse proportionality. In an equal manner to the evaluation of the measurements using perchloric acid, both film stress and volumetric charge are averaged over five cycles. This yields an amplitude for the film stress of $\Delta\sigma = 503.2 \pm 0.5\,\mathrm{kPa}$. The volumetric charge q_{V} remains in the range of -0.8 to $+0.8\,\mathrm{mC\,mm^{-3}}$. In the relation of $\Delta\sigma$ to q_{V} the same hysteresis is present, as depicted in the appendix in Figure A.5(b). Thus, the hysteresis seems not to depend on the type of anion used. The fit yields a film stress charge coupling coefficient of $-374 \pm 2\,\mathrm{mV}$. Compared to $HClO_4$ this means a larger ξ in terms of absolute value. This increase might be explained by a difference in the electrosorption of ion species used – perchlorate in comparison to chloride anions.

4.3.2. Actuation Kinetics

In a next measurement, the kinetics of the actuation mechanism are characterised. A step-coulombmetry measurement with a rectangular potential E is performed, as described in the methods section 3.1, while the response of the film stress and the volumetric charge are measured. The measurement is performed in an $HClO_4$ electrolyte and is depicted in Figure 4.12(a) and (b). Section (a) of the graph shows the measurement over a total of five cycles of up and down potential steps from 0.0 V to 0.9 V and back. Potential E, volumetric charge q_{V} and film stress $\Delta\sigma$ are plotted versus time t. On a decreasing potential step, the film stress increases to a plateau of $+310\,\mathrm{kPa}$ while q_{V} asymptotically decreases to a level of $-0.182\,\mathrm{mC\,mm^{-3}}$. Vice versa, upon a potential increase to 0.9 V, film stress and volumetric charge reverse to values of $-65\,\mathrm{kPa}$ and $+0.125\,\mathrm{mC\,mm^{-3}}$, respectively. Thus, it is interesting to note that the volumetric charge amplitude is about

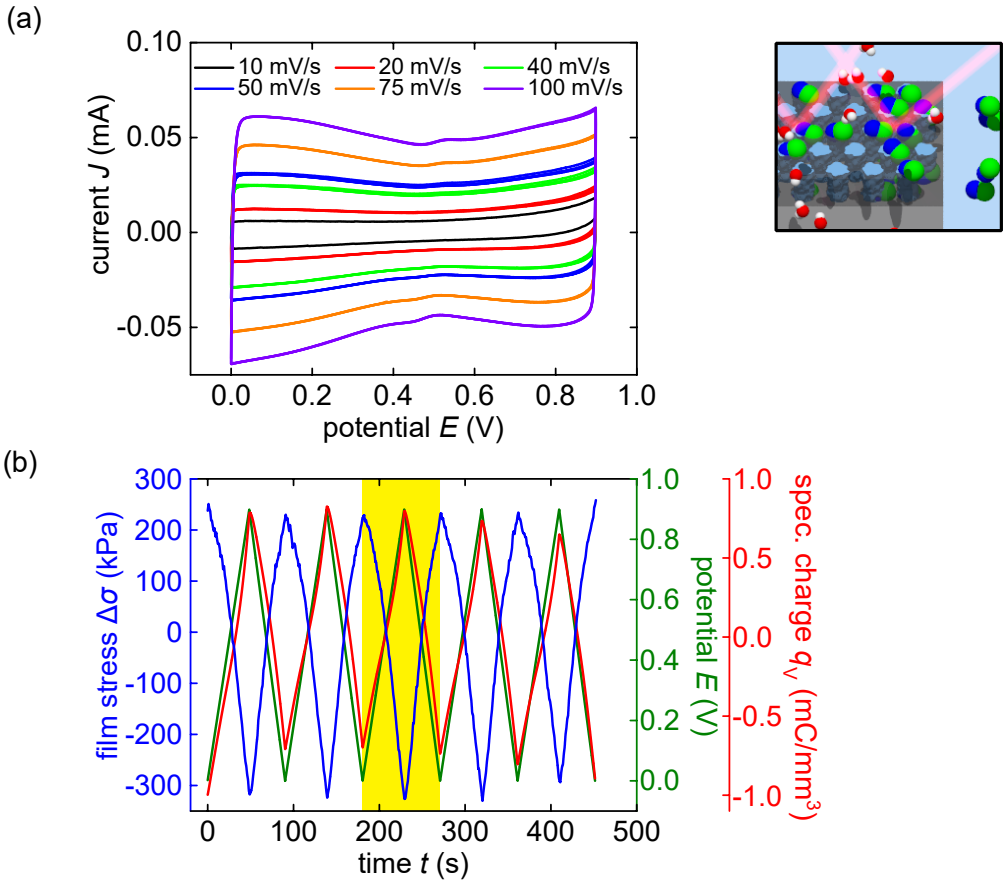

Figure 4.11.: **In situ laser cantilever bending experiments on electrosorption-induced actuation of porous silicon immersed in isotonic saline solution.** (a) CV measurements in an isotonic saline solution (154 mmol L^{-1} NaCl aq.) with different scan rates, $10 - 100\,mV\,s^{-1}$, in the potential range of $0.0 - 0.9\,V$. The obtained capacitance is $c_{pSi,CB,iso} = 0.473 \pm 0.003\,mF$, cf. Figure A.5(a) in the appendix. (b) Respective curves of the actuation measurement conducted with $10\,mV\,s^{-1}$ in a plot versus time. Five representative potential cycles with E (green), q_V (red) and $\Delta\sigma$ (blue). The analysis of film stress $\Delta\sigma$ versus accumulated volume specific charge q_V averaged over five cycles yields $\xi = -374 \pm 2\,mV$, see Figure A.5(b) in the appendix.

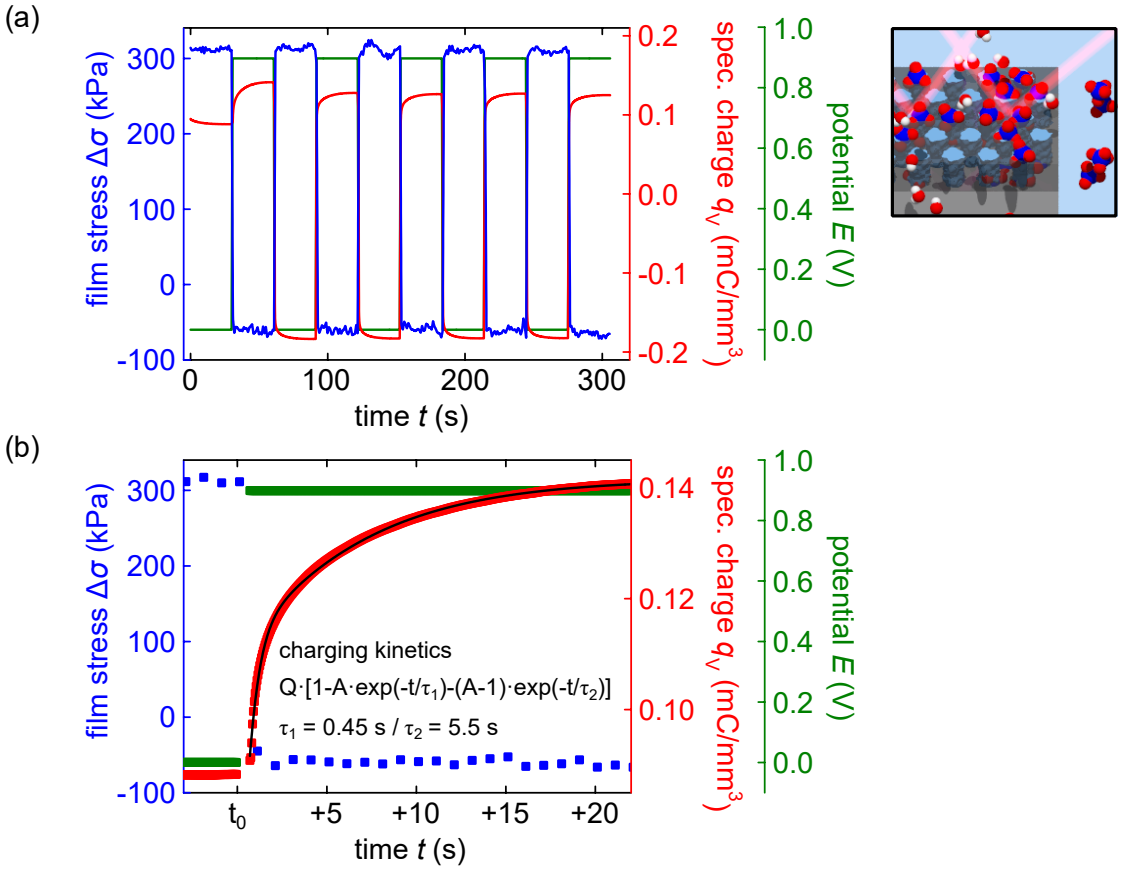

Figure 4.12.: **Kinetic laser cantilever bending measurement of electrosorption-induced actuation of porous silicon.** Step-coulombmetry measurement of actuation kinetics performed in $HClO_4$ with potential E (green) steps of 0.0 V to 0.9 V and back while film stress $\Delta\sigma$ (blue) and volumetric charge q_V (red) are measured. (a) Entirety of the measurement with five cycles of up and down steps, whereas part (b) shows a close up of the first potential increase at time t_0. In (b) the course of q_V is approximated by a fit with the sum of two exponential functions (black), according to equation 4.1.

an order of magnitude smaller than amplitude $q_{\mathrm{V_{avg}}}$ in the respective CV measurement – especially, since the measurements are conducted in the same potential range. In the rectangular potential measurement a value of approximately $+0.3\,\mathrm{mC\,mm^{-3}}$ is obtained, whereas the charge amplitude for the respective CV measurement is $1.54 \pm 0.04\,\mathrm{mC\,mm^{-3}}$. This comparison indicates that the manner in which the potential is applied has a noticeable influence on the amount of charge accumulated, which is indeed also observed for nanoporous carbon.[256]
The course of q_V upon charging and discharging is approximated by a fit in the form of a sum of two exponential functions

$$q_\mathrm{V} = Q_\mathrm{ampl} \cdot [1 - A \cdot \exp(-t/\tau_1) - (1 - A) \cdot \exp(-t/\tau_2)]\,, \tag{4.1}$$

where Q_ampl and A denote parameters for the fit amplitude. τ_1 and τ_2 yield characteristic time constants of the two exponential functions. An approach according to equation 4.1 has been reported to appropriately fit the charge course of supercapacitor materials in response to square potential steps.[256, 257] Section (b) of Figure 4.12 depicts an example of the function to fit q_V on a potential increase. It is visible that the function approximates the course well. For each of the five potential increases and decreases q_V is approximated and subsequently the fit parameters are averaged. The characteristic response times τ_1 and τ_2 are of particular interest and will be compared to the mechanical response dynamics. The averaging procedure yields $\tau_{1,q_\mathrm{V},\mathrm{decr}} = 0.072 \pm 0.005\,\mathrm{s}$ for the fast volumetric charge decrease, $\tau_{2,q_\mathrm{V},\mathrm{decr}} = 3.3 \pm 0.5\,\mathrm{s}$ for the slow volumetric charge decrease, $\tau_{1,q_\mathrm{V},\mathrm{incr}} = 0.46 \pm 0.02\,\mathrm{s}$ for the fast volumetric charge increase and $\tau_{2,q_\mathrm{V},\mathrm{incr}} = 5.7 \pm 0.1\,\mathrm{s}$ for the slow volumetric charge increase. Thus, the porous silicon charge transfer operates on two different time scales. For both parameters, i.e. τ_1 and τ_2, the response time is noticeably quicker upon discharging than charging. The film stress $\Delta\sigma$ reaction to the change in potential is faster than the time resolution of the laser cantilever bending setup, as shown in Figure 4.12(b), where $\Delta\sigma$ is shown in a close up. $\Delta\sigma$ basically decreases from the upper to the lower level within one single measurement point. Therefore, the mechanical response of porous silicon can be narrowed down to a time scale below 1 s. It is thus faster than the overall charge transfer dynamics. Due to their similar time scales, the kinetics of the $\Delta\sigma$ response seem to be associated with the faster charge transfer process, i.e. the one described by τ_1. It can only be speculated, but it might be that a fast formation of the Stern layer closest to the wall is responsible. By contrast, a slower build up of the diffuse Guy-Chapman layer would thereby only negligibly contribute to the electrochemo-mechanical coupling.
The timescale t_c of charge transfer may be estimated by considering ion diffusion. Assuming an ideal cylindrical pore [258, 259]

$$t_\mathrm{c} = \frac{\lambda_\mathrm{D}}{r}\frac{\ell_\mathrm{pore}^2}{\mathcal{D}}, \tag{4.2}$$

where r denotes the pore radius and is, as determined above, $r = 3.3\,\mathrm{nm}$. $\ell_\mathrm{pore} = 630\,\mathrm{nm}$ is the pore length or the thickness of the porous silicon layer. λ_D is the Debye length, introduced in section 2.2, and according to equation 2.5, $\lambda_\mathrm{D} = 0.304\,\mathrm{nm}$, with a perchlorate concentration of $1\,\mathrm{mol\,L^{-1}}$. $\mathcal{D}$ denotes the diffusion coefficient and can be approximated by $\approx 2 \cdot 10^{-9}\,\mathrm{m^2\,s^{-1}}$.[260] With these values the timescale equals $t_\mathrm{c} \approx 18\,\mu\mathrm{s}$. Thus, t_c is much smaller than the experimentally determined time scales of charge transfer. However, silicon oxide exposed to aqueous electrolytes is, at least partially, hydroxylated and

thus hydrophilic. The formation of approximately 1 nm thick interfacial water layers of a viscous character is experimentally found.[261–264] These layers are also investigated in computer simulations.[265–267] The self diffusivity of water in these layers is suggested to exponentially increase towards the surface. The extent of this effect can reach up to two orders of magnitude larger than in bulk water.[267] Hence, the deviation of the idealistic assumptions made in equation 4.2 and the significantly retarded observed charge transfer, might be ascribed to these interfacial layers. In particular, assuming a bulk diffusivity for the perchlorate ions inside a highly porous material might be imprecise because of distinct confinement effects of the pores. The large roughness of the pSi pore wall, with its side-pores, might furthermore add to the retardation, as an effective diffusion length could be increased.

4.3.3. Bulk Silicon Surfaces

The electrochemo-mechanical response of porous silicon has been investigated extensively. In addition to these experiments, an equivalent study on a planar, bulk silicon surface will be discussed. These comparative measurements enable detailed mechanistic as well as quantitative insight into the porous silicon actuation itself.
Oxidised bulk silicon, used for the cantilever bending study, is prepared with the established procedure. The back side is covered by a non-conductive thermal oxide layer, as described in the methods and materials section 3.5.2. On the front side, in an $HClO_4$ electrolyte a potential of 1.2 V is applied for a time of 15 h so that current J approaches a value of approximately 50 nA. Next, CV measurements in the potential range of 0.3 V to 1.1 V are performed to confirm the capacitive characteristics of the bulk silicon sample. Indeed, the measurement, depicted in Figure 4.13(a), compares well to the measurement on bulk silicon already performed and discussed above in section 4.1 in response to Figure 4.6. A capacitance of $c_{\mathrm{Si,CB}} = 10.07 \pm 0.08\,\mu\mathrm{F}$ is obtained, see Figure A.6 in the appendix. Thus, the bulk silicon has a surface area of $A_{\mathrm{Si,CB}} = c_{\mathrm{Si,CB}}/c^*_{\mathrm{Si}} = 6.38 \pm 0.05\,\mathrm{cm}^2$, which fits well to the geometrically determined surface area. The accumulated charge will be normalised to this specific surface area $A_{\mathrm{Si,CB}}$ in the actuation measurements analysis.
A laser cantilever bending measurement is conducted during a CV to validate if a changing potential and thereby capacitively accumulated charge in the electric double layer induces a measurable change in surface stress of planar, bulk silicon. The respective measurement conducted in the same potential range with a scan rate of $20\,\mathrm{mV\,s^{-1}}$ is depicted in Figure 4.13(b). The bending of the wafer is already converted to a change in surface stress Δf by equation 3.8. Indeed, the cantilever bending setup is able to detect a quantifiable change in Δf upon a linearly varying potential E. Due to its importance, to highlight this point – the laser cantilever bending setup provides the necessary sensitivity to measure an electrosorption-induced actuation of bulk silicon. The measurement shows that the change in surface stress Δf coincides in phase with applied potential E and the surface specific charge q_{A}. So, an increase in potential accumulates charge on the silicon electrolyte interface and leads to an increase in surface stress. Vice versa, a potential decrease causes a decrease in q_{A} and surface stress. The amplitude of the surface stress, averaged over the ten displayed cycles is $8.9 \pm 0.5\,\mathrm{mN\,m^{-1}}$. Δf has a noticeably lower signal to noise ratio, compared to the measurement of the porous silicon film stress $\Delta\sigma$. This can be explained by the respective bending radius of the two different samples. For

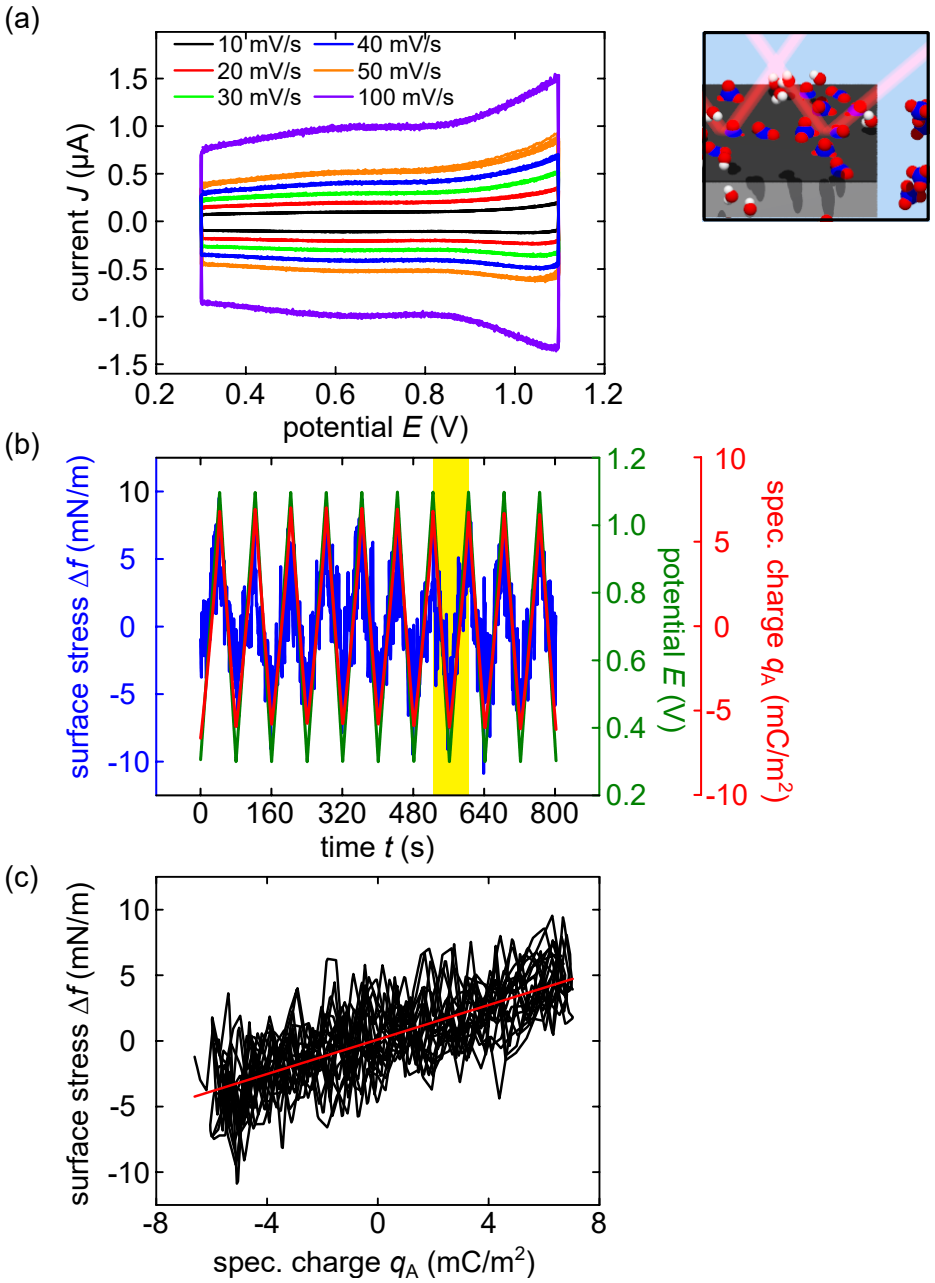

Figure 4.13.: **In situ laser cantilever bending experiments on electrosorption-induced actuation of planar, bulk silicon.** (a) CV measurements on planar, bulk silicon in perchloric acid performed in the laser cantilever setup with scan rates from $10\,\mathrm{mV\,s^{-1}}$ to $100\,\mathrm{mV\,s^{-1}}$ in the potential region of 0.3 V to 1.1 V. (b) Change in surface stress Δf (blue) during a CV measurement, performed with a scan rate of $20\,\mathrm{mV\,s^{-1}}$ with potential E (green) cycled in the range of 0.3 V to 1.1 V in $HClO_4$ with the accompanying signal of surface area specific capacitance q_A (red). (c) Change in surface stress Δf versus specific charge q_A. Independent determination of the electrocapillary coupling coefficient ς by linear regression, which yields a value of $\varsigma = +0.657 \pm 0.007\,\mathrm{V}$.

the electrosorption-induced actuation of porous silicon the peak-to-peak value of $\Delta\kappa^{-1}$ is approximately $0.7\,\mathrm{km}^{-1}$ and thus about one order of magnitude larger than the value for the bulk silicon sample, which is approximately $0.04\,\mathrm{km}^{-1}$.
Figure 4.13(c) shows a plot of Δf with respect to q_A. The plot emphasises the linear relation of the two variables even more. The electrochemo-mechanical coupling of surface stress to accumulated charge is evaluated by a linear fit to the data. It is indicated by a red line. The slope of the fit marks the electrocapillary coupling parameter ς and amounts to $\varsigma = +0.657 \pm 0.007\,\mathrm{V}$. Thus, the absolute value of the electrocapillary coupling parameter for an oxidised silicon surface is approximately a third of $\varsigma_\mathrm{Au} = -2.0\,\mathrm{V}$ for gold. However, the fact that the sign of ς is positive for an oxidised silicon surface, distinctively distinguishes silicon. All in all, the successful determination of the material parameter ς for silicon is significant, as it is a useful materials parameter in the context of electrochemical investigations of silicon. The experimental quantification of ς for silicon marks a first, as far as the author can tell.

4.3.4. Surface Tension at Bulk Silicon Surfaces

Overall, the in situ laser cantilever bending setup enables a direct measurement and characterisation of the surface stress Δf on a planar, bulk material's interface with an electrolyte solution. Thus, as an independent method, the setup is suitable for a reliable determination of the electrocapillary coupling parameter ς of silicon, which is a fundamental materials parameter. As already described in section 2.5, the in situ cantilever bending setup furthermore enables a simultaneous measurement of surface stress Δf and surface tension $\Delta\gamma$. A change in surface tension is inferred from the electrochemical signal of the CV measurement. $\Delta\gamma$ is equated to the surface specific charge, as described by the variation of the Lippmann equation 2.61. Through integrating $\mathrm{d}\gamma = -q_\mathrm{V}\mathrm{d}E$, see equation 2.58, a potential-dependent description of the surface tension in the form of $\Delta\gamma(E) = \gamma(E) - \gamma_0$ can be obtained.[10] Thus, to highlight this point, an integration of the measured surface specific charge with respect to the applied potential yields the respective change in surface tension $\Delta\gamma$. The result is shown in Figure 4.14. It is clearly visible that the obtained shape of the surface tension is in the characteristic form of a negative parabola that decreases when the potential departs from the maximum. This characteristic course is in accordance with equation 2.59. Thus, the two fundamental electrocapillary quantities react in distinctly different manners, as the surface stress Δf varies linearly with both the potential and the surface specific charge, as Figure 4.13(a) and especially (b) display. Furthermore, the amplitude of the surface stress δf is larger by a factor of approximately four. The maximum of the $\Delta\gamma$ curve has here arbitrarily been set to zero since the method does not allow an absolute determination of the state of surface tension, only the relative change $\Delta\gamma$. Furthermore, the Figure displays three curves, for three different potentials of zero charge E_zc of 0.55 V, 0.60 V and 0.65 V. The determination of E_zc requires an independent method. Knowledge of E_zc would be ideal for a complete electrochemical characterisation of bulk silicon, albeit the necessary challenging measurement.[80, 268, 269] However, in this work, E_zc is not of relevance since the discussion of surface tension on bulk silicon is only briefly introduced to demonstrate the distinct differences between the two parameters surface stress and tension.

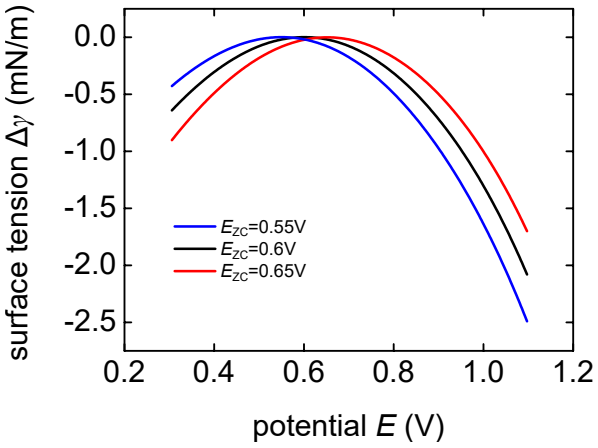

Figure 4.14.: **Surface tension analysis of bulk silicon.** Analysis of the change of surface tension $\Delta\gamma$ of the planar, bulk silicon sample installed in the in situ laser cantilever bending setup during a CV measurement. The q_A signal from the CV measurement, depicted in Figure 4.13(a), conducted with $20\,\mathrm{mV\,s^{-1}}$ in the potential range of 0.3 V to 1.1 V, is integrated with respect to E. The result is surface tension in dependence of applied potential E, with the characteristic parabola shape.

4.3.5. n-Type Porous Silicon

The experiments up until this point have been performed on p-type bulk or porous silicon. For n-type silicon, an opposite proportionality in the electrochemo-mechanical coupling of surface stress in response to the presence of charge carriers in the electric double layer is predicted, as described in section 2.5.[82] Thus, an increase of potential and an accumulation of charge carriers would lead to an expansion of the porous silicon and not a contraction, as observed for p-type porous silicon, see Figure 4.10(c), and vice versa. In situ dilatometry measurements on double epi-layer n-type porous silicon are conducted to explore if the described dependence is observed. Moreover, an in situ laser cantilever bending experiment on n-type bulk silicon is performed to investigate the actuation characteristics of the planar, non-porous surface.
n-type double epi-layer porous silicon is fabricated according to the details in section 3.2. The thicknesses of the porous silicon layers on front and back side are determined by SEM micrographs. They are 43 µm and 45 µm with 20 µm of bulk silicon remaining in between. A nitrogen sorption isotherm, depicted in Figure 4.15(a), shows the typical characteristics as discussed above for p-type porous silicon concerning Figure 4.1(c). The evaluation for n-type porous silicon leads to a slightly larger pore radius of $r = 6.01\,\mathrm{nm}$ and a smaller porosity of $\Phi_{\mathrm{n-type}} = 27.82\,\%$. Overall, the fabricated n-type porous silicon has very similar morphological characteristics as its p-type counterpart. Small side-pores, which branch off the main pore, are also found in n-type porous silicon, see Figure 4.15(b), although these are not as distinct as in p-type porous silicon.
The sample is equally prepared by an anodic oxidation step in $HClO_4$ for 14 h. For a significant decrease of current J to a final value of 13 µA a higher potential of 2 V has to be applied. This can be attributed to the doping type, as discussed in section 2.3, since

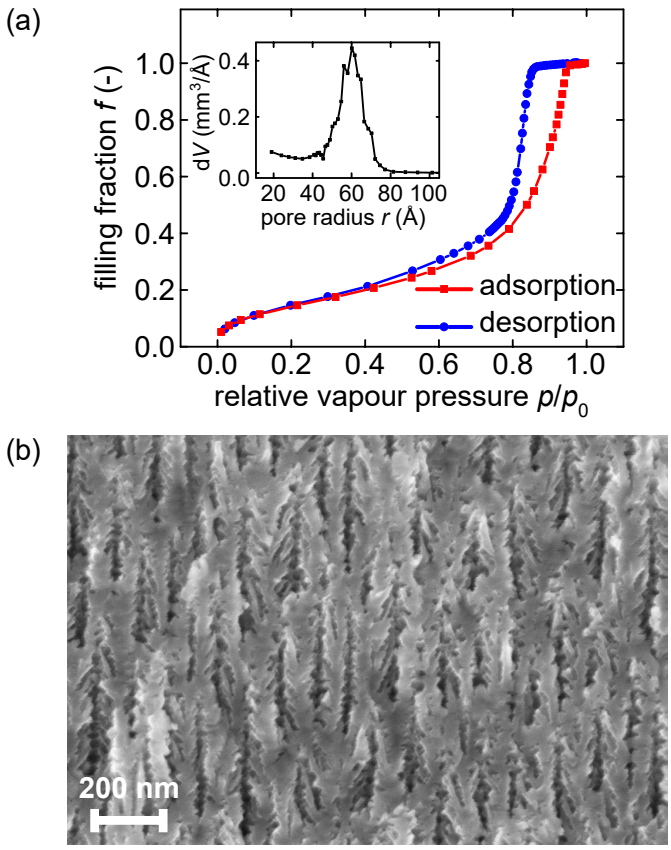

Figure 4.15.: **n-type porous silicon.** (a) Nitrogen sorption isotherm recorded of double epi-layer porous silicon which has been fabricated from n-type silicon as a base material. The inset shows the pore radius distribution obtained by an analysis with the BJH model. (b) SEM profile micrograph of n-type porous silicon.

the necessary hole charge carriers for the oxidation have to be produced by an increased potential. In literature a potential of 2 V has been reported for the doping level of this silicon type, which fits perfectly.[270] CV measurements conducted in the potential range of 0.3 V to 0.4 V with scan rates of up to 50 mV s^{-1}, depicted in Figure 4.16(a), display the characteristics for a purely capacitive CV behaviour. The analysis of the measurements, depicted in Figure A.7 in the appendix, yields a linear dependence of averaged current J on the scan rate and a capacitance of $c_{\mathrm{n-type}} = 1.06 \pm 0.025$ mF, which is in the same order of magnitude as the capacitance for p-type porous silicon. However, this specific potential range and scan rate is not sufficient to resolve an actuation. Therefore, the potential range is stretched to an upper vertex point of 1.45 V, up to which the CV may be described as mostly capacitive. For scan rates from 75 mV s^{-1} to 300 mV s^{-1} it is possible to resolve an actuation. The actuation measurement with the fastest scan rate is shown in Figure 4.16(b). It is visible that the change in strain ε follows the potential E and the accumulated specific charge q_{V} in an inversely proportional manner. In this regard n-type porous silicon is equal to p-type one. However, the analysis of the resulting coupling of ε to q_{V}, which are both averaged over the five depicted cycles, shows that

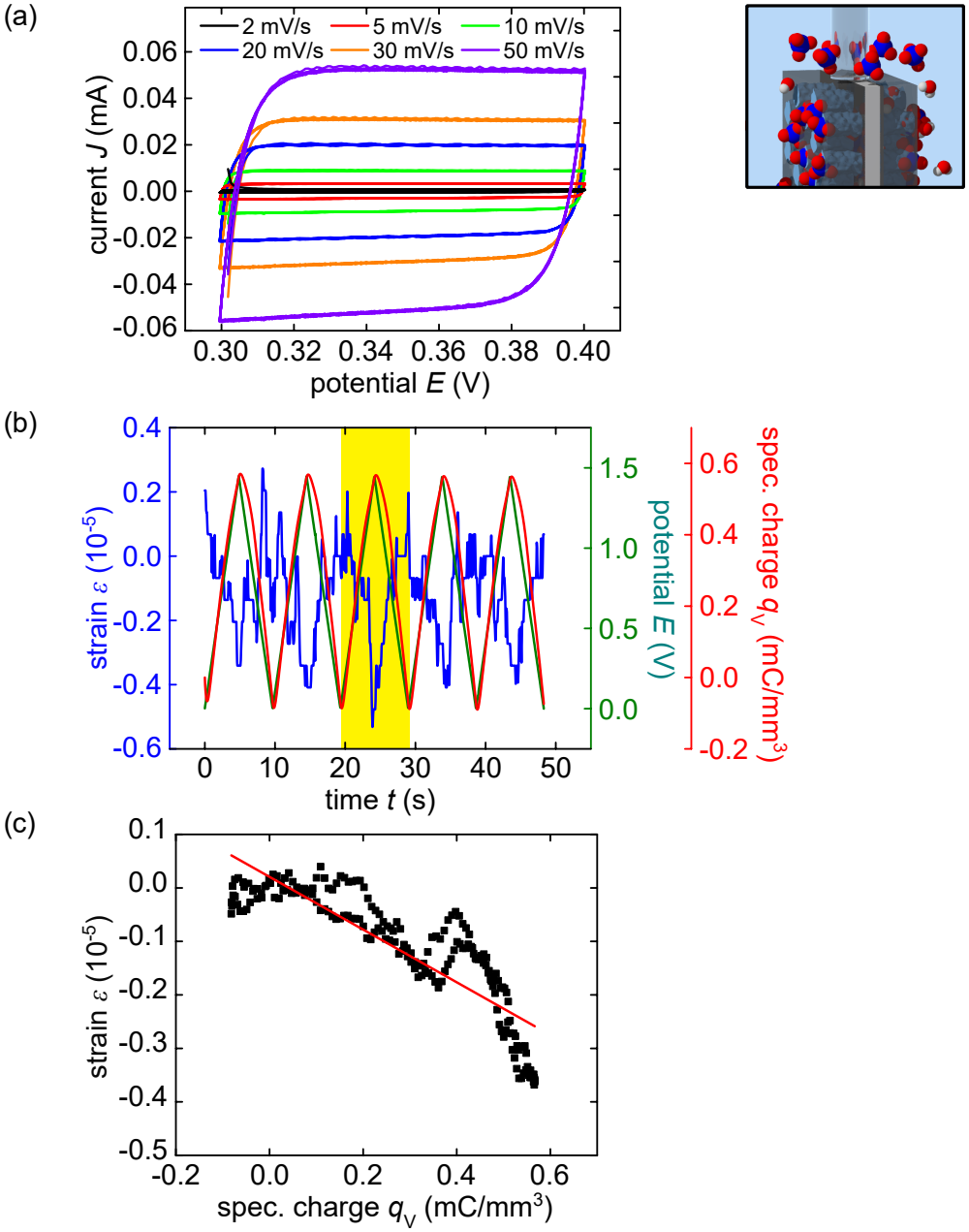

Figure 4.16.: **Electrochemical and actuation characterisation of n-type porous silicon.** (a) CV measurements with different scan rates in the potential region of 0.3 V to 0.4 V. (b) Electrochemical actuation measurement with a scan rate of 300 mV s^{-1} in $HClO_4$ displayed versus time, as five potential cycles of E (green), q_V (red) and ε (blue). (c) Averaged strain ε versus accumulated volume specific charge q_V. The respective linear fit yields $A^*_{n-type} = -0.0049 \pm 0.0002\,mm^3\,C^{-1}$.

the relation between strain and charge is not as linear as for p-type porous silicon. The relation for n-type porous silicon is depicted in Figure 4.16(c). Furthermore, the fit for the resulting strain-charge coupling parameter $A^*_{\mathrm{n-type}} = -0.005 \pm 0.002\,\mathrm{mm^3\,C^{-1}}$ only has a coefficient of determination $\mathrm{R}^2 = 0.75$, which reflects the poor linear fit. $A^*_{\mathrm{n-type}}$ is about 38 % smaller than for p-type porous silicon.
Next, n-type bulk silicon is investigated in the in situ laser cantilever bending setup. It is equally undergoing an anodic oxidation procedure, by applying a potential of 2.0 V for 15 h. After the anodic oxidation procedure, a CV measurement is conducted from 0.0 V to 4.0 V with a scan rate of $500\,\mathrm{mV\,s^{-1}}$, as the CV measurement is capacitive in this potential region, see Figure A.8 in the appendix. A noticeable change in surface stress Δf can be observed in response to the applied potential E and is shown in Figure 4.17(a). In particular, the surface stress changes linearly with E and also with accumulated surface charge q_{A}. Most importantly, the surface stress change is in phase with the two. This also becomes apparent in a plot of surface stress versus accumulated charge, as depicted in Figure 4.17(b). The electrocapillary coupling parameter is determined as $\varsigma_{\mathrm{n-type}} = +0.500 \pm 0.001\,\mathrm{V}$ and is thus about 2/3 of the value for p-type bulk silicon. The dependence of Δf on E and q_{A} has a positive sign. Therefore, it can be ascertained that the proportionality of p-type and n-type bulk silicon is the same and an opposite proportionality, as predicted in literature [82] cannot be confirmed here. However, it has to be mentioned that the cited work simulates pure silicon surfaces, in contrast to the oxidised surfaces investigated here. Overall, neither the dilatometry study on porous silicon nor the in situ cantilever bending experiment on bulk silicon reveal a mechanistic difference of electrochemo-mechanical coupling in n-type compared to p-type silicon.

4.3.6. Analysis of Electrosorption-Induced Actuation

The measurements conducted here, demonstrate that an actuation effect through the accumulation of charge carriers on the surface, thus an electrosorption-induced actuation, can actually be observed on porous silicon and bulk silicon. Next, the analysis of the results will focus on the mechanistic comparison of planar, bulk silicon with the morphologically more complicated porous silicon material. Therefore, a modelling approach is adduced as a means of evaluation the dependence of a microscopical length change $\delta l/l$ on surface stress Δf. The study of the model assumes various pore geometries. A model assuming granular array of solid spheres is used to approximate the isotropic porous media nanoporous gold. For this specific material, the model is able to achieve a good agreement with a conducted numerical simulation.[271] Another pore model assumes an idealised porous material morphology that possesses straight, cylindrical pores with a smooth pore wall.[271] These pores are hexagonally arranged and parallelly oriented and the pores stretch orthogonally to the sample surface from top to bottom.[271] Thus, the model appropriately replicates the basic properties of porous silicon as a first order approximation and is therefore utilised here. Accordingly, the change in length $\delta l/l$ is described by [271]

$$\delta l/l = \delta\varepsilon = -\frac{\alpha f}{3K}\frac{(1-\nu)}{(1-2\nu)}, \tag{4.3}$$

where α denotes the fraction of solid volume and is therefore related to the porosity by $\alpha = 1 - \Phi$. $K = 97.8\,\mathrm{GPa}$ and $\nu = \nu_{110} = 0.064$, as stated in section 2.1, are bulk

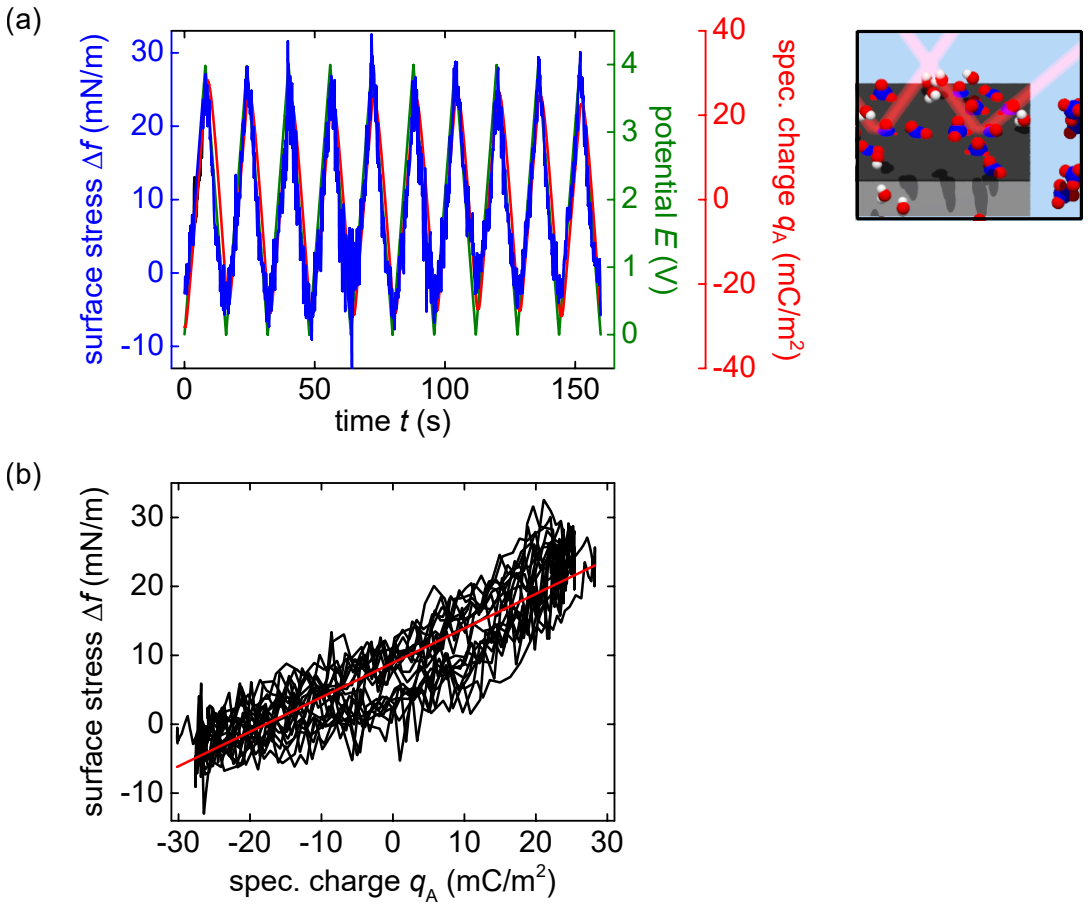

Figure 4.17.: **Electrosorption-induced actuation on n-type planar, bulk silicon.** (a) Change in surface stress Δf (blue) during a CV measurement, performed with a scan rate of $500\,\mathrm{mV\,s^{-1}}$ with potential E (green) cycled in the range of 0.0 V to 4.0 V in $HClO_4$ with surface area specific capacitance q_A (red). (b) Change in surface stress Δf versus specific charge q_A. Determination of the electrocapillary coupling coefficient ς by linear regression, which yields a value of $\varsigma_{n-type} = +0.500 \pm 0.001\,\mathrm{V}$.

modulus of silicon and Poisson's ratio in the [110] direction, respectively. $\delta l/l$ is identified with the here used quantity ε for strain, see equation 2.65. An expression for an effective strain-charge coupling coefficient A^*, see equation 2.66, can thus be introduced as

$$A^* = \frac{\mathrm{d}\varepsilon}{\mathrm{d}q_\mathrm{V}} = -\frac{\alpha}{3K}\frac{(1-\nu)}{(1-2\nu)}\frac{\mathrm{d}f}{\mathrm{d}q_\mathrm{V}} = -\frac{\alpha}{3K}\frac{(1-\nu)}{(1-2\nu)}\varsigma. \tag{4.4}$$

With the value of $\varsigma = +0.657\,\mathrm{V}$ determined for bulk silicon in the respective actuation measurement, see Figure 4.13, the strain-charge coupling parameter equates $A^*_{\mathrm{Si,CB}} = -0.0015 \pm 0.0002\,\mathrm{mm^3\,C^{-1}}$.

Next, a strain-charge coupling coefficient is determined for porous silicon. Essentially, the stress related characteristic parameters gained from the in situ cantilever study are converted to strain related quantities and, thus, allow a comparison between bulk silicon and porous silicon results. If the porous silicon layer is assumed to be in a state of plane stress, the characteristic film stress charge coupling coefficient ξ is transformed into a strain coupling parameter by

$$A^* = \frac{\varepsilon_{||}}{q_\mathrm{V}} = \frac{1}{Y_{||}}\xi. \tag{4.5}$$

Here, $\xi = -296 \pm 1\,\mathrm{mV}$ is used, which is determined in the measurement with a $HClO_4$ electrolyte, see Figure 4.10. $\varepsilon_{||}$ and $Y_{||}$ denote the strain as well as the Young's modulus in the plane of the porous silicon film. This analysis of the strain-charge coupling parameter according to the equation requires a comprehensive knowledge about the mechanical properties, in particular the in-plane Young's modulus. For its determination an independent measurement method has to be deployed.

Porous silicon represents a challenging material for the assessment of its mechanical properties due to the anisotropic crystal structure, see section 2.1, and intricate sample geometry, i.e. thin porous silicon layers. This sample geometry renders techniques, such as tensile test measurements or compression tests in a universal testing machine, hard to conduct. Indentation, another example of a classical method, has been utilised to investigate the elastic properties of porous silicon, under the assumption of mechanically isotropy of the material, though.[272] Such an assumption represents a gross underestimation of the material's complexity, neglecting the impact of the porous silicon pores, in particular their orientation, collective morphology and crystalline matrix.[273] Apart from indentation, other frequently used methods are in the realm of ultrasound techniques, either pulse-echo or through-transmission in the MHz range or acoustic microscopy in the GHz range, another example being laser ultrasonics.[274–276] However, these only yield a comprehensive characterisation of the material if bulk sound waves are probed in different crystallographic directions of the material. Evidently, this requirement poses an obstacle for the prevalent thin-film sample geometry of porous silicon. Moreover, usually a transducer is attached to the material under investigation. The coupling between material and transducer is ensured by a liquid coupling medium. As the pore diameter is small, high capillary pressures are present in the pores when in contact with a liquid. Liquids readily imbibe into the pores and, thus, would alter the measured mechanical properties of the hybrid system of porous material and fluid. Inelastic neutron scattering, on the other hand, probes the porous material on the atomic level and yields a measure of stiffness of the pore wall matrix.[273] However, it does not supply information about the effective properties of the whole porous material. Another approach to gain information

about porous silicon's mechanical properties is to study adsorption-induced deformation of the porous silicon matrix.[64] In the cited reference the Gibson-Ashby approximation of the porous structure as a honeycomb is used.[277] This assumption leads to an effective Young's modulus of the material which is extremely sensitive on the average thickness and lengths of the pore walls. Therefore, slight deviations in the determination of the pore structure's measures lead to large divergences of the Young's modulus.[112] Furthermore, this approach assumes that the pore walls are all equally load bearing, which is not valid as will be discussed in section 5.4.3.
In this thesis, it has been possible to establish a technique of laser-excited elastic guided wave characterisation within the scope of a master thesis supervised by the author.[278] Elastic guided waves, first described by Horace Lamb, can be observed in thin samples shaped like plates, with a thickness in the range of the bulk wavelength.[279] A comprehensive analysis of these elastic guided waves enables the determination of porous silicon mechanics owing to their dispersive character and multimodal nature. This pertains in particular also to in-plane mechanical properties. Overall, a laser excited elastic guided waves study reveals that the porous silicon layer has a crystal symmetry that differs a lot from bulk silicon. The pore-induced anisotropy predominates the intrinsic bulk silicon crystallinity. Hence, the porous silicon crystal symmetry is approximated as in-plane, transverse isotropic. Thereby, the cubic symmetry within the pore walls is effectively broken by the actual pores themselves.[177] All in all, the in plane Young's modulus, see equation 4.5, for the in plane, transverse isotropy obeys [280]

$$\frac{1}{Y_{||}} = \frac{c_{33}}{-2{c_{13}}^2 + c_{33} \cdot (c_{11} + c_{12})} \approx \frac{1}{26.1\,\mathrm{GPa}}, \tag{4.6}$$

where c_i are the respective elastic coefficients, which are $c_{11} = 22\,\mathrm{GPa}$, $c_{13} = 8\,\mathrm{GPa}$ and $c_{33} = 33.2\,\mathrm{GPa}$.[177] The elastic coefficient c_{12} is difficult to determine and can here only be approximated by a stability criterium, as $c_{12} \leq c_{13}$. Therefore, the value determined for $1/Y_{||}$, see equation 4.6, represents solely a lower limit. Even so, the in plane Young's modulus $Y_{||}$ is significantly smaller than the bulk silicon's Young's moduli in the three crystallographic directions, cf. section 2.1. Equation 4.5 yields a value for the strain-charge coupling coefficient $A^*_\mathrm{pSi,CB} = -0.011 \pm 0.004\,\mathrm{mm^3\,C^{-1}}$. The strain-charge coefficient would translate to a strain amplitude of a free standing porous silicon sample of $\varepsilon_\mathrm{avg,pSi,CB} = A^*_\mathrm{pSi,CB} \cdot q_{\mathrm{V_{avg}}} = ((1.69 \pm 0.04) \cdot 10^{-3})\,\%$ or approximately 50.5 µm for the used sample of length l. It is important to mention that larger strain amplitudes can be achieved by increasing the ratio h_l/h of the porous silicon layer thickness with respect to the adjacent bulk silicon or even removing the bulk-silicon support entirely. However, as stated in the methods section 3.5.2, h_l/h is supposed to be below a factor of $2 \cdot 10^{-3}$ to ensure a correct stress analysis, which is the aim of this study.
Overall, the two values for the strain-charge coupling coefficient A^* derived from the measurement of bulk silicon $A^*_\mathrm{Si,CB}$ and porous silicon $A^*_\mathrm{pSi,CB}$ in a laser cantilever bending setup, are approximately as large as the value determined in the dilatometer study on the double epi-layer porous silicon material. Thus, surprisingly, the clamping of the bulk silicon layer in the middle of the two porous silicon layers seems to have a negligible effect on the actuation – at least if the clamping bulk silicon layer is thinner than the adjacent porous silicon layers.
A noticeable difference of about one order of magnitude between the two values $A^*_\mathrm{Si,CB}$ and $A^*_\mathrm{pSi,CB}$ is present, though. The value determined for porous silicon is larger than the bulk

silicon value in absolute terms. One reason for this deviation is certainly that the model assumptions underlying the bulk silicon analysis, see equation 4.4, deviate a lot from the actual porous silicon, investigated here. Firstly, the assumption of a hexagonal arrangement of the pores does not hold true to the actual porous material. Instead of cylindrical pores with smooth pore walls, the real pore meanders and distinct side-pores frequently branch off, observed above in the SEM micrographs and the nitrogen sorption isotherm measurements. These side-pores may be regarded as an utmost increased roughness of the pore wall. For metals with large Poisson's ratios, i.e. gold or copper, such a surface roughness impairs the electrochemo-mechanical coupling of electrosorption-induced mechanical actuation. Astonishingly, by contrast, for silicon the opposite holds true. Thus, an increased surface roughness even causes an enhanced coupling and could explain the difference between the two values for A^*.[281]
Nanoporous gold represents a well investigated material with regard to electrosorption-induced actuation.[72] A strain-charge coupling coefficient of $A^*_{\mathrm{npg}} = +0.0475 \pm 0.0010$ $\mathrm{mm^3\,C^{-1}}$ has been determined.[182] Notably, the sign of A^*_{npg} is positive. Thus, in contrast to electrochemo-mechanical coupling in porous silicon, an accumulation of charge carriers on the nanoporous gold surface leads to an expansion and vice versa. The strain-charge coupling coefficient determined here for porous silicon is in the same order of magnitude as A^*_{npg}, albeit A^*_{npg} exceeding it by a factor of approximately four. Yet, nanoporous gold has a much higher porosity, in the referenced study it amounts to $\Phi = 0.74\,\%$. Moreover, the porous morphology of nanoporous gold is entirely different. Nanoporous gold has a uniform network of ligaments that isotropically branch out through the entirety of the material, whereas pores in porous silicon are highly anisotropic, as discussed in section 2.4. Nanoporous gold is also a distinctly different material with respect to its electrical conductivity. Its base material gold is an excellent conductor. Thus, electrons on the solid side of the electrolyte interface, which counter the ionic charges, are only distributed over a few Å beneath the interface.[10] By contrast, silicon is a semiconducting material. Therefore, electrons assemble over the width of an emerging space charge region in an oxidised pSi pore wall in contact with an electrolyte, as discussed in sections 2.2.3 and 4.1. Equation 2.21 gives the width w of the SCR as

$$w = \sqrt{-\frac{2\varepsilon_{\mathrm{r}}\varepsilon_0}{eN_{\mathrm{a}}}(V_{\mathrm{m}} - V_{\mathrm{fb}} - \frac{k_{\mathrm{B}}T}{e})}. \tag{4.7}$$

With the knowledge of the flatband potential V_{fb} and the doping concentration N_{a} from the EIS analysis, see section 4.1, the width of the SCR at the lower and upper vertex potential is calculated. That means, the applied potential V_{m} in the equation is set to 0 V and 0.9 V. The width amounts to $8.9 \pm 0.2\,\mathrm{nm}$ and $6.5 \pm 0.2\,\mathrm{nm}$, respectively. The charge carriers would therefore spread over a wider layer in silicon as compared to gold. The difference is about an order of magnitude. The charge carriers, which essentially cause the surface stress through their assembly in the SCR, are not as concentrated, as in a metal. Hence, the actuation in response to an accumulation of an equal amount of charge would presumably be smaller, which is consistent with the measurement results obtained here.

5. Electrochemical Actuation of Polypyrrole-Porous-Silicon Hybrids

In this section the electrochemical properties and the actuation of the second material type will be investigated – polypyrrole-filled porous silicon. First of all the synthesis of the hybrid material and the resulting electrochemical properties will be examined. Afterwards, the investigation of the electrochemical actuation with two different methods will be discussed. The first method is an in situ dilatometry study which yields macroscopic characteristics, whereas an in situ X-ray diffraction study is used to study the electrochemical actuation of the hybrid material on a microscopical level.

5.1. Synthesis

The synthesis of the porous silicon and polypyrrole hybrid material is conducted by electrochemical polymerisation of pyrrole monomers inside the pore space of the porous silicon. The details of the procedure are given in the methods section 3.4. In short, a porous silicon sample is mounted in a polymerisation cell and the polymerisation solution is filled into the cell. The synthesis is conducted by galvanostatic electrochemical polymerisation. That means, a constant current is applied between the porous silicon and a counter electrode while the potential evolution is measured by an Ag/AgCl reference electrode. An exemplary potential evolution is shown in Figure 5.1(a) for a 25.4 µm thick porous silicon epi-layer. The characteristic regimes, introduced in the methods section, are clearly visible for the sample here. As the current is initially switched on, the potential instantly increases from its OCP to a value of about 0.7 V. The following, first stage is characterised by a slow increase to approximately 0.85 V within one hour. This stage marks the oxidation of the pSi pore walls and the onset of polymerisation by the nucleation of polypyrrole chains at the bottom of the pores.[227] Next, the constant potential plateau for about one hour signals the continued polymerisation of polypyrrole inside the pores from bottom to top. The following onset of the potential increase is assigned to a transition stage. The pores fill gradually and as the polymer increasingly polymerises on the outer surface, the potential transitions to a higher value until a second plateau is reached. The time of pore filling t_p and the subsequent start of the transition regime is determined via two linear fits of the potential plateau and the transition stage. These fits are shown in Figure 5.1(a) and yield a value of $t_\mathrm{p} = 2.13\,\mathrm{h}$.
For the material investigated in the following the electrochemical polymerisation is stopped before the second potential plateau is reached, as a polymer film on top would be detrimental to the hybrids actuation characteristics. Such a potential course with a timely interruption of the polymerisation process in a porous silicon epi-layer with an equal thickness of 25.4 µm is exemplarily shown in the appendix in Figure A.9. In the case of this specific synthesis the change in weight through the polymerisation is $\Delta m_\mathrm{PPy} = 9.9\,\mathrm{mg}$. As described in the methods section, the gain in mass is monitored by gravimetric meas-

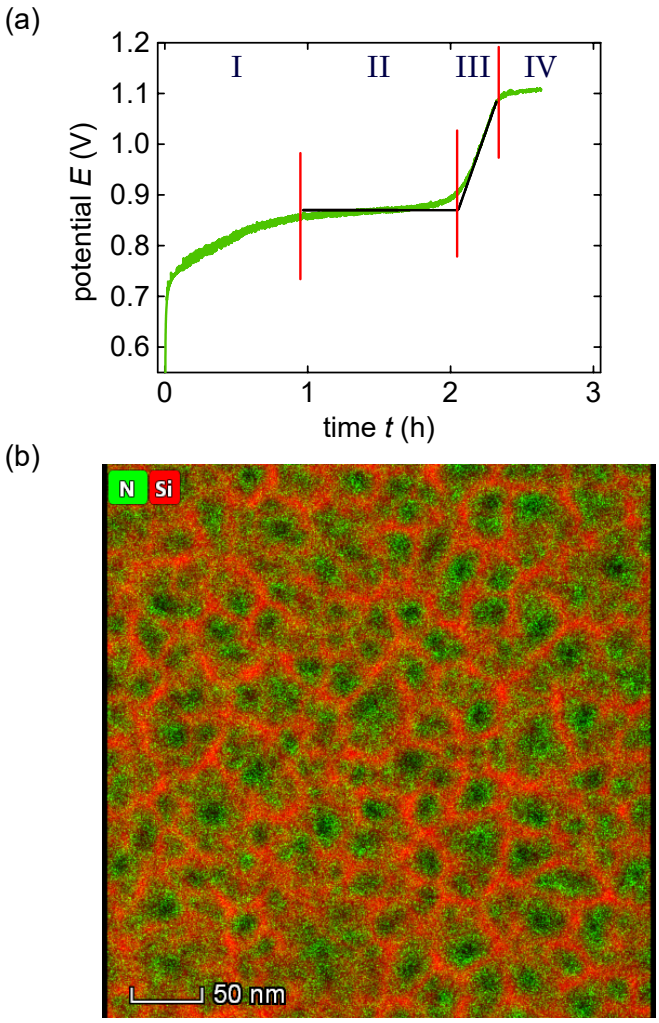

Figure 5.1.: **Electrochemical polymerisation of polypyrrole in porous silicon.** (a) Time evolution of potential E during the electrochemical polymerisation of pyrrole in a porous silicon epi-layer with a thickness of 25.4 µm. The characteristic regimes of polymer nucleation (I), pore filling (II), transition (III) and the eventual polymerisation on the outer surface (IV) are indicated and discussed in the main text. The graphic also depicts the fits to determine the filling of the pores. (b) Transmission electron micrograph in top view of a porous silicon and polypyrrole hybrid membrane. An EDX measurement is overlaid over the micrograph. Colour green indicates polypyrrole by the nitrogen signal and red marks the silicon pore walls.

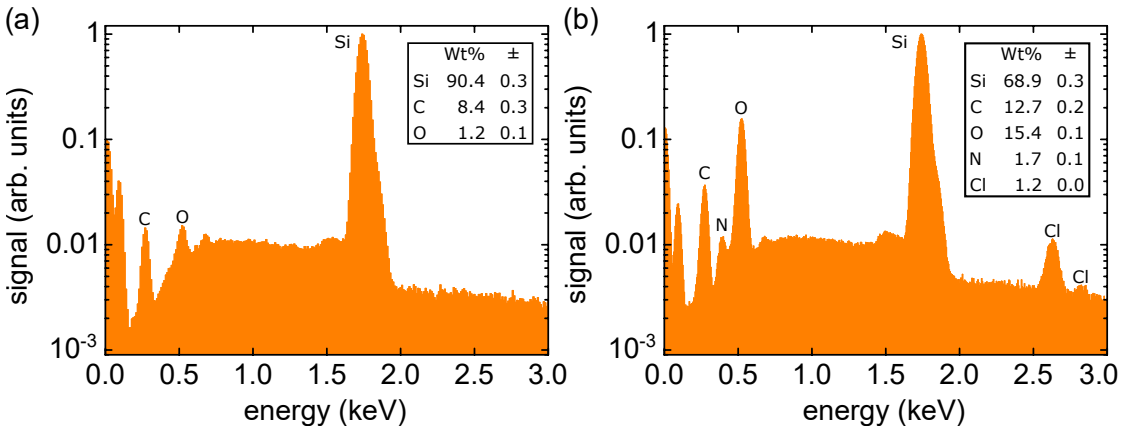

Figure 5.2.: **Energy dispersive X-ray measurement of a polypyrrole porous silicon hybrid.** EDX measurement recorded in an SEM for (a) an as-prepared and (b) a polypyrrole-porous-silicon hybrid. The peaks of silicon (Si), carbon (C) and oxygen (O) are marked and, visible only in (b), nitrogen (N) and chlorine (Cl). The legend states the weight percentage (Wt%) of the respective elements.

urements before and after the polymerisation process. Although the silicon pore walls are oxidised to some extend, the change in mass is here ascribed to the synthesised polymer inside the pores for a qualitative assertion. The lateral size of the porous silicon layer equals the size of the electrochemical polymerisation cell, i.e. 7.84 cm^2. Hence, knowing the thickness of the porous silicon epi-layer yields its outer volume. A value of $\Phi = 45.7\,\%$ is determined for its porosity in a nitrogen sorption isotherm, see appendix Figure A.10. Thus, Δm_{PPy} is normalised to the pore volume, which yields a density of $\rho_{\mathrm{PPy}} = 1.09\,\mathrm{g\,cm^{-3}}$. A bulk polypyrrole film synthesised under comparable conditions has a density of $1.5\,\mathrm{g\,cm^{-3}}$.[282] Thus, the degree of filling amounts to approximately 73 %. It should be noted that the here determined filling degree would rather indicate a reasonable lower boundary, as it has been reported in literature that the polymer density in confinement of porous silicon is reduced.[227]

A transmission electron micrograph is depicted in Figure 5.1(b) and shows the synthesised polypyrrole-porous-silicon hybrid material. The picture shows a thinned slice, extracted from the middle of the material, in top view. An EDX measurement is overlaid over the TEM picture. The element specific EDX signal of silicon and the nitrogen atom of the pyrrole monomer unit are indicated by the colour code. The silicon pores, visible by the red signal, are equal to the porous silicon structure already seen in Figure 4.1(a). The polymer is located in the pore space, as the EDX signal of the polymer fills the space between the silicon pore walls. Note, however that in some pores a reduction of signal intensity towards the middle of the pore is visible, in particular for larger pores. So the polymer density seems to be higher at the pore walls. This observation might be the origin of the overall reduced polymer density inside porous silicon.

An EDX measurement conducted on the whole profile of the polypyrrole-filled epi-layer is depicted in Figure 5.2. Whereas (a) shows the spectrum of as-prepared pSi, (b) depicts the results of polypyrrole-filled porous silicon. The nitrogen signal indicates the presence of polypyrrole in the porous silicon. Moreover, an increase of carbon with respect to

the as-prepared state is noticeable, which can also be ascribed to the polymer. A chlorine signal is present as well due to the perchlorate anions that are incorporated into the polypyrrole. The EDX measurement also yields roughly a doubling of oxygen compared to the as-prepared porous silicon. One contributing factor might be the oxygen atoms in the perchlorate anions. Furthermore, the pSi pore walls are oxidised before the procedure, while being in contact with the ambient atmosphere, as well as in the initial stage of the polymerisation process.[227] However, the anodic oxidation is not to such an extend as for the deliberately oxidised porous silicon. For the latter the amount of oxygen marked by the weight percentage is roughly twice as high, see Figure 4.4(b).
Figure A.11(a) in the appendix shows another synthesis of polypyrrole inside an equal porous silicon epi-layer, but for this synthesis the current is stopped at roughly 1.2 h, which translates to roughly half of pore filling time t_p of a completed polymerisation. The potential course shows that the initial nucleation stage is as long as for the full process. An EDX measurement, see Figure A.11(b), on this halted synthesis sample yields a weight percentage of nitrogen which is about one third as for the completed synthesis. The weight percentage of oxygen, however, is approximately as high as for the completed synthesis. Thus, the initial stage oxidises the silicon pore walls to the same degree. The polymerisation of porous silicon sets in after this initial stage. Thus, half of the filling time does not result in a half-filled PPy-pSi sample. Overall, the EDX measurements corroborate that polypyrrole is successfully synthesised in porous silicon.
The polypyrrole-porous-silicon hybrid material discussed until this point is synthesised by applying a constant current of 2 mA, i.e. a current density of $0.255\,\mathrm{mA\,cm^{-2}}$. Figure 5.3(a) depicts potential courses of the polypyrrole synthesis with different current magnitudes in identical pSi epi-layers. Firstly, it is apparent that increasing currents of 4 mA and 6 mA lead to an onset of the transition stage in a non-linear manner. The non-linear dependence of pore filling time t_p on current J is also depicted in Figure 5.3(b). The initial stage however, does not eminently shorten with an increasing current. Overall, this behaviour is in agreement with literature.[283] Figure 5.3(c) shows the resulting, gravimetrically determined mass of polypyrrole m_{PPy} inside the pores. It is visible that an applied current of 2 mA has the largest polypyrrole yield. Thus, it is the current magnitude chosen for the synthesis in this work. A larger or smaller current magnitude appears to fill the pores too quick or too slow, respectively, and does not produce a dense polymer.
The successful polymerisation of polypyrrole in a 25.4 µm porous silicon epi-layer has been demonstrated and investigated for different synthesis aspects, such as the polymerisation current. Within the framework of this work, several epi-layers have been filled by polypyrrole. Figure 5.4 depicts the pore filling times t_p of porous silicon epi-layers with thicknesses of up to 105 µm. Thus, the aspect ratio of the pSi pore radius and pore depth exceeds 1 : 16000. Highlighting this, the electrochemical polymerisation of polypyrrole in such high aspect ratio pores has not been demonstrated in literature.[113, 206, 283–289] Figure 5.4 also shows that the dependence of t_p on pore depth d is linear. A linear fit to the data yields a polymerisation rate per pore depth of $266\,\mathrm{s\,\mu m^{-1}}$. The linear dependence confirms that the electrochemical polymerisation process of polypyrrole in porous silicon is not limited by the diffusion of pyrrole monomers inside the pores.[290] That means, the rate limiting mechanism, even at such high aspect ratios, would be the oxidation of pyrrole monomers.

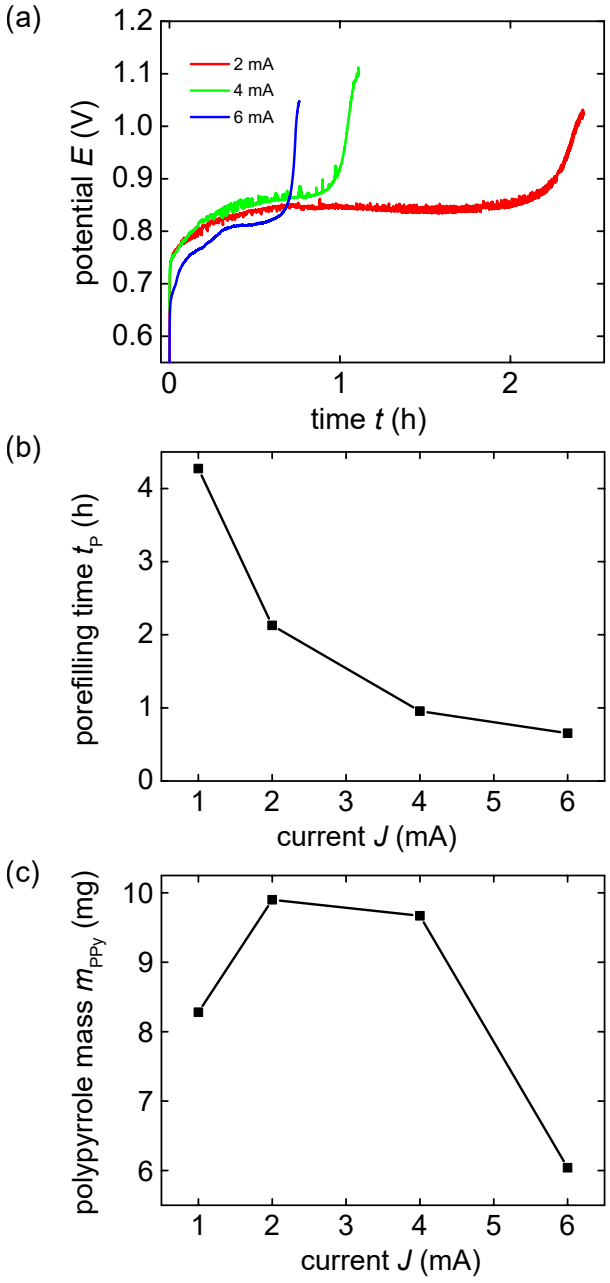

Figure 5.3.: **Electrochemical polymerisation of polypyrrole in porous silicon with different current magnitudes.** (a) Time Evolution of potential E during the electrochemical polymerisation in 25.4 µm thick porous silicon with different current magnitudes of 2 mA, 4 mA and 6 mA. (b) Pore filling time t_p in dependence of current magnitude J. (c) Mass m_PPy of polypyrrole synthesised in the pSi pore space in dependence of current magnitude J.

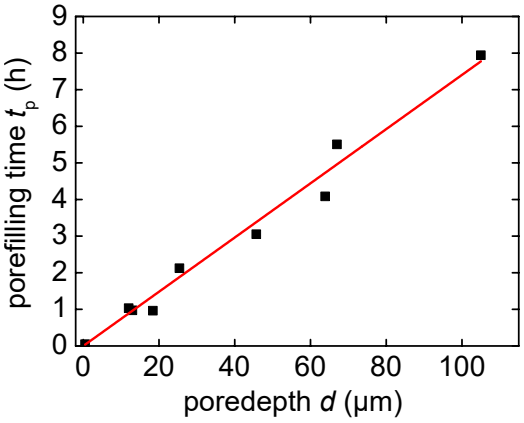

Figure 5.4.: **Pore-depth-dependent synthesis of polypyrrole in porous silicon.** Pore filling time t_p for different depths of porous silicon epi-layer pores up to 105 µm.

5.2. Electrochemical Characterisation

As the successful synthesis of polypyrrole inside porous silicon has been ascertained, the electrochemical properties of the hybrid material are investigated. Firstly, a potential range feasible for the capacitive charging of the hybrid material has to be determined. Therefore, a CV measurement in the potential range of 0.2 V to 1.4 V with a scan rate of 5 mV s^{-1} for a total of 15 cycles is conducted in 1 mol L^{-1} perchloric acid for a polypyrrole porous silicon hybrid epi-layer with a thickness of 25.4 µm. Figure 5.5(a) shows the resulting course of current J. First of all, the current pronouncedly increases non-linearly towards the upper vertex potential of 1.4 V in the first scan. However, it is clearly visible that a capacitive area is encompassed by the course of J on the down-sweep, in particular in the lower potential range up to approximately 0.8 V. In total, the course is similar to the CV measurements conducted for the as-prepared porous silicon without the polymer filling, cf. Figure 4.2(a). The polypyrrole is over-oxidised, which leads to the drastic increase of the current towards the upper vertex potential.[291] The peak current at the upper vertex even increases from cycle one to three apparently caused by a rapid progression of the over-oxidation from the first cycle. However, on the down-sweep of the third cycle after the current peak the current is noticeably smaller in absolute terms as compared to the first cycle. Thus, the polypyrrole's capacitance is reduced. The further cycles corroborate this effect. The peak current decreases as well as the constant current level in the lower potential region from cycle to cycle. On the 15th and last cycle, the current of up- and down-sweep in the lower potential region virtually lies on zero. These high potentials lead to an over-oxidation of the polypyrrole.[291] The over-oxidation destroys the polymer so that its capacitance gradually declines. These high potentials are to be avoided. Interestingly, an equal experiment on a bulk polypyrrole film leads to a much quicker destruction of the polymer. The respective CV measurement is depicted in the appendix in Figure A.12. For a bulk polypyrrole film the over-oxidation commences on the first cycle at 1.05 V when the current abruptly decreases due to the beginning destruction of the polypyrrole film. Thus, the over-oxidation of polypyrrole inside porous silicon is distinctly slower, i.e. higher potentials and more cycles are required for over-oxidation to

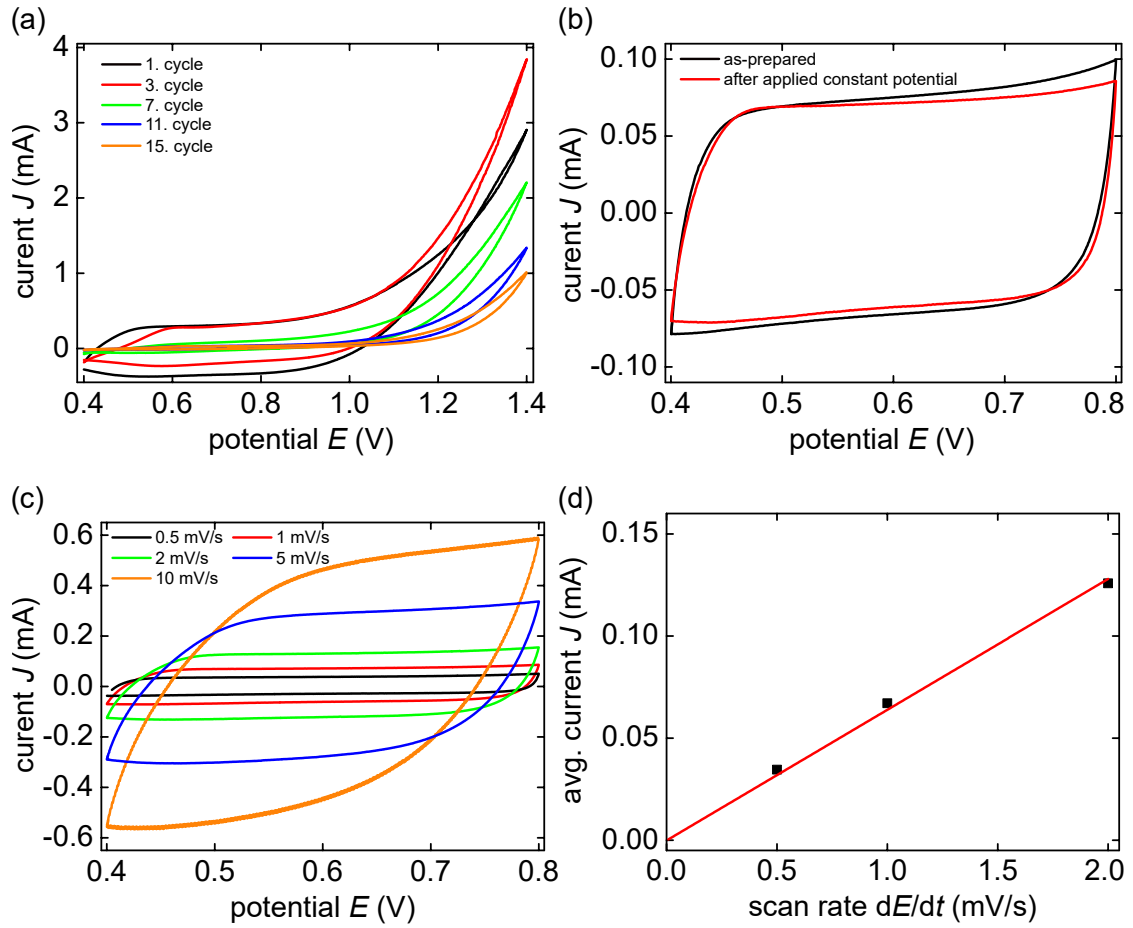

Figure 5.5.: **Electrochemical characterisation of polypyrrole porous silicon hybrids.** Electrochemical characterisation of a polypyrrole-filled porous silicon epi-layer with a thickness of 25.4 µm in 1 mol L^{-1} perchloric acid. (a) Cyclic voltammetry measurement in the potential range of 0.4 V to 1.4 V with a scan rate of 5 mV s^{-1} for a total of 15 cycles. (b) CV measurement with a reduced upper vertex potential of 0.8 V and a scan rate of 1 mV s^{-1} for as-prepared PPy-pSi (black) in comparison with the same sample after an applied constant potential step of 0.8 V for 6 h (red). (c) CVs in the potential range of 0.4 V to 0.8 V with scan rates of $0.5 - 10$ mV s^{-1}. (d) Averaged values for current J from the CV measurements depicted in (c), in the range of 0.55 V to 0.65 V. Plotted versus increasing scan rate dE/dt. The red line indicates a linear fit and yields a capacitance of $c_{\mathrm{pSi,PPy}} = 64 \pm 1$ mF.

occur. A diffusion limitation of anions inside the pores, which will be further discussed below, might lead to the observed behaviour.
To avoid over-oxidation, the upper vertex potential is reduced to 0.8 V. The respective measurement with a scan rate of $1\,\mathrm{mV\,s^{-1}}$ exhibits a virtually ideal capacitive behaviour, see Figure 4.2(b). A minor increase towards the upper vertex potential is still visible. As over-oxidation should not occur in this potential region, the increase might be ascribed to un-polymerised pyrrole monomer units. A constant potential of 0.8 V is applied for 6 h to assure that the polymerisation is brought to a close. The CV measurement is repeated and the direct comparison between the two shows that the increase towards the upper vertex has been reduced, while the constant current levels are essentially equal. Thus, with the help of the applied constant potential, the chosen potential region is suitable for electrochemical actuation measurements and a further electrochemical characterisation.
As described in the methods section (see section 3.1) the potentiostat has two different modes to conduct CV measurements, i.e. step-wise and linear. Figure A.13 in the appendix depicts two CVs conducted with the step-wise and the linear method with the same parameters, i.e. a scan rate of $10\,\mathrm{mV\,s^{-1}}$ in the potential region of 0.4 V to 0.8 V. The measurements do not show a significant difference between the two methods. Thus, in this work CVs are conducted with the step-wise method, as a lower minimum scan rate is required than the linear method provides.
Figure 5.5(c) shows CV measurements conducted with scan rates of $0.5\,\mathrm{mV\,s^{-1}}$ to $10\,\mathrm{mV\,s^{-1}}$ on the same 25.4 µm thick PPy-pSi sample. In particular, the CV measurements with scan rates up to $1\,\mathrm{mV\,s^{-1}}$ exhibit an unaltered capacitive behaviour. At $2\,\mathrm{mV\,s^{-1}}$ the course of current J starts to have an extended period until a constant current level is reached on the up-sweep. At higher scan rates this becomes even more pronounced. For $10\,\mathrm{mV\,s^{-1}}$ the current level after the initial stage commences to show a linear increase. These characteristics are typical for a diffusion limitation of ionic charge transport, in this case in the polymer within the pSi pores.[214, 249] Therefore, the capacitance is determined with the established procedure but only up to a scan rate of $1\,\mathrm{mV\,s^{-1}}$. The currents are averaged in the potential range of 0.55 V to 0.65 V and are plotted versus the scan rate in Figure 5.5(d). The linear fit of the data yields a capacitance of $c_{\mathrm{pSi,PPy}} = 64 \pm 1\,\mathrm{mF}$. The lateral size of the sample is $0.576\,\mathrm{cm^2}$. With the thickness of 25.4 µm, a capacitance per outer volume of the porous silicon layer of $43\,745\,\mathrm{mF\,cm^{-3}}$ is obtained. In comparison to porous silicon without the polypyrrole filling, the capacitance is about 30 times larger. Thus, the electric double layer as a surface capacitance is smaller normalised to the sample volume than the volumetric capacitance of the polymer inside the pores.
The method introduced here to electrochemically determine the capacitance, see section 3.1 and equation 3.2, can also be applied to bulk polypyrrole films. For a polypyrrole film, synthesised under equal conditions and investigated with the same anion, a volume specific capacitance of $0.24\,\mathrm{F\,mm^{-3}}$ is found.[213] This value would suggest a polypyrrole volume of $c_{\mathrm{pSi,PPy}}/0.24\,\mathrm{F\,mm^{-3}} = 0.267\,\mathrm{mm^3}$. With respect to the pSi pore space, i.e. the outer volume of the sample times its porosity $0.576\,\mathrm{cm^2} \cdot 25.4\,\mu\mathrm{m} \cdot 45.7\,\%$, the polypyrrole exhibits a filling degree of 40 %. This value is comparatively smaller to 73 %, which is the filling degree based on the polypyrrole mass, see section 5.1. Thus, it seems that the geometrical confinement through the pSi pores leads to a comparatively dense polypyrrole in comparison with a polymer film, but it alters the electrochemical capacitance. One might speculate that the structure of porous-silicon-confined polypyrrole impedes the incorporation of anions into the polymer chains.

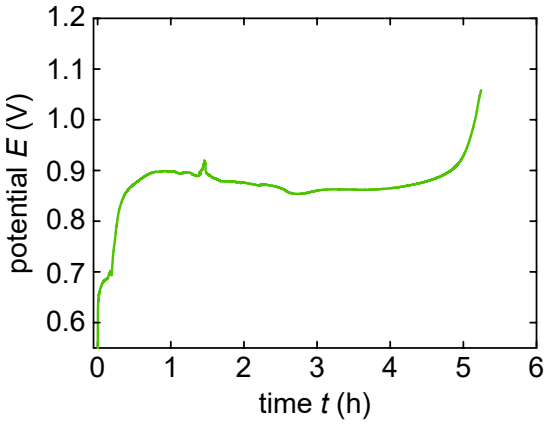

Figure 5.6.: **Electrochemical polymerisation of polypyrrole in a porous silicon membrane.** Time evolution of potential E during the electrochemical polymerisation of pyrrole with a current density of $0.4\,\mathrm{mA\,cm^{-2}}$ in a porous silicon membrane with a thickness of 85 µm.

5.3. Polypyrrole-Porous-Silicon Membranes

Up to this point, the electrochemical polymerisation of polypyrrole is demonstrated for epi-layers. However, for electrochemical actuation measurements of the PPy-pSi hybrid material in the in situ dilatometry setup, a polypyrrole-filled membrane would be beneficial, as an epi-layer is still clamped by the adjacent bulk silicon layer. Figure 5.6 depicts the successful electrochemical polymerisation of polypyrrole in an 85 µm thick membrane with a lateral size of $1.008\,\mathrm{cm^2}$. The course of potential E shows the typical characteristics, already established for the synthesis in an epi-layer. The initial increasing-potential stage of polypyrrole nucleation lasts for approximately one hour and thus equally long as for the epi-layer synthesis. The subsequent potential plateau lasts for about four hours until the pores are filled and the transition stage begins. The course of potential E in the plateau stage has slightly more deflections than seen for synthesis in an epi-layer, cf. Figure 5.1(a). These can possibly be ascribed to a slightly worse contact through the sputtered gold layer at the bottom of the membrane. The plateau potential has a value around 0.9 V, which fits to the synthesis in an epi-layer. The pore filling time is determined to be $t_\mathrm{p} = 4.9\,\mathrm{h}$. Thus, the polymerisation is approximately 1.5 h faster than in an epi-layer of equal thickness, which would last 6.3 h according to the linear fit performed in Figure 5.4. The reason for the faster polymerisation rate is that a slightly higher current density is applied – $0.4\,\mathrm{mA\,cm^{-2}}$ instead of $0.255\,\mathrm{mA\,cm^{-2}}$. In an equally thick membrane with the lower current density the filling time t_p equals 6.9 h, which is more in the range of the polymerisation rate predicted for an epi-layer.
The charge Q that is consumed in the electrochemical polymerisation is measured by the potentiostat during the process. Information about the weight of the synthesised polypyrrole can be inferred by relating Q to the theoretically achievable polymer

$$m_{\mathrm{PPy,theor.}} = \frac{Q \cdot M_{\mathrm{PPy}}}{z \cdot \mathrm{F}}, \tag{5.1}$$

where M_{PPy} denotes the formula weight of synthesised polypyrrole. It is obtained from the molar mass of a monomer unit but also considers incorporated $\mathrm{ClO_4^-}$-anions. It equals

$96.78\,\mathrm{g\,mol^{-1}}$.[283] F is the Faraday constant and z gives the number of electrons used in the polymerisation process of two monomers. In literature z is estimated to be 2.25.[204] For the polymerisation process investigated here, i.e. presented in Figure 5.6, the consumed charge amounts to $Q = 7.605\,\mathrm{C}$. Thus, the theoretical weight is 3.39 mg and therefore coincides well with the gravimetrically determined weight difference of 3.45 mg. The density of the polymer inside the pSi pore space is $0.81\,\mathrm{g\,cm^{-3}}$. The density is lower compared to the density of polypyrrole inside the epi-layer $1.09\,\mathrm{g\,cm^{-3}}$, see section 5.1.
Figure 5.7 depicts the electrochemical characterisation of a PPy-pSi membrane. Part (a) shows CV measurements with different scan rates from $1\,\mathrm{mV\,s^{-1}}$ to $200\,\mathrm{mV\,s^{-1}}$. For this specific sample the potential range has to be adjusted to obtain a capacitive cycling behaviour. The vertex potentials are reduced by 0.2 V so that the CV measurement is conducted from 0.2 V to 0.6 V. The CV conducted with a scan rate $1\,\mathrm{mV\,s^{-1}}$ exhibits ideal capacitive characteristics. However, increasing the scan rate results in a tilt of the CV curves, an increase to $4\,\mathrm{mV\,s^{-1}}$ already shows this. The diffusion limitation known from the epi-layer is present. The CV curves with higher scan rates do not expand but rather merely tilt. Nonetheless, the currents are averaged in the potential range of 0.35 V to 0.45 V and plotted versus the respective scan rate, see Figure 5.7(b). The averaged currents asymptotically approach a level of 35 mA. Hence, the linear fit to determine the capacitance is only carried out up to $3\,\mathrm{mV\,s^{-1}}$. It yields $9.8 \pm 0.9\,\mathrm{mF}$. The capacitance normalised to the outer volume of the membrane is then $39\,820\,\mathrm{mF\,cm^{-3}}$, which is in good agreement with the volume specific capacitances determined for epi-layer samples. Overall, the PPy-pSi membrane performs similarly to an epi-layer with respect to their electrochemical properties.
It is possible to further evaluate the diffusion limitation by determining an apparent diffusion coefficient $\mathcal{D}$ of the perchlorate anions in the polypyrrole. By taking into consideration the electrode material's thickness h, the potential window $E_\mathrm{w} = 0.4\,\mathrm{V}$ of the CV measurement and a critical scan rate $(\mathrm{d}E/\mathrm{d}t)_\mathrm{crit.}$, $\mathcal{D}$ can be calculated by [292, 293]

$$\mathcal{D} = \frac{h^2}{\tau}, \quad \text{with} \quad \tau = \frac{E_\mathrm{w}}{(\mathrm{d}E/\mathrm{d}t)_\mathrm{crit.}}, \tag{5.2}$$

where τ denotes the time constant of the process. Here the electrode thickness h is assumed as half of the sample thickness, as the membranes are accessible for ions from both front and back side. By contrast, the cited works investigate polymer films on an ion-impermeable substrate. The critical scan rate $(\mathrm{d}E/\mathrm{d}t)_\mathrm{crit.}$ is determined according to the procedure depicted in Figure 5.7(c).[292] The abscissa shows the inverse square root of the scan rate, while the ordinate denotes the capacitance C for the respective scan rate. C is estimated by dividing the averaged current by the scan rate, see (b) of the same Figure. It can clearly be seen that two regimes are present. Capacitance values for larger scan rates and, thus, smaller $(\mathrm{d}E/\mathrm{d}t)^{-0.5}$, have a linear dependence with a larger slope. Vice versa, smaller scan rates have capacitances linearly following with a smaller slope. The two regimes are approximated by linear functions. The intersection point yields the critical scan rate.[292] Here, it amounts to $(\mathrm{d}E/\mathrm{d}t)_\mathrm{crit.} = 4.04\,\mathrm{mV\,s^{-1}}$. Hence, a diffusion coefficient of $\mathcal{D}_{\mathrm{ClO_4,PPy}} = 1.46 \cdot 10^{-7}\,\mathrm{cm^2\,s^{-1}}$ is obtained. In literature a range of diffusion coefficients is reported. The diffusion coefficient significantly depends on the synthesis conditions, i.e. the species of counter ion and its concentration, solvent and oxidation state. Values in literature vary from $1 \cdot 10^{-12}\,\mathrm{cm^2\,s^{-1}}$ to $1 \cdot 10^{-6}\,\mathrm{cm^2\,s^{-1}}$.[294–297] The diffusion coefficient of the polypyrrole film with the specifications most similar to the here synthesised hybrid

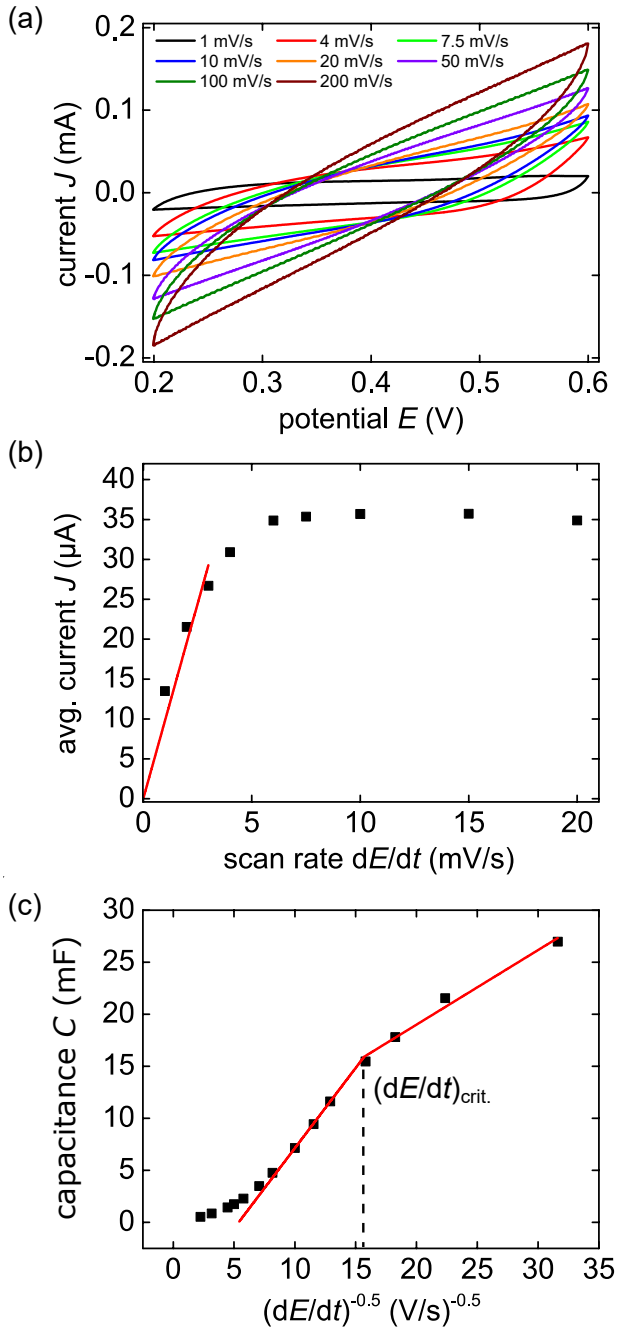

Figure 5.7.: **Electrochemical characterisation of a polypyrrole porous silicon membrane in perchloric acid.** Electrochemical characterisation of a PPy-pSi membrane in $1\,\mathrm{mol\,L^{-1}}$ perchloric acid. (a) CV measurements in the potential range of 0.2 V to 0.6 V with different scan rates from $1\,\mathrm{mV\,s^{-1}}$ to $200\,\mathrm{mV\,s^{-1}}$. (b) Averaged current values for the CV measurements in (a). Averaged in the range of 0.35 V to 0.45 V and plotted versus increasing scan rate $\mathrm{d}E/\mathrm{d}t$. The red line indicates a linear regression. Due to diffusion limitation, the determination of capacitance is only implemented up to a scan rate of $3\,\mathrm{mV\,s^{-1}}$. It yields a capacitance of $9.8 \pm 0.9\,\mathrm{mF}$. (c) Scan rate specific capacitance C, obtained by the averaged currents from (b) divided by the respective scan rate, plotted versus the scan rate to the power of -0.5. The point of transition determines the critical scan rate $(\mathrm{d}E/\mathrm{d}t)_{\mathrm{crit.}}$.

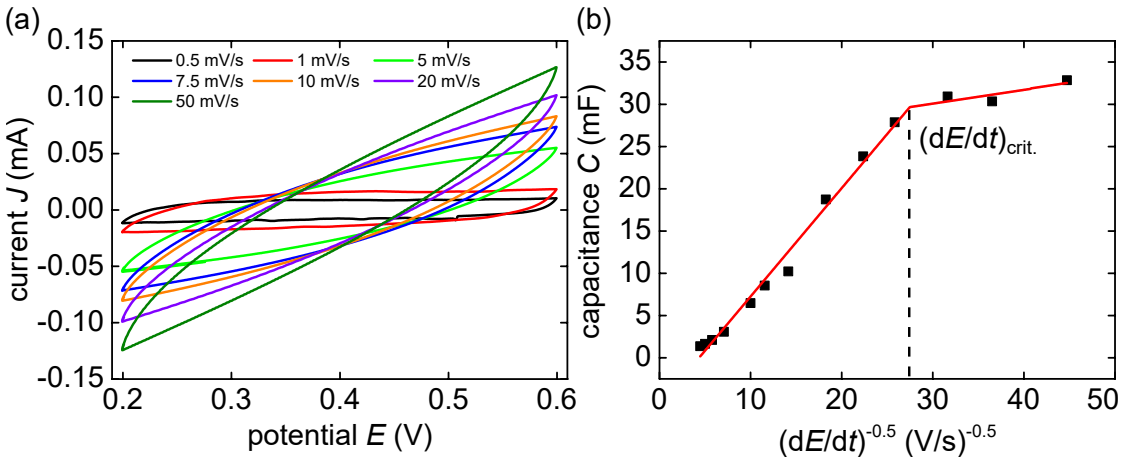

Figure 5.8.: **Electrochemical characterisation of a polypyrrole porous silicon membrane in isotonic saline solution.** Electrochemical characterisation of a PPy-pSi membrane in 154 mmol L^{-1} aqueous sodium chloride solution. (a) CV measurements from 0.2 V to 0.6 V with scan rates from 0.5 mV s^{-1} to 50 mV s^{-1}. (b) Scan rate specific capacitance C, plotted versus the scan rate to the power of −0.5 with the critical scan rate $(dE/dt)_{crit.}$.

is on the upper end of the range at $1 \cdot 10^{-6}$ cm^2 s^{-1}. Thus, it would mean a faster diffusion in a polypyrrole film than in the here investigated PPy-pSi hybrid material, which seems reasonable.

The electrochemical characterisation is repeated for the same sample but with a different electrolyte solution – an aqueous sodium chloride solution with a concentration of 154 mmol L^{-1}. The results are displayed in Figure 5.8. Part (a) shows CV measurements in the same potential region of 0.2 V to 0.6 V with scan rates ranging from 0.5 mV s^{-1} to 50 mV s^{-1}. The same significant diffusion limitation is visible in the CVs. Higher scan rates than 5 mV s^{-1} do not lead to a significant, proportional increase of the constant current level. Rather, the square like current course starts to tilt. The capacitance is only determined up to a scan rate of 2 mV s^{-1}, see Figure A.14 in the appendix. A capacitance of 13.3 ± 0.7 mF, or 54 264 mF cm^{-3} normalised to the outer volume of the porous silicon membrane, is determined. Thus, the capacitance is slightly larger for isotonic saline solution than for perchloric acid. Figure 5.8(b) shows the determination of the critical scan rate $(dE/dt)_{crit.}$. Again, the scan rate specific capacitance, which is estimated from the averaged current values, cf. Figure A.14, is divided by the respective scan rate. As before, two regimes are visible and $(dE/dt)_{crit.} = 1.3$ mV s^{-1} is at the transition of the two regimes. A diffusion coefficient of $\mathcal{D}_{Cl,PPy} = 4.74 \cdot 10^{-8}$ cm^2 s^{-1} is obtained. This value for chloride anions is approximately an order of magnitude smaller than for perchlorate anions. It is also approximately a factor of ten smaller than in a bulk polypyrrole film.[298] Thus, for both electrolyte solutions investigated here, the diffusion coefficient appears to be smaller for a PPy-pSi hybrid than for a pure bulk polypyrrole film, which would emphasise the impact of the porous structure on diffusion. Furthermore, the here determined diffusion coefficients for the PPy-pSi hybrid are smaller than the anions self diffusion coefficient in a bulk electrolyte solution.[260]

5.4. Dilatometry

In the previous section the electrochemical characterisation and control of a PPy-pSi membrane is established. Thus, in this section the electrochemical actuation measurement in the in situ dilatometry setup is discussed. The membrane is electrically contacted, installed in the dilatometer and the glass beaker is filled with $1\,\mathrm{mol\,L^{-1}}$ perchloric acid. The sample has a length of $l_0 = 0.626 \pm 0.005\,\mathrm{mm}$, a width of $3.49 \pm 0.01\,\mathrm{mm}$ and a thickness of $85 \pm 1\,\mu\mathrm{m}$ resulting in an outer volume of $0.19 \pm 0.03\,\mathrm{mm^3}$. The electrochemical actuation measurement is depicted in Figure 5.9. A CV measurement in the potential range of 0.4 V to 0.9 V with a scan rate of $10\,\mathrm{mV\,s^{-1}}$ is conducted. The respective CV measurement is shown in the appendix in Figure A.15 and it shows a mostly capacitive behaviour with a capacitance of $12.1 \pm 0.7\,\mathrm{mF}$. This value translates to $63\,680\,\mathrm{mF\,cm^{-3}}$, which is the largest volume specific capacitance of all investigated PPy-pSi hybrids. Towards the upper vertex potential Faradaic currents are visible, likely from an oxidation of the pSi pore walls. This effect is accounted for by subtracting the charge that is consumed in this process.
While the CV is conducted, the change in sample length l is recorded and therefore enables a detailed characterisation of the electrochemical actuation effect. Furthermore, while the potential is reversibly changed from the lower to the upper vertex potential, the charge is recorded. Five representative cycles of potential E are shown in Figure 5.9(a), plotted versus time t. In (b) the charge response, normalised to the sample volume q_V, upon the change of potential is depicted. Clearly, the transferred charge linearly and in phase coincides with the applied potential. So, an increasing potential results in an insertion of charge carriers into the polymer and, vice versa, a potential decrease leads to an ejection of charge carriers. Figure 5.9(c) shows the resulting change in strain $\varepsilon = \Delta l / l_0$. The repeated change of E from the lower to the upper vertex potential equally linearly changes strain ε. Increasing the potential leads to an accumulation of charge carriers and, in return, to an expansion of the polymer and the PPy-pSi hybrid in total. A subsequent decrease in potential reduces the charge and the sample contracts. The process shows no sign that the actuation amplitude decreases and it reproducibly reaches the same level. A CV conducted on the same sample with 15 cycles further illustrates this, as shown in Figure A.16 in the appendix. Most importantly, the dependence of strain ε on potential and volumetric charge is positive. By contrast, the dependence for electrosorption-induced actuation on porous silicon, not filled with polypyrrole, is negative. As above for the unfilled porous silicon, further information about the electrochemical actuation can be inferred by averaging both volumetric charge q_V and strain ε for up- and down-sweep of the five cycles. Thereby, peak-to-peak amplitudes of $\varepsilon_{\mathrm{avg,PPy-pSi}} = (+0.044 \pm 0.002)\,\%$ and $q_{\mathrm{V\,avg,PPy-pSi}} = 0.034 \pm 0.002\,\mathrm{C\,mm^{-3}}$ are obtained. The strain amplitude translates to a change in sample length of $0.313 \pm 0.001\,\mu\mathrm{m}$. In comparison to unfilled porous silicon, as a first result it can be registered that the achievable strain $\varepsilon_{\mathrm{avg,PPy-pSi}}$ in a similar potential range is about an order of magnitude larger than for the electrosorption-induced actuation in plain porous silicon $\varepsilon_{\mathrm{avg,pSi,CB}} = ((1.69 \pm 0.04) \cdot 10^{-3})\,\%$. However, the two actuation mechanisms differ and thus, the strain-charge coupling coefficient is determined to permit a comparison. Figure 5.10 provides a plot of ε versus q_V, both averaged over five cycles in the same potential range associated with Figure 5.9. The graph shows that the relation of the two variables is highly linear and confirms that a robust actuation functionality exists. The corresponding linear fit yields a strain-charge of $A^*_{\mathrm{PPy-pSi}} = +0.0103 \pm 0.0001\,\mathrm{mm^3\,C^{-1}}$.

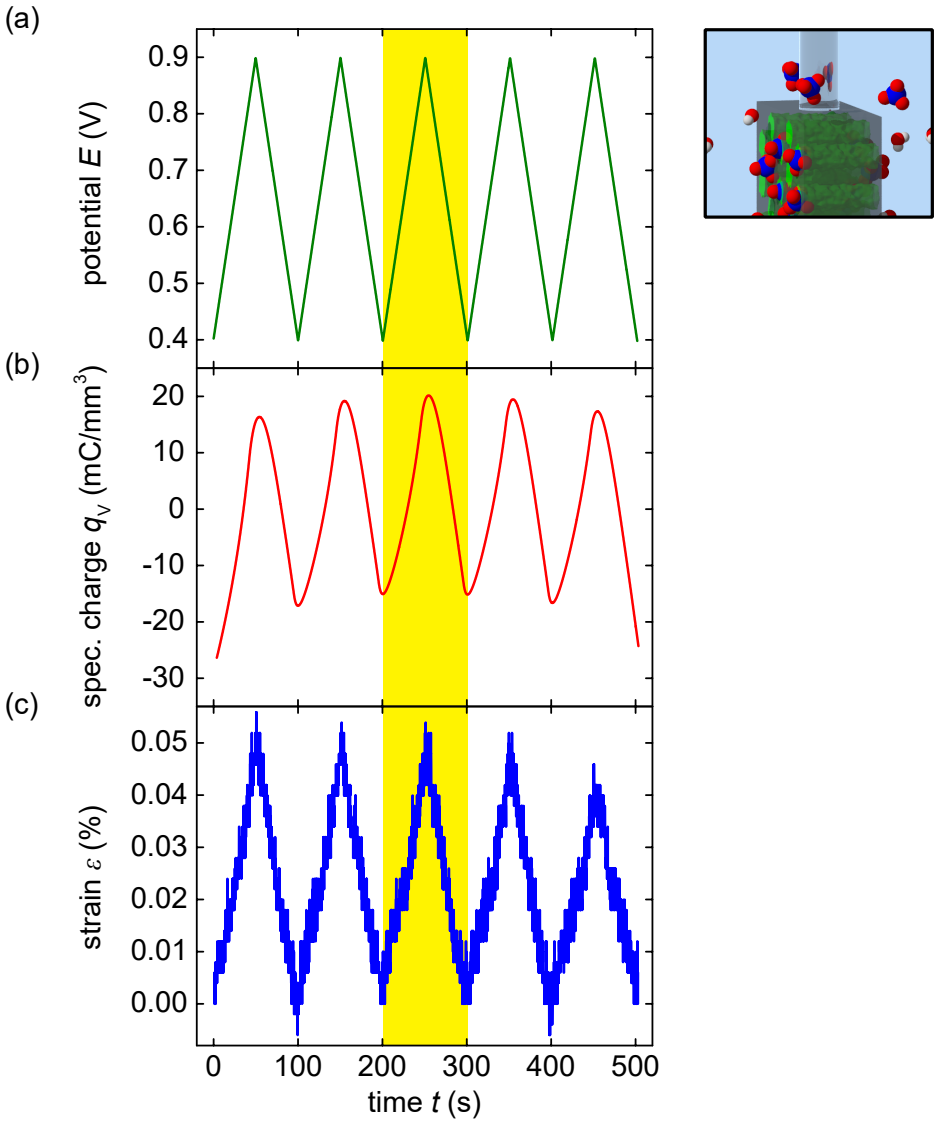

Figure 5.9.: **Electrochemical actuation of a polypyrrole porous silicon membrane.** In situ dilatometry measurement of a PPy-pSi membrane in perchloric acid in the potential range of 0.4 V to 0.9 V with a scan rate of 10 mV s^{-1}. Five representative cycles of (a) potential E, (b) resulting volumetric charge q_V and (c) introduced effective strain ε of the PPy-pSi membrane hybrid.

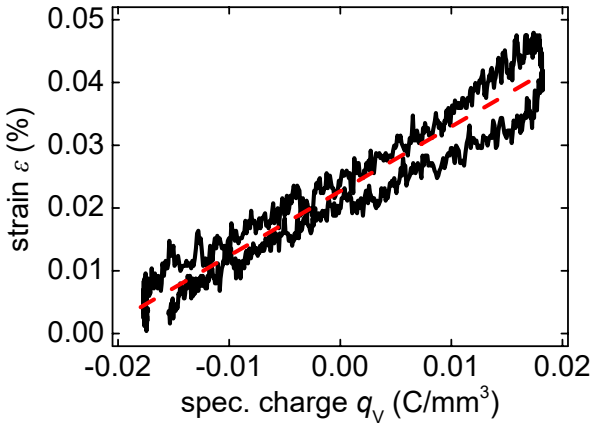

Figure 5.10.: **Strain-charge coupling parameter of a polypyrrole porous silicon membrane.** Strain ε versus accumulated volumetric charge q_V to determine the strain-charge coupling parameter A^* by a linear fit, which results in a value of $A^*_{PPy-pSi} = 0.0103 \pm 0.0001\,mm^3\,C^{-1}$.

The value is, in absolute terms, approximately equally large as the value obtained for plain porous silicon $A^*_{pSi,CB} = -0.011 \pm 0.004\,mm^3\,C^{-1}$. However, it should be stressed again that the dependence of strain on charge is of opposite nature, as symbolised by the opposite sign of the strain-charge coupling coefficient.
Polypyrrole can also be integrated into other porous materials, for example nanoporous gold.[299–301] The isotropic pore network consisting of ligaments is, as already mentioned, highly conductive. Rather than filling the entire pore space, as in the case of the here presented PPy-pSi hybrid, polypyrrole is deposited on the ligament surface of nanoporous gold. The electrochemical actuation depends on the thickness of the polypyrrole film.[299, 300] The strain-charge coupling parameter A^* reaches from approximately $0.015\,mm^3\,C^{-1}$ to $0.07\,mm^3\,C^{-1}$ for polypyrrole thicknesses of 10 nm and 40 nm, respectively.[302] Hence, A^* for PPy-npg is larger than for PPy-pSi but still in the same order of magnitude.

5.4.1. Actuation Kinetics

The kinetic properties of the electrochemical actuation are determined by step-coulombmetry as before in the case of the electrosorption-induced actuation of plain porous silicon, see Figure 4.12. The square potential is applied from 0.4 V to 0.8 V for five consecutive potential steps. An exemplary cycle of strain ε and volumetric charge q_V is depicted in Figure 5.11. Upon increasing potential E to 0.8 V, the associated strain saturates at a level of 0.015 % and q_V reaches approximately $0.04\,C\,mm^{-3}$. Vice versa, ε and q_V approach zero when the potential is lowered to 0.4 V. The actuation amplitude is smaller than for an applied CV potential, whereas q_V is at an equal level, see Figure 5.9. For the fit of both variables, simple exponential functions in the form of [112]

$$A * (1 - \exp(-(t - t_0)/\tau)) \tag{5.3}$$

for the potential increase and

$$A * \exp(-(t - t_0)/\tau) \tag{5.4}$$

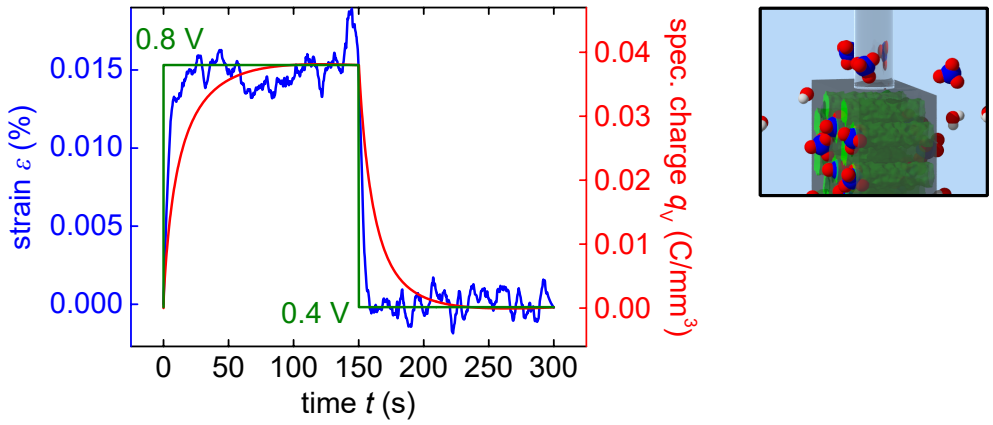

Figure 5.11.: **Kinetic dilatometry measurement on the electrochemical actuation of a polypyrrole porous silicon hybrid.** Step-coulombmetry in perchloric acid to determine the electrochemical actuation kinetics. The applied potential E (green) is changed in a step-like manner from 0.4 V to 0.8 V and back while incorporated volumetric charge q_V (red) and strain ε (blue) are measured. The respective variables are plotted versus time t.

for the potential decrease are used, where A and t_0 are fit parameters for the amplitude and a time shift. τ denotes the characteristic time constant of the respective process, i.e. the incorporation and ejection of charge carriers and the respective response of the strain. The analysis yields values of: $\tau_{q_V,\mathrm{incr}} = 16.52 \pm 0.07\,\mathrm{s}$ for the volume-specific charge increase, $\tau_{\varepsilon,\mathrm{incr}} = 4.3 \pm 0.2\,\mathrm{s}$ for the strain increase, $\tau_{q_V,\mathrm{decr}} = 14.31 \pm 0.07\,\mathrm{s}$ for the volume-specific charge decrease and $\tau_{\varepsilon,\mathrm{decr}} = 2.8 \pm 0.1\,\mathrm{s}$ for the strain decrease. Hence, the strain response time is an order of magnitude smaller than the charge response for both directions of potential alteration. Different effects might contribute to this outcome. The polypyrrole inside the pores might reach its yield limit at 2 MPa, where plastic deformation sets in.[303] Hence, the polypyrrole and the whole hybrid material is not expanding any further, although more anions are incorporated. The already investigated diffusion limitation can also hinder a faster transfer of anions. Additionally, as discussed in section 5.1 the polypyrrole filling of the pores has a lower density compared to bulk polypyrrole. Thus, the polypyrrole might be undergoing a process of increasing its density by closing out hollow voids inside its structure when it expands due to anion incorporation. Polypyrrole would still incorporate anions but the polymer expansion would then be rather directed inwards and would not lead to a strain transfer onto the porous silicon structure.
The here determined diffusion coefficient for perchloric acid $\mathcal{D}_{\mathrm{ClO_4,PPy}}$ suggests a characteristic diffusion time from the bulk electrolyte to the centre of the membrane of approximately 122 s. As a first order estimate, it fits the here determined values relatively well. Compared to the kinetic properties of electrosorption-induced actuation in plain porous silicon, see section 4.3, the characteristic time scale of the electrochemical actuation on the PPy-pSi is about an order of magnitude larger. Hence, the diffusion limitation is more distinct for the polypyrrole-filled porous silicon. Nevertheless, in both cases the actuation response is at least an order of magnitude faster than the flow of charge carriers, which

would suggest that the pores play a major role in these processes. Thus, the pores seem to be the primary reason for a restricted charge transport, while the mechanic response is not affected.

5.4.2. Isotonic Saline Solution

The effect of a different electrolyte on the electrochemical actuation of the polypyrrole-porous-silicon hybrid material is studied with an isotonic saline solution. In section 5.3 it is established that a PPy-pSi hybrid shows equal electrochemical features in perchloric acid as well as isotonic saline solution. The characteristic capacitive behaviour is present in both electrolytes and the obtained capacitances are in good agreement with each other. Thus, an in situ dilatometry investigation on the electrochemical actuation with perchloric acid as well as isotonic saline solution is conducted to ascertain whether an influence of the electrolyte type on the actuation of PPy-pSi is present while it exhibits equal capacitive features. A second PPy-pSi membrane is fabricated. The potential curve during the electrochemical polymerisation is shown in the appendix in Figure A.17 and has similar characteristics as observed before, see Figure 5.6. However, the initial polymer nucleation stage is more extended and the transition stage begins later than expected for an epi-layer of equal thickness. Additionally, the density of polypyrrole inside the pore space amounts to approximately $0.65\,\mathrm{g\,cm^{-3}}$, so less than $0.81\,\mathrm{g\,cm^{-3}}$ determined for the other PPy-pSi membrane, see section 5.3. The differences in the synthesis may be due to an inferior contact on the sputtered gold layer at the bottom where the polymer nucleates.
A sample is prepared for the in situ dilatometry experiment, as described in the methods section 3.5.1. The length of the installed sample is $l_0 = 0.12\,\mathrm{cm}$. First, the actuation properties with perchloric acid are examined and afterwards compared to isotonic saline solution. A resulting electrochemical actuation measurement is shown in Figure 5.12(a). The Figure shows five representative potential cycles and the corresponding accumulated volumetric charge q_V and the effective strain ε. The measurement exhibits the already established characteristics, i.e. the strain linearly coincides in-phase with E and q_V. The amplitudes of the strain and volumetric charge are $(0.012 \pm 0.002)\,\%$ and $21.560 \pm 0.007\,\mathrm{mC\,mm^{-3}}$, respectively. Figure 5.12(b) shows a plot of ε versus q_V. A linear fit to the data yields a strain-charge coupling parameter of $A^* = 0.0054 \pm 0.0001\,\mathrm{mm^3\,C^{-1}}$. It is apparent that a larger hysteresis is present than for the other PPy-pSi sample depicted in Figure 5.10. Moreover, the determined strain-charge coupling coefficient is approximately 50 % smaller. This reduction can likely be ascribed to the differences during the synthesis procedure. However, it will be investigated for this specific sample if a change of electrolyte solution has an influence on the actuation properties. Since comparative measurements are performed on the same sample, a direct, quantitative evaluation of the electrolyte influence is possible.
Figure 5.13 displays the resulting electrochemical actuation measurement in isotonic saline solution. The potential range and the scan rate are the same. The strain essentially shows the same electrochemical actuation characteristics. The volumetric charge has an oscillation amplitude of $21.800 \pm 0.003\,\mathrm{mC\,mm^{-3}}$, which agrees well with the value for perchloric acid $21.560 \pm 0.007\,\mathrm{mC\,mm^{-3}}$. Thus, the hybrid material's capacitance for the two monovalent anions does not differ. However, it is apparent that the ε amplitude is smaller than in the case of perchloric acid. Averaging over five cycles yields an average strain amplitude of $(0.0053 \pm 0.0005)\,\%$, which is merely approximately half as large to

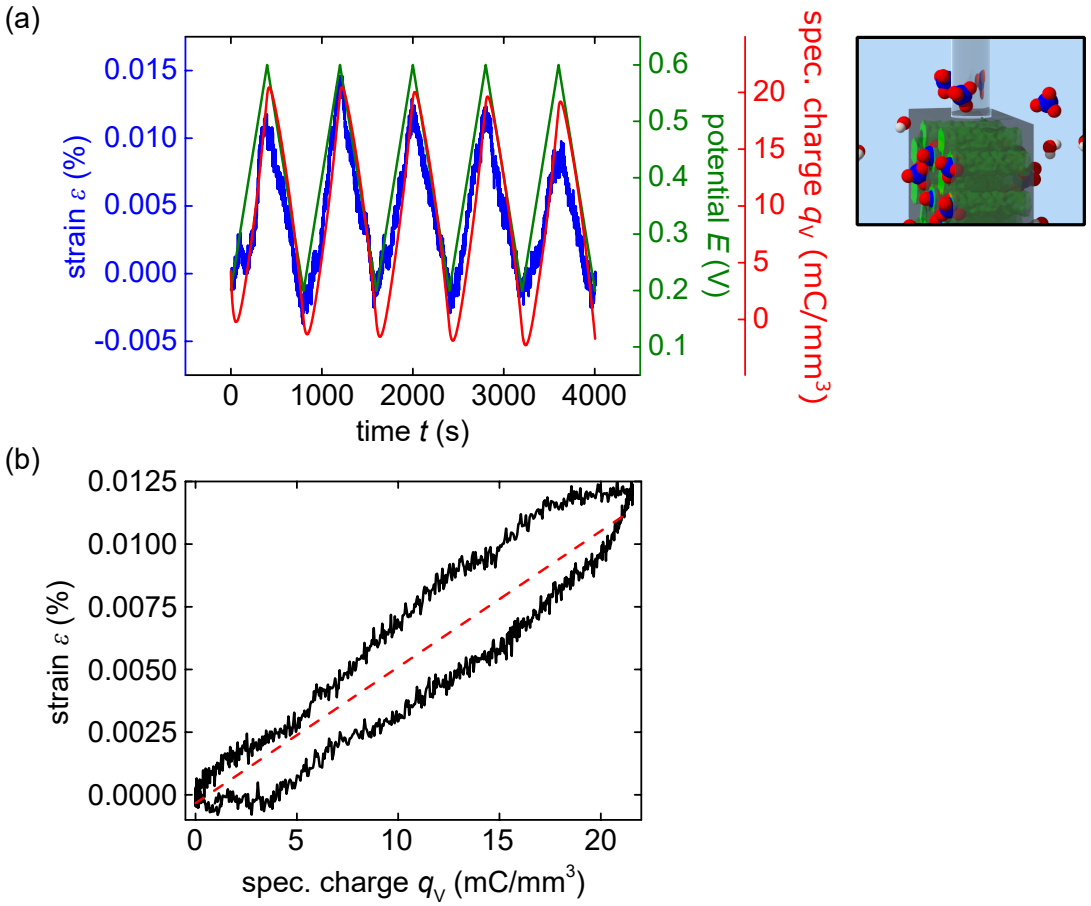

Figure 5.12.: **Electrochemical actuation of a polypyrrole porous silicon membrane in perchloric acid.** (a) In situ dilatometry measurement of a PPy-pSi membrane in perchloric acid in the potential range of 0.2 V to 0.6 V with a scan rate of $1\,\mathrm{mV\,s^{-1}}$. Five representative cycles of potential E (green), volumetric charge q_V (red) and effective strain ε (blue) of a PPy-pSi membrane hybrid. (b) Strain ε versus accumulated volumetric charge q_V to determine the strain-charge coupling parameter via a linear fit, which yields $A^* = 0.0054 \pm 0.0001\,\mathrm{mm^3\,C^{-1}}$.

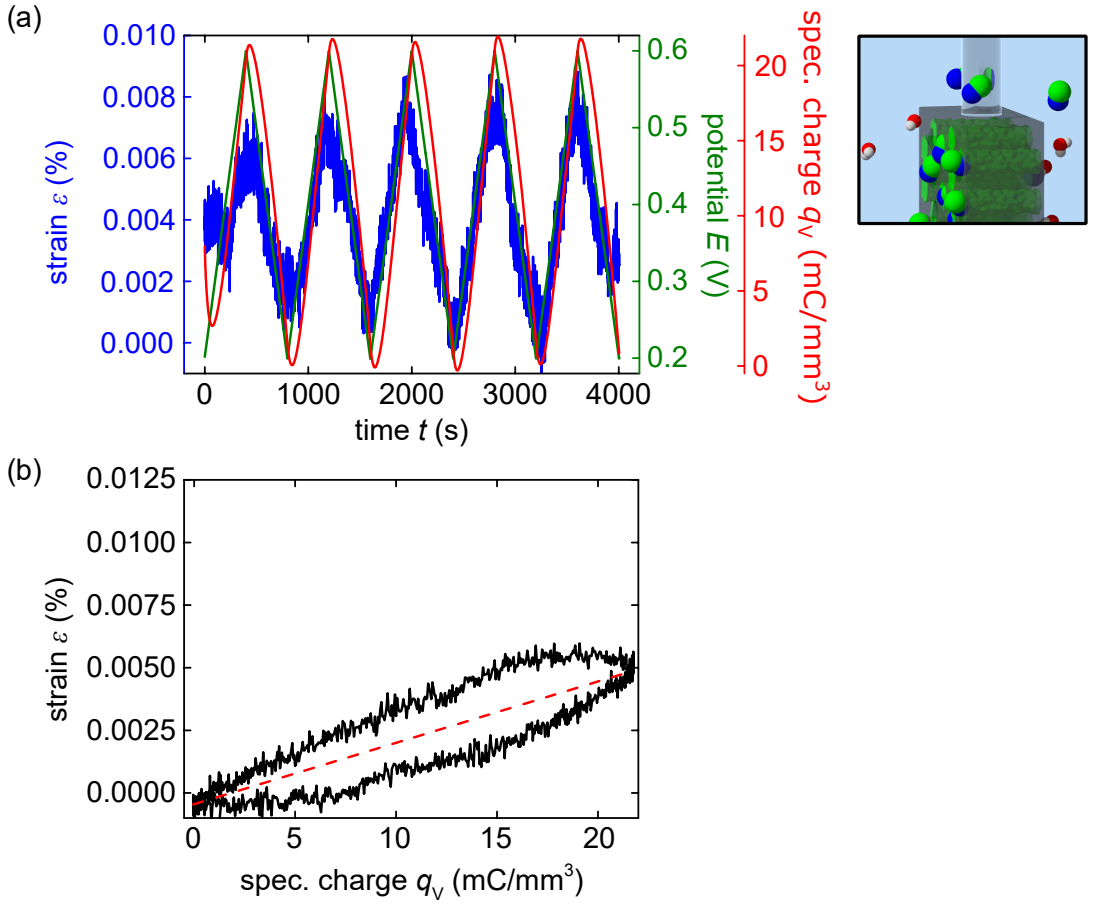

Figure 5.13.: **Electrochemical actuation of a polypyrrole porous silicon membrane in isotonic saline solution.** (a) In situ dilatometry measurement of a PPy-pSi membrane in isotonic saline solution in the potential range of 0.2 V to 0.6 V with a scan rate of 1 mV s^{-1}. Five representative cycles of potential E (green), volumetric charge q_V (red) and effective strain ε (blue) of the same PPy-pSi membrane hybrid, as in Figure 5.12. (b) Strain ε, displayed on the same scale as in Figure 5.12, versus accumulated volumetric charge q_V. Determined strain-charge coupling parameter is $A^* = 0.0025 \pm 0.0001$ mm^3 C^{-1}.

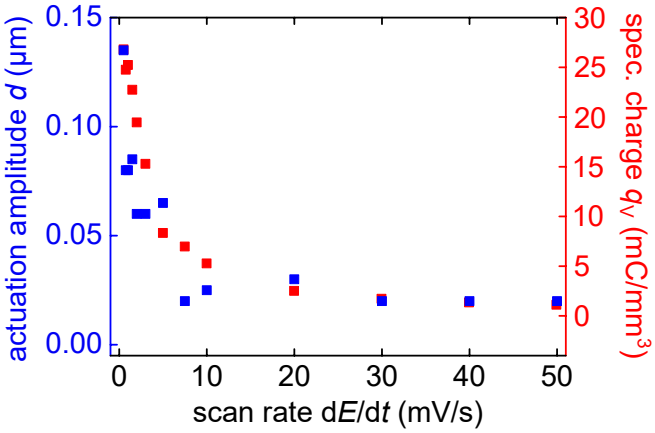

Figure 5.14.: **Electrochemical actuation amplitude in isotonic saline solution.** Electrochemical actuation amplitudes (blue) from different measurements of a PPy-pSi membrane in isotonic saline solution, averaged in the potential range of 0.2 V to 0.6 V with different scan rates from 0.5 mV s^{-1} to 50 mV s^{-1}. The volumetric charge q_V amplitude (red) is obtained by averaging over the cycles of the respective CV.

an equal amount of incorporated anions. The plot of ε versus q_V confirms this, as depicted in Figure 5.13(b). Interestingly, the same hysteresis is present for the isotonic saline solution. So the reason for it does not seem to be the electrolyte. Rather, it is likely that the synthesis of this specific PPy-pSi hybrid is responsible for the observed hysteresis. The resulting strain-charge coupling coefficient is $A^* = 0.0025 \pm 0.0001\,\mathrm{mm^3\,C^{-1}}$, which is only about 45 % of the value for perchloric acid. For a polypyrrole film prepared on a metal substrate it has been reported that the electrochemical actuation response strongly depends on the size of the anion.[304] The polypyrrole film actuation amplitude caused by an electrolyte containing Cl^- is about 30 % smaller than for ClO_4^- anions.[304] Evidently, for the electrochemical actuation of polypyrrole incorporated into porous silicon, a similar point can be made.

Figure 5.14 shows a graph of the electrochemical actuation amplitude which is averaged over five potential cycles during CV measurements with different scan rates in the potential range of 0.2 V to 0.6 V. The amplitude is plotted versus the scan rate from 0.5 mV s^{-1} to 50 mV s^{-1} along the respective amplitude of the volumetric charge q_V. The amplitude reduces with an increasing scan rate, from approximately 0.13 µm to approaching a level of 0.03 µm. Similarly, the volumetric charge reduces with increasing scan rates. Increased scan rates lead to a significantly reduced incorporation of anions and the PPy-pSi hybrid is not expanding as much. This investigation emphasises the results from the coulombmetry measurement with an applied square potential, see Figure 5.11. Overall, the rate of potential change has a remarkable influence on the ion capacitance and the actuation response of the PPy-pSi hybrid material.

5.4.3. Micromechanical Simulation Analysis

A micromechanical modelling approach enables further insight into the electrochemical actuation process of PPy-pSi.[112] The details of the model creation are given in reference

[112] and shall here only be briefly summarised followed by the main results. A TEM top view section, as depicted in Figure 5.1, is converted into a $2^1/_2$-dimensional finite element model (FEM) according to the pixels of the TEM image. The image is assumed to be extendable in the third dimension of the image plane. The pixel greyscale value of the TEM picture defines which sections are attributed to the silicon scaffold of the pore wall and the pore space, respectively. The mechanical properties of bulk silicon, see section 2.1, is accordingly assigned to pore wall segments.[112, 122] Therefore, the greyscale threshold that defines pore wall and pore space has to be chosen carefully. Firstly, an FEM model with a pore space unfilled and not occupied by polypyrrole is investigated. A tension is applied to this FEM model in one lateral direction and hence, it is possible to determine the Young's modulus of the model. Applying this procedure for models of different thresholds yields their Young's moduli. Hence, the model that matches the experimentally determined Young's modulus is obtained.[112] Interestingly, at this threshold, the anisotropy of the Young's modulus between [100] and [110] directions is negligible [112], which coincides well with the result of the laser-excited elastic guided wave study introduced above [177]. Moreover, the stress distribution within the silicon pore walls reveals that only a section, which represents approximately 70 % of the porous silicon mass, contributes to the load transfer from bottom to top of the model.
Next, the sections which represent pore space are assigned polypyrrole mechanical values, i.e. a Young's modulus of $500 \pm 10\,\mathrm{MPa}$ and a Poisson's ratio of 0.35.[97, 112, 213] The resulting Young's modulus of the PPy-pSi hybrid is approximately 40 % larger than for the unfilled porous silicon. The polypyrrole filling of the pores enables an enhanced load transfer through additionally activated pore walls and thereby could be described as a glue material.
For the modelling of the electrochemical actuation characteristics, the polypyrrole phase in the model is equipped with a volume change property. Polypyrrole gradually swells and hence, the entire FEM model of the hybrid material expands until the experimentally determined strain amplitude of $\varepsilon_{\mathrm{avg,PPy-pSi}}$ is achieved. At this point polypyrrole exhibits a stress-free swelling of 0.77 %. A polypyrrole film with an equal perchlorate doping has a uniaxial strain-charge coupling coefficient of $0.17\,\mathrm{mm^3\,C^{-1}}$, as stated in section 2.6 in the theory chapter. Hence, the charge $q_{\mathrm{V\,avg,PPy-pSi}}$ incorporated during the electrochemical actuation studied here would lead to a strain of 0.58 %. This strain is in close proximity to the simulated value of 0.77 %, although the polypyrrole is within the pSi pore space and not in the shape of a film. Furthermore, in this state of maximum PPy-pSi expansion, the simulation shows that the pSi pore walls are in an even more uniform stress state so that effectively 83 % of the pore walls is affected. The polypyrrole incorporated into the pores here shows pressures of up to 15 MPa for smaller pores and slightly less, i.e. $8 - 12\,\mathrm{MPa}$, for larger pores. Surprisingly, despite these high pressures, the stress within the polypyrrole in a number of pores exceeds the yield limit of 2 MPa. Plastic flow would occur in the polypyrrole in these pores. Therefore, plasticity as a probable reason for the notable difference in the actuation kinetics compared to the charging kinetics would be supported by these numerical simulations.

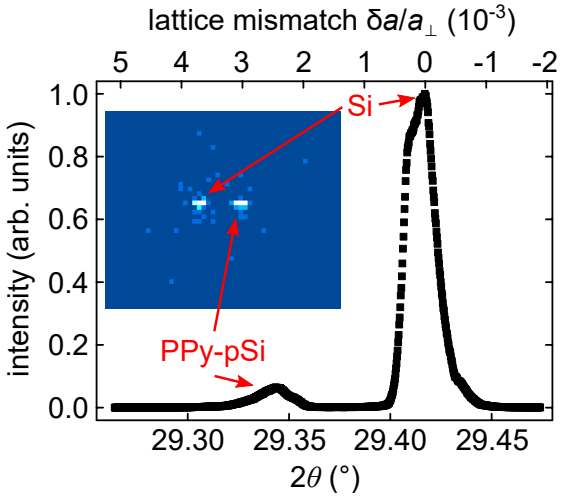

Figure 5.15.: **X-ray diffraction measurement on 400 Bragg peak for an as-prepared polypyrrole porous silicon hybrid.** XRD $\theta - 2\theta$ scan on an as-prepared, 25.4 µm thick PPy-pSi epi-layer on the 400 Bragg peak in reflection geometry. Ordinate shows the intensity in arbitrary units in linear scale, normalised to the silicon peak (Si) intensity. The abscissa shows angle 2θ at the bottom. At the top, the corresponding lattice mismatch $\delta a/a_\perp$ with respect to the main silicon peak is shown. Clearly visible are the 400 Bragg peak from the silicon layer and the smaller peak from the hybrid PPy-pSi layer. The inset depicts an actual detector image with the Si and PPy-pSi peak for illustrating purposes.

5.5. X-Ray Diffraction

This section will present the results of the comprehensive in situ X-ray diffraction study on the electrochemical actuation of a polypyrrole-porous-silicon hybrid material. First, the measurement in the out-of-plane measurement geometry will be presented, along a detailed explanation on the electrochemical control of the experiment and electrochemical characterisation. Next, the kinetics of the actuation will be explored. At the end, the results of the in-plane geometry will be discussed.

5.5.1. Out-of-Plane Lattice Strain

The first XRD measurement is conducted on sample S_{refl} in reflection geometry and without an electrolyte solution in the cell. The PPy-pSi sample S_{refl} is in an as-prepared state and the 400 peak is investigated in a $\theta - 2\theta$ scan. The resulting measurement is depicted in Figure 5.15. The graph shows the presence of two Bragg peaks in the $\theta - 2\theta$ measurement. These are due to the bulk silicon and the PPy-pSi layer. The larger, Si peak, is at an angle of approximately $2\theta \approx 29.42\,°$. The ordinate is normalised to the intensity of this peak and displayed in a linear scale. Figure A.18 in the appendix displays a close up of the Si peak. Clearly visible are the error bars for each measurement point. The second, PPy-pSi peak is at $2\theta \approx 29.34\,°$, albeit with about one tenth of the intensity. These two distinctive 400 Bragg peaks in a $\theta - 2\theta$ measurement are characteristic of

a layered sample with adjacent, monocrystalline layers of porous silicon and underlying bulk silicon, as described in sections 2.4 and 3.5.3. The difference in intensity between these peaks is ascribed to the different thicknesses of the PPy-pSi and the silicon layer, respectively. In contrast to the 500 µm thick bulk silicon layer, the PPy-pSi layer has only a thickness of 25.4 µm at only roughly half of the density of bulk silicon. Hence, the PPy-pSi layer has a smaller scattering volume and a lower Bragg peak intensity.[238]
The PPy-pSi Bragg peak is at a smaller 2θ angle than the Si Bragg peak. Therefore, the lattice mismatch $\delta a/a$ is positive, according to equation 3.13. Hence, the lattice of the porous silicon layer is expanded in the out-of-plane direction. Both Bragg peaks are approximated by a fit-function to determine their precise 2θ angles. Then, it is possible to obtain a value for $\delta a/a_\perp$ by the splitting of the peaks and, thus, a result, exceeding the mere observation that the lattice is expanded.
The fit extension LIPRAS for Matlab is used for this purpose.[305] Both peaks do not feature a clear symmetric shape, which resembles a Lorentz or Gauss profile. Rather, a broad shoulder at a slightly lower 2θ distorts the Si peak. Furthermore, the Si peak also exhibits a foot at a higher angle. Distortions to the Si peak in such a layered sample can occur due to a bending of the sample.[238] The distortions and their reasons will be debated further below. The Si peak is approximated with several fit-functions to account for the distortions. The resulting fit is conducted with four pseudo-Voigt functions [306] and is depicted in Figure 5.16(a). One function is utilised for the main peak and independent functions each cover the large shoulder at a smaller 2θ and the shoulder and the foot at larger 2θ. The resulting fit, in total, approximates the entire peak well, as displayed in Figure 5.16(a).[1] In the further analysis, as a value for the Si main peak the 2θ peak value of the partial fit to the largest main peak is used. The result for the Si peak, displayed in Figures 5.15 and 5.16(a), is $2\theta = (29.4159 \pm 0.0003)\,°$.[2] The angular uncertainty is determined here according to the description in the methods section 3.5.3. The value for 2θ is slightly larger in comparison to the angle $2\theta = 29.3934\,°$, calculated by equation 3.10. The disparity might be due to a slight misalignment of the sample with respect to both, the sample holder and the beam. However, as explicitly emphasised in the methods section 3.5.3, a perfect alignment is not required, as both the Si and pSi peak will be affected by a misalignment equally and only the difference in θ of the peaks determines $\delta a/a_\perp$.
The underlying Si layer can be considered to clamp the porous silicon layer. The lattice planes, oriented perpendicular to the boundary of Si and pSi layer, can therefore be considered as constrained to the interatomic spacing of the adjacent bulk silicon, i.e. the Si lattice constant would be imprinted on the pSi in the in-plane direction.[8] Hence, the pSi lattice constant in the out-of-plane direction increases and, in this direction, compensates the strains evolving in the entire lattice.[8] Important to note here is that this directional difference of the pSi lattice parameters could lead to a bending of the sample. For plain, unfilled porous silicon the curvature has not been found to significantly affect the XRD measurement if the area of the beam is limited.[8] Additionally, the bulk silicon layer here has a thickness of 500 µm compared to the 25.4 µm of the PPy-pSi layer to suppress the occurrence of a possible curvature. However, the additional peaks and the overall asymmetric peak shape for the Si peak is striking. The large shoulder, almost resembling a

[1] The adjusted r^2 value of the fit amounts to 99.36 %.
[2] The fit yields a peak for the shoulder of $2\theta = 29.4094\,°$ and $2\theta = 29.4317\,°$ for the foot.

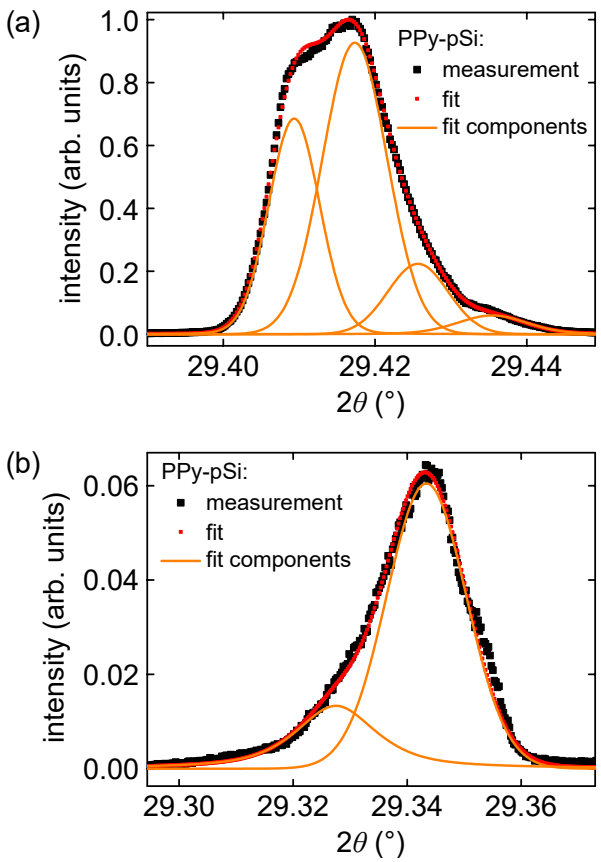

Figure 5.16.: **Applied fit-functions on the 400 Bragg peak.** Fit-functions applied to the 400 Bragg peak of (a) bulk Si and (b) the PPy-pSi hybrid in the out-of-plane direction of the $\theta - 2\theta$ scan in reflection geometry depicted in Figure 5.15. The single components that approximate the different peak features, are displayed as well as the resulting total fit of the entire peak.

second peak, might very well be due to a bending of the wafer. An increasing porous silicon thickness has been reported to substantially distort the Si peak.[238] The filling of polypyrrole inside the pore space alone might lead to such a bending effect. Lastly, the observed foot of the Si peak at higher angles, is possibly the result of a diffuse scattering of the porous silicon structure.[141]
The described fit procedure is applied to the PPy-pSi peak as well. As the peak only shows a distortion to smaller 2θ values in the form of a shoulder on the main PPy-pSi peak, two independent fit-functions suffice, as depicted in Figure 5.16(b). The main PPy-pSi peak is located at $2\theta = (29.3437 \pm 0.0003)\,°$.
Two effects may contribute to the distortion of the PPy-pSi peak. Firstly, an irregular filling by PPy of the pSi pores could lead to a divergence of strained areas at the interface between polymer and pore wall. The measured lattice mismatch might then be distinctly irregular in dependence of the polymer filling. Secondly, side-pores, already discussed in section 4.3, might be the reason for a divergence in strain distribution in the porous silicon layer. This irregular porous microstructure may lead to a spread in the distribu-

tion of micro-strains and hence an asymmetric peak shape.[307] As the side-pores branch off the main pore, they do not substantially contribute to a load transfer in macroscopic tension.[112] Thus, strains in the pSi lattice due to polypyrrole expansion might influence these side-pores distinctively different than in the main pore. Whereas an out-of-plane expansion of the pSi lattice in the main pore may occur, the expansion might not be as strong in sections where side-pores are located. Side-pores constitute essentially a broadening of the pore wall. Stresses caused by polymer swelling would be distributed over a larger fraction of the pore wall. Therefore, they would generate smaller strains. Additionally, the side-pores might also not be filled to the same degree with polypyrrole as the main pore. Hence, a different transfer onto the pore wall lattice might result, which would also entail a distortion of the PPy-pSi peak. Furthermore, an oxidation of the silicon pore walls during the first stage of the polymerisation process or at unfilled pore sections during the electrochemical experiments might lead to a broadening of the PPy-pSi peak. An oxidation of the pore walls leads to a stress in porous silicon, as already observed for unfilled porous silicon, see Figure 4.6(a). Such an influence through a progressive oxidation has already been observed on the lattice mismatch $\delta a/a_{\perp}$.[141]

As is established and discussed above, with the specific fitting procedure the 2θ position of the main Si and the main PPy-pSi peak are obtained. This specific fitting protocol is deployed for all $\theta - 2\theta$ scans here. The separation between the peaks yields a lattice mismatch of $\delta a/a_{\perp} = (+2.40 \pm 0.01) \cdot 10^{-3}$ for as-prepared PPy-pSi. Such a positive lattice mismatch in the out-of-plane direction is characteristic for an XRD investigation on a pSi epi-layer with underlying bulk Si.[8, 141, 178, 235–238] A comparison of the lattice mismatch $\delta a/a_{\perp}$ for PPy-pSi to an unfilled pSi epi-layer requires equal porous silicon characteristics with respect to porosity and pore diameter. Porous silicon synthesised from silicon with an identical resistivity and with an equal final porosity has a lattice mismatch of $+5.2 \cdot 10^{-4}$.[141] Thus, the polypyrrole filling itself, without an applied potential, is responsible for a noticeable $\delta a/a_{\perp}$ increase by a factor of approximately 4.5. It can be assessed that the polypyrrole filling leads to a significant lattice strain and an expansion of the pSi lattice in the out-of-plane direction. Generally, such a significant pSi lattice strain is possible and a lattice mismatch as high as $+0.002$ has been reported, albeit for porous silicon with a vastly different pore morphology, i.e. higher porosity and larger pore diameter.[141] This concludes the assessment of the as-prepared PPy-pSi.

Next, perchloric acid is filled into the cell and is allowed to imbibe into the PPy-pSi sample for 15 min. Afterwards, a $\theta - 2\theta$ scan is conducted within the same range as for the as-prepared material. It is compared to the as-prepared scan to investigate if a change in pSi lattice mismatch is observed due to the infiltration of perchloric acid. The resulting measurement is displayed in Figure 5.17. The Si main peaks of the two measurements are at the same value. However, the PPy-pSi peak is slightly shifted after the liquid uptake. The resulting lattice mismatch amounts to $(+2.48 \pm 0.01) \cdot 10^{-3}$, which is a small difference to the as-prepared state but still detectable. The lattice mismatch is larger compared to the as-prepared state. Hence, the pSi lattice expands further upon the liquid infiltration in the out-of-plane direction. The difference in lattice mismatch between the two states is $\delta a/a_{\perp_{\text{prep/liqu}}} = (+0.8 \pm 0.1) \cdot 10^{-4}$ and is thus two orders of magnitude smaller than the lattice mismatch of the two states themselves. A comparable in situ study investigated the adsorption of pentane vapour in porous silicon, which yields $+1.8 \cdot 10^{-4}$ between as-prepared porous silicon and fully pentane-filled porous silicon. For both studies the difference in lattice mismatch $\delta a/a_{\perp}$ is positive. The lattice expands further on adsorp-

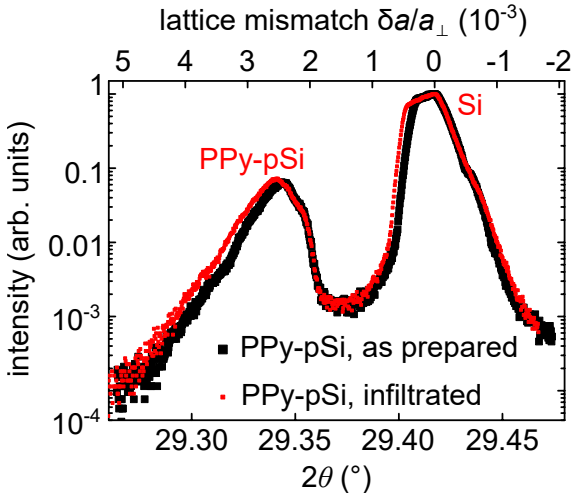

Figure 5.17.: **X-ray diffraction measurement on 400 Bragg peak for a liquid-infiltrated polypyrrole porous silicon hybrid.** XRD $\theta - 2\theta$ scan of $HClO_4$ infiltrated PPy-pSi on the 400 Bragg peak in reflection geometry, with the intensity on the ordinate in arbitrary units in logarithmic scale and normalised to the Si peak. Electrolyte-infiltrated (red) in comparison to the as-prepared state (black).

tion, which can be associated with the Bangham effect. Surface stress at the pore wall is reduced due to molecular adsorption.[65]. However, the amplitude of the lattice mismatch $\delta a/a_\perp$ change is about twice as large for the pentane vapour adsorption than the liquid imbibition of the here investigated PPy-pSi. The results are not easy to compare, as the effect of pentane adsorption is measured in porous silicon with a larger porosity of 80 %. As stiffness decreases in porous silicon with increasing porosity [8], surface stress changes might result in larger lattice mismatches in porous silicon with higher porosities.

5.5.2. Out-of-Plane Lattice Strain - Electrochemical Dependence and Kinetics

The counter electrode and the reference electrode are inserted into the in situ XRD measurement cell and all electrodes are connected to the potentiostat so that electrochemical measurements can be performed. First it is checked whether sample S_{refl} shows the typical electrochemical characteristics. A CV measurement is conducted. The respective measurement is depicted in Figure A.19 in the appendix. A capacitive behaviour is observed in the potential region of $0.4-0.8\,V$, although a diffusion limitation is visible for a higher scan rate of $10\,mV\,s^{-1}$. Overall, the electrochemical characteristics are in accordance with the behaviour here established for PPy-pSi, see section 5.2. The accompanying capacitance is $34.7 \pm 0.5\,mF$. S_{refl} has an area of $46.61\,mm^2$. Hence, the volume normalised capacitance is $29300 \pm 400\,mF\,cm^{-3}$, which matches the capacitance determined for PPy-pSi in sections 5.2 and 5.3. So overall, the electrochemical properties of S_{refl} are as desired and the potential dependent lattice mismatch can be examined.
A full $\theta-2\theta$ scan is time consuming. Thus, a CV measurement, even with a slow scan rate,

is too quick to conduct it in parallel to several, subsequent $\theta - 2\theta$ scans. Thus, another method is applied. The potential is successively adjusted to discrete potential steps of 0.4, 0.6 and 0.8 V and reversed. At each step the potential is retained constant. In response, the current either has a drastic up or downward slope, depending if the potential step is an increase or decrease, before asymptotically approaching zero. Figure A.20 shows the respective step wise potential course and two exemplary current responses to an increasing and decreasing potential step, respectively. The current is integrated to obtain the charge incorporated at each step. When the initial alteration has passed and the current reaches a stable level, the $\theta - 2\theta$ scan is started. The next potential step is set at the end of the scan. By these means a CV measurement is mimicked.
Figure 5.18(a) shows two exemplary $\theta - 2\theta$ scans for two potential steps of 0.4 V and 0.8 V, which are recorded in succession. The main silicon peak does not markedly shift with a change of potential. However, the PPy-pSi peak exhibits a clear shift to larger values of 2θ with the 0.8 V potential step, as shown in the inset in Figure 5.18(a). In particular, the right edge of the peak shifts noticeably. The lattice mismatch $\delta a/a_\perp$ is calculated according to the fitting procedure and is shown in dependence of potential steps E in Figure 5.18(b). The graphic also displays the volumetric charge q_V for each potential step. Lattice mismatch $\delta a/a_\perp$ clearly follows the applied potential E and the incorporated charge q_V in phase. Thus, the applied potential leads to an incorporation of charge carriers and also to an increase of $\delta a/a_\perp$, so an expansion of the pSi lattice in the out-of-plane direction. Vice versa, reducing the potential expels charge carriers and the lattice contracts. The lattice mismatch $\delta a/a_\perp$ shifts from a level of approximately $+0.0028$ to $+0.0030$. A $\delta a/a_\perp$ average of the central potential cycles (cycles two to ten) yields $\delta a/a_{\perp_\mathrm{avg}} = +(1.50 \pm 0.04) \cdot 10^{-4}$. Overall, the electrochemical actuation expressed in lattice mismatch $\delta a/a_\perp$ can be designated as reversible and reproducible.
The reproducibility and linearity of the lattice mismatch actuation is further examined by an applied linearly changing CV potential. The incidence and exit angle θ are fixed so that $2\theta = 29.3443\,°$. At his angle the diffraction condition is in the middle of the right PPy-pSi peak edge. Hence, the intensity will increase or decrease when the peak shifts to smaller or larger 2θ-angles with the applied potential. As the diffraction condition is in the middle of the peak edge, the intensity change will be maximal. The intensity is summed in time intervals of 1 s. Only a change in intensity is measured. For a comparison to other results, the intensity change needs to be converted into a lattice mismatch with the following procedure. The fit parameters of the last preceding full $\theta - 2\theta$ scan are used. All fit parameters are held constant and the 2θ value of the PPy-pSi peak is adjusted so that the intensity of the time dependent scan is met. The PPy-pSi peak position then yields the lattice mismatch in the time dependent measurement. The resulting measurement is shown in Figure 5.19. The measurement is conducted in the same potential range. q_V is also determined. Clearly, lattice mismatch $\delta a/a_\perp$ coincides linear and in phase with the applied potential E and volumetric charge q_V, thus confirming the results from the step-wise potential method. The amplitude over the potential cycles is $+(1.55 \pm 0.03) \cdot 10^{-4}$ and is thus consistent with the step-wise lattice mismatch average $\delta a/a_{\perp_\mathrm{avg}}$.
A square potential with potential steps of 0.4 V and 0.8 V is applied to probe the kinetics of the lattice mismatch. The steps last for 15 s. The method to measure the lattice mismatch change in response to the applied square potential has to be adapted. The previous method sums over the central detector region, see methods section 3.5.3, and for the applied CV potential, the temporal resolution is 1 s. However, the temporal resolution

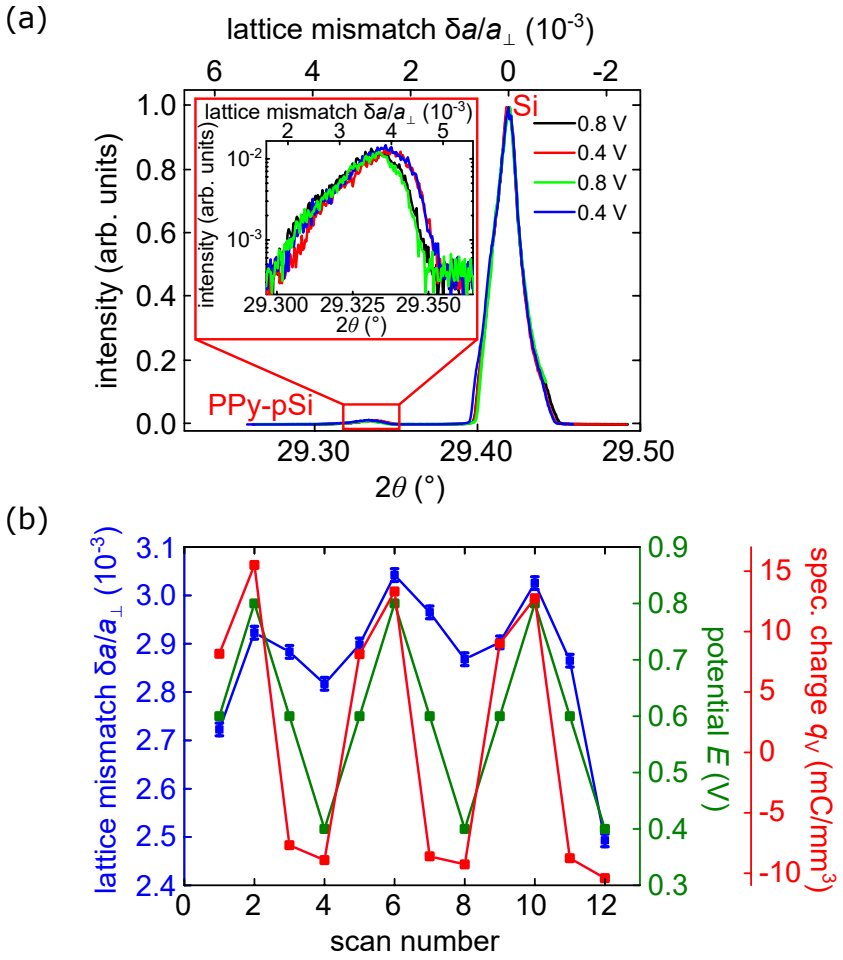

Figure 5.18.: **Potential dependent XRD measurements and out-of-plane lattice mismatch determination.** (a) Potential dependent $\theta - 2\theta$ scans on the 400 Bragg peak of a PPy-pSi epi-layer in perchloric acid in out-of-plane direction with potential steps of 0.4 V and 0.8 V, respectively. The inset represents a zoom onto the PPy-pSi peak in logarithmic scale. (b) Resulting lattice mismatch $\delta a/a_\perp$ (blue) together with charge q_V (red), normalised to the volume of the porous silicon layer, in dependence of the applied potential E (green) at each step.

has to be increased for the quick $\delta a/a_\perp$ response upon an instant changing potential. The time resolution is adjusted to 0.1 s. The lattice mismatch is obtained by evaluating the actual detector pictures, recorded with the increased time resolution. The incidence angle is set to the PPy-pSi peak at $2\theta = 29.3342\,°$. Thus, the diffraction condition focuses the PPy-pSi peak to maximise its intensity. The Si peak is also visible on the detector pictures. A profile of the two peaks is obtained from the detector picture. The lattice mismatch is determined by approximating the two peaks with Lorentzian functions. An exemplary detector image and its extracted profile is displayed in Figure 5.20(a). The fit yields the position of the peaks in detector pixels. With the knowledge of the size of a pixel p, the incident angle θ and the distance of sample to detector $\mathcal{L}$, the pixel position

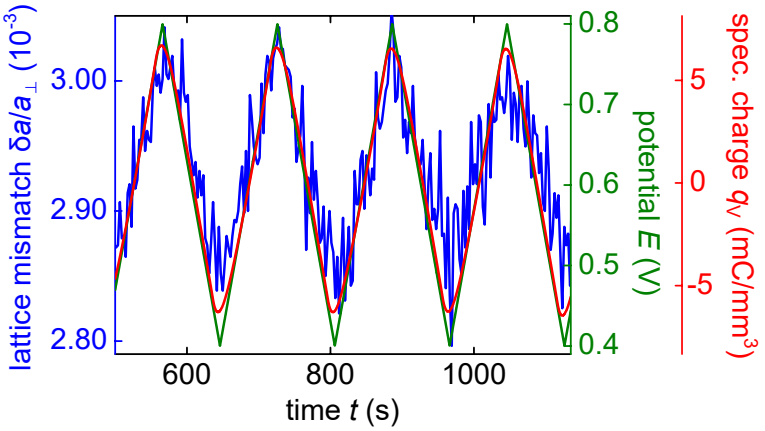

Figure 5.19.: **Lattice mismatch in dependence of a cyclic voltammetry measurement.** Lattice mismatch $\delta a/a_\perp$ (blue) along volume specific charge q_V (red) in dependence of an applied, linearly changing CV potential E (green).

is transformed into 2θ values and, thus, finally a value for $\delta a/a_\perp$ is obtained. By all these means the temporal resolution suffices the requirement of the step-coulombmetry.
Figure 5.20(b) shows the resulting lattice mismatch $\delta a/a_\perp$ and the volumetric charge q_V in response to the step-coulombmetry. The same potential dependence observed in response to the CV potential is present, as $\delta a/a_\perp$ increases upon a potential increase and vice versa. Overall, the same characteristics as observed for the macroscopic electrochemical actuation of the membrane, see Figure 5.11, are present. $\delta a/a_\perp$ replicates the square form of the potential course. The course of q_V is significantly different, as it takes longer to start to settle. The exponential fit-functions known from equations 5.3 and 5.4 are used to approximate the course of $\delta a/a_\perp$ and q_V to obtain characteristic time constants of the respective processes. The fits yield averaged values of 1.6 ± 0.1 s and 8.07 ± 0.08 s for the response of $\delta a/a_\perp$ and q_V upon a potential increase, respectively. For a potential decrease the values are 1.9 ± 0.2 s for $\delta a/a_\perp$ and 7.57 ± 0.06 s for q_V. Thus, a significant difference for the reaction of the lattice mismatch compared to the charge movement is present, as the latter is slower by a factor of leastwise four for both directions of potential change. That means, the observations for the macroscopic actuation kinetics study by in situ dilatometry on a PPy-pSi membrane can be replicated here on the microscopic level of the crystal lattice. Again, the probable reasons for this disparity are the diffusion limitation, the densification of the polypyrrole filling and the onset of plastic deformation. However, the reaction time of the lattice is slightly faster with values of 1.6 s and 1.9 s for increasing and decreasing potentials, compared to 4.26 s and 2.8 s for the macroscopic strain reaction.

5.5.3. In-Plane Lattice Strain

For sample S_{trans} an XRD measurement is conducted in the transmission geometry so that the lattice mismatch in the in-plane direction, i.e. the 044 Bragg peak, is probed. In the initial measurement the electrolyte solution $HClO_4$ is filled into the cell and imbibes into the sample S_{trans}, but no potential is applied. It is in an as-prepared, electrolyte-infiltrated state. The resulting $\theta - 2\theta$ scan from approximately $2\theta \approx 42.08\,^\circ$ to $42.095\,^\circ$

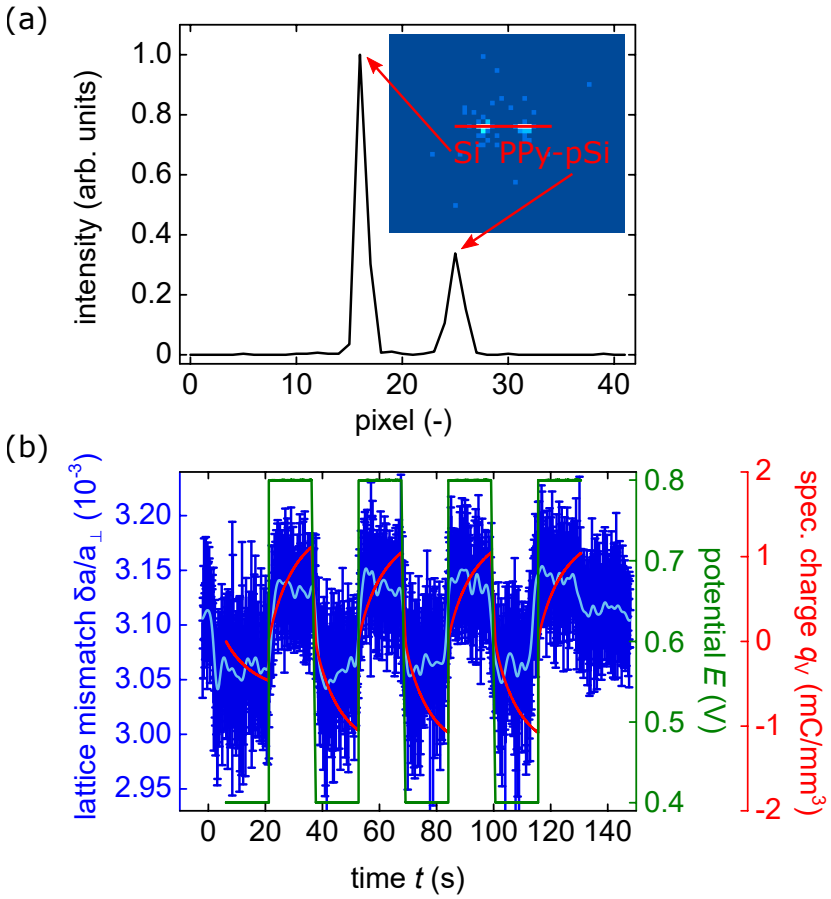

Figure 5.20.: **Actuation kinetics of lattice mismatch by step-coulombmetry.** (a) Exemplary detector image with the Si main peak and the PPy-pSi peak visible. A profile of the two peaks is extracted and displayed in the main graph, which shows the pixel position and the intensity normalised to the Si peak. (b) Step-coulombmetry with a temporal resolution of 0.1 s for the determination of the electrochemical actuation kinetics. Potentials E (green) of 0.4 V and 0.8 V are applied in steps, which last 15 s. Volumetric charge q_V (red) is displayed along the resulting lattice mismatch $\delta a/a_\perp$ (blue, with the average in turquoise).

is displayed in Figure 5.21 in comparison to the same measurement for an equal porous silicon sample but without the polypyrrole filling of the pore space. The measurement shows that a second peak at higher 2θ is present, which has about half the intensity of the Si main peak. Again pseudo-Voigt functions are used to approximate the peaks and extract the peak positions. The main silicon peak is at $2\theta = (42.0847 \pm 0.0002)\,°$ and the PPy-pSi peak at $2\theta = (42.0899 \pm 0.0002)\,°$. As the PPy-pSi peak is at a larger 2θ angle than the Si main peak, the lattice mismatch $\delta a/a_{||}$ has a negative sign. Hence, the lattice of the porous silicon layer is contracted with respect to the bulk silicon lattice constant. The two determined peaks yield a value of $\delta a/a_{||} = (-1.17 \pm 0.07) \cdot 10^{-4}$. In comparison to the out-of-plane direction, $\delta a/a_{||}$ has an opposite sign and it is approximately one order

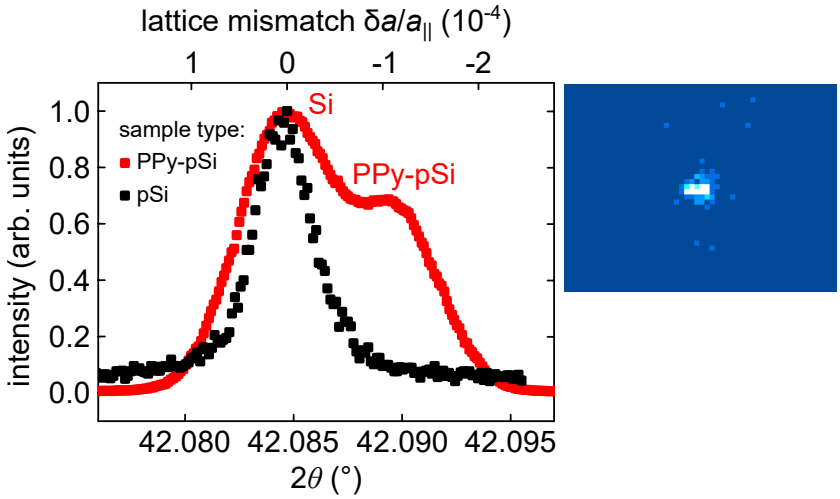

Figure 5.21.: **X-ray diffraction measurement for an as-prepared polypyrrole porous silicon hybrid on the 044 Bragg peak.** XRD $\theta-2\theta$ scan of a 25.4 µm thick as-prepared PPy-pSi epi-layer in perchloric acid on the 044 Bragg peak in transmission geometry (red), which shows a Si main peak and a second PPy-pSi peak. The latter peak is not visible in the comparison to an equal scan of porous silicon without the PPy pore filling (black). The intensity is normalised to the silicon peak (Si) intensity and the abscissa shows angle 2θ at the bottom and the corresponding lattice mismatch $\delta a/a_{\perp}$ with respect to the silicon peak at the top. The inset depicts an actual detector image, in which the Si and PPy-pSi peaks are visible.

of magnitude smaller in absolute terms.
Since the underlying bulk silicon clamps the porous silicon layer, a lattice mismatch between the Si and the pSi lattice in-plane is not to be expected. Rather, induced stress would be released via the out-of-plane lattice mismatch.[8] For a $\theta - 2\theta$ scan on an equal sample with a porous silicon layer which has no polypyrrole pore filling it is ascertained that the second peak is not visible, as Figure 5.21 displays. Plain porous silicon only shows one clear peak at identical Si peak position. A very slight deviation on the bottom of the peak towards higher 2θ might be present, but by no means it is markedly visible. The absence of the PPy-pSi peak means that the pSi lattice has the same lattice constant as the underlying bulk silicon. The emergence of the second peak can be ascribed to the PPy filling of the pores. Evidently, the polymer is responsible for causing significant strains on the in-plane lattice so that a separate peak becomes measurable. Such an additional peak is not even observed when stress is exerted onto the pSi lattice by a significant oxidation.[141] The in-plane lattice mismatch is reported in the referenced experiment as an estimate of $\delta a/a_{||} = 0 \pm 5 \cdot 10^{-5}$.[141] Therefore, the in-plane lattice mismatch measured here, is beyond the cited margin of uncertainty by about one order of magnitude.
Interestingly, the in-plane lattice mismatch determined here, is negative and the lattice is contracted in-plane. Assuming the pore walls possess bulk silicon's Poisson's ratio [273], such a contraction is to be expected to some extend, as the lattice expands in the out-of-plane direction. Sections of the silicon pore walls, which are highly strained in the out-of-plane direction, might cause significant lateral contractions.

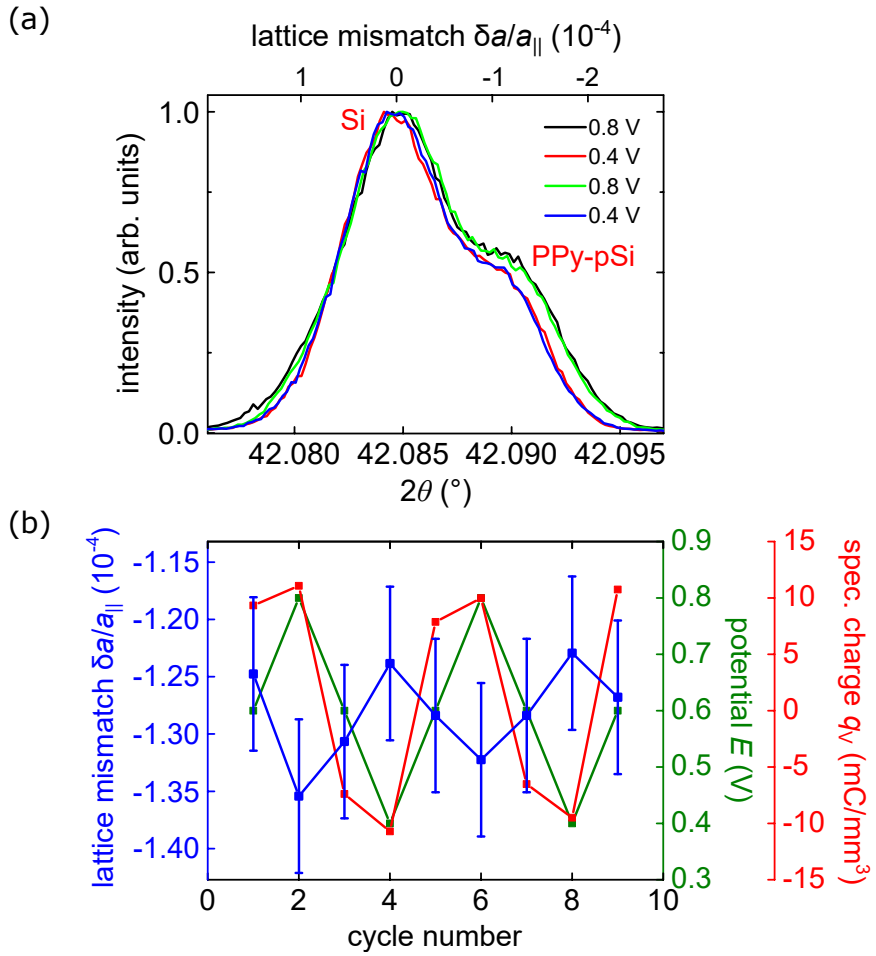

Figure 5.22.: **Potential dependent XRD measurements and in-plane lattice mismatch determination.** (a) Potential dependent $\theta - 2\theta$ scans on the 044 Bragg peak of a 25.4 µm thick as-prepared PPy-pSi epi-layer in perchloric acid in in-plane direction with potential steps of 0.4 V and 0.8 V, respectively. (b) Resulting lattice mismatch $\delta a/a_{||}$ (blue) together with volumetric charge q_V (red), in dependence of the applied potential E (green) at each step.

Lattice mismatch $\delta a/a_{||}$ for sample S_{trans} is measured also in dependence of an applied potential with the introduced step-wise method. The sample also shows the established capacitive behaviour, see Figure A.21 in the appendix. Four exemplary $\theta - 2\theta$ scans are depicted in Figure 5.22(a). The PPy-pSi peak shifts noticeably to smaller 2θ and thus, to smaller lattice mismatch $\delta a/a_{||}$ values for the higher potential steps of 0.8 V. The lattice mismatch $\delta a/a_{||}$, along volumetric charge q_V for all potential steps is displayed in (b). q_V oscillates between a level of $\pm 10\,\mathrm{mC\,mm^{-3}}$. The course replicates the reflection measurement well, see Figure 5.18(b), which exhibits an equal range for q_V. This result stands to reason, as both samples have similar capacitances. The in-plane lattice mismatch, on the other hand, exhibits a distinctively different behaviour. For increasing potential steps, $\delta a/a_{||}$ exhibits an even larger decrease to negative values. So, the lattice contracts further

in-plane. Vice versa, a $\delta a/a_{||}$ increase, i.e. a lattice expansion, is observed for smaller potential steps. Thus, the dependency of $\delta a/a_{||}$ on E is of opposite nature, compared to the out-of-plane lattice mismatch $\delta a/a_{\perp}$. Even though the uncertainty is relatively larger for the $\delta a/a_{||}$ variation, an lattice mismatch potential dependence can unmistakably be identified. The amplitude of the lattice mismatch averaged over cycles number two to nine amounts to $\delta a/a_{||_{\text{avg}}} = -(1.06 \pm 0.09) \cdot 10^{-5}$. Again, the same scale difference is observed, as $\delta a/a_{||_{\text{avg}}}$ is approximately one order of magnitude smaller than $\delta a/a_{\perp_{\text{avg}}}$.
A summary of the results of the in situ X-ray diffraction experiment on the electrochemical actuation of the PPy-pSi hybrid is specified in Figure 5.23.
Apart from PPy-pSi hybrids, unfilled, anodically oxidised porous silicon has also been investigated in the out-of-plane direction with the in situ XRD measurement procedure. The lattice mismatch $\delta a/a_{\perp}$ on the 400 Bragg peak is probed. A lattice mismatch $\delta a/a_{\perp} \neq 0$ on porous silicon can be confirmed. However, the measurements with stepwise applied potentials do not provide conclusive evidence about the dependence of $\delta a/a_{\perp}$ on applied potentials within the margin of uncertainty, see Figure A.22 in the appendix.

5.5.4. Micromechanical Simulation Analysis

The results of the in situ XRD study may be further examined by a micromechanical simulation analysis. Such a study, as also discussed in section 5.4.3, yields inside into the mechanistic characteristics of the actuation process on the pore scale.[243] For the purpose of obtaining a three-dimensional (3D) FEM model of porous silicon that resembles its morphology as closely as possible, a TEM tomography on the PPy-pSi is performed. A series of TEM detector pictures of a thin, needle-shaped PPy-pSi sample is recorded while it is rotated. The single TEM pictures are reconstructed to form a 3D model.[243] The creation of the model and the most important simulation results are here summarised. Such a tomography model clearly depicts the side-pores branching off from the main pore. Interestingly, also pore-interconnections between main pores are present [243], which have been intensively discussed with respect to their importance for self-diffusion [17] and cavitation events in porous silicon [308].
The pixels of the tomography model are transferred to an FEM model of the material, which is made up of voxels. The model is calibrated by the porosity of macroscopic PPy-pSi.[243] The elements of the model are individually assessed with respect to their mechanical properties and in particular their strain state, referred to as micro-strains.[243] Thus, it is possible to gain information about the strain distribution on the micro-structure level. The X-ray beam has a larger size than the microstructure model and, thus, averages over a larger PPy-pSi volume. So, the analysis of the strain of the whole model volume is prone to artefacts and errors due to the limited model volume when compared to the results of the XRD study. Rather, the distribution of the micro-strains allows a comparison.
The micro-strain distribution is calibrated to reproduce the measured out-of-plane lattice mismatch from the XRD measurements on as-prepared and electrolyte-infiltrated PPy-pSi. For the calibration, the surface of the silicon pore walls is strained on purpose. The resulting micro-strain distribution can be transformed into a series of 2θ values. Qualitatively, it matches the shape of the PPy-pSi Bragg peak, which is depicted in Figure 5.16(b).[243] However, the range of the 2θ distribution is much wider in the model, as the porous silicon microstructure is quite irregular. This irregularity can lead to a large

reflection geometry probing 400		**lattice mismatch $\delta a/a_{\perp}$ (10^{-3})**	**lattice mismatch amplitude A (10^{-4})**
PPy-pSi - as-prepared	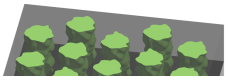	+(2.40 ± 0.01)	(0.8 ± 0.1)
PPy-pSi - electrolyte-infiltrated 1M $HClO_4$	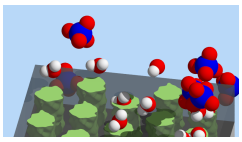	+(2.48 ± 0.01)	
PPy-pSi - potential applied: 0.8 V	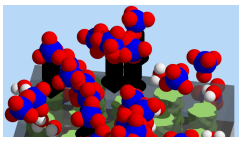	+(3.00 ± 0.05)	(1.50 ± 0.04)
PPy-pSi - potential applied: 0.4 V	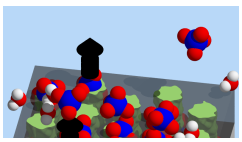	+(2.85 ± 0.03)	
transmission geometry probing 044		**lattice mismatch $\delta a/a_{\parallel}$ (10^{-4})**	**lattice mismatch amplitude A (10^{-5})**
PPy-pSi - electrolyte-infiltrated 1M $HClO_4$	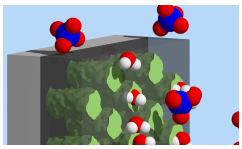	-(1.17 ± 0.07)	
PPy-pSi - potential applied: 0.8 V	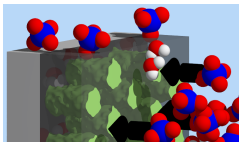	-(1.34 ± 0.02)	-(1.06 ± 0.09)
PPy-pSi - potential applied: 0.4 V	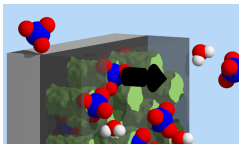	-(1.234 ± 0.005)	

Figure 5.23.: **Overall results of the in situ XRD experiment on the electrochemical actuation of a polypyrrole porous silicon hybrid.** Out-of-plane lattice mismatch $\delta a/a_{\perp}$ for the reflection geometry, probing the 400 Bragg peak and in-plane lattice mismatch $\delta a/a_{||}$ for the transmission geometry, probing the 044 Bragg peak, for all states of the PPy-pSi hybrid.

range of micro-strain distribution and thus an altered shape of the Bragg peak.
It is possible to model the electrochemical actuation of PPy-pSi by an applied potential by assigning an expansion property to the PPy phase in the model.[243] Again, the micro-strain distribution is used to tune the expansion property to match the measured out-of-plane lattice mismatch for the applied potentials of 0.4 V and 0.8 V, see Figure 5.23.
As a result, the PPy phase is found to experience a volumetric swelling of 2.3 % and 3.2 %, respectively, for the two potentials.[243] Pressures of up to 55 MPa at an applied potential of 0.8 V are determined.[243] Remarkably, the swelling, as well as the pressure, is larger than for the micromechanical study conducted obtained from a single TEM picture in a $2^1/_2$D FEM model, see section 5.4.3. Thus, the third, out-of-plane dimension significantly adds to the complexity of the material and cannot be easily neglected.
Furthermore, in the simulation the peak of the in-plane micro-strain distribution shifts slightly but noticeably to negative values, while the out-of-plane strain is positive. The out-of-plane strain also changes with a positive dependence on the applied potential. Both of these outcomes reproduce the results of the experimental XRD study well. In an analysis of the model, it is determined that the larger strains are located at sites in the pore walls that may be described as notches. At these thin cross-sections the out-of-plane strains are concentrated, whereas thicker parts of the pore wall experience lower strains. Interestingly, the distribution of the in-plane strain component correlates with the notch sections. The occurrence of the in-plane strain in the XRD measurements can be attributed to these sections that experience a high out-of-plane strain. Ultimately, the in-plane strain is due to transverse contraction of these silicon pore wall notches. Simultaneously, large parts of the remaining pore wall with a thicker cross-section are unstrained in the in-plane direction. It explains why the extent of the in-plane lattice mismatch in the XRD study is an order of magnitude smaller, whereas the clamping of the underlying bulk silicon leads to an expansion of PPy-pSi due to polymer swelling directed in the out-of-plane direction.
Overall, such a comprehensive approach of a TEM-tomography- based model combined with micromechanical simulations complements the here presented in situ XRD study on the electrochemical actuation of PPy-pSi well. It enables insight on the scale of single pores up to the entire PPy-pSi hybrid material behaviour.[243]

5.6. Performance of Polypyrrole-Porous-Silicon Actuators

The polypyrrole-porous-silicon hybrid material can be evaluated in terms of its supercapacitor properties.[113] Supercapacitors are characterised by the parameters energy and power density. The energy density $\mathcal{E}_\mathrm{V}$ is estimated in a straightforward manner by [309]

$$\mathcal{E}_\mathrm{V} = \frac{1}{2} c E^2, \tag{5.5}$$

where c denotes capacitance and E the potential range. For the hybrid material a capacitance of $63.68\,\mathrm{F\,cm^{-3}}$ is determined at the beginning of section 5.4 for a potential range of $0.4 - 0.9\,\mathrm{V}$. By taking into account the density of the material, i.e. $1.49\,\mathrm{g\,cm^{-3}}$, an energy density of $\mathcal{E}_\mathrm{V} = 1.48\,\mathrm{W\,h\,kg^{-1}}$ is determined. The power density $\mathcal{P}_\mathrm{V}$ is obtained, by considering the time it takes to completely discharge the material. Here, a typical discharge time of $\tau_{q_\mathrm{V},\mathrm{decr}} = 14.31\,\mathrm{s}$ is determined, see Figure 5.11. Thus, the power density amounts to $1.48\,\mathrm{W\,h\,kg^{-1}}/14.31\,\mathrm{s} = 374\,\mathrm{W\,kg^{-1}}$ for the hybrid material. Both densities are well in range of energy and power densities observed for similar PPy-pSi hybrids.[113]

The energy and power density for plain porous silicon, without the polypyrrole filling, are $\mathcal{E}_V = 0.13\,\mathrm{W\,h\,kg^{-1}}$ and $\mathcal{P}_V = 141\,\mathrm{W\,kg^{-1}}$ and thus, well below the PPy-pSi hybrid's supercapacitor features. However, it has to be stated that it has not been the explicit goal of this work to create a material with outstanding supercapacitor properties. Dedicated materials exist whose intrinsic properties are more suited to fulfil the task of a supercapacitor. For instance, graphene-based supercapacitors exhibit energy densities up to $90\,\mathrm{W\,h\,kg^{-1}}$ and power densities of approximately $10\,000\,\mathrm{W\,kg^{-1}}$.[310]
A critical performance parameter that characterises actuators is work density. It quantifies mechanical work performed by the actuator against an external load. Normalised to the actuator volume, it is denoted as $\mathcal{W}_V$ and calculated by [74, 212]

$$\mathcal{W}_V = \frac{1}{4} Y \varepsilon_{ampl}^2, \tag{5.6}$$

where Y is the Young's modulus and ε_{ampl} the maximum strain amplitude. The equation is valid if the occurring maximal load $\varsigma_{max} = {}^1\!/_2 Y \varepsilon_{ampl}^2$ does not exceed the material's yield limit [74]. The actuation experiments on porous silicon and the polypyrrole-porous-silicon hybrid fulfil this constraint. The performance parameters of the here discussed materials are summarised in Table 5.1.
The strain amplitude of porous silicon, determined in section 4.3, in a potential regime of 0.0 V to 0.9 V amounts to $\varepsilon_{avg,pSi,CB} = ((1.69 \pm 0.04) \cdot 10^{-3})\,\%$ and its Young's modulus in-plane, i.e. in load direction, is $Y_{||} = 26.1\,\mathrm{GPa}$, determined in section 4.3. Hence, the work density amounts to $w_{V,pSi} = 1.9 \cdot 10^{-3}\,\mathrm{kJ\,m^{-3}}$, normalised to material volume or $w_{V,pSi} = 1.7 \cdot 10^{-3}\,\mathrm{J\,kg^{-1}}$ normalised to the mass by taking account the material's density of $1.07\,\mathrm{g\,cm^{-3}}$.
Nanoporous gold constitutes another type of porous material that exhibits electrosorption-induced actuation in aqueous electrolyte solutions.[10] The strain amplitude measured for npg amounts to $(4.7 \cdot 10^{-3})\,\%$ with a Young's modulus of 1.03 GPa.[299] Hence, the volumetric work density is $\mathcal{W}_V = 5.5 \cdot 10^{-4}\,\mathrm{kJ\,m^{-3}}$. Note however that this value is obtained for npg that is submitted to a plastic deformation of 18 % pre-measurement, which enhances the Young's modulus. A plastic deformation of only 3 % results in a Young's modulus of approximately 200 MPa [299], an identical strain amplitude and thus, a volumetric work density of $1.1 \cdot 10^{-4}\,\mathrm{kJ\,m^{-3}}$, merely a fifth of the original value. In comparison to porous silicon the volumetric work density of npg is smaller by a factor of approximately three. Since npg has a much higher density, porous silicon's work density normalised to mass $\mathcal{W}_m$ is even larger by a factor of more than fifteen.
Equation 5.6 shows that the work density depends quadratically on the achievable strain amplitude but only linearly on Young's modulus. The filling of polypyrrole in the pSi pore space increases the Young's modulus of the hybrid by only approximately 4 GPa.[112] Thus, an enhancement of the strain amplitude by the polypyrrole filling has a significant impact on the work density. The hybrid material has a strain amplitude of $\varepsilon_{avg,PPy-pSi} = (+0.044 \pm 0.002)\,\%$ in the potential regime of 0.4 V to 0.9 V, see section 5.4, so approximately thirty times larger. Accordingly, the hybrid's volumetric work density $\mathcal{W}_V = 1.46\,\mathrm{kJ\,m^{-3}}$ is about three orders of magnitude larger. As the densities of the two materials are similar, the work density per mass is also larger for the hybrid material. Per mass a value of $0.98\,\mathrm{J\,kg^{-1}}$ is obtained, by taking into account the hybrid's density of $1.49\,\mathrm{g\,cm^{-3}}$.
As described above, polypyrrole can be deposited on the inner surface area of npg. Here,

we compare the PPy-pSi hybrid to PPy-npg, which has a PPy film thickness ranging from 10.2 nm to 30.3 nm. These represent a volume share of 10 % and 30 %, respectively.[299] Their volumetric work densities amount to $0.1 - 6.7\,\mathrm{kJ\,m^{-3}}$.[302] The PPy-pSi hybrid is well within that range. When normalised to mass, its work density is on par with the upper end of the range since its density is lower. Note that the PPy-npg samples are again 15 % pre-deformed so that the stated work densities represent upper limits.
Lastly, the performance of the pSi and PPy-pSi actuators are compared to common piezo ceramic materials, which show strain amplitudes of up to 0.1 % [311–313] and have maximal Young's moduli around 80 GPa [314]. The result of these maximum values would be a volumetric work density of $\mathcal{W}_\mathrm{V} = 17.5\,\mathrm{kJ\,m^{-3}}$. Actual, commercially available piezo actuators, lead-zirconium-titanate (pzt) based, are PZT8 and PZT4.[314] PZT4 has a piezoelectric coefficient of $d_{33} = 372\,\mathrm{pC\,N^{-1}}$.[314] With a typical applied electric field of $U = 2\,\mathrm{kV\,mm^{-1}}$ [313] a strain amplitude of $Ud_{33} = 0.074\,\%$ is obtained. With a Young's modulus of 58.9 GPa and a density of $7.65\,\mathrm{g\,cm^{-3}}$ [314] it is possible to estimate work densities of $8.15\,\mathrm{kJ\,m^{-3}}$ and $1.06\,\mathrm{J\,kg^{-1}}$ normalised to volume and mass, respectively. The volumetric work density is slightly exceeding the one of the here investigated PPy-pSi. Overall, it can be ascertained that the PPy-pSi hybrid's work density per mass is on par with commercially available piezo materials.

Table 5.1.: **Performance parameters of porous silicon and polypyrrole-porous-silicon in comparison to different materials.** Performance of the here investigated porous silicon (pSi) and polypyrrole-porous-silicon (PPy-pSi) as specified by the work density normalised to the material volume and mass. The performance is compared to the electrosorption-induced actuation of nanoporous gold (npg) and electrochemical actuation of polypyrrole-nanoporous gold hybrid materials (PPy-npg). The latter is displayed with polypyrrole film thicknesses of 10.2 nm and 30.3 nm.[299, 302] The work density for npg and PPy-npg are stated in load direction, in which the strain is measured. However, these actuator materials isotropically expand and contract in all directions.[74, 182] Hence, the work density would be larger by a factor of three. Here, only the unidirectional strain and work density is considered for a better comparison to the PPy-pSi hybrids. Moreover, the nanoporous gold is plastically pre-deformed by 18 % and 15 % for npg and PPy-npg, respectively.[299] This procedure enhances Y and, in the case of PPy-npg, also $\varepsilon_{\mathrm{ampl}}$.[299] Additionally, two classical lead-zirconium-titanate piezo-actuator are listed – PZT4 and PZT8.[314] The strain amplitude is computed by assuming an applied electrical field of $U = 2\,\mathrm{kV\,mm^{-1}}$ [313] and piezoelectric coefficient $d_{33} = 372\,\mathrm{pC\,N^{-1}}$ (PZT4) and $d_{33} = 275\,\mathrm{pC\,N^{-1}}$ (PZT8)[314].

material	$\varepsilon_{\mathrm{ampl}}$	Y	density	work density	
				$\mathcal{W}_{\mathrm{V}}$	$\mathcal{W}_{\mathrm{m}}$
	%	GPa	$\mathrm{g\,cm^{-3}}$	$\mathrm{kJ\,m^{-3}}$	$\mathrm{J\,kg^{-1}}$
pSi	$1.69 \cdot 10^{-3}$	26.1	1.07	$1.9 \cdot 10^{-3}$	$1.7 \cdot 10^{-3}$
PPy-pSi	0.044	30.1	1.49	1.46	0.98
npg	$4.7 \cdot 10^{-3}$	1	5.2	$5.5 \cdot 10^{-4}$	$1.1 \cdot 10^{-4}$
PPy-npg	0.10 – 0.51	0.5 – 1.0	5.4 – 5.7	0.1 – 6.7	$2.2 \cdot 10^{-2}$ – 1.2
PZT4	0.074	58.9	7.65	8.15	1.06
PZT8	0.055	80	7.75	6.05	0.78

6. Conclusion

Overall in this work, the successful demonstration of electrochemical actuation in porous silicon is presented. The electrosorption-induced mechanical actuation of electrolyte-filled porous silicon, i.e. without the polypyrrole pore filling, is extensively studied. A detailed electrochemical characterisation of its behaviour in acidic and salt solutions leads to a deeper understanding of porous silicon. An anodic oxidation leads to a stable electrochemical behaviour. Porous silicon as well as bulk silicon electrodes exhibit near ideal polarisability in aqueous electrolytes. With respect to its actuation mechanism, it is established that an induced surface stress change through the accumulation of electrolyte anions in the electric double layer is responsible for the stable and highly reproducible actuation of the entire porous silicon structure. Surprisingly, the electrosorption-induced actuation in porous silicon exhibits an inverse proportionality on applied potential and accumulated charge. That means, porous silicon expands upon a potential reduction and a thereby caused charge ejection, which is in clear contrast to other nanoporous materials, especially metals. The electrocapillary coupling parameter $\varsigma = +0.657 \pm 0.007\,\mathrm{V}$ is successfully determined for a bulk silicon surface for the first time in this thesis. On a microscopical level, the cause of electrosorption-induced actuation is embedded in a change of surface stress. Due to the combined approach of in situ dilatometry and laser cantilever bending, it can be corroborated that this relation also holds true for porous silicon. The qualitative analysis of the actuation with respect to the porous silicon mechanics and in comparison to surface-stress-induced actuation at bulk silicon surfaces particularly highlights the importance of the porous silicon morphology on the single-pore scale, its semiconductor features and the formation of silicon oxides. In this regard, future research on tuning the pore morphology of porous silicon to obtain smoother pore walls and in particular a higher electrochemically addressable surface area would be beneficial for the electrosorption-induced actuation. Moreover, the influence of the doping concentration on the electrosorption-induced actuation could be a further topic to investigate. The doping could be for example adjusted after the porous silicon synthesis by a re-doping procedure.[315]

Furthermore, within the framework of this work comprehensive research has been conducted to gain a deeper understanding of the mechanics of porous silicon. Porous silicon represents a challenging material for the assessments of its mechanical properties due to its anisotropic crystal structure coupled with the intricate, thin layer sample geometry. A technique of laser-excited elastic guided wave characterisation, established here for the measurement on porous silicon, allows a detailed analysis of porous silicon mechanics including the elastic coefficients. It reveals that porous silicon possesses an in-plane, transverse isotropy, in which the pore structure itself offsets the cubic symmetry within the pore walls.

All in all, the presented work demonstrates the robustness of porous silicon with regard to potential actuation applications which utilise the electrochemo-mechanical coupling occurring at silicon surfaces. Akin to a variety of studies which demonstrate the versatile nature

of liquid-filled porous silicon with respect to, for instance, phase selection controlled by the pore confinement [18, 316], an adaptable wetting [317], photonic properties [40, 318], a controllable pore wall topography [319] and liquid-influenced mechanical properties [38, 320], this work shows that porous silicon is a candidate for a facilely and straightforwardly fabricated, material-integrated actuator functionality.
The integration of the electroactive, electrically conductive polymer polypyrrole into the porous structure, is the second main approach to achieve an actuator functionality in porous silicon. The presented work shows that a robust, highly reproducible electrochemical actuation of a polypyrrole porous silicon hybrid material is achieved. In this work polypyrrole-filled porous silicon is prepared with a higher aspect ratio of pore length to pore diameter than reported before in literature. Furthermore, not only porous silicon epi-layers with dead-end pores but also open-pore membranes are successfully functionalised, which has not been reported yet. A comprehensive investigation of the synthesis process as well as the electrochemical behaviour demonstrates that the hybrid material exhibits characteristics known from studies on polypyrrole in thin-film geometries. Thus, the study of the actuation functionality of the hybrid material is performed under an electrochemical control that is well established. The study is here successfully carried out both in acidic aqueous solutions as well as an isotonic saline solution. In both electrolytes a highly controllable, repeatable mechanical actuation is demonstrated. The change in strain of the polypyrrole porous silicon hybrid follows the applied potential and the accumulated charge with a highly linear dependency in phase. This is also reflected in the strain-charge coupling coefficient which has a positive sign. By contrast, the electrosorption-induced actuation of unfilled porous silicon exhibits an inverse dependency of actuation strain on potential and charge. Interestingly, it is found that the amplitude of the strain-charge coupling coefficient is similar for both actuation mechanisms investigated in this work. The achievable strain amplitudes, however, are one order of magnitude larger for the polypyrrole porous silicon hybrid material. The actuation performance with respect to the strain-charge coupling coefficient is comparable to a polypyrrole nanoporous gold hybrid material. Furthermore, it is corroborated that the actuation performance strongly depends on the type of anion.
The macroscopic actuation measurements are complemented by a high resolution in situ X-ray diffraction measurements that yield extensive insight into the electrochemical actuation on the microscopic level of the pSi pore wall crystal lattice. With two different measurement geometries it is possible to investigate the actuation impact of the polypyrrole filling on the pore walls in the in-plane and out-of-plane direction of a PPy-pSi epi-layer. In both directions the crystal-lattice-level actuation clearly linearly follows applied potential and accumulated charge. A TEM-tomography-based micromechanical simulation successfully links microscopic and macroscopic level. Furthermore, it confirms the results obtained on the porous silicon mechanics in the independent laser-excited elastic guided wave study. Namely, the in-plane mechanical behaviour is prevalently isotropic, even though the monocrystalline silicon pore walls are anisotropic in their elasticity. All in all, the polypyrrole porous silicon hybrid material exhibits a robust actuator functionality. In comparison to classical piezo actuators and polypyrrole-functionalised nanoporous gold, the PPy-pSi hybrid material performs well with regard to its work density.
In particular, this work demonstrates the benefit of combining the preparation of porous materials in a self-organised manner in combination with self-assembled functionalisation on the single nanopore scale, especially, as functional nanocomposites integrated in

a macroscopic device constitute a particular challenge [321]. This approach enables the fabrication of reliable three-dimensional materials. Furthermore, porous silicon and the PPy-pSi hybrid solely comprises a combination of light, abundantly available elements as hydrogen, carbon, silicon, oxygen, nitrogen and chloride on different scales to achieve its functionality, resembling thereby biological multiscale composites.[114] That means in particular, the here investigated materials do not contain any heavy-metals, which are often responsible for the high performance of piezo-ceramics.
Porous silicon with its versatile, manifold features such as the abundance of surface modification routes, structuring processes and functionalities, e.g. its photoluminescence [35, 52], in combination with the here introduced, robust actuation functionality, has the possibility to prompt novel domains of applications. These could possibly include a combination with electrochemical energy storages [23, 28, 29, 31, 113], fluidics [15, 322], sensorics [51, 323] and integrated, on-chip photonics [324]. Biology is another field of research that could profit from porous silicon actuators. In biological systems, mechanical stress influences living tissue with regard to its growth, its form and even function.[325–327] A mechanical impulse alters cells. The cell morphology, the signalling between cells and transcription of genes is influenced by piezo-channels for example.[328] Since both porous silicon and polypyrrole are biocompatible, the hybrid material and the mechanical stimulation they provide could be utilised in biological or bio-medical environments. Thus, mechanical impulses could be converted to a biomedical signal on the single-cell level.
It can also be envisioned that both porous silicon and the PPy-pSi hybrid material exhibit the inverse functionality to an actuation. Thus, a mechanical load would result in a change in potential and accumulated charge. Since both the movement of anions in pSi and PPy-pSi and their mechanical response is highly reversible, an applied external load should also lead to a change of the amount of incorporated ions and therefore in potential between the material and electrolyte. Nanoporous gold for example clearly exhibits this inverse actuation functionality.[182] For the polypyrrole-functionalised material it is still under discussion what the exact cause of this inverse effect in the polymer is. It is either attributed to an ion motion induced by stress gradients, Donnan potentials that emerge at the polypyrrole-electrolyte interface or a mixture of the two.[329] The comparison with other actuator materials shows, however, that achievable strain amplitudes are in the same range for the here investigated materials. Thus, it would be interesting to study porous silicon with regard to an electrical potential emergence through mechanical loads or its use as a strain sensor. In terms of (bio-)medical technologies and applications, porous silicon could be employed as a stress sensor in vivo or generally in aqueous electrolytes, e.g. for structural health monitoring [326, 327].
Another type of sensor might be realised by coupling the actuation effect with the unique photoluminescence property of porous silicon. The photoluminescent response of porous silicon is utilised for different sensing applications. Changes in the surface chemistry for example are eminently sensitively detected by a shift of the photoluminescence peak in intensity or wavelength.[57] A change in strain of the porous silicon pore walls could possibly affect the photoluminescence in a similar manner. The thickness of the pore walls is the origin of the quantum-wire effect, which gives microporous silicon its photoluminescent properties. Thus, a reversible straining of the pore walls, as studied in this work in detail, should have a significant impact on the photoluminescent response. However, the type of porous silicon studied here is not exhibiting any photoluminescence according to literature.[35] Therefore, it has to be investigated if an electrochemo-mechanical coupling

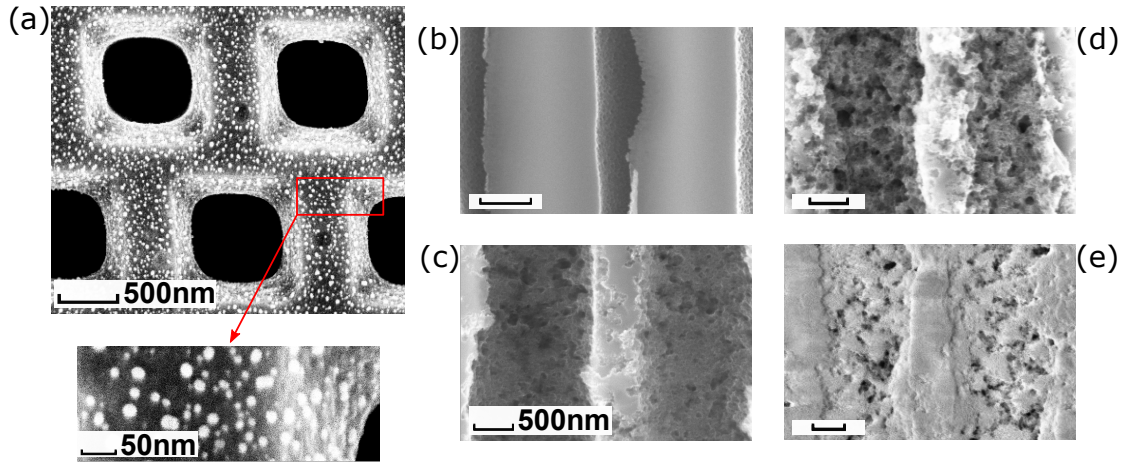

Figure 6.1.: **Hierarchically porous silicon.** (a) Top view of photolithographically produced macropores arranged in a hexagonal pattern. The membrane is covered with precipitated silver nanoparticles, also shown in a magnification in the inset. The nanoparticles are introducing the mesoporous pore network in the pore wall between macropores in a further MACE etching process, which has not yet been performed for the depicted membrane. (b)-(e) Side view of two macropores with a pore wall in between in different stages of the preparation process. Each scale bar represents 500 nm. (b) Macroporous membrane without the mesoporous pore network. (c) The silver nanoparticles are starting to migrate further into the membrane and a meso-pore formation ensues at the beginning of the MACE etching process. (d) The nanoparticles are starting to etch deeper into the pore wall so that the macropores start to be interconnected. (e) A thermal oxidation that preserves the porous features results in hierarchically porous silica. Adapted with permission from reference [330].

is also present in microporous silicon and determine the magnitude of the effect. Research in this direction could open up a pathway to a porous-silicon-based optical strain sensor which is able to operate in aqueous electrolytes.
A general approach to further improve functional characteristics is the introduction of hierarchically porous silicon. A hierarchical pore structure encompasses nanopores in the low mesoporous regime, i.e. pore diameters in the proximity of $10-60$ nm, together with larger macropores. The latter enable a fast ion transport, comparable to bulk electrolyte properties, without the strong confinement effects of smaller pores, while a functionalisation on the level of the nanopores is providing a large effective mechanical response. Overall, this hierarchical approach is a promising concept that can achieve a substantial increase in dynamic functional capacity. The same basic working principle is utilised in nature by pore-capillary-networks such as biological tissues, which combine nano and macropores to achieve mass transport capabilities, while having a large inner surface area that provides functionality and an overall lightweight, robust structure.[114, 331–334] Conceiving artificial materials that exhibit a hierarchical porosity attracts attention as an active research field, especially with regard to their fabrication methods.[22, 333, 335–344] Recently such

hierarchical materials have been realised in nanoporous gold [345] or ceramics [346]. In particular, a hierarchically porous structure in the common, mainstream semiconductor silicon would be interesting for a variety of fields. So far, a hierarchical structure has been implemented in porous nanoparticles or epi-layers with dead-end pores.[347–350] Within the framework of this thesis, it has been possible to fabricate hierarchically porous silicon membranes by using different processing techniques within the scope of a master thesis supervised by the author.[330, 351, 352] A wafer-scale synthesis of up to 300 µm thick membranes is achieved by combining photolithography-prepared macropores with self-organised metal-assisted chemical etching (MACE) for nanopores. From a materials science standpoint, this approach bridges the gap between two fundamental methods, i.e. bottom-up and top-down, to achieve a tailored material synthesis. The pores in the resulting porous material are bimodally distributed. The macropores have a diameter in the range of 1 µm and are organised in a hexagonal pattern, as depicted in Figure 6.1(a). The second part of the preparation process aims to embed a mesoporous pore network within the macropore pore walls, which are shown in Figure 6.1(b). A MACE approach, which works without an applied current and is independent of the silicon crystal orientation, is chosen.[52, 353–357] So far, MACE is primarily utilised to synthesise silicon nanowires [353, 358–361] and rarely porous silicon structures [362]. Silver nanoparticles are deposited onto the macroporous membrane by a precipitation reaction, see Figure 6.1(a) and the magnified inset. In an HF solution together with an oxidising agent, the nanoparticles catalyse a reduction-oxidation reaction, during which holes are injected into the silicon pore walls, which, in turn, enable the removal of silicon atoms by HF molecules. Interestingly, it is found that the nanoparticles are mobile during this process.[352] They are etching into the pore wall before detaching, entering into solution and reattaching at another site and repeating the etching of silicon. Thus, the nanoparticles may be considered as self-propelled particles that autonomously create the desired mesoporous pore-space between the macropores.[352] Adjusting the concentration of the particles and the chemical conditions enables tailored pore characteristics as visible when comparing Figure 6.1(c) with 6.1(d).[352] Lastly, a thermal oxidation step transforms hierarchically porous silicon without any major changes in its structure into a monolithic, amorphous hierarchically porous silica material, which could be beneficial for optical applications. An example of its structure is shown in Figure 6.1(e).

Overall, in this work it can be ascertained that the actuation performance on the basis of the work density of porous-silicon-based actuators is in the range of other porous materials and classical piezo ceramics. However, in comparison especially to piezo ceramics the kinetics of porous silicon actuators occur on another time scale. The step-coulombmetry experiments reveal that the hydrodynamic flow and the anions in their diffusion and drift-dynamics are limited in the pore space due to strong confinement effects and interactions with the pore wall. This applies in particular to the polypyrrole-functionalised porous silicon. The resulting switching times are on the scale of seconds, whereas piezo ceramics are operating with achievable actuation rates in the kHz-regime or even higher [60, 314]. The hierarchically porous structure of the material is a promising approach for future research to significantly improve the actuation kinetics while maintaining the overall mechanical actuation performance.

Bibliography

[1] A. Uhlir Jr, "Electrolytic shaping of germanium and silicon", Bell System Technical Journal **35**, 333–347 (1956).

[2] V. Lehmann and U. Gösele, "Porous silicon formation: A quantum wire effect", Applied Physics Letters **58**, 856 (1991).

[3] L. T. Canham, "Silicon quantum wire array fabrication by electrochemical and chemical dissolution of wafers", Applied Physics Letters **57**, 1046–1048 (1990).

[4] V. Lehmann and U. Gösele, "Porous silicon: Quantum sponge structures grown via a self-adjusting etching process", Advanced Materials **4**, 114–116 (1992).

[5] T. Lane and S. Burns, "Silica, silicon and silicones... unraveling the mystery", Immunology of Silicones, 3–12 (1996).

[6] N. N. Greenwood and A. Earnshaw, *Chemistry of the elements* (Elsevier, 2012).

[7] V. Lehmann, *Electrochemistry of silicon: Instrumentation, science, materials and applications* (Wiley-VCH, Weinheim, 2002).

[8] K. Barla, R. Herino, G. Bomchil, J. Pfister and A. Freund, "Determination of lattice parameter and elastic properties of porous silicon by X-ray diffraction", Journal of Crystal Growth **68**, 727–732 (1984).

[9] P. Wiltzius, F. Bates, S. Dierker and G. Wignall, "Structure of porous vycor glass", Physical Review A **36**, 2991 (1987).

[10] J. Weissmüller, R. Viswanath, D. Kramer, P. Zimmer, R. Würschum and H. Gleiter, "Charge-induced reversible strain in a metal", Science **300**, 312–315 (2003).

[11] G. Martínez-Edo, A. Balmori, I. Pontón, A. Martí del Rio and D. Sánchez-García, "Functionalized ordered mesoporous silicas (MCM-41): Synthesis and applications in catalysis", Catalysts **8**, 617 (2018).

[12] D. Zhao, J. Sun, Q. Li and G. D. Stucky, "Morphological control of highly ordered mesoporous silica SBA-15", Chemistry of Materials **12**, 275–279 (2000).

[13] F. Kleitz, S. H. Choi and R. Ryoo, "Cubic Ia3d large mesoporous silica: Synthesis and replication to platinum nanowires, carbon nanorods and carbon nanotubes", Chemical Communications, 2136–2137 (2003).

[14] S. Leonard, J. Mondia, H. Van Driel, O. Toader, S. John, K. Busch, A. Birner, U. Gösele and V. Lehmann, "Tunable two-dimensional photonic crystals using liquid crystal infiltration", Physical Review B **61**, R2389 (2000).

[15] S. Gruener and P. Huber, "Knudsen diffusion in silicon nanochannels", Physical Review Letters **100**, 064502 (2008).

[16] G. Gor, L. Bertinetti, N. Bernstein, T. Hofmann, P. Fratzl and P. Huber, "Elastic response of mesoporous silicon to capillary pressures in the pores", Applied Physics Letters **106**, 261901 (2015).

[17] D. Kondrashova, A. Lauerer, D. Mehlhorn, H. Jobic, A. Feldhoff, M. Thommes, D. Chakraborty, C. Gommes, J. Zecevic, P. De Jongh, A. Bunde, J. Kärger and R. Valiullin, "Scale-dependent diffusion anisotropy in nanoporous silicon", Scientific Reports **7**, 1–10 (2017).

[18] P. Huber, "Soft matter in hard confinement: Phase transition thermodynamics, structure, texture, diffusion and flow in nanoporous media", Journal of Physics: Condensed Matter **27**, 103102 (2015).

[19] O. Vincent, A. Szenicer and A. D. Stroock, "Capillarity-driven flows at the continuum limit", Soft Matter **12**, 6656–6661 (2016).

[20] L. G. Cencha, G. Dittrich, P. Huber, C. L. Berli and R. Urteaga, "Precursor film spreading during liquid imbibition in nanoporous photonic crystals", Physical Review Letters **125**, 234502 (2020).

[21] T. Hofmann, D. Wallacher, P. Huber and K. Knorr, "Triple point behavior of Ar and N_2 in mesopores", Journal of Low Temperature Physics **140**, 91–103 (2005).

[22] H. Jia, X. Li, J. Song, X. Zhang, L. Luo, Y. He, B. Li, Y. Cai, S. Hu, X. Xiao, C. Wang, K. M. Rosso, R. Yi, R. Patel and J.-G. Zhang, "Hierarchical porous silicon structures with extraordinary mechanical strength as high-performance lithium-ion battery anodes", Nature Communications **11**, 1–9 (2020).

[23] G. Zhu, D. Chao, W. Xu, M. Wu and H. Zhang, "Microscale silicon-based anodes: Fundamental understanding and industrial prospects for practical high-energy lithium-ion batteries", ACS Nano **15**, 15567–15593 (2021).

[24] X. Zhang, D. Kong, X. Li and L. Zhi, "Dimensionally designed carbon–silicon hybrids for lithium storage", Advanced Functional Materials **29**, 1806061 (2019).

[25] X. H. Liu, J. W. Wang, S. Huang, F. Fan, X. Huang, Y. Liu, S. Krylyuk, J. Yoo, S. A. Dayeh, A. V. Davydov, S. X. Mao, S. T. Picraux, S. Zhang, J. Li, T. Zhu and J. Y. Huang, "In situ atomic-scale imaging of electrochemical lithiation in silicon", Nature Nanotechnology **7**, 749–756 (2012).

[26] C. K. Chan, H. Peng, G. Liu, K. McIlwrath, X. F. Zhang, R. A. Huggins and Y. Cui, "High-performance lithium battery anodes using silicon nanowires", Nature Nanotechnology **3**, 31–35 (2008).

[27] P. Gao, X. Huang, Y. Zhao, X. Hu, D. Cen, G. Gao, Z. Bao, Y. Mei, Z. Di and G. Wu, "Formation of Si hollow structures as promising anode materials through reduction of silica in $AlCl_3$–NaCl molten salt", ACS Nano **12**, 11481–11490 (2018).

[28] C. Tang, Y. Liu, C. Xu, J. Zhu, X. Wei, L. Zhou, L. He, W. Yang and L. Mai, "Ultrafine nickel-nanoparticle-enabled SiO_2 hierarchical hollow spheres for high-performance lithium storage", Advanced Functional Materials **28**, 1704561 (2018).

[29] D. Chen, X. Mei, G. Ji, M. Lu, J. Xie, J. Lu and J. Y. Lee, "Reversible lithium-ion storage in silver-treated nanoscale hollow porous silicon particles", Angewandte Chemie **124**, 2459–2463 (2012).

[30] C. Yang, Y. Zhang, J. Zhou, C. Lin, F. Lv, K. Wang, J. Feng, Z. Xu, J. Li and S. Guo, "Hollow Si/SiO_x nanosphere/nitrogen-doped carbon superstructure with a double shell and void for high-rate and long-life lithium-ion storage", Journal of Materials Chemistry A **6**, 8039–8046 (2018).

[31] Y. Yao, M. T. McDowell, I. Ryu, H. Wu, N. Liu, L. Hu, W. D. Nix and Y. Cui, "Interconnected silicon hollow nanospheres for lithium-ion battery anodes with long cycle life", Nano Letters **11**, 2949–2954 (2011).

[32] K. Valalaki, P. Benech and A. Galiouna Nassiopoulou, "High Seebeck coefficient of porous silicon: Study of the porosity dependence", Nanoscale Research Letters **11**, 1–8 (2016).

[33] N. Gostkowska-Lekner, D. Kojda, J.-E. Hoffmann, M. May, P. Huber, K. Habicht and T. Hofmann, "Synthesis of organic–inorganic hybrids based on the conjugated polymer P3HT and mesoporous silicon", Microporous and Mesoporous Materials **343**, 112155 (2022).

[34] S. Mariazzi, B. Rienäcker, R. M. Maffei, L. Povolo, S. Sharma, R. Caravita, L. Penasa, P. Bettotti, M. Doser and R. Brusa, "Forward emission of positronium from nanochanneled silicon membranes", Physical Review B **105**, 115422 (2022).

[35] L. Canham, *Handbook of porous silicon* (Springer, 2015).

[36] X. Wang, W. Gonçalves, D. Lacroix, M. Isaiev, S. Gomés and K. Termentzidis, "Thermal conductivity temperature dependence of water confined in nanoporous silicon", Journal of Physics: Condensed Matter **34**, 305701 (2022).

[37] P. Lishchuk, D. Andrusenko, M. Isaiev, V. Lysenko and R. Burbelo, "Investigation of thermal transport properties of porous silicon by photoacoustic technique", International Journal of Thermophysics **36**, 2428–2433 (2015).

[38] J. Zhang, B. Chen, X. Chen and X. Hou, "Liquid-based adaptive structural materials", Advanced Materials **33**, 2005664 (2021).

[39] A. V. Kityk, M. Busch, D. Rau, S. Calus, C. V. Cerclier, R. Lefort, D. Morineau, E. Grelet, C. Krause, A. Schönhals, B. Frick and P. Huber, "Thermotropic orientational order of discotic liquid crystals in nanochannels: An optical polarimetry study and a Landau–de Gennes analysis", Soft Matter **10**, 4522–4534 (2014).

[40] K. Sentker, A. W. Zantop, M. Lippmann, T. Hofmann, O. H. Seeck, A. V. Kityk, A. Yildirim, A. Schönhals, M. G. Mazza and P. Huber, "Quantized self-assembly of discotic rings in a liquid crystal confined in nanopores", Physical Review Letters **120**, 067801 (2018).

[41] C. R. Ocier, C. A. Richards, D. A. Bacon-Brown, Q. Ding, R. Kumar, T. J. Garcia, J. Van De Groep, J.-H. Song, A. J. Cyphersmith, A. Rhode, A. N. Perry, A. J. Littlefield, J. Zhu, D. Xie, H. Gao, J. F. Messinger, M. L. Brongersma, K. C. Toussaint, L. L. Goddard and P. V. Braun, "Direct laser writing of volumetric gradient index lenses and waveguides", Light: Science & Applications **9**, 1–14 (2020).

[42] M. P. Stewart and J. M. Buriak, "Chemical and biological applications of porous silicon technology", Advanced Materials **12**, 859–869 (2000).

[43] M. J. Sailor, "Chemical reactivity and surface chemistry of porous silicon", in *Handbook of porous silicon*, edited by L. Canham (Springer International Publishing, 2014), pp. 355–380.

[44] C. Chiappini, E. De Rosa, J. O. Martinez, X. Liu, J. Steele, M. M. Stevens and E. Tasciotti, "Biodegradable silicon nanoneedles delivering nucleic acids intracellularly induce localized in vivo neovascularization", Nature Materials **14**, 532–539 (2015).

[45] L. T. Canham, "Bioactive silicon structure fabrication through nanoetching techniques", Advanced Materials **7**, 1033–1037 (1995).

[46] L. Canham, C. Reeves, A. Loni, M. Houlton, J. Newey, A. Simons and T. Cox, "Calcium phosphate nucleation on porous silicon: Factors influencing kinetics in acellular simulated body fluids", Thin Solid Films **297**, 304–307 (1997).

[47] L. Canham, "Biomedical applications of porous silicon", Properties of Porous Silicon **18**, 12–22 (1997).

[48] A. Tzur-Balter, Z. Shatsberg, M. Beckerman, E. Segal and N. Artzi, "Mechanism of erosion of nanostructured porous silicon drug carriers in neoplastic tissues", Nature Communications **6**, 1–8 (2015).

[49] D. N. Kumar, S. Reingewirtz, M. Shemesh, R. Suckeveriene and G. Shtenberg, "Dnazyme-based biosensor for sub ppb lead ions detection using porous silicon Fabry-Pérot interferometer", Sensors and Actuators B: Chemical **362**, 131761 (2022).

[50] V. Vendamani, S. N. Rao, A. P. Pathak and V. R. Soma, "Silicon nanostructures for molecular sensing: A review", ACS Applied Nano Materials **5**, 4550–4582 (2022).

[51] V. S.-Y. Lin, K. Motesharei, K.-P. S. Dancil, M. J. Sailor and M. R. Ghadiri, "A porous silicon-based optical interferometric biosensor", Science **278**, 840–843 (1997).

[52] M. J. Sailor, *Porous silicon in practice - preparation, characterization and applications* (Wiley-VCH, Weinheim, 2011).

[53] M. Sailor, "Sensor applications of porous silicon", Properties of Porous Silicon **18**, 364–370 (1997).

[54] E. C. Wu, J.-H. Park, J. Park, E. Segal, F. Cunin and M. J. Sailor, "Oxidation-triggered release of fluorescent molecules or drugs from mesoporous Si microparticles", ACS Nano **2**, 2401–2409 (2008).

[55] S. Micera and E. Redolfi Riva, "Wireless neuromodulation with porous silicon", Nature Materials **21**, 614–616 (2022).

[56] K.-P. S. Dancil, D. P. Greiner and M. J. Sailor, "A porous silicon optical biosensor: Detection of reversible binding of IgG to a protein A-modified surface", Journal of the American Chemical Society **121**, 7925–7930 (1999).

[57] M. J. Sailor and E. C. Wu, "Photoluminescence-based sensing with porous silicon films, microparticles, and nanoparticles", Advanced Functional Materials **19**, 3195–3208 (2009).

[58] A. Prominski, J. Shi, P. Li, J. Yue, Y. Lin, J. Park, B. Tian and M. Y. Rotenberg, "Porosity-based heterojunctions enable leadless optoelectronic modulation of tissues", Nature Materials **21**, 647–655 (2022).

[59] A. Lugstein, M. Steinmair, A. Steiger, H. Kosina and E. Bertagnolli, "Anomalous piezoresistance effect in ultrastrained silicon nanowires", Nano Letters **10**, 3204–3208 (2010).

[60] H. Janocha, *Actuators* (Springer, 2004).

[61] Q. Zhao, J. W. Dunlop, X. Qiu, F. Huang, Z. Zhang, J. Heyda, J. Dzubiella, M. Antonietti and J. Yuan, "An instant multi-responsive porous polymer actuator driven by solvent molecule sorption", Nature Communications **5**, 1–8 (2014).

[62] C. Ganser, G. Fritz-Popovski, R. Morak, P. Sharifi, B. Marmiroli, B. Sartori, H. Amenitsch, T. Griesser, C. Teichert and O. Paris, "Cantilever bending based on humidity-actuated mesoporous silica/silicon bilayers", Beilstein Journal of Nanotechnology **7**, 637–644 (2016).

[63] D. Van Opdenbosch, G. Fritz-Popovski, W. Wagermaier, O. Paris and C. Zollfrank, "Moisture-driven ceramic bilayer actuators from a biotemplating approach", Advanced Materials **28**, 5235–5240 (2016).

[64] A. Grosman, J. Puibasset and E. Rolley, "Adsorption-induced strain of a nanoscale silicon honeycomb", Europhysics Letters **109**, 56002 (2015).

[65] G. Y. Gor, P. Huber and N. Bernstein, "Adsorption-induced deformation of nanoporous materials—a review", Applied Physics Reviews **4**, 011303 (2017).

[66] E. Rolley, N. Garroum and A. Grosman, "Using capillary forces to determine the elastic properties of mesoporous materials", Physical Review B **95**, 064106 (2017).

[67] L. Kong and W. Chen, "Carbon nanotube and graphene-based bioinspired electrochemical actuators", Advanced Materials **26**, 1025–1043 (2014).

[68] J. Liang, Y. Huang, J. Oh, M. Kozlov, D. Sui, S. Fang, R. H. Baughman, Y. Ma and Y. Chen, "Electromechanical actuators based on graphene and graphene/Fe_3O_4 hybrid paper", Advanced Functional Materials **21**, 3778–3784 (2011).

[69] L. Liu, L. Su, Y. Lu, Q. Zhang, L. Zhang, S. Lei, S. Shi, M. D. Levi and X. Yan, "The origin of electrochemical actuation of MnO_2/Ni bilayer film derived by redox pseudocapacitive process", Advanced Functional Materials **29**, 1806778 (2019).

[70] V. Morozov, A. Zegrya, G. G. Zegrya and G. G. Savenkov, "Piezoelectric properties of porous silicon", JETP Letters **114**, 625–629 (2021).

[71] S. H. Baek, J. Park, D. M. Kim, V. A. Aksyuk, R. R. Das, S. D. Bu, D. A. Felker, J. Lettieri, V. Vaithyanathan, S. S. N. Bharadwaja, N. Bassiri-Gharb, Y. B. Chen, H. P. Sun, C. M. Folkman, H. W. Jang, D. J. Kreft, S. K. Streiffer, R. Ramesh, X. Q. Pan, S. Trolier-McKinstry, D. G. Schlom, M. S. Rzchowski, R. H. Blick and C. B. Eom, "Giant piezoelectricity on Si for hyperactive MEMS", Science **334**, 958–961 (2011).

[72] H.-J. Jin and J. Weissmüller, "Bulk nanoporous metal for actuation", Advanced Engineering Materials **12**, 714–723 (2010).

[73] E. Seker, M. L. Reed and M. R. Begley, "Nanoporous gold: Fabrication, characterization, and applications", Materials **2**, 2188–2215 (2009).

[74] H.-J. Jin, X.-L. Wang, S. Parida, K. Wang, M. Seo and J. Weissmüller, "Nanoporous Au-Pt alloys as large strain electrochemical actuators", Nano Letters **10**, 187–194 (2010).

[75] R. Viswanath and J. Weissmüller, "Electrocapillary coupling coefficients for hydrogen electrosorption on palladium", Acta Materialia **61**, 6301–6309 (2013).

[76] L.-H. Shao, J. Biener, H.-J. Jin, M. M. Biener, T. F. Baumann and J. Weissmüller, "Electrically tunable nanoporous carbon hybrid actuators", Advanced Functional Materials **22**, 3029–3034 (2012).

[77] H. v. Helmholtz, "Ueber einige Gesetze der Vertheilung elektrischer Ströme in körperlichen Leitern, mit Anwendung auf die thierisch-elektrischen Versuche (Schluss.)", Annalen der Physik **165**, 353–377 (1853).

[78] J. Weissmüller, "Electrocapillarity of solids and its impact on heterogeneous catalysis", in *Electrocatalysis* (Wiley Online Library, 2013) Chap. 5, pp. 163–220.

[79] F. Weigend, F. Evers and J. Weissmüller, "Structural relaxation in charged metal surfaces and cluster ions", Small **2**, 1497–1503 (2006).

[80] M. Smetanin, R. Viswanath, D. Kramer, D. Beckmann, T. Koch, L. Kibler, D. Kolb and J. Weissmüller, "Surface stress-charge response of a (111)-textured gold electrode under conditions of weak ion adsorption", Langmuir **24**, 8561–8567 (2008).

[81] R. Raiteri and H.-J. Butt, "Measuring electrochemically induced surface stress with an atomic force microscope", The Journal of Physical Chemistry **99**, 15728–15732 (1995).

[82] S. Hoppe, A. Michl, J. Weissmüller and S. Müller, "Ab-initio modeling of electromechanical coupling at Si surfaces", Journal of Applied Physics **116**, 073507 (2014).

[83] M. Satoh, K. Kaneto and K. Yoshino, "Dependences of electrical and mechanical-properties of conducting polypyrrole films on conditions of electrochemical polymerization in an aqueous-medium", Synthetic Metals **14**, 289–296 (1986).

[84] M. Ma, L. Guo, D. G. Anderson and R. Langer, "Bio-inspired polymer composite actuator and generator driven by water gradients", Science **339**, 186–189 (2013).

[85] J. D. Madden, P. G. Madden and I. W. Hunter, "Conducting polymer actuators as engineering materials", in Smart structures and materials 2002: Electroactive polymer actuators and devices (eapad), Vol. 4695 (2002), pp. 176–191.

[86] Q. Pei and O. Inganas, "Electrochemical applications of the bending beam method; A novel way to study ion transport in electroactive polymers", Solid State Ionics **60**, 161–166 (1993).

[87] J. Madden, R. Cush, T. Kanigan and I. Hunter, "Fast contracting polypyrrole actuators", Synthetic Metals **113**, 185–192 (2000).

[88] E. Jager, E. Smela and O. Inganas, "Microfabricating conjugated polymer actuators", Science **290**, 1540–1545 (2000).

[89] T. Shoa, M. Cole, N. R. Munce, V. Yang and J. D. Madden, "Polypyrrole operating voltage limits in aqueous sodium hexafluorophosphate", in Electroactive polymer actuators and devices (eapad) 2007, Vol. 6524 (SPIE, 2007), pp. 606–613.

[90] T. Shoa, J. D. Madden, T. Mirfakhrai, G. Alici, G. M. Spinks and G. G. Wallace, "Electromechanical coupling in polypyrrole sensors and actuators", Sensors and Actuators A: Physical **161**, 127–133 (2010).

[91] J. Madden, N. Vandesteeg, P. Anquetil, P. Madden, A. Takshi, R. Pytel, S. Lafontaine, P. Wieringa and I. Hunter, "Artificial muscle technology: Physical principles and naval prospects", IEEE Journal of Oceanic Engineering **29**, 706–728 (2004).

[92] T. F. Otero, "Artificial muscles, electrodissolution and redox processes in conducting polymers", in *Handbook of organic conductive molecules and polymers*, Vol. 4, edited by H. S. Nalwa (John Wiley & Sons: New York, NY, USA, 1997), pp. 518–594.

[93] R. Balint, N. J. Cassidy and S. H. Cartmell, "Conductive polymers: Towards a smart biomaterial for tissue engineering", Acta Biomaterialia **10**, 2341–2353 (2014).

[94] E. Smela, "Conjugated polymer actuators for biomedical applications", Advanced Materials **15**, 481–494 (2003).

[95] J. Bredas and G. Street, "Polarons, bipolarons, and solitons in conducting polymers", Accounts of Chemical Research **18**, 309–315 (1985).

[96] P. Burgamyer and R. Murray, "An ion gate membrane: Electrochemical control of ion permeability through a membrane with an embedded electrode", Journal of the American Chemical Society **104**, 6139–6140 (1982).

[97] T. F. Otero, J. J. Lopez Cascales and G. Vazquez Arenas, "Mechanical characterization of free-standing polypyrrole film", Materials Science and Engineering C-Biomimetic and Supramolecular Systems **27**, 18–22 (2007).

[98] T. Shoa, T. Mirfakhrai and J. D. W. Madden, "Electro-stiffening in polypyrrole films: Dependence of Young's modulus on oxidation state, load and frequency", Synthetic Metals **160**, 1280–1286 (2010).

[99] T. A. Skotheim and J. Reynolds, *Handbook of conducting polymers* (CRC press, 2007).

[100] S. Rajagopalan, M. Sawan, E. Ghafar-Zadeh, O. Savadogo and V. P. Chodavarapu, "A polypyrrole-based strain sensor dedicated to measure bladder volume in patients with urinary dysfunction", Sensors **8**, 5081–5095 (2008).

[101] S. T. McGovern, M. Abbot, R. Emery, G. Alici, V.-T. Truong, G. M. Spinks and G. G. Wallace, "Evaluation of thrust force generated for a robotic fish propelled with polypyrrole actuators", Polymer International **59**, 357–364 (2010).

[102] T. Otero, H. Grande and J. Rodriguez, "Reversible electrochemical reactions in conducting polymers: A molecular approach to artificial muscles", Journal of Physical Organic Chemistry **9**, 381–386 (1996).

[103] Y.-J. Qiu and J. R. Reynolds, "Dopant anion controlled ion transport behavior of polypyrrole", Polymer Engineering & Science **31**, 417–421 (1991).

[104] T. Mirfakhrai, J. D. W. Madden and R. H. Baughman, "Polymer artificial muscles", Materials Today **10**, 30–38 (2007).

[105] P. H. Lakner, M. Brinker, C. Seitz, L. Jacobse, V. Vonk, M. Lippmann, S. Volkov, P. Huber and T. F. Keller, "Probing the electrolyte transfer in ultrathin polypyrrole films by in situ X-ray reflectivity and electrochemistry", Langmuir **36**, 13448–13456 (2020).

[106] G. Spinks, V. Mottaghitalab, M. Bahrami-Saniani, P. Whitten and G. Wallace, "Carbon-nanotube-reinforced polyaniline fibers for high-strength artificial muscles", Advanced Materials **18**, 637–640 (2006).

[107] E. Smela, W. Lu and B. Mattes, "Polyaniline actuators - part 1. PANI(AMPS) in HCl", Synthetic Metals **151**, 25–42 (2005).

[108] Y. Sonoda, W. Takashima and K. Kaneto, "Characteristics of soft actuators based on polypyrrole films", Synthetic Metals **119**, 267–268 (2001).

[109] G. Spinks, L. Liu, G. Wallace and D. Zhou, "Strain response from polypyrrole actuators under load", Advanced Functional Materials **12**, 437–440 (2002).

[110] E. Smela, O. Inganas and I. Lundstrom, "Controlled folding of micromter-size structures", Science **268**, 1735–1738 (1995).

[111] A. Hutchison, T. Lewis, S. Moulton, G. Spinks and G. Wallace, "Development of polypyrrole-based electromechanical actuators", Synthetic Metals **113**, 121–127 (2000).

[112] M. Brinker, G. Dittrich, C. Richert, P. Lakner, T. Krekeler, T. F. Keller, N. Huber and P. Huber, "Giant electrochemical actuation in a nanoporous silicon-polypyrrole hybrid material", Science Advances **6**, eaba1483 (2020).

[113] A. S. Westover, J. W. Tian, S. Bernath, L. Oakes, R. Edwards, F. N. Shabab, S. Chatterjee, A. V. Anilkumar and C. L. Pint, "A multifunctional load-bearing solid-state supercapacitor", Nano Letters **14**, 3197–3202 (2014).

[114] M. Eder, S. Amini and P. Fratzl, "Biological composites—complex structures for functional diversity", Science **362**, 543–547 (2018).

[115] P. Fratzl and R. Weinkamer, "Nature's hierarchical materials", Progress in Materials Science **52**, 1263–1334 (2007).

[116] R. A. Serway and J. W. Jewett, *Principles of physics*, Vol. 1 (Saunders College Pub. Fort Worth, TX, 1998).

[117] Y. Hayamizu, T. Hamaguchi, S. Ushio, T. Abe and F. Shimura, "Temperature dependence of minority-carrier lifetime in iron-diffused p-type silicon wafers", Journal of Applied Physics **69**, 3077–3081 (1991).

[118] O. Madelung, *Semiconductors: Data handbook* (Springer Science & Business Media, 2004).

[119] M. Grundmann, *Physics of semiconductors*, Vol. 11 (Springer, 2010).

[120] X. G. Zhang, *Electrochemistry of silicon and its oxide* (Springer Science & Business Media, 2007).

[121] J. Czochralski, "Ein neues Verfahren zur Messung der Kristallisationsgeschwindigkeit der Metalle", Zeitschrift für physikalische Chemie **92**, 219–221 (1918).

[122] M. A. Hopcroft, W. D. Nix and T. W. Kenny, "What is the Young's modulus of silicon?", Journal of Microelectromechanical Systems **19**, 229–238 (2010).

[123] R. Gross and A. Marx, *Festkörperphysik* (de Gruyter, 2018).

[124] M. Levinshtein, *Handbook series on semiconductor parameters*, Vol. 1 (World Scientific, 1997).

[125] H.-J. Butt, K. Graf and M. Kappl, *Physics and chemistry of interfaces* (John Wiley & Sons, 2003).

[126] G. A. Edwards, A. J. Bergren and M. D. Porter, "Chemically modified electrodes", in *Handbook of electrochemistry*, edited by C. G. Zoski (Elsevier, Amsterdam, 2007), pp. 295–327.

[127] A. J. Bard, L. R. Faulkner and H. S. White, *Electrochemical methods: Fundamentals and applications* (John Wiley & Sons, 2001).

[128] M. Madou, B. Loo, K. Frese and S. R. Morrison, "Bulk and surface characterization of the silicon electrode", Surface Science **108**, 135–152 (1981).

[129] L. Bousse, N. F. De Rooij and P. Bergveld, "Operation of chemically sensitive field-effect sensors as a function of the insulator-electrolyte interface", IEEE Transactions on Electron Devices **30**, 1263–1270 (1983).

[130] R. Memming, *Semiconductor electrochemistry* (John Wiley & Sons, 2015).

[131] K. Gelderman, L. Lee and S. Donne, "Flat-band potential of a semiconductor: Using the Mott–Schottky equation", Journal of Chemical Education **84**, 685 (2007).

[132] N. Sato, *Electrochemistry at metal and semiconductor electrodes* (Elsevier, 1998).

[133] H. Gleiter, J. Weissmüller, O. Wollersheim and R. Würschum, "Nanocrystalline materials: A way to solids with tunable electronic structures and properties?", Acta Materialia **49**, 737–745 (2001).

[134] J.-N. Chazalviel, "Electrochemical transfer via surface states: A new formulation for the semiconductor/electrolyte interface", Journal of The Electrochemical Society **129**, 963 (1982).

[135] G. Oskam, J. Schmidt and P. Searson, "Electrical properties of n-type (III) Si in aqueous $K_4Fe(CN)_6$ solution: II. Intensity modulated photocurrent spectroscopy", Journal of the Electrochemical Society **143**, 2538 (1996).

[136] K. Uosaki and H. Kita, "Effects of the Helmholtz layer capacitance on the potential distribution at semiconductor/electrolyte interface and the linearity of the Mott-Schottky plot", Journal of The Electrochemical Society **130**, 895–897 (1983).

[137] E. Gileadi, *Electrosorption* (Springer Science & Business Media, 2012).

[138] J.-H. Wei and S.-C. Lee, "The structure change of liquid phase deposited silicon oxide by water dilution", Journal of the Electrochemical Society **144**, 1870 (1997).

[139] J. M. Aitken and E. A. Irene, "Silicon dioxide films in semiconductor devices", in *Treatise on materials science & technology*, Vol. 26 (Elsevier, 1985), pp. 1–56.

[140] B. E. Deal and A. Grove, "General relationship for the thermal oxidation of silicon", Journal of Applied Physics **36**, 3770–3778 (1965).

[141] D. Buttard, D. Bellet and G. Dolino, "X-ray-diffraction investigation of the anodic oxidation of porous silicon", Journal of Applied Physics **79**, 8060–8070 (1996).

[142] S. K. Ghandhi, *VLSI fabrication principles: Silicon and gallium arsenide* (John Wiley & Sons, 2008).

[143] D. Gräf, M. Grundner, R. Schulz and L. Mühlhoff, "Oxidation of HF-treated Si wafer surfaces in air", Journal of Applied Physics **68**, 5155–5161 (1990).

[144] S. Raider, R. Flitsch and M. Palmer, "Oxide growth on etched silicon in air at room temperature", Journal of the Electrochemical Society **122**, 413 (1975).

[145] M. Morita, T. Ohmi, E. Hasegawa, M. Kawakami and K. Suma, "Control factor of native oxide growth on silicon in air or in ultrapure water", Applied Physics Letters **55**, 562–564 (1989).

[146] W. Ranke and Y. Xing, "Orientation dependent adsorption on a cylindrical silicon crystal: I. Water", Surface Science **157**, 339–352 (1985).

[147] W. Ranke and Y. Xing, "Orientation dependent adsorption on a cylindrical silicon crystal: II. Oxygen", Surface Science **157**, 353–370 (1985).

[148] Y. Chabal and S. Christman, "Evidence of dissociation of water on the Si (100) 2x1 surface", Physical Review B **29**, 6974 (1984).

[149] D. Gräf, M. Grundner and R. Schulz, "Reaction of water with hydrofluoric acid treated silicon (111) and (100) surfaces", Journal of Vacuum Science & Technology A: Vacuum, Surfaces, and Films **7**, 808–813 (1989).

[150] M. Miyamoto, T. Tatsuno and Y. Ohta, "Advanced ultrapure water by HF addition", Journal of the Electrochemical Society **140**, 2546 (1993).

[151] A. V. Rao and J.-N. Chazalviel, "Chemical trends in the electromodulated infrared vibrational spectroscopy of various silicon/electrolyte interfaces", Journal of the Electrochemical Society **134**, 2777 (1987).

[152] F. Ozanam and J.-N. Chazalviel, "In-situ infrared vibrational study of the early stages of silicon oxidation at the interface with a non-aqueous electrolyte", Journal of Electroanalytical Chemistry and Interfacial Electrochemistry **269**, 251–266 (1989).

[153] H. Lewerenz, "Anodic oxides on silicon", Electrochimica Acta **37**, 847–864 (1992).

[154] F. Himpsel, F. McFeely, A. Taleb-Ibrahimi, J. Yarmoff and G. Hollinger, "Microscopic structure of the SiO_2/Si interface", Physical Review B **38**, 6084 (1988).

[155] K. Beckmann and N. Harrick, "Hydrides and hydroxyls in thin silicon dioxide films", Journal of The Electrochemical Society **118**, 614 (1971).

[156] K. Ghowsi and R. J. Gale, "Theoretical model of the anodic oxidation growth kinetics of Si at constant voltage", Journal of the Electrochemical Society **136**, 867 (1989).

[157] H. Ubara, T. Imura and A. Hiraki, "Formation of Si-H bonds on the surface of microcrystalline silicon covered with SiO_x by HF treatment", Solid State Communications **50**, 673–675 (1984).

[158] A. Pasquarello, M. S. Hybertsen and R. Car, "Theory of Si 2p core-level shifts at the Si (001)-SiO_2 interface", Physical Review B **53**, 10942 (1996).

[159] S. Watanabe, M. Shigeno, N. N. N. Nakayama and T. I. T. Ito, "Silicon-monohydride termination of silicon-111 surface formed by boiling water", Japanese Journal of Applied Physics **30**, 3575 (1991).

[160] G. Trucks, K. Raghavachari, G. Higashi and Y. Chabal, "Mechanism of HF etching of silicon surfaces: A theoretical understanding of hydrogen passivation", Physical Review Letters **65**, 504 (1990).

[161] G. Willeke and K. Kellermann, "Crystalline silicon etching in quiescent concentrated aqueous HF solutions", Semiconductor Science and Technology **11**, 415 (1996).

[162] O. Glembocki, E. Palik, G. De Guel and D. Kendall, "Hydration model for the molarity dependence of the etch rate of Si in aqueous alkali hydroxides", Journal of the Electrochemical Society **138**, 1055 (1991).

[163] S. Hu and D. Kerr, "Observation of etching of n-type silicon in aqueous HF solutions", Journal of the Electrochemical Society **114**, 414 (1967).

[164] P. Allongue, V. Kieling and H. Gerischer, "Etching mechanism and atomic structure of H-Si (111) surfaces prepared in NH_4F", Electrochimica Acta **40**, 1353–1360 (1995).

[165] R. Dreiner, "A-C properties of anodic oxide films on silicon", Journal of The Electrochemical Society **113**, 1210 (1966).

[166] D. J. Monk, D. S. Soane and R. T. Howe, "A review of the chemical reaction mechanism and kinetics for hydrofluoric acid etching of silicon dioxide for surface micromachining applications", Thin Solid Films **232**, 1–12 (1993).

[167] P. O'Keeffe, Y. Aoyagi, S. Komuro, T. Kato and T. Morikawa, "Room-temperature backbond oxidation of the porous silicon surface by oxygen radical irradiation", Applied Physics Letters **66**, 836–838 (1995).

[168] B. J. Wiersma, Y. Tak and K. R. Hebert, "Passivation of surfaces within aluminum etch tunnels", Journal of the Electrochemical Society **138**, 371 (1991).

[169] K. S. Sing, "Reporting physisorption data for gas/solid systems with special reference to the determination of surface area and porosity (recommendations 1984)", Pure and Applied Chemistry **57**, 603–619 (1985).

[170] I. Ronga, A. Bsiesy, F. Gaspard, R. Herino, M. Ligeon, F. Muller and A. Halimaoui, "Electrical characterization of the silicon-electrolyte interface in the conditions of porous silicon formation", Journal of The Electrochemical Society **138**, 1403 (1991).

[171] H. Föll, M. Christophersen, J. Carstensen and G. Hasse, "Formation and application of porous silicon", Materials Science and Engineering: R: Reports **39**, 93–141 (2002).

[172] M. Christophersen, S. Langa, J. Carstensen, I. Tiginyanu and H. Föll, "A comparison of pores in silicon and pores in III–V compound materials", physica status solidi (a) **197**, 197–203 (2003).

[173] H. Unno, K. Imai and S. Muramoto, "Dissolution reaction effect on porous-silicon density", Journal of the Electrochemical Society **134**, 645 (1987).

[174] R. Herino, G. Bomchil, K. Barla, C. Bertrand and J. L. Ginoux, "Porosity and pore size distributions of porous silicon layers", Journal of the Electrochemical Society **134**, 1994–2000 (1987).

[175] M. Thönissen, S. Billat, M. Krüger, H. Lüth, M. Berger, U. Frotscher and U. Rossow, "Depth inhomogeneity of porous silicon layers", Journal of Applied Physics **80**, 2990–2993 (1996).

[176] V. Lehmann, "The physics of macropore formation in low doped n-type silicon", Journal of the Electrochemical Society **140**, 2836–2843 (1993).

[177] M. Thelen, N. Bochud, M. Brinker, C. Prada and P. Huber, "Laser-excited elastic guided waves reveal the complex mechanics of nanoporous silicon", Nature Communications **12**, 1–10 (2021).

[178] G. Dolino, D. Bellet and C. Faivre, "Adsorption strains in porous silicon", Physical Review B **54**, 17919–17929 (1996).

[179] W. Haiss, "Surface stress of clean and adsorbate-covered solids", Reports on Progress in Physics **64**, 591 (2001).

[180] J. Weissmüller and J. W. Cahn, "Mean stresses in microstructures due to interface stresses: A generalization of a capillary equation for solids", Acta Materialia **45**, 1899–1906 (1997).

[181] R. Shuttleworth, "The surface tension of solids", Proceedings of the Physical Society. Section A **63**, 444–457 (1950).

[182] C. Stenner, L.-H. Shao, N. Mameka and J. Weissmüller, "Piezoelectric gold: Strong charge-load response in a metal-based hybrid nanomaterial", Advanced Functional Materials **26**, 5174–5181 (2016).

[183] M. Smetanin, D. Kramer, S. Mohanan, U. Herr and J. Weissmüller, "Response of the potential of a gold electrode to elastic strain", Physical Chemistry Chemical Physics **11**, 9008–9012 (2009).

[184] Y. Umeno, C. Elsässer, B. Meyer, P. Gumbsch, M. Nothacker, J. Weißmüller and F. Evers, "Ab initio study of surface stress response to charging", Europhysics Letters **78**, 13001 (2007).

[185] M. Smetanin, Q. Deng and J. Weissmüller, "Dynamic electro-chemo-mechanical analysis during cyclic voltammetry", Physical Chemistry Chemical Physics **13**, 17313–17322 (2011).

[186] M. C. Lafouresse, U. Bertocci, C. R. Beauchamp and G. R. Stafford, "Simultaneous electrochemical and mechanical impedance spectroscopy using cantilever curvature", Journal of The Electrochemical Society **159**, H816–H822 (2012).

[187] Q. Deng and J. Weissmuller, "Electrocapillary coupling during electrosorption", Langmuir **30**, 10522–10530 (2014).

[188] W. Demtröder, *Experimentalphysik 3: Atome, Moleküle und Festkörper* (Springer-Verlag, 2016).

[189] D. Walton, "Electrically conducting polymers", Materials & Design **11**, 142–152 (1990).

[190] J. M. G. Cowie and V. Arrighi, *Polymers: Chemistry and physics of modern materials* (CRC press, 2007).

[191] A. M. Bryan, L. M. Santino, Y. Lu, S. Acharya and J. M. D'Arcy, "Conducting polymers for pseudocapacitive energy storage", Chemistry of Materials **28**, 5989–5998 (2016).

[192] A. J. Heeger, "Semiconducting and metallic polymers: The fourth generation of polymeric materials (nobel lecture)", Angewandte Chemie International Edition **40**, 2591–2611 (2001).

[193] A. J. Heeger, S. Kivelson, J. Schrieffer and W.-P. Su, "Solitons in conducting polymers", Reviews of Modern Physics **60**, 781–850 (1988).

[194] S. Roth and D. Carroll, *One-dimensional metals: Conjugated polymers, organic crystals, carbon nanotubes and graphene* (John Wiley & Sons, 2015).

[195] A. J. Epstein, H. Rommelmann, M. Abkowitz and H. Gibson, "Anomalous frequency-dependent conductivity of polyacetylene", Physical Review Letters **47**, 1549–1553 (1981).

[196] H. Shirakawa, Y.-X. Zhang, T. Okuda, K. Sakamaki and K. Akagi, "Various factors affecting the synthesis of highly conducting polyacetylene", Synthetic Metals **65**, 93–101 (1994).

[197] A. B. Kaiser, "Systematic conductivity behavior in conducting polymers: Effects of heterogeneous disorder", Advanced Materials **13**, 927–941 (2001).

[198] K. Cheung, D. Bloor and G. Stevens, "The influence of unusual counterions on the electrochemistry and physical properties of polypyrrole", Journal of Materials Science **25**, 3814–3837 (1990).

[199] G. G. Wallace, P. R. Teasdale, G. M. Spinks and L. A. Kane-Maguire, *Conductive electroactive polymers: Intelligent polymer systems* (CRC press, 2008).

[200] S. Sadki, P. Schottland, N. Brodie and G. Sabouraud, "The mechanisms of pyrrole electropolymerization", Chemical Society Reviews **29**, 283–293 (2000).

[201] C. C. Bof Bufon, J. Vollmer, T. Heinzel, P. Espindola, H. John and J. Heinze, "Relationship between chain length, disorder, and resistivity in polypyrrole films", The Journal of Physical Chemistry B **109**, 19191–19199 (2005).

[202] P. Pfluger and G. Street, "Chemical, electronic, and structural properties of conducting heterocyclic polymers: A view by XPS", The Journal of Chemical Physics **80**, 544–553 (1984).

[203] J. Joo, J. Lee, J. Baeck, K. Kim, E. Oh and J. Epstein, "Electrical, magnetic, and structural properties of chemically and electrochemically synthesized polypyrroles", Synthetic Metals **117**, 45–51 (2001).

[204] A. F. Diaz, J. I. Castillo, J. Logan and W.-Y. Lee, "Electrochemistry of conducting polypyrrole films", Journal of Electroanalytical Chemistry and Interfacial Electrochemistry **129**, 115–132 (1981).

[205] A. F. Diaz and J. I. Castillo, "A polymer electrode with variable conductivity: Polypyrrole", Journal of the Chemical Society, Chemical Communications **9**, 397–398 (1980).

[206] F. A. Harraz, "Electrochemical formation of a novel porous silicon/polypyrrole hybrid structure with enhanced electrical and optical characteristics", Journal of Electroanalytical Chemistry **729**, 68–74 (2014).

[207] G. Mitchell and A. Geri, "Molecular organisation of electrochemically prepared conducting polypyrrole films", Journal of Physics D: Applied Physics **20**, 1346–1353 (1987).

[208] G. Mitchell, F. Davis and M. Kiani, "Influence of synthesis on the structure of electrochemically prepared electrically conducting polymers", British Polymer Journal **23**, 157–164 (1990).

[209] S. Pruneanu, W. Graupner, L. Oniciu, M. Brie and R. Turcu, "Electrochemical and X-ray diffraction studies on polypyrrole films", Materials Chemistry and Physics **46**, 55–60 (1996).

[210] K. Naoi, M. Lien and W. H. Smyrl, "Quartz crystal microbalance study: Ionic motion across conducting polymers", Journal of The Electrochemical Society **138**, 440 (1991).

[211] C. Lopez, M. M. Viegas, G. Bidan and E. Vieil, "Comparison of ion exchange properties of polypyrrole with and without immobilized dopants by optical beam deflection", Synthetic Metals **63**, 73–78 (1994).

[212] A. Mazzoldi, A. D. Santa and D. D. Rossi, "Conducting polymer actuators: Properties and modeling", in *Polymer sensors and actuators* (Springer, 2000), pp. 207–244.

[213] B. Roschning and J. Weissmüller, "Stress-charge coupling coefficient for thin-film polypyrrole actuators - investigation of capacitive ion exchange in the oxidized state", Electrochimica Acta **318**, 504–512 (2019).

[214] C. H. Hamann, A. Hamnett and W. Vielstich, *Electrochemistry* (Wiley-VCH, Weinheim, 2007).

[215] N. Mameka, "Surface-controlled mechanical properties of bulk nanoporous gold", PhD thesis (Technische Universität Hamburg, 2016).

[216] N. Elgrishi, K. J. Rountree, B. D. McCarthy, E. S. Rountree, T. T. Eisenhart and J. L. Dempsey, "A practical beginner's guide to cyclic voltammetry", Journal of Chemical Education **95**, 197–206 (2018).

[217] P. S. Germain, W. G. Pell and B. E. Conway, "Evaluation and origins of the difference between double-layer capacitance behaviour at Au-metal and oxidized Au surfaces", Electrochimica Acta **49**, 1775–1788 (2004).

[218] *Nova - user manual*, English, version 2.1.5, Metrohm Autolab B.V. (2021).

[219] B.-A. Mei, O. Munteshari, J. Lau, B. Dunn and L. Pilon, "Physical interpretations of Nyquist plots for EDLC electrodes and devices", The Journal of Physical Chemistry C **122**, 194–206 (2018).

[220] V. Jović and B. Jović, "EIS and differential capacitance measurements onto single crystal faces in different solutions: Part I: Ag (111) in 0.01 M NaCl", Journal of Electroanalytical Chemistry **541**, 1–11 (2003).

[221] B.-A. Mei, J. Lau, T. Lin, S. H. Tolbert, B. S. Dunn and L. Pilon, "Physical interpretations of electrochemical impedance spectroscopy of redox active electrodes for electrical energy storage", The Journal of Physical Chemistry C **122**, 24499–24511 (2018).

[222] P. R. Gray, P. Hurst, R. G. Meyer and S. Lewis, *Analysis and design of analog integrated circuits* (Wiley, 2001).

[223] P. Kumar and P. Huber, "Effect of etching parameter on pore size and porosity of electrochemically formed nanoporous silicon", Journal of Nanomaterials **2007**, 089718 (2007).

[224] H. Föll, J. Carstensen, M. Christophersen and G. Hasse, "A new view of silicon electrochemistry", physica status solidi (a) **182**, 7–16 (2000).

[225] Y. H. Ogata, A. Koyama, F. A. Harraz, M. S. Salem and T. Sakka, "Electrochemical formation of porous silicon with medium-sized pores", Electrochemistry **75**, 270–272 (2007).

[226] S. Brunauer, P. H. Emmett and E. Teller, "Adsorption of gases in multimolecular layers", Journal of the American Chemical Society **60**, 309–319 (1938).

[227] J. Schultze and K. Jung, "Regular nanostructured systems formed electrochemically: Deposition of electroactive polybithiophene into porous silicon", Electrochimica Acta **40**, 1369–1383 (1995).

[228] J. Kanungo and S. Basu, "Ohmic and rectifying contacts to porous silicon", in *Handbook of porous silicon*, edited by L. Canham (Springer International Publishing Cham, 2014), pp. 705–714.

[229] J. A. Floro, E. Chason and S. R. Lee, "Real time measurement of epilayer strain using a simplified wafer curvature technique", Materials Research Society Symposium Proceedings **405**, 381 (1995).

[230] J. Floro, E. Chason, S. Lee, R. Twesten, R. Hwang and L. Freund, "Real-time stress evolution during Si_{1-x} Ge_x heteroepitaxy: Dislocations, islanding, and segregation", Journal of Electronic Materials **26**, 969–979 (1997).

[231] G. G. Stoney, "The tension of metallic films deposited by electrolysis", Proceedings of the Royal Society of London. Series A, Containing Papers of a Mathematical and Physical Character **82**, 172–175 (1909).

[232] M. F. Doerner and W. D. Nix, "Stresses and deformation processes in thin films on substrates", Critical Reviews in Solid State and Material Sciences **14**, 225–268 (1988).

[233] M. Brinker and P. Huber, "Wafer-scale electroactive nanoporous silicon: Large and fully reversible electrochemo-mechanical actuation in aqueous electrolytes", Advanced Materials **34**, 2105923 (2022).

[234] W. D. Nix, "Mechanical properties of thin films", Metallurgical Transactions A **20**, 2217 (1989).

[235] D. Bellet, S. Billat, G. Dolino, M. Ligeon, C. Meyer and F. Muller, "X-ray study of the anodic oxidation of p+ porous silicon", Solid State Communications **86**, 51–54 (1993).

[236] D. Bellet and G. Dolino, "X-ray observation of porous-silicon wetting", Physical Review B **50**, 17162 (1994).

[237] D. Bellet and G. Dolino, "X-ray diffraction studies of porous silicon", Thin Solid Films **276**, 1–6 (1996).

[238] I. Young, M. Beale and J. Benjamin, "X-ray double crystal diffraction study of porous silicon", Applied Physics Letters **46**, 1133–1135 (1985).

[239] D. Bangham and N. Fakhoury, "The expansion of charcoal accompanying sorption of gases and vapours", Nature **122**, 681–682 (1928).

[240] G. Y. Gor and N. Bernstein, "Revisiting Bangham's law of adsorption-induced deformation: Changes of surface energy and surface stress", Physical Chemistry Chemical Physics **18**, 9788–9798 (2016).

[241] R. C. Cammarata and K. Sieradzki, "Surface and interface stresses", Annual Review of Materials Science **24**, 215–234 (1994).

[242] G. Y. Gor, P. Huber and J. Weissmüller, "Elastocapillarity in nanopores: Sorption strain from the actions of surface tension and surface stress", Physical Review Materials **2**, 086002 (2018).

[243] M. Brinker, M. Thelen, M. May, D. Rings, T. Krekeler, P. Lakner, T. F. Keller, F. Bertram, N. Huber and P. Huber, "How nanoporous silicon-polypyrrole hybrids flex their muscles in aqueous electrolytes: In operando high-resolution X-ray diffraction and electron tomography-based micromechanical computer simulations", Physical Review Materials **6**, 116002 (2022).

[244] D. Chernyshov, V. Dyadkin, H. Emerich, G. Valkovskiy, C. J. McMonagle and W. van Beek, "On the resolution function for powder diffraction with area detectors", Acta Crystallographica Section A: Foundations and Advances **77**, 497–505 (2021).

[245] E. P. Barrett, L. G. Joyner and P. P. Halenda, "The determination of pore volume and area distributions in porous substances. I. Computations from nitrogen isotherms", Journal of the American Chemical Society **73**, 373–380 (1951).

[246] A. Bsiesy, F. Gaspard, R. Herino, M. Ligeon, F. Muller and J. Oberlin, "Anodic oxidation of porous silicon layers formed on lightly p-doped substrates", Journal of the Electrochemical Society **138**, 3450–3456 (1991).

[247] F. Gaspard, A. Halimaoui and G. Sarrabayrouse, "Electrical properties of thin anodic silicon dioxide layers grown in pure water", Revue de Physique Appliquée **22**, 65–69 (1987).

[248] A. Muñoz, A. Moehring and M. Lohrengel, "Anodic oxidation of chemically hydrogenated Si (100)", Electrochimica Acta **47**, 2751–2760 (2002).

[249] P. Daubinger, J. Kieninger, T. Unmüssig and G. A. Urban, "Electrochemical characteristics of nanostructured platinum electrodes–a cyclic voltammetry study", Physical Chemistry Chemical Physics **16**, 8392–8399 (2014).

[250] W. Guo, S. K. Anantharajan, K. Liu and H. Deng, "Investigation of electrochemical oxidation behaviors and mechanism of single-crystal silicon (100) wafer under potentiostatic mode", Coatings **10**, 586 (2020).

[251] L. H. Brickwedde, "Properties of aqueous solutions of perchloric acid", Journal of Research of the National Institute of Standards and Technology **42**, 309–329 (1949).

[252] S. Merazga, A. Cheriet, K. M'hammedi, A. Mefoued and N. Gabouze, "Investigation of porous silicon thin films for electrochemical hydrogen storage", International Journal of Hydrogen Energy **44**, 9994–10002 (2019).

[253] P. Searson and X. Zhang, "The potential distribution at the silicon/electrolyte interface in HF solutions", Electrochimica Acta **36**, 499–503 (1991).

[254] S. Ottow, G. Popkirov and H. Föll, "Determination of flat-band potentials of silicon electrodes in HF by means of AC resistance measurements", Journal of Electroanalytical Chemistry **455**, 29–37 (1998).

[255] A. Hamelin, "Note on the behaviour of the (111) gold face in electrolytic solutions", Journal of Electroanalytical Chemistry and Interfacial Electrochemistry **210**, 303–309 (1986).

[256] K. Breitsprecher, M. Janssen, P. Srimuk, B. L. Mehdi, V. Presser, C. Holm and S. Kondrat, "How to speed up ion transport in nanopores", Nature Communications **11**, 1–10 (2020).

[257] C. Péan, C. Merlet, B. Rotenberg, P. A. Madden, P.-L. Taberna, B. Daffos, M. Salanne and P. Simon, "On the dynamics of charging in nanoporous carbon-based supercapacitors", ACS Nano **8**, 1576–1583 (2014).

[258] P. Biesheuvel, Y. Fu and M. Z. Bazant, "Diffuse charge and Faradaic reactions in porous electrodes", Physical Review E **83**, 061507 (2011).

[259] A. Gupta, P. J. Zuk and H. A. Stone, "Charging dynamics of overlapping double layers in a cylindrical nanopore", Physical Review Letters **125**, 076001 (2020).

[260] S. R. Heil, M. Holz, T. M. Kastner and H. Weingärtner, "Self-diffusion of the perchlorate ion in aqueous electrolyte solutions measured by 35 Cl NMR spin–echo experiments", Journal of the Chemical Society, Faraday Transactions **91**, 1877–1880 (1995).

[261] M. P. Goertz, J. Houston and X.-Y. Zhu, "Hydrophilicity and the viscosity of interfacial water", Langmuir **23**, 5491–5497 (2007).

[262] S. Gruener, T. Hofmann, D. Wallacher, A. V. Kityk and P. Huber, "Capillary rise of water in hydrophilic nanopores", Physical Review E **79**, 067301 (2009).

[263] D. Ortiz-Young, H.-C. Chiu, S. Kim, K. Voïtchovsky and E. Riedo, "The interplay between apparent viscosity and wettability in nanoconfined water", Nature Communications **4**, 1–6 (2013).

[264] A. Jani, M. Busch, J. B. Mietner, J. Ollivier, M. Appel, B. Frick, J.-M. Zanotti, A. Ghoufi, P. Huber, M. Fröba and D. Morineau, "Dynamics of water confined in mesopores with variable surface interaction", The Journal of Chemical Physics **154**, 094505 (2021).

[265] C. Sendner, D. Horinek, L. Bocquet and R. R. Netz, "Interfacial water at hydrophobic and hydrophilic surfaces: Slip, viscosity, and diffusion", Langmuir **25**, 10768–10781 (2009).

[266] A. Schlaich, E. W. Knapp and R. R. Netz, "Water dielectric effects in planar confinement", Physical Review Letters **117**, 048001 (2016).

[267] A. Schlaich, J. Kappler and R. R. Netz, "Hydration friction in nanoconfinement: From bulk via interfacial to dry friction", Nano Letters **17**, 5969–5976 (2017).

[268] D. Dickertmann, F. Koppitz and J. Schultze, "Eine Methode zum Ausschluss von Randeffekten bei elektrochemischen Messungen an Einkristallen: Test anhand der Adsorptionssysteme Ag/Pb2+ und Au/Cu2+", Electrochimica Acta **21**, 967–971 (1976).

[269] A. Hamelin, "Double-layer properties at sp and sd metal single-crystal electrodes", in *Modern aspects of electrochemistry*, edited by B. Conway, R. White and J. O. Bockris, 16 (Plenum, 1985) Chap. 1, pp. 1–101.

[270] H. Hasegawa, S. Arimoto, J. Nanjo, H. Yamamoto and H. Ohno, "Anodic oxidation of hydrogenated amorphous silicon and properties of oxide", Journal of The Electrochemical Society **135**, 424 (1988).

[271] J. Weissmüller, H.-L. Duan and D. Farkas, "Deformation of solids with nanoscale pores by the action of capillary forces", Acta Materialia **58**, 1–13 (2010).

[272] D. Bellet, P. Lamagnere, A. Vincent and Y. Brechet, "Nanoindentation investigation of the Young's modulus of porous silicon", Journal of Applied Physics **80**, 3772–3776 (1996).

[273] T. Hofmann, D. Wallacher, R. Toft-Petersen, B. Ryll, M. Reehuis and K. Habicht, "Phonons in mesoporous silicon: The influence of nanostructuring on the dispersion in the Debye regime", Microporous and Mesoporous Materials **243**, 263–270 (2017).

[274] R. Da Fonseca, J. Saurel, A. Foucaran, J. Camassel, E. Massone, T. Taliercio and Y. Boumaiza, "Acoustic investigation of porous silicon layers", Journal of Materials Science **30**, 35–39 (1995).

[275] A. Doghmane, Z. Hadjoub, M. Doghmane and F. Hadjoub, "Microacoustic evaluation of elastic parameters of highly porous silicon layers", Semiconductor Physics, Quantum Electronics & Optoelectronics **9** (2006).

[276] S. Zharkii, A. Karabutov, I. Pelivanov, N. Podymova and V. Y. Timoshenko, "Laser ultrasonic study of porous silicon layers", Semiconductors **37**, 468–472 (2003).

[277] L. J. Gibson, "Cellular solids", Mrs Bulletin **28**, 270–274 (2003).

[278] M. Thelen, "Investigation of electrosorption-induced actuation and mechanical behaviour of nanoporous silicon", MA thesis (Technische Universität Hamburg, 2019).

[279] H. Lamb, "On waves in an elastic plate", Proceedings of the Royal Society of London. Series A, Containing papers of a mathematical and physical character **93**, 114–128 (1917).

[280] V. Lubarda and M. Chen, "On the elastic moduli and compliances of transversely isotropic and orthotropic materials", Journal of Mechanics of Materials and Structures **3**, 153–171 (2008).

[281] J. Weissmüller and H. Duan, "Cantilever bending with rough surfaces", Physical Review Letters **101**, 146102 (2008).

[282] A. Diaz, A. Martinez, K. Kanazawa and M. Salmón, "Electrochemistry of some substituted pyrroles", Journal of Electroananalytical Chemistry **130**, 181–187 (1981).

[283] F. Harraz, "Electrochemical polymerization of pyrrole into nanostructured p-type porous silicon", Journal of the Electrochemical Society **153**, C349–C356 (2006).

[284] A. Nahor, O. Berger, Y. Bardavid, G. Toker, Y. Tamar, L. Reiss, M. Asscher, S. Yitzchaik and A. Sa'Ar, "Hybrid structures of porous silicon and conjugated polymers for photovoltaic applications", physica status solidi c **8**, 1908–1912 (2011).

[285] F. A. Harraz, M. S. Salem, T. Sakka and Y. H. Ogata, "Hybrid nanostructure of polypyrrole and porous silicon prepared by galvanostatic technique", Electrochimica Acta **53**, 3734–3740 (2008).

[286] J. Moreno, M. Marcos, F. Agullo-Rueda, R. Guerrero-Lemus, R. Martin-Palma, J. Martinez-Duart and J. Gonzalez-Velasco, "A galvanostatic study of the electrodeposition of polypyrrole into porous silicon", Thin Solid Films **348**, 152–156 (1999).

[287] J. Dian, M. Konečnỳ, G. Broncová, M. Kronďák and I. Matolínová, "Electrochemical fabrication and characterization of porous silicon/polypyrrole composites and chemical sensing of organic vapors", Int. J. Electrochem. Sci **8**, 1559–1572 (2013).

[288] K. Fukami, F. A. Harraz, T. Yamauchi, T. Sakka and Y. H. Ogata, "Fine-tuning in size and surface morphology of rod-shaped polypyrrole using porous silicon as template", Electrochemistry Communications **10**, 56–60 (2008).

[289] F. A. Harraz, "Impregnation of porous silicon with conducting polymers", physica status solidi c **8**, 1883–1887 (2011).

[290] D. M. Ruthven, J. Kärger and D. N. Theodorou, *Diffusion in nanoporous materials* (John Wiley & Sons, 2012).

[291] T. Lewis, G. Wallace, C. Kim and D. Kim, "Studies of the overoxidation of polypyrrole", Synthetic Metals **84**, 403–404 (1997).

[292] J. Zhu, Y. Xu, J. Wang, J. Lin, X. Sun and S. Mao, "The effect of various electrolyte cations on electrochemical performance of polypyrrole/RGO based supercapacitors", Physical Chemistry Chemical Physics **17**, 28666–28673 (2015).

[293] G. Torres-Gómez, E. M. Tejada-Rosales and P. Gómez-Romero, "Integration of hexacyanoferrate as an active species in a molecular hybrid material. Transport properties and application of polyaniline/hexacyanoferrate as a cathode in rechargeable lithium batteries", Chemistry of Materials **13**, 3693–3697 (2001).

[294] E. Genies, G. Bidan and A. Diaz, "Spectroelectrochemical study of polypyrrole films", Journal of Electroanalytical Chemistry and Interfacial Electrochemistry **149**, 101–113 (1983).

[295] A. Hallik, A. Alumaa, J. Tamm, V. Sammelselg, M. Väärtnõu, A. Jänes and E. Lust, "Analysis of electrochemical impedance of polypyrrole-sulfate and polypyrrole-perchlorate films", Synthetic Metals **156**, 488–494 (2006).

[296] I. J. Suarez, T. F. Otero and M. Marquez, "Diffusion coefficients in swelling polypyrrole: ESCR and Cottrell models", The Journal of Physical Chemistry B **109**, 1723–1729 (2005).

[297] X. Ren and P. G. Pickup, "Ion transport in polypyrrole and a polypyrrole/polyanion composite", The Journal of Physical Chemistry **97**, 5356–5362 (1993).

[298] J. Lopez Cascales and T. Otero, "Molecular dynamic simulation of the hydration and diffusion of chloride ions from bulk water to polypyrrole matrix", The Journal of Chemical Physics **120**, 1951–1957 (2004).

[299] B. Roschning and J. Weissmüller, "Nanoporous-gold-polypyrrole hybrid materials for millimeter-sized free standing actuators", Advanced Materials Interfaces **7**, 2001415 (2020).

[300] K. Wang, C. Stenner and J. Weissmüller, "A nanoporous gold-polypyrrole hybrid nanomaterial for actuation", Sensors and Actuators B: Chemical **248**, 622–629 (2017).

[301] J. Li, J. Markmann and N. Mameka, "Enhanced electrochemical actuation of nanoporous gold-polypyrrole hybrid under load", Applied Physics Letters **121**, 021901 (2022).

[302] B. Roschning, "Herstellung und chemo-elektromechanische Charakterisierung von Aktoren aus nanoporösem Gold und Polypyrrol", PhD thesis (Technische Universität Hamburg, 2020).

[303] S. Gnegel, J. Li, N. Mameka, N. Huber and A. Düster, "Numerical investigation of polymer coated nanoporous gold", Materials **12**, 2178 (2019).

[304] K. Kaneto, Y. Sonoda and W. Takashima, "Direct measurement and mechanism of electro-chemomechanical expansion and contraction in polypyrrole films", Japanese Journal of Applied Physics **39**, 5918–5922 (2000).

[305] G. Esteves, K. Ramos, C. M. Fancher and J. L. Jones, *Lipras: Line-Profile Analysis Software*, 2017.

[306] F. Sánchez-Bajo and F. Cumbrera, "The use of the pseudo-Voigt function in the variance method of X-ray line-broadening analysis", Journal of Applied Crystallography **30**, 427–430 (1997).

[307] P. Abramof, A. Beloto, A. Ueta and N. Ferreira, "X-ray investigation of nanostructured stain-etched porous silicon", Journal of Applied Physics **99**, 024304 (2006).

[308] M. Bossert, A. Grosman, I. Trimaille, F. Souris, V. Doebele, A. Benoit-Gonin, L. Cagnon, P. Spathis, P.-E. Wolf and E. Rolley, "Evaporation process in porous silicon: Cavitation vs pore blocking", Langmuir **37**, 14419–14428 (2021).

[309] S. Zhang and N. Pan, "Supercapacitors performance evaluation", Advanced Energy Materials **5**, 1401401 (2015).

[310] C. Liu, Z. Yu, D. Neff, A. Zhamu and B. Z. Jang, "Graphene-based supercapacitor with an ultrahigh energy density", Nano Letters **10**, 4863–4868 (2010).

[311] I. W. Hunter and S. Lafontaine, "A comparison of muscle with artificial actuators", in Technical digest IEEE solid-state sensor and actuator workshop (IEEE, 1992), pp. 178–185.

[312] Q. Zhang, V. Bharti and X. Zhao, "Giant electrostriction and relaxor ferroelectric behavior in electron-irradiated poly (vinylidene fluoride-trifluoroethylene) copolymer", Science **280**, 2101–2104 (1998).

[313] J. Rödel, W. Jo, K. T. Seifert, E.-M. Anton, T. Granzow and D. Damjanovic, "Perspective on the development of lead-free piezoceramics", Journal of the American Ceramic Society **92**, 1153–1177 (2009).

[314] D. A. DeAngelis and G. W. Schulze, "Performance of PZT8 versus PZT4 piezoceramic materials in ultrasonic transducers", Physics Procedia **87**, 85–92 (2016).

[315] Y. Li, N. Van Toan, Z. Wang, K. F. B. Samat and T. Ono, "Formation and evaluation of silicon substrate with highly-doped porous Si layers formed by metal-assisted chemical etching", Nanoscale Research Letters **16**, 1–8 (2021).

[316] A. Henschel, T. Hofmann, P. Huber and K. Knorr, "Preferred orientations and stability of medium length n-alkanes solidified in mesoporous silicon", Physical Review E **75**, 021607 (2007).

[317] G. Nagayama, R. Ando and T. Tsuruta, "Microscopic wetting at microstructured surface of porous silicon", in International conference on micro/nanoscale heat transfer, Vol. 3 (2009), pp. 623–628.

[318] K. Sentker, A. Yildirim, M. Lippmann, A. W. Zantop, F. Bertram, T. Hofmann, O. H. Seeck, A. V. Kityk, M. G. Mazza, A. Schönhals and P. Huber, "Self-assembly of liquid crystals in nanoporous solids for adaptive photonic metamaterials", Nanoscale **11**, 23304–23317 (2019).

[319] W. Wang, J. V. Timonen, A. Carlson, D.-M. Drotlef, C. T. Zhang, S. Kolle, A. Grinthal, T.-S. Wong, B. Hatton, S. H. Kang, S. Kennedy, J. Chi, R. T. Blough, M. Sitti, L. Mahadevan and J. Aizenberg, "Multifunctional ferrofluid-infused surfaces with reconfigurable multiscale topography", Nature **559**, 77–82 (2018).

[320] R. W. Style, R. Tutika, J. Y. Kim and M. D. Bartlett, "Solid–liquid composites for soft multifunctional materials", Advanced Functional Materials **31**, 2005804 (2021).

[321] M. R. Begley, D. S. Gianola and T. R. Ray, "Bridging functional nanocomposites to robust macroscale devices", Science **364**, eaav4299 (2019).

[322] O. Vincent, D. A. Sessoms, E. J. Huber, J. Guioth and A. D. Stroock, "Drying by cavitation and poroelastic relaxations in porous media with macroscopic pores connected by nanoscale throats", Physical Review Letters **113**, 134501 (2014).

[323] J. M. Lauerhaas and M. J. Sailor, "Chemical modification of the photoluminescence quenching of porous silicon", Science **261**, 1567–1568 (1993).

[324] A. H. Atabaki, S. Moazeni, F. Pavanello, H. Gevorgyan, J. Notaros, L. Alloatti, M. T. Wade, C. Sun, S. A. Kruger, H. Meng, K. Al Qubaisi, I. Wang, B. Zhang, A. Khilo, C. V. Baiocco, M. Popović, V. M. Stojanović and R. J. Ram, "Integrating photonics with silicon nanoelectronics for the next generation of systems on a chip", Nature **556**, 349–354 (2018).

[325] M. Gómez-González, E. Latorre, M. Arroyo and X. Trepat, "Measuring mechanical stress in living tissues", Nature Reviews Physics **2**, 300–317 (2020).

[326] W. Wang, J. Li, H. Liu and S. Ge, "Advancing versatile ferroelectric materials toward biomedical applications", Advanced Science **8**, 2003074 (2021).

[327] P. Jain, W. Liu, S. Zhu, C. Y.-Y. Chang, J. Melkonian, F. E. Rockwell, D. Pauli, Y. Sun, W. R. Zipfel, N. M. Holbrook, S. J. Riha, M. A. Gore and A. D. Stroock, "A minimally disruptive method for measuring water potential in planta using hydrogel nanoreporters", Proceedings of the National Academy of Sciences **118**, e2008276118 (2021).

[328] L. He, G. Si, J. Huang, A. D. Samuel and N. Perrimon, "Mechanical regulation of stem-cell differentiation by the stretch-activated piezo channel", Nature **555**, 103–106 (2018).

[329] V. Woehling, G. T. Nguyen, C. Plesse, Y. Petel, Y. Dobashi, J. D. Madden, C. A. Michal and F. Vidal, "Study of the piezoionic effect and influence of electrolyte in conducting polymer based soft strain sensors", Multifunctional Materials **2**, 045002 (2019).

[330] S. Gries, "Silbernanopartikel induzierte nasschemische Synthese von hierarchisch porösem Silizium und dessen strukturelle Charakterisierung", MA thesis (Technische Universität Hamburg, 2020).

[331] C. D. Murray, "The physiological principle of minimum work: I. The vascular system and the cost of blood volume", Proceedings of the National Academy of Sciences **12**, 207–214 (1926).

[332] X. Zheng, G. Shen, C. Wang, Y. Li, D. Dunphy, T. Hasan, C. J. Brinker and B. L. Su, "Bio-inspired Murray materials for mass transfer and activity", Nature Communications **8**, 1–9 (2017).

[333] X.-Y. Yang, L.-H. Chen, Y. Li, J. C. Rooke, C. Sanchez and B.-L. Su, "Hierarchically porous materials: Synthesis strategies and structure design", Chemical Society Reviews **46**, 481–558 (2017).

[334] O. Gang, P. Huber, A. Karim, I. Zvonkina, S.-W. Lee, J.-W. Kim, D. K. Roper and W. J. Li, *Soft matter and biomaterials on the nanoscale*, Vol. 1 (World Scientific, Aug. 2020).

[335] H. Sai, K. W. Tan, K. Hur, E. Asenath-Smith, R. Hovden, Y. Jiang, M. Riccio, D. A. Muller, V. Elser, L. A. Estroff, S. M. Gruner and U. Wiesner, "Hierarchical porous polymer scaffolds from block copolymers", Science **341**, 530–534 (2013).

[336] J. Hwang, S. Kim, U. Wiesner and J. Lee, "Generalized access to mesoporous inorganic particles and hollow spheres from multicomponent polymer blends", Advanced Materials **30**, 1801127 (2018).

[337] S. Lopez-Orozco, A. Inayat, A. Schwab, T. Selvam and W. Schwieger, "Zeolitic materials with hierarchical porous structures", Advanced Materials **23**, 2602–2615 (2011).

[338] H. Li, F. Meng, S. Zhang, L. Wang, M. Li, L. Ma, W. Zhang, W. Zhang, Z. Yang, T. Wu, S. Lee, F. Huo and J. Lu, "Crystal-growth-dominated fabrication of metal–organic frameworks with orderly distributed hierarchical porosity", Angewandte Chemie International Edition **59**, 2457–2464 (2020).

[339] W. Huo, X. Zhang, E. Tervoort, S. Gantenbein, J. Yang and A. R. Studart, "Ultrastrong hierarchical porous materials via colloidal assembly and oxidation of metal particles", Advanced Functional Materials **30**, 2003550 (2020).

[340] M. Bilo, M. Münzner, C. Küster, D. Enke, Y. J. Lee and M. Fröba, "Structural changes of hierarchically nanoporous organosilica/silica hybrid materials by pseudomorphic transformation", Chemistry–A European Journal **26**, 11220–11230 (2020).

[341] M. Rebber, M. Trommler, I. Lokteva, S. Ehteram, A. Schropp, S. König, M. Fröba and D. Koziej, "Additive-free, gelled nanoinks as a 3D printing toolbox for hierarchically structured bulk aerogels", Advanced Functional Materials **32**, 2112914 (2022).

[342] F. Putz, S. Scherer, M. Ober, R. Morak, O. Paris and N. Hüsing, "3D printing of hierarchical porous silica and α-quartz", Advanced Materials Technologies **3**, 1800060 (2018).

[343] F. Putz, L. Ludescher, M. S. Elsaesser, O. Paris and N. Hüsing, "Hierarchically organized and anisotropic porous carbon monoliths", Chemistry of Materials **32**, 3944–3951 (2020).

[344] C. Balzer, A. M. Waag, F. Putz, N. Hüsing, O. Paris, G. Y. Gor, A. V. Neimark and G. Reichenauer, "Mechanical characterization of hierarchical structured porous silica by in situ dilatometry measurements during gas adsorption", Langmuir **35**, 2948–2956 (2019).

[345] S. Shi, Y. Li, B.-N. Ngo-Dinh, J. Markmann and J. Weissmüller, "Scaling behavior of stiffness and strength of hierarchical network nanomaterials", Science **371**, 1026–1033 (2021).

[346] J. Condi Mainardi, C. Bonini Demarchi, M. Mirdrikvand, M. N. Karim, W. Dreher, K. Rezwan and M. Maas, "3D bioprinting of hydrogel/ceramic composites with hierarchical porosity", Journal of Materials Science **57**, 3662–3677 (2022).

[347] M. Berdys, A. Koreniuk, K. Maresz, W. Pudło, A. B. Jarzębski and J. Mrowiec-Białoń, "Fabrication and performance of monolithic continuous-flow silica microreactors", Chemical Engineering Journal **282**, 137–141 (2015).

[348] E. Mäkilä, A.-M. Anton Willmore, H. Yu, M. Irri, M. Aindow, T. Teesalu, L. T. Canham, K. W. Kolasinski and J. Salonen, "Hierarchical nanostructuring of porous silicon with electrochemical and regenerative electroless etching", ACS Nano **13**, 13056–13064 (2019).

[349] B. M. Bang, H. Kim, H.-K. Song, J. Cho and S. Park, "Scalable approach to multi-dimensional bulk Si anodes via metal-assisted chemical etching", Energy & Environmental Science **4**, 5013–5019 (2011).

[350] V. Lehmann, "Porous silicon matrix for chemical synthesis and chromatograpy", physica status solidi (a) **202**, 1365–1368 (2005).

[351] S. Gries, M. Brinker and P. Huber, *Hierarchically porous structure and process for producing same* (International patent WO2022058610A1, 24.03.2022).

[352] S. Gries, M. Brinker, B. Zeller-Plumhoff, D. Rings, T. Krekeler, I. Greving and P. Huber, "Wafer-scale fabrication of hierarchically porous silicon and silica by active nanoparticle-assisted chemical etching and pseudomorphic thermal oxidation", Small, under review (2022).

[353] Z. Huang, N. Geyer, P. Werner, J. De Boor and U. Gösele, "Metal-assisted chemical etching of silicon: A review", Advanced Materials **23**, 285–308 (2011).

[354] N. Geyer, B. Fuhrmann, H. S. Leipner and P. Werner, "Ag-mediated charge transport during metal-assisted chemical etching of silicon nanowires", ACS Applied Materials & Interfaces **5**, 4302–4308 (2013).

[355] H. Han, Z. Huang and W. Lee, "Metal-assisted chemical etching of silicon and nanotechnology applications", Nano Today **9**, 271–304 (2014).

[356] E. Pinna, S. Le Gall, E. Torralba, G. Mula, C. Cachet-Vivier and S. Bastide, "Mesopore formation and silicon surface nanostructuration by metal-assisted chemical etching with silver nanoparticles", Frontiers in Chemistry **8**, 658 (2020).

[357] K. Peng, A. Lu, R. Zhang and S.-T. Lee, "Motility of metal nanoparticles in silicon and induced anisotropic silicon etching", Advanced Functional Materials **18**, 3026–3035 (2008).

[358] K. Peng, J. Hu, Y. Yan, Y. Wu, H. Fang, Y. Xu, S. Lee and J. Zhu, "Fabrication of single-crystalline silicon nanowires by scratching a silicon surface with catalytic metal particles", Advanced Functional Materials **16**, 387–394 (2006).

[359] F. J. Wendisch, M. Rey, N. Vogel and G. R. Bourret, "Large-scale synthesis of highly uniform silicon nanowire arrays using metal-assisted chemical etching", Chemistry of Materials **32**, 9425–9434 (2020).

[360] Y. Chen, C. Zhang, L. Li, C.-C. Tuan, F. Wu, X. Chen, J. Gao, Y. Ding and C.-P. Wong, "Fabricating and controlling silicon zigzag nanowires by diffusion-controlled metal-assisted chemical etching method", Nano Letters **17**, 4304–4310 (2017).

[361] Y. Chen, L. Li, C. Zhang, C.-C. Tuan, X. Chen, J. Gao and C.-P. Wong, "Controlling kink geometry in nanowires fabricated by alternating metal-assisted chemical etching", Nano Letters **17**, 1014–1019 (2017).

[362] X. Li and P. Bohn, "Metal-assisted chemical etching in HF/H_2O_2 produces porous silicon", Applied Physics Letters **77**, 2572–2574 (2000).

[363] A. J. Bard, A. B. Bocarsly, F. R. F. Fan, E. G. Walton and M. S. Wrighton, "The concept of Fermi level pinning at semiconductor/liquid junctions. Consequences for energy conversion efficiency and selection of useful solution redox couples in solar devices", Journal of the American Chemical Society **102**, 3671–3677 (1980).

A. Complementary Figures

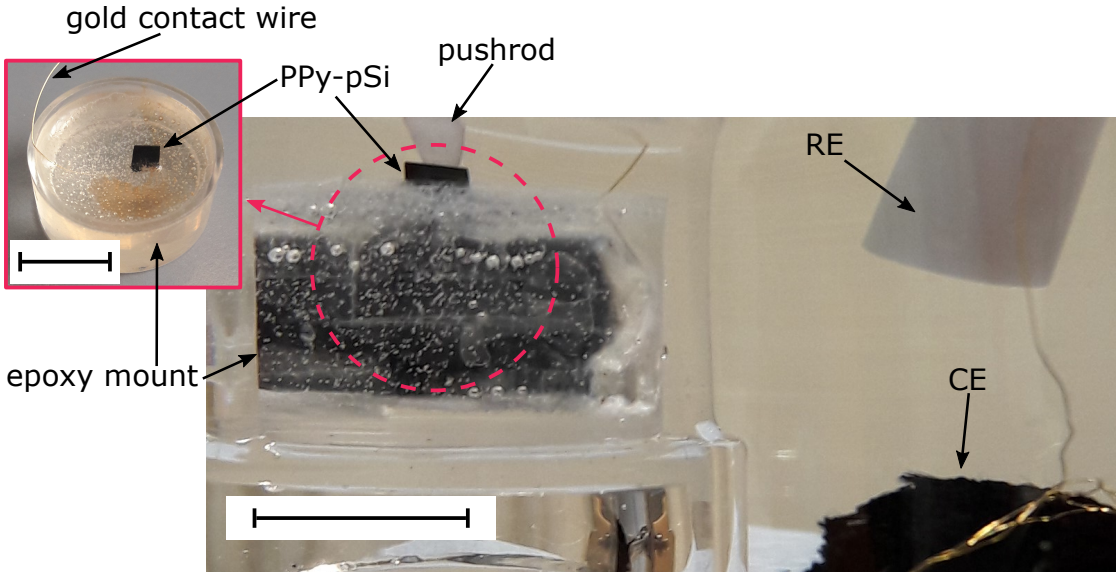

Figure A.1.: **Dilatometry setup for in situ actuation measurements.** (a) Picture of the in situ dilatometry setup with the epoxy-encased PPy-pSi membrane immersed in electrolyte solution and installed in the dilatometer with the glass pushrod on top. The membrane is contacted by a gold wire and connected to a potentiostat, which also contacts a reversible hydrogen RE and a carbon cloth CE. The inset shows a picture of the as-prepared epoxy-encased PPy-pSi membrane. The scale bars represent 1 ± 0.1 cm and provide an approximate length scale.

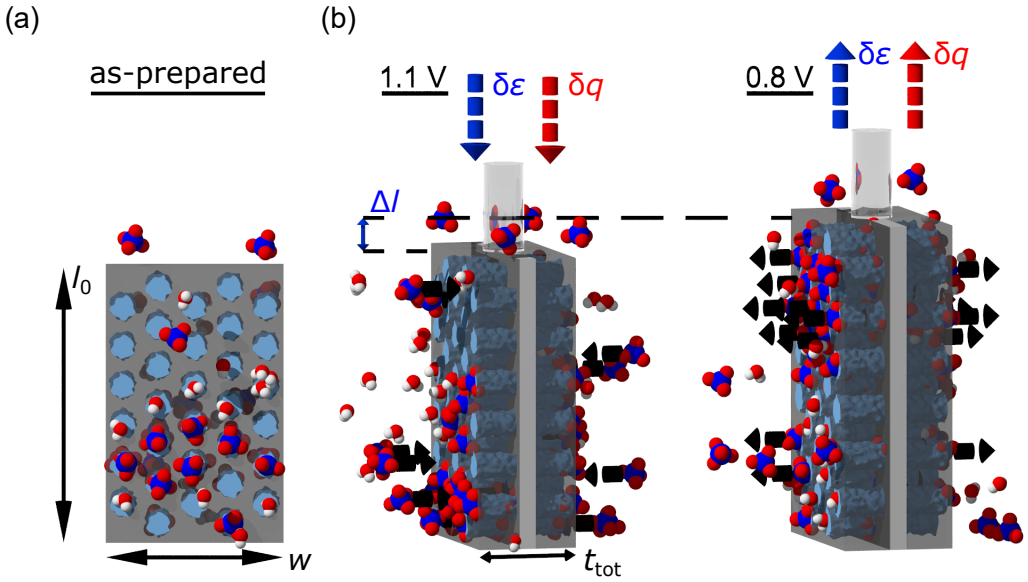

Figure A.2.: **Electrosorption-induced actuation mechanism of electrolyte-infiltrated porous silicon.** (a) The sample consists of two symmetrical porous layers (in dark grey) attached to a remaining bulk silicon layer in the middle (light grey). The pores are filled with electrolyte solution indicated by the blue colour and the ClO_4^- (blue, red) and H_2O (red, white) molecules. The dimensions of the as-prepared sample are length l_0, width w and total thickness t_{tot} (two porous layers in addition to the remaining bulk silicon layer in between). (b) The left section illustrates the case of an applied potential of 1.1 V. The ClO_4^- anions are accumulated on the porous silicon pore surface resulting in the contraction of the sample. Vice versa, in the right section a potential of 0.8 V is applied and the anions are expelled followed by the subsequent expansion of the sample. The change in length is indicated by Δl.

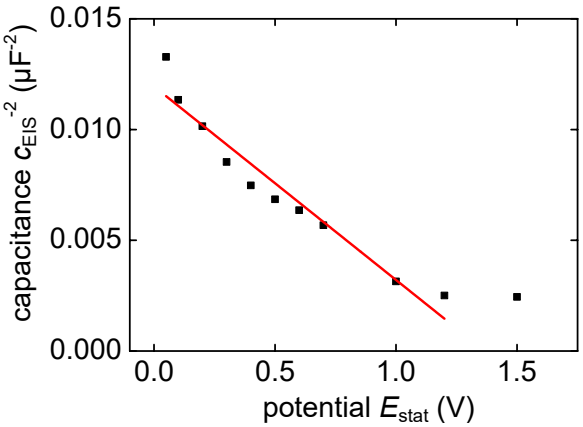

Figure A.3.: **Electrochemical impedance spectroscopy of electric double layer charging of an anodically oxidised bulk silicon electrode.** Mott-Schottky plot of an anodically oxidised porous silicon electrode in $1\,\mathrm{mol\,L^{-1}}$ perchloric acid. The capacitances determined by EIS are plotted in the form of c_{EIS}^{-2} versus the respective static potential E_{stat}. c_{EIS} is determined via EIS measurements with frequencies in the range of 1 MHz to 500 mHz and static potentials in the range of $0.05 - 1.5\,\mathrm{V}$. A linear fit to the Mott-Schottky plot yields a flatband potential of $V_{\mathrm{fb}} = 1.4 \pm 0.1\,\mathrm{V}$ and a doping concentration of $N_{\mathrm{a}} = (2.6 \pm 0.3) \cdot 10^{19}\,\mathrm{cm^{-3}}$.

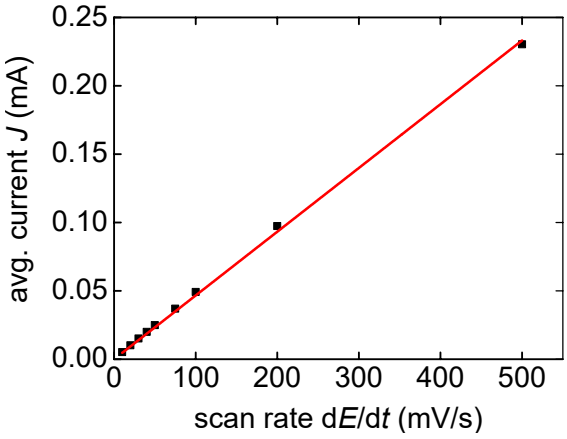

Figure A.4.: **Capacitance determination of a porous silicon sample installed in the cantilever bending setup.** Values for current J from CV measurements depicted in Figure 4.9(b), averaged in the potential range of 0.35 V to 0.45 V. Values are plotted versus increasing potential scan rate $\mathrm{d}E/\mathrm{d}t$ from $10\,\mathrm{mV\,s^{-1}}$ to $500\,\mathrm{mV\,s^{-1}}$. The red line shows a linear regression. It yields a capacitance of $c_{\mathrm{pSi,CB}} = 0.466 \pm 0.004\,\mathrm{mF}$.

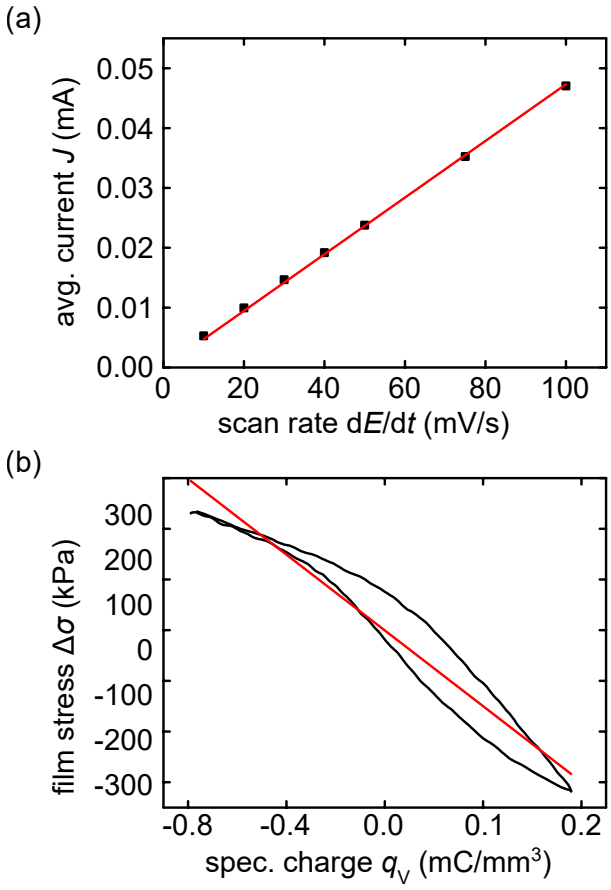

Figure A.5.: **Actuation parameters of the cantilever bending experiments in isotonic saline solution.** (a)Values for current J from CV measurements depicted in Figure 4.11(a), averaged in the potential range of 0.35 V to 0.45 V. Values are plotted versus increasing potential scan rate $\mathrm{d}E/\mathrm{d}t$ from $10\,\mathrm{mV\,s^{-1}}$ to $100\,\mathrm{mV\,s^{-1}}$. A linear regression (red line) yields a capacitance of $c_{\mathrm{pSi,CB,iso}} = 0.473 \pm 0.003\,\mathrm{mF}$. (b) Averaged film stress $\Delta\sigma$ versus averaged accumulated volume specific charge q_{V}, from Figure 4.11(b), and a linear fit, which yields a stress charge coupling parameter of $\xi = -374 \pm 2\,\mathrm{mV}$.

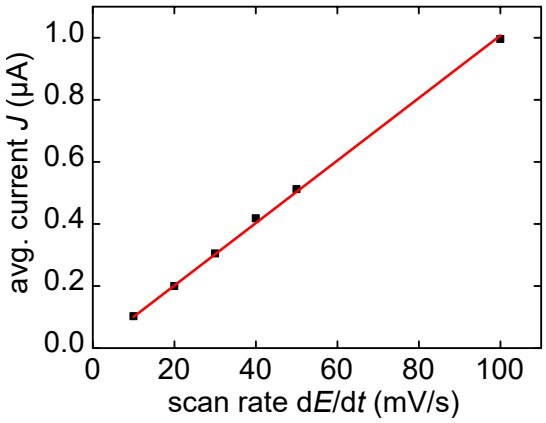

Figure A.6.: **Capacitance determination of a bulk silicon sample measured in the cantilever bending setup.** Values for current of J, averaged, from the CV measurements depicted in Figure 4.13(a), in the range of 0.6 V to 0.8 V and plotted versus increasing scan rate $\mathrm{d}E/\mathrm{d}t$. The red line indicates a linear regression and yields a capacitance of $c_{\mathrm{Si,CB}} = 10.07 \pm 0.08\,\mu\mathrm{F}$.

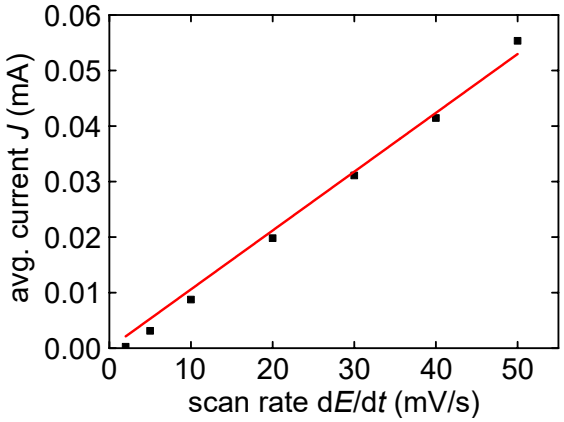

Figure A.7.: **Capacitance determination of n-type porous silicon.** Averaged values of current J in the CV measurement with potential range 0.3 V to 0.4 V, which is depicted in Figure 4.16(a). Values of J for different scan rates $2-50\,\mathrm{mV\,s^{-1}}$ plotted versus the respective scan rate. The capacitance derived from a linear fit amounts to $c_{\mathrm{n-type}} = 1.06 \pm 0.025\,\mathrm{mF}$.

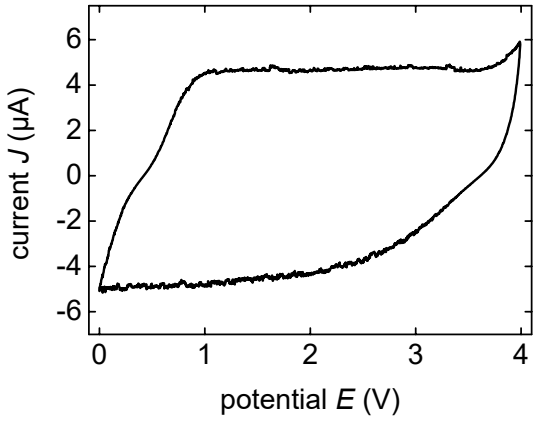

Figure A.8.: **Cyclic voltammetry measurement of n-type bulk silicon.** CV measurement on planar, n-type bulk silicon in perchloric acid performed in the laser cantilever setup for the measurement depicted in Figure 4.17. CV is conducted with a scan rate of $500\,\mathrm{mV\,s^{-1}}$ in the potential region of 0.0 V to 4.0 V.

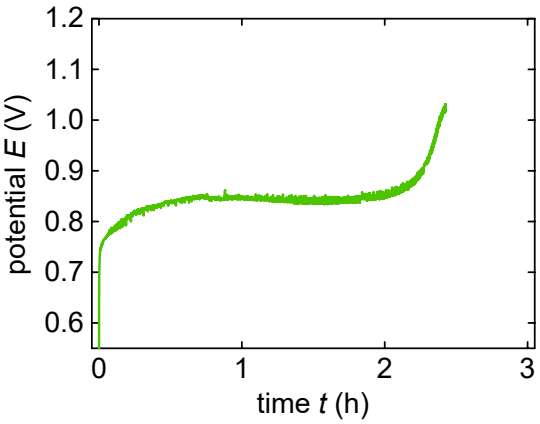

Figure A.9.: **Electrochemical polymerisation of polypyrrole in porous silicon.** Time evolution of potential E during the electrochemical polymerisation of pyrrole in a porous silicon epi-layer. The potential is stopped before the transition stage to a polymerisation of bulk polypyrrole on top occurs.

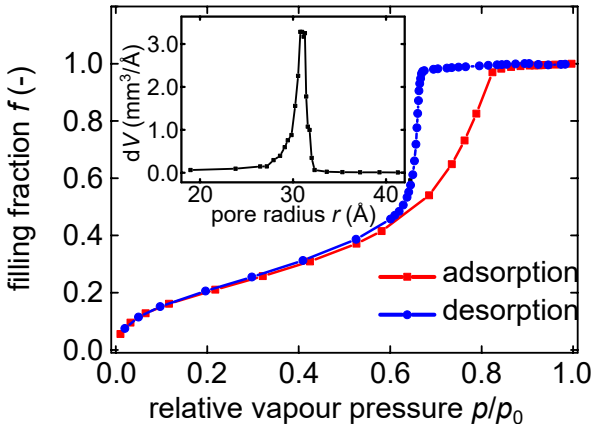

Figure A.10.: **Nitrogen sorption isotherm of a porous silicon epi-layer used for the filling by polypyrrole.** Nitrogen sorption isotherm measurement recorded for a porous silicon epi-layer with a thickness of 25.4 µm, which is investigated with regard to a polypyrrole filling in section 5.1. The inset shows the pore radius distribution obtained by analysis with the BJH model.

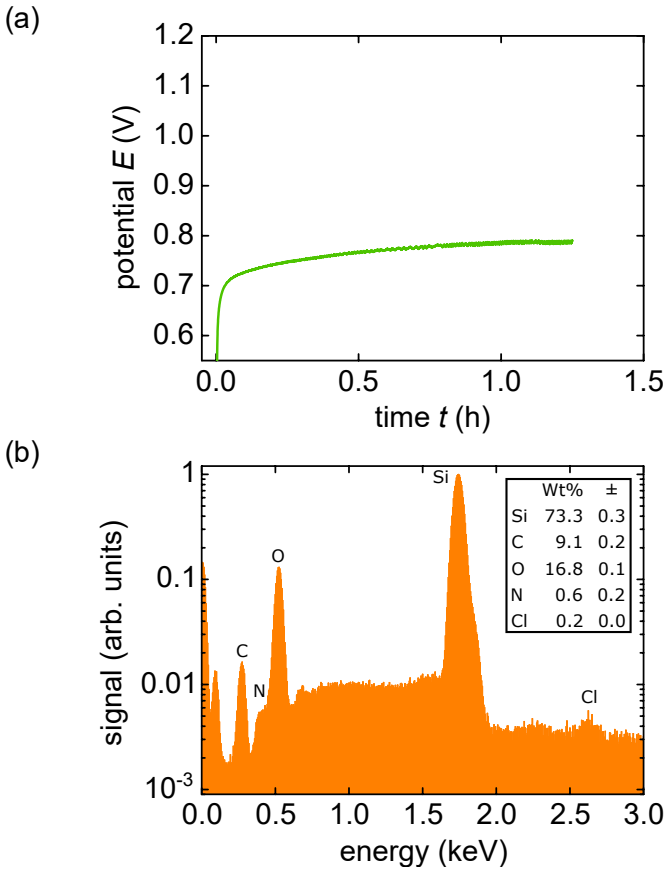

Figure A.11.: **Electrochemical polymerisation of polypyrrole porous silicon with a shorter polymerisation time.** (a) Electrochemical polymerisation of pyrrole in a porous silicon epi-layer with a thickness of 25.4 µm stopped at 1.2 h, which translates to approximately half of the pore filling time t_p determined for an equal epi-layer, see Figure 5.1(a). (b) Energy dispersive X-ray measurement recorded for a half-synthesised polypyrrole porous silicon hybrid.

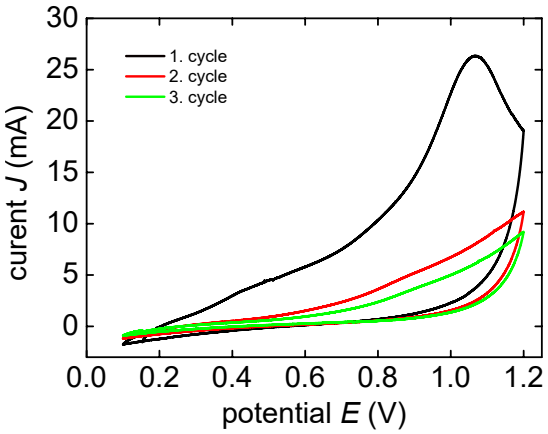

Figure A.12.: **Over-oxidation of bulk polypyrrole film.** CV measurement of a bulk polypyrrole film with a thickness of 500 nm. Conducted in the potential range of 0.1 V to 1.2 V with a scan rate of 10 mV s^{-1} in 1 mol L^{-1} perchloric acid. On the first cycle the over-oxidation of the polypyrrole is clearly visible at approximately 1.05 V when the current abruptly decreases due to the destruction of the film.

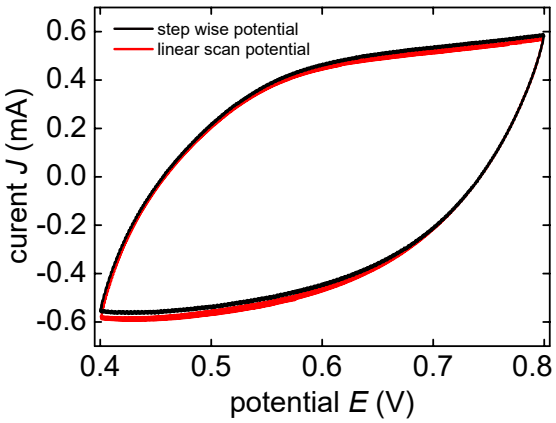

Figure A.13.: **Comparison of step-wise and linear cyclic voltammetry measurement.** CV measurements on a 25.4 µm thick polypyrrole-filled porous silicon epi-layer by a step-wise (black) and linear (red) procedure. The CVs are conducted in 1 mol L^{-1} perchloric acid with a scan rate of 10 mV s^{-1} in the potential region of 0.4 V to 0.8 V.

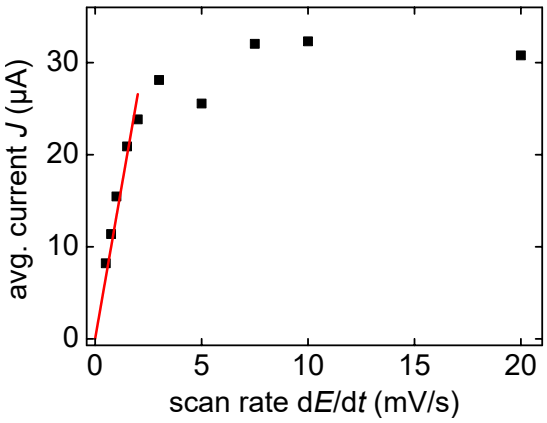

Figure A.14.: **Capacitance determination for a polypyrrole porous silicon membrane in isotonic saline solution.** Current values for the CV measurements conducted in isotonic saline solution depicted in Figure 5.8(a), averaged from 0.35 V to 0.45 V and plotted versus scan rate $\mathrm{d}E/\mathrm{d}t$. The red line is a linear regression for the determination of the capacitance, limited up to a scan rate of $2\,\mathrm{mV\,s^{-1}}$. It yields a capacitance of $13.3 \pm 0.7\,\mathrm{mF}$.

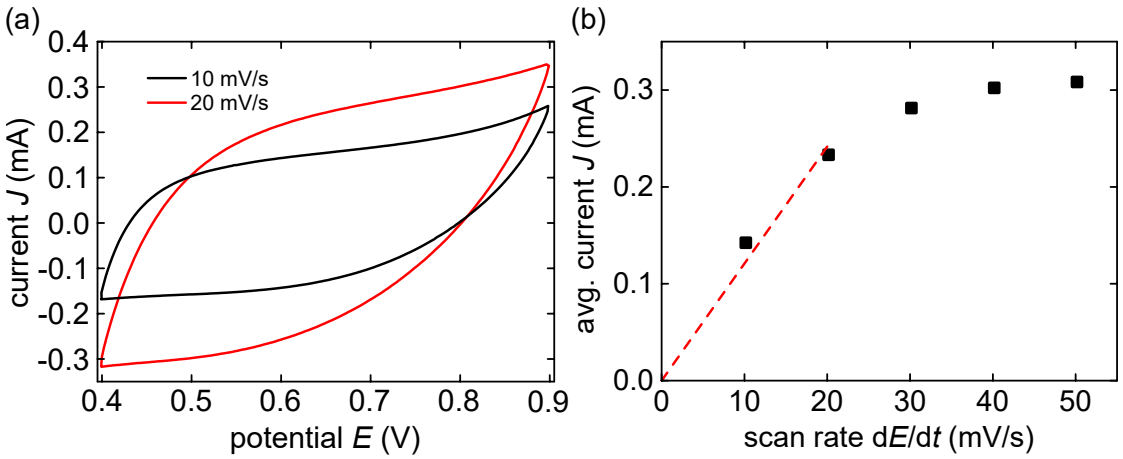

Figure A.15.: **Electrochemical characterisation for a electrochemical actuation measurement in the dilatometer.** (a) CV measurement of a PPy-pSi membrane installed in the in situ dilatometry setup, see Figure 5.9. CV conducted in $1\,\mathrm{mol\,L^{-1}}$ perchloric acid from 0.4 V to 0.9 V with scan rates of $10\,\mathrm{mV\,s^{-1}}$ and $20\,\mathrm{mV\,s^{-1}}$. Note that at $20\,\mathrm{mV\,s^{-1}}$ a diffusion limitation becomes visible. (b) Plot of averaged currents of the respective CV measurements versus their scan rate. The capacitance of the PPy-pSi hybrid is determined by a linear fit of the first two data points, which yields $12.1 \pm 0.7\,\mathrm{mF}$.

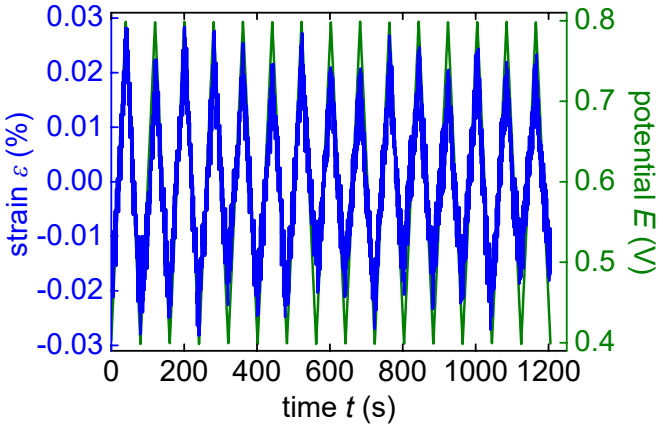

Figure A.16.: **Electrochemical actuation of a polypyrrole porous silicon membrane.** In situ dilatometry measurement of a PPy-pSi membrane in perchloric acid in the potential range of 0.4 V to 0.9 V with a scan rate of 10 mV s^{-1} with 15 representative cycles of potential E and effective strain ε of the same PPy-pSi membrane hybrid also shown in Figure 5.9.

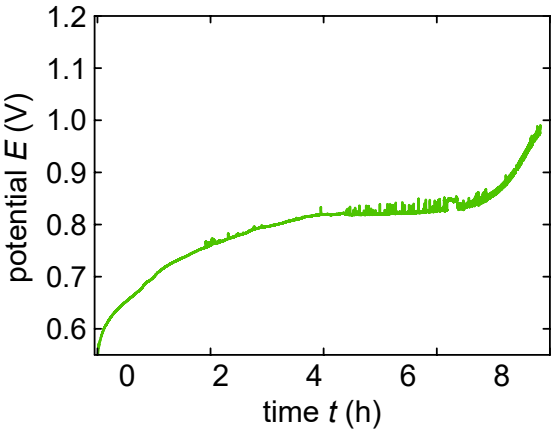

Figure A.17.: **Electrochemical polymerisation of polypyrrole in a porous silicon membrane.** Time evolution of potential E during the electrochemical polymerisation of pyrrole with a current density of 0.255 mA cm^{-2} in a porous silicon membrane with a thickness of 70 µm. The lateral size of the porous silicon membrane amounts to 1.981 cm^2. The mass difference through the polymer filling is 0.004 51 g, which results in a density of polypyrrole inside the pore space of 0.65 g cm^{-3}.

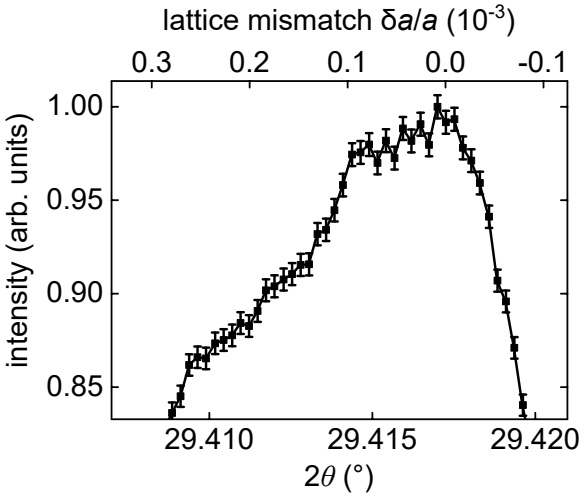

Figure A.18.: **X-ray diffraction measurement of 400 silicon Bragg peak with error bars.** Close up of the 400 Si Bragg peak in the out-of-plane direction for as-prepared PPy-pSi sample S_{refl}, extracted from the $\theta - 2\theta$ scan displayed in Figure 5.15. Ordinate is displayed in linear scale, normalised to the intensity of the peak. Lower abscissa shows angle 2θ and upper abscissa the lattice mismatch $\delta a/a_{\perp}$. The intensity uncertainty, i.e. the error bars, for every single data point is derived from the angular uncertainty, see equation 3.14

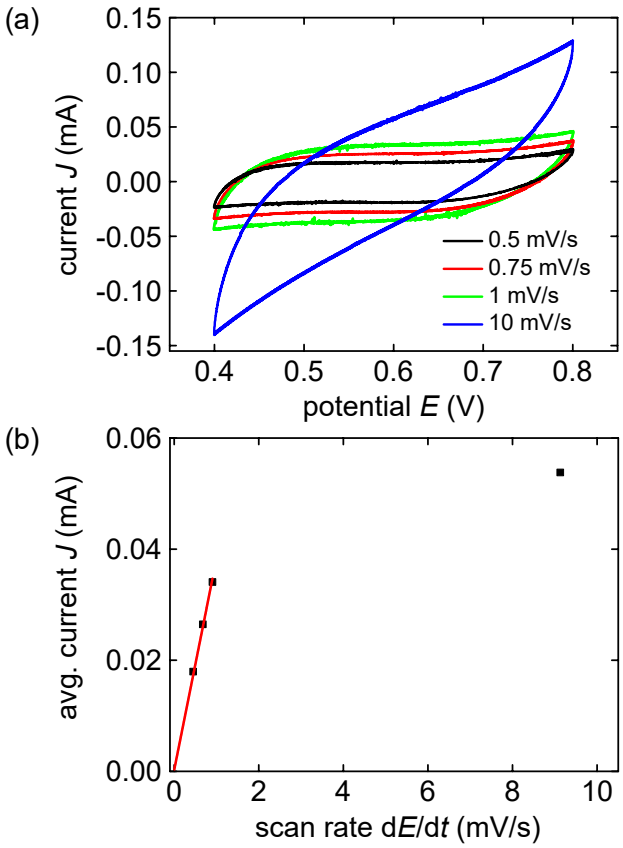

Figure A.19.: **Electrochemical characterisation of S_{refl}.** (a) Exemplary cyclic voltammetry measurements of PPy-pSi hybrid sample S_{refl} of the in situ XRD study on electrochemical characterisation in reflection geometry. Conducted in $1\,\mathrm{mol\,L^{-1}}$ $HClO_4$ electrolyte solution. The potential range is $0.4 - 0.8\,\mathrm{V}$ and scan rates are increasing from $0.5\,\mathrm{mV\,s^{-1}}$ to $10\,\mathrm{mV\,s^{-1}}$. (b) Averaged current in the potential range of $0.55 - 0.65\,\mathrm{V}$ plotted versus the respective scan rate to determine the capacitance by a linear fit, indicated by the red line. Due to diffusion limitation, only the first three data points are considered, which yields a capacitance of $34.7 \pm 0.5\,\mathrm{mF}$ or $29300 \pm 400\,\mathrm{mF\,cm^{-3}}$ normalised to the pSi layer volume.

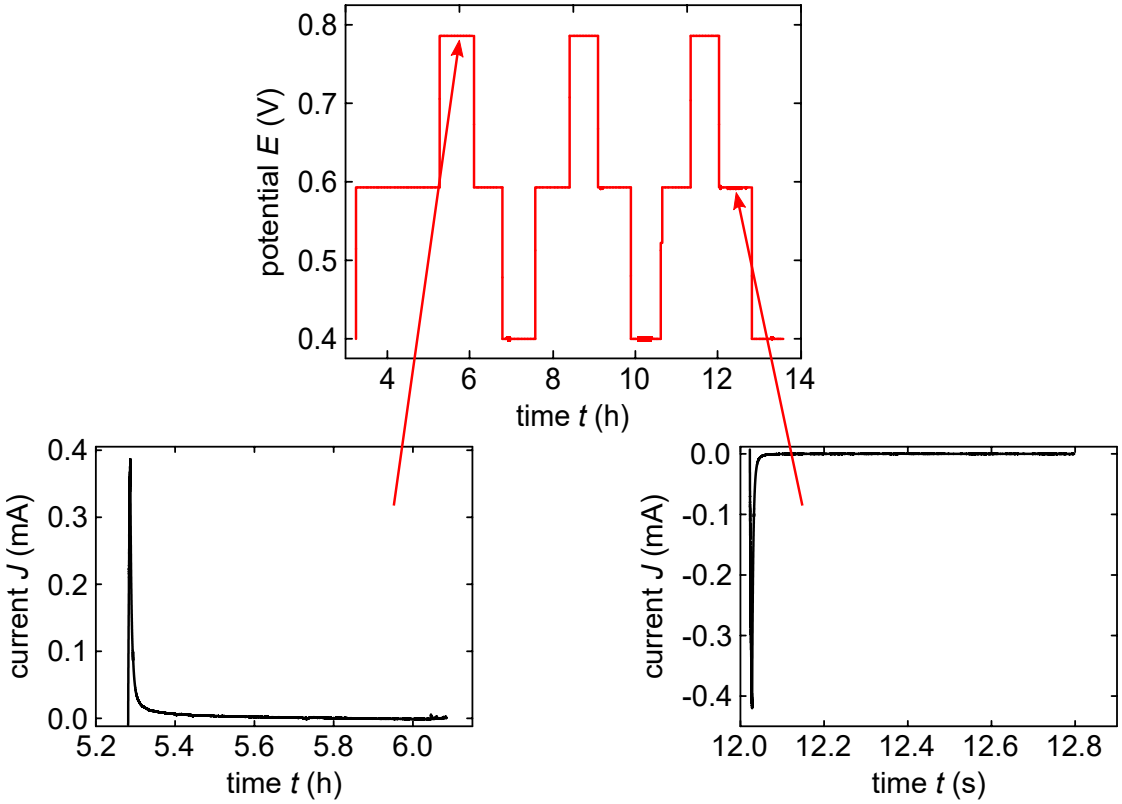

Figure A.20.: **Electrochemical control during the XRD measurement.** Method to assert electrochemical control during a $\theta - 2\theta$ measurement, see Figure 5.18. Upper graph depicts the stepwise adjustment of potential 0.4 V over 0.6 V to 0.8 V and back. Each potential step is applied for the duration of the XRD measurement. The two lower graphs exemplarily show the response of current J at an increasing (left) and decreasing (right) potential step. The charge q_V can be inferred by integration of current J.

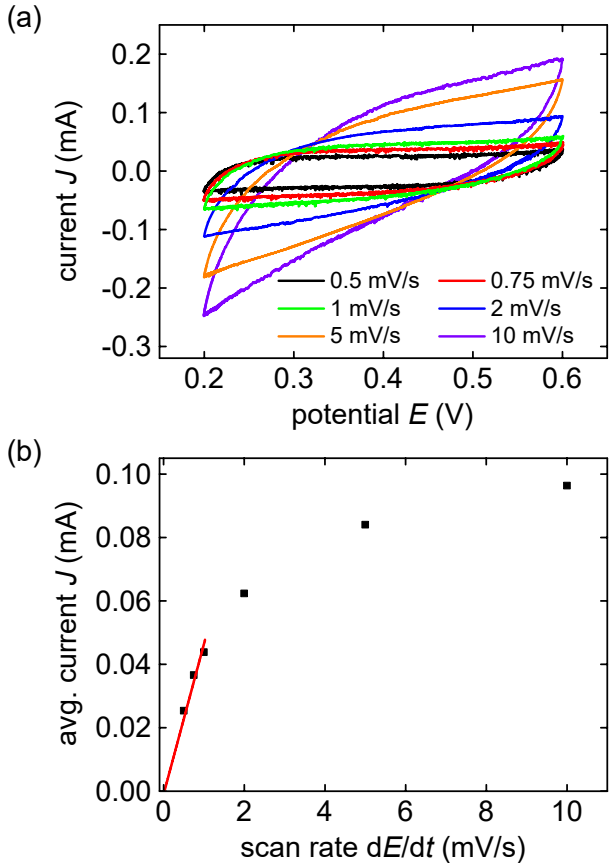

Figure A.21.: **Electrochemical characterisation of S_{trans}.** (a) Exemplary cyclic voltammetry measurements of PPy-pSi hybrid sample S_{trans} of the in situ XRD study on electrochemical characterisation in transmission geometry. Conducted in $1\,mol\,L^{-1}$ $HClO_4$ electrolyte solution. The potential range is $0.4 - 0.8\,V$ and scan rates increase from $0.5\,mV\,s^{-1}$ to $10\,mV\,s^{-1}$. (b) Averaged current in the potential range of $0.55 - 0.65\,V$ plotted versus the respective scan rate to determine the capacitance by a linear fit, indicated by the red line. A diffusion limitation is present. Thus, not all data points are considered for a fit to obtain the capacitance. Here, only the first three data points are considered. The obtained volumetric capacitance is $49.4 \pm 0.9\,mF$ or $30800 \pm 600\,mF\,cm^{-3}$ normalised to volume. Its capacitance compares well to the one of S_{refl}.

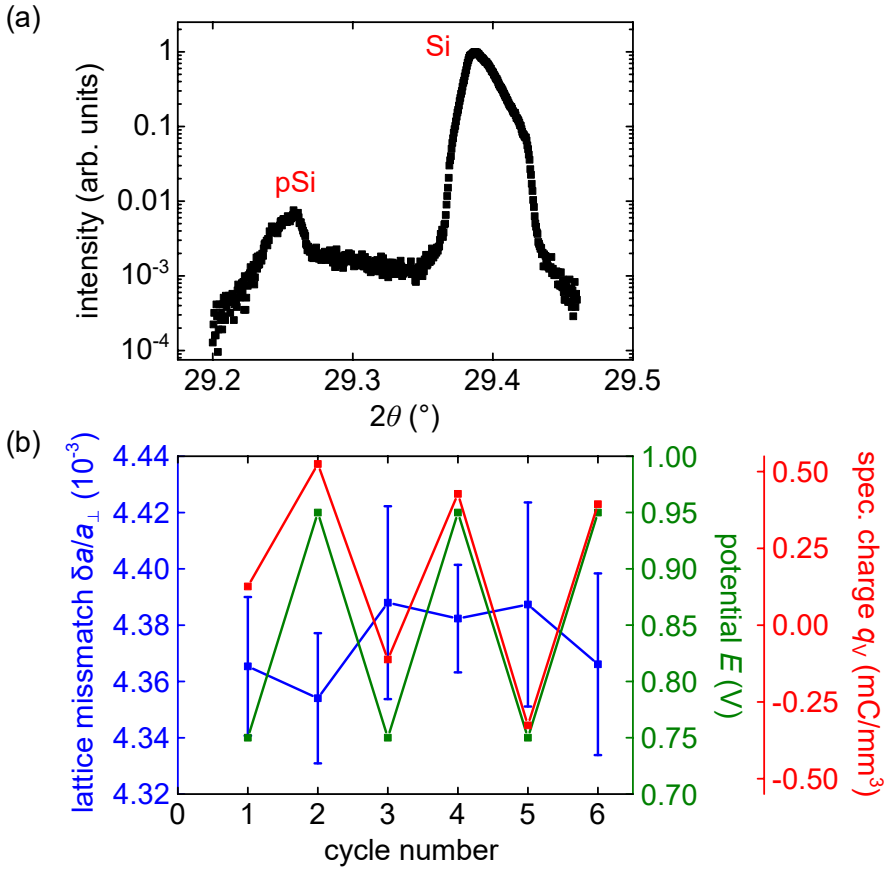

Figure A.22.: **X-ray diffraction measurement on** 400 **Bragg peak for anodically oxidised porous silicon.** (a) XRD $\theta - 2\theta$ scan of porous silicon on the 400 Bragg peak in reflection geometry. An anodic oxidation of the porous silicon sample is performed with an applied potential of 1.2 V for 16.5 h, as established in section 4.1. Ordinate shows the intensity in arbitrary units in logarithmic scale, normalised to the silicon peak (Si) intensity. The abscissa shows angle 2θ. Clearly visible are the 400 Bragg peak from the silicon layer and the smaller peak from the porous silicon layer. The established fit procedure yields $2\theta = (23.389 \pm 0.002)\,^\circ$ and $2\theta = (29.2590 \pm 0.0004)\,^\circ$ for Si main and pSi peak. The shape of both peaks is different to the PPy-pSi sample, cf. Figure 5.17. The shoulder on the Si peak is not as pronounced and the pSi peak is narrower. The lattice mismatch amounts to $\delta a/a_\perp = (+4.31 \pm 0.07) \cdot 10^{-3}$, which is about twice as large as the lattice mismatch in out-of-plane direction of the PPy-pSi hybrid. Thus, the oxidation procedure leads to a significant strain, which has also been observed in literature.[141] (b) Lattice mismatch $\delta a/a_\perp$ (blue) in dependence of applied potential steps (green) from 0.75 V to 0.95 V and the resulting volumetric charge q_V (red). Within the error bars, no dependence of $\delta a/a_\perp$ on E can be ascertained.

B. Surface States

This supplementary section adds information on surface states. They are not essential to the understanding of this work but are interesting in the context of anodic oxidation and the overall properties of the silicon electrolyte interface.
A Lewis acid site accepts electron pairs from an adsorbed molecule and thus renders the solution more acidic. For instance a Lewis acid site might attract a hydroxide ion (OH^-) from water. Conversely, a Lewis basic site acts as an electron pair donor with respect to an adsorbed molecule and thus causes a basic shift in the electrolyte. An example would be the adsorption of a hydrogen ion (H^+). Lewis sites contribute to the electric double layer and they also contribute to an adsorption of ions and thus to the occupation of intrinsic active surface sites.[120] At the silicon surface basic Lewis sites are dominant as silicon features a swift hydrogen adsorption.
In genera,l the energy of surface states can be considered as bands because a variety of surface inhomogeneities, as vacancies, steps, kinks, emergent dislocations and other atoms lead to a broadening of the specific surface state energy. In the case of an emerging bulk silicon oxide film on the silicon surface, different states and charges which exist in the oxide film can also be considered as surface states.
A realistic description of the surface states in semiconductors is an intricate task due to the abundance of different types of surface states.[134] Generally, the surface states are energetically located within the bandgap of the semiconductor. The respective charge density Q_{SS} is a function of the band bending potential V_S. A quantitative description can only be obtained for some idealising assumptions. In this regard, it is assumed that the surface states are located, for instance, at a single energy level or are uniformly distributed. The latter is described for acceptor surface states with a centre energy of E_0 as [363]

$$Q_{SS} \approx eN_{SS}\left(E_0 - eV_S - E_F\right) \cdot \frac{1}{E_0}, \tag{B.1}$$

where N_{SS} is the total number of surface states per cm^2. Q_{SS} becomes zero if $eV_S = E_0 - E_F$. In contrast, if the surface states are at a single energy E_{SS}, Q_{SS} is approximated by [363]

$$Q_{SS} \approx \frac{eN_{SS}}{1 + g_{SS}^{-1} \exp\left(-\frac{E_{SS} - 2V_S - E_F}{k_B T}\right)}, \tag{B.2}$$

where g_{SS} denotes the degeneracy of the energy level. The differential capacitance associated with the surface states can be expressed by

$$C_{SS} = \frac{\mathrm{d}Q_{SS}}{\mathrm{d}V_S}. \tag{B.3}$$

This capacitance differentiates itself from the space charge region capacitance C_{scr} or the Helmholtz layer capacitance C_H, in that there is no length scale related to the surface state capacitance.

A high density of surface states might influence the Mott-Schottky plot since the assumption of $C_{SS} \ll C_{scr}$ is not valid. The Mott-Schottky plot is then divided into three regions. Fully unoccupied donor surface states or fully occupied acceptor surface states result in an evolving positive surface charge of $+Q_d$ and $-Q_a$, respectively. For both cases the Mott-Schottky plot has the same slope as without assumed surface states. Yet, for mono-energetic surface state, V_{fb} is shifted either to higher values by $+Q_d/V_H$ for donor or to lower values by $-Q_a/V_H$ for acceptor surface states. In the Mott-Schottky plot this becomes apparent by a changing intersect. In an intermediate region, between the two extreme occupancy cases, the Fermi level might be pinned in the potential range of the two types of surface states. An applied potential is therefore rather dropped in the Helmholtz layer and not in the SCR. Thus, the capacitance measured in this intermediate region has no or only a small dependence on a changing potential. The lower the slope in this central region is, the higher the density of surface states.